Plasma Physics Reports, Vol. 27, No. 6, 2001, pp. 455–461. Translated from Fizika Plazmy, Vol. 27, No. 6, 2001, pp. 483–490.

DUSTY PLASMA

Shock Structure Formation in Dusty Plasmas

S. I. Popel*, A. P. Golub'*, T. V. Losseva*, R. Bingham, and S. Benkadda*****

**Institute of Geosphere Dynamics, Leninskiĭ pr. 38-6, Moscow, 117979 Russia*

***Rutherford Appleton Laboratory, Chilton, Didcot, Oxfordshire, OX11 OQX, UK*

****Equipe Dynamique des Systèmes Complexes, CNRS–Université de Provence, Centre de Saint Jérôme, Case 321, F-13397 Marseille Cedex 20, France*

Received October 17, 2000

Abstract—The problem of the evolution of a perturbation in a dusty plasma and its transformation into a nonlinear wave structure is considered. A computational method that allows one to solve the set of nonlinear evolutionary equations describing variable-charge dust grains, Boltzmann electrons, and inertial ions is developed. Exact steady-state solutions corresponding to ion-acoustic shock structures associated with anomalous dissipation originating from dust grain charging are found taking into account the effect of electron and ion charge separation. The role of this effect increases with the speed of the shock. The evolutions of an initial soliton (which is a steady-state wave solution in a plasma containing dust grains with a constant charge) and an initially immobile perturbation with a constant increased ion density are investigated. In a charge-varying dusty plasma, the soliton evolves into a nonsteady shock wave structure that propagates at a constant speed and whose amplitude decreases with time. The initially immobile perturbation with a constant increased ion density evolves into a shock structure similar to a steady-state shock wave. In the latter case, the compression shock wave is accompanied by a rarefaction region (dilatation wave), which finally leads to the destruction of the shock structure. The solution of the problem of the evolution of a perturbation and its transformation into a shock wave in a charge-varying dusty plasma opens up the possibility of describing real phenomena (such as supernova explosions) and laboratory and active space experiments. © *2001 MAIK "Nauka/Interperiodica".*

1. INTRODUCTION

Plasma–dust systems usually cannot survive in the absence of either external sources of electrons and ions or plasma particle fluxes from dust-free regions. The electron and ion fluxes are absorbed by dust grains; as a result, the charges of the latter vary. The enhanced dissipativity of the plasma–dust system originating from dust grain charging [1] points to the decisive role of dissipative structures (similar to shock waves) in dusty plasmas.

Shock waves often arise in nature because of the balance between nonlinear effects leading to wave breaking and dispersion or dissipative effects. For collisional and collisionless shock waves, the shock structure is determined by the friction between the particles [2] or the wave–particle interaction [3], respectively. In dusty plasmas, anomalous dissipation that originates from dust charging results in the possibility of the existence of a new kind of shock wave related to this dissipation. These shock waves are collisionless in the sense that they do not involve electron–ion collisions. However, in contrast to classical collisionless shock waves, the dissipation due to dust charging involves interaction of the electrons and ions with dust grains in the form of microscopic grain currents. The case of a fairly intense shock wave corresponds to ion-acoustic wave propagation. The main results concerning this new kind of ion acoustic shock were obtained in [4–6]. Recently, the first laboratory experimental results confirming the effect of negatively charged dust on the formation of an ion-acoustic shock were obtained [7, 8].

The importance of shock waves in dusty plasmas is associated with different astrophysical applications [5]. For example, according to modern concepts [9], the formation of stars occurs mainly in interstellar dust–molecular clouds after compression shock waves have propagated through them, creating the initial density condensations for further gravitational contraction. The presence of dust in interstellar clouds can significantly influence the magnitude of the sound velocity, not to mention the shock wave propagation. The investigation of shock waves related to the dissipation originating from dust particle charging may also be important [5, 6, 10] for the description of shocks in supernova explosions, particle acceleration in shocks, the explanation of the results of active space experiments involving the release of a gaseous substance in the Earth's ionosphere, etc.

In spite of the importance of shock structures in dusty plasmas, the question of whether the evolution of an arbitrary perturbation leads to the formation of shocks in a charge-varying dusty plasma is still open. All previous investigations have dealt with steady or quasi-steady shocklike solutions. However, it is the solution of the problem of the evolution of a perturbation and its transformation into a shock wave that will allow us to investigate in detail (taking into account charge-varying macroparticles) real phenomena (such

1063-780X/01/2706-0455$21.00 © 2001 MAIK "Nauka/Interperiodica"

as supernova explosions) and laboratory and active space experiments. Furthermore, the solution of this problem makes it possible to understand whether the shock structures are the main nonlinear wave structures in dusty plasmas.

This paper is the first one that deals with the problem of the evolution of a perturbation in a charge-varying dusty plasma and its transformation into a nonlinear wave structure. We consider the case of the plasma and wave parameters corresponding to those of [4], in which the possibility of the existence of steady-state shock wave solutions related to the dissipation originating from dust particle charging was shown. In Section 2, we describe the main assumptions and basic equations and present the exact steady-state solutions of the problem. We take into account the effect of charge separation, which was neglected in [4], and, thus, refine the results of [4]. In Section 3, we describe the numerical method used to investigate the evolution of a perturbation in a dusty plasma. In Sections 4 and 5, we consider the evolution of different initial perturbations. In Section 4, the evolution of a soliton (which is a steady-state wave solution in a plasma containing macroparticles with a constant charge [11]) is studied. In Section 5, we consider the evolution of an intense, initially immobile perturbation with a constant increased ion density. A summary of our findings and conclusions are given in Section 6.

2. STEADY-STATE SHOCK WAVE SOLUTIONS

We assume that a dusty plasma possesses the following properties [4, 5]:

(i) The electron and ion plasma components are collisionless and unmagnetized. The plasma contains dust grains; in an unperturbed state, it is uniform.

(ii) The time scale corresponds to ion-acoustic wave propagation.

(iii) The dust grain charge varies solely due to the microscopic electron and ion grain currents originating from the potential difference between the plasma and the grain surface.

(iv) The average radius a of dust grains is much smaller than the electron Debye length λ_D, the spatial scale of perturbations, and the distance between the plasma particles.

(v) Dust grains are negatively charged (the absolute charge value can exceed $10^3 e$, where $-e$ is the electron charge).

(vi) Dust grains are massive ($m_i Z_d \ll m_d$, where $m_{i,d}$ are the ion and dust masses and $q_d(x) = -Z_d e$ is the average dust grain charge). In this case, the dust can be considered immobile and the density n_d is constant on the ion-acoustic time scale.

(vii) In the absence of perturbations, the quasineutrality condition $n_{i0} = n_{e0} + Z_d n_d$ (where the subscript 0 denotes unperturbed quantities) holds.

(viii) The orbit-limited probe model [12, 13] is valid.

(ix) Nonlinear waves propagate along the x-axis.

To consider the problem of the evolution of a perturbation and its transformation into a nonlinear wave structure in a charge-varying dusty plasma, we use the same set of equations as in [4]. The average charge of the immobile dust grains is governed by the charge conservation law [11, 14, 15]

$$\partial_t q_d = I_e(q_d) + I_i(q_d), \tag{1}$$

where the microscopic electron and ion grain currents (for equilibrium electrons and kinetic ions) are [13, 15–17]

$$I_e \approx -\pi a^2 e\left(\frac{8T_e}{\pi m_e}\right)^{1/2} n_e \exp\left(\frac{eq_d}{aT_e}\right), \tag{2}$$

$$I_i = \sqrt{\frac{\pi}{2}} a^2 v_{Ti} e n_i \left[2\exp\left(-\frac{v_i^2}{2v_{Ti}^2}\right) + \sqrt{2\pi}\frac{v_{Ti}}{v_i}\left(1 + \frac{v_i^2}{v_{Ti}^2} - \frac{2eq_d}{am_i v_{Ti}^2}\right)\mathrm{erf}\left(\frac{v_i}{\sqrt{2}v_{Ti}}\right)\right]. \tag{3}$$

Here, m_e is the electron mass, T_j and v_{Tj} are the temperature and thermal velocity of the jth species ($j = i, e$), v_i is the ion fluid velocity, and $\mathrm{erf}(x)$ is the error function. We use the complete formula for I_i [16] in order to account for slow ions, which should be included for physical consistency in the low-φ region of the shock structure [4]. The ions and electrons entering the dust grain recombine into neutral atoms, which then reenter the plasma and reionize, thus preserving the number of ions and electrons.

The electron density is assumed to obey the Boltzmann distribution ($n_e = n_{e0}\exp(e\varphi/T_e)$) with a constant temperature T_e. The ion density n_i and velocity v_i obey the ion conservation equations (continuity and momentum transfer equations); we also assume that $v_i \gg v_{Ti}$, which imposes a lower limit on the magnitude of the electrostatic potential φ of nonlinear waves. Furthermore, we use Poisson's equation for the electrostatic potential:

$$\partial_{xx}^2 \varphi = 4\pi e(n_e + Z_d n_d - n_i). \tag{4}$$

In [4], quasi-steady structures moving with a speed V ($v_{Ti} < V \ll v_{Te}$) in the x direction and satisfying the above equations were considered. Such structures are shock waves that exist because of the efficient dissipation related to dust grain charging. In [4], the profiles of steady-state shocks (whose parameters depend on $\xi = x - Vt$ only) were obtained under the assumption that the left-hand side of Poisson's equation is negligibly small. Thus, the effect of charge separation was neglected.

We investigated the influence of this effect on the propagation of steady-state shocks. This effect does not influence the conditions under which shock waves exist. In particular, steady-state shocks exist for the Mach numbers $M \equiv V/c_s$ (where $c_s = (T_e/m_i)^{1/2}$ is the ion-acoustic speed) that obey the inequalities

$$1 + Z_{d0}d = M_1^2 \geq M^2 > M_0^2 \equiv 1 + \frac{z_0}{G + z_0 Z_{d0} d}, \quad (5)$$

where $G = [1 + (z_0 + T_i/T_e)^{-1}]^{-1}$, $d = n_{d0}/n_{e0}$, and $z_0 = Z_{d0}e^2/aT_e$. The range of Mach numbers that is determined by inequalities (5) is rather narrow. For example, for $Z_{d0}d = 2$, $T_e/T_i = 10$, and $a/\lambda_D = 0.01$ we have $M_0 \approx 1.42$ and $M_1 \approx 1.73$.

The effect of the electron and ion charge separation manifests itself in the appearance of oscillations in the shock wave profile. The effect becomes stronger as M increases. This is seen from Figs. 1 and 2, which show steady-state shock wave solutions for two cases. In Fig. 1, the profiles of the potential $\varphi(\xi)$; the electric field $E = -d_\xi\varphi$; the normalized charge perturbation δz; and the ion density n_i, normalized to the unperturbed electron density n_{e0}, are presented for $Z_{d0}d = 2$, $T_e/T_i = 10$, $a/\lambda_D = 0.01$, and $M = 1.5$. Here, we introduced the following dimensionless variables: $e\varphi/T_e \longrightarrow \varphi$, $\xi/\lambda_D \longrightarrow \xi$, $\delta z = -e\delta q_d/aT_e$, and $\delta q_d = q_d - q_{d0}$. In this case, oscillations in the shock structure profiles are very small and the effect of charge separation is suppressed. Figure 2 shows the same profiles for the same plasma and dust parameters as in Fig. 1, but for $M = 1.68$. In Fig. 2, the effect of electron and ion charge separation is significant. The fact that the dust does not contribute to this effect is clearly seen in Fig. 2c; one can see that there are no oscillations in the profile of the perturbations of the normalized dust grain charge δz. We emphasize that oscillations in the ion-acoustic shock wave profile related to the effect of charge separation in a dusty plasma were observed experimentally in [7].

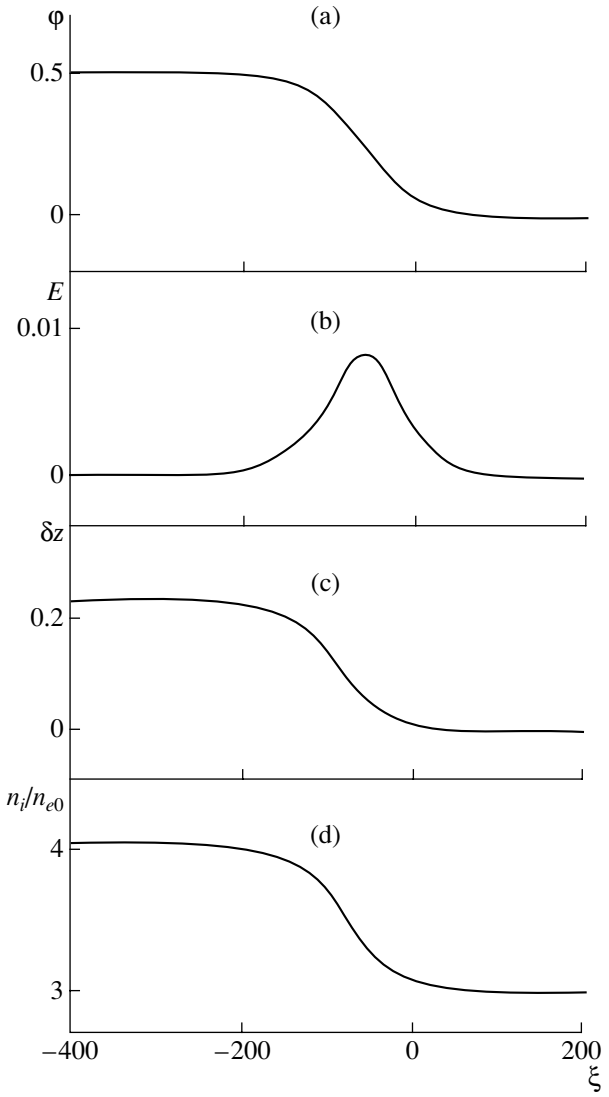

Fig. 1. Profiles of (a) $\varphi(\xi)$, (b) $E(\xi) = -d_\xi\varphi(\xi)$, (c) $\delta z(\xi)$, and (d) $n_i(\xi)/n_{e0}$ in a steady-state shock wave structure for $Z_{d0}d = 2$, $T_e/T_i = 10$, $a/\lambda_D = 0.01$, and $M = 1.5$.

3. COMPUTATIONAL METHOD

To consider the evolution of a perturbation in a charge-varying dusty plasma and its transformation into a nonlinear wave structure, we have developed the following computational method.

To solve the continuity equation and the momentum transfer equation for ions, we use the modification LCPFCT of the flux-corrected transport (FCT) algorithm with fourth-order phase accuracy, second-order time accuracy, and minimum residual diffusion [18]. The FCT is a monotonic, conservative, and positivity-preserving algorithm. This means that the algorithm is accurate and resolves steep gradients (including grid scale resolution). When a convected quantity (such as the ion density) is initially positive, it remains positive and no new maxima or minima are introduced due to numerical errors during convection.

The formulation of the LCPFCT transport algorithm consists of the following four sequential stages:

(i) computation of the intermediate value of the convected quantity taking into account stabilizing diffusion and selection of the diffusion coefficients in order to satisfy monotonicity,

(ii) computation of the raw antidiffusive fluxes,

(iii) correction or limitation of these fluxes to assure monotonicity, and

(iv) performance of the indicated antidiffusive correction.

To solve Eq. (1) for dust grain charging, we use the well-known Runge-Kutta method [19] with fourth-order accuracy. Poisson's equation (4) is solved numerically using the sweep method [18].

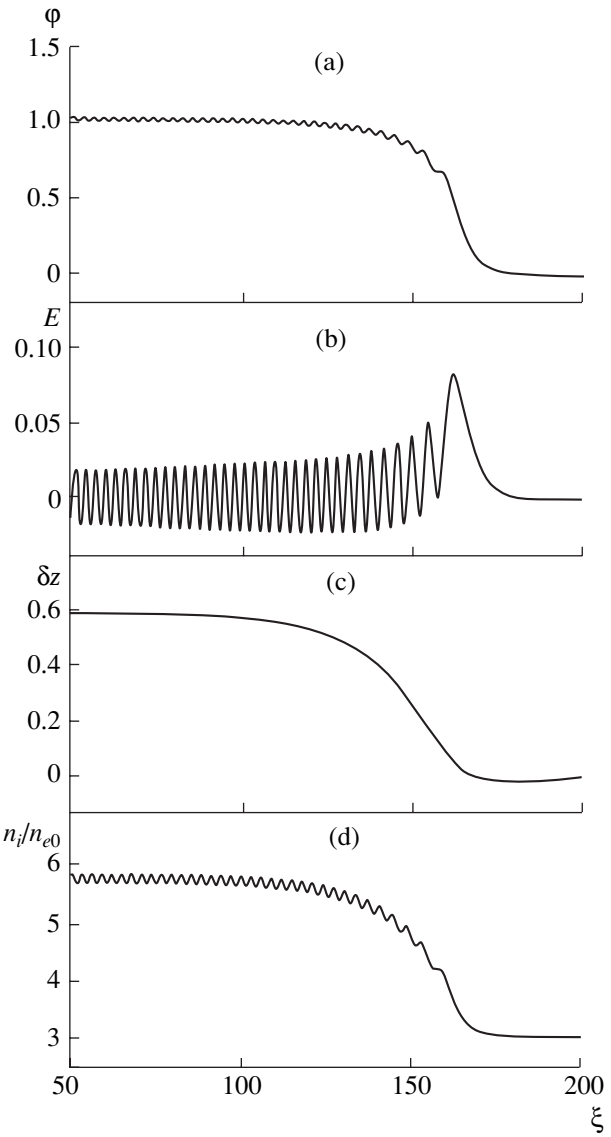

Fig. 2. Profiles of (a) $\varphi(\xi)$, (b) $E(\xi) = -d_\xi\varphi(\xi)$, (c) $\delta z(\xi)$, and (d) $n_i(\xi)/n_{e0}$ in a steady-state shock wave structure. The parameters are $Z_{d0}d = 2$, $T_e/T_i = 10$, $a/\lambda_D = 0.01$, and $M = 1.68$.

The total set of equations is solved using the following operation sequence (at every time step):

(i) integration of the conservation equations,

(ii) integration of the equation for dust grain charging, and

(iii) integration of Poisson's equation.

These three stages are related to each other by the iteration procedure, which is controlled by the charge density convergence.

The above computational method was tested by the examples of steady-state soliton solutions in dusty plasmas (without allowance for dust grain charging) and the steady-state shock wave solutions presented in Figs. 1 and 2 (with allowance for dust grain charging). The tests showed that the corresponding steady-state solutions remained the same when solving time-dependent problems.

4. EVOLUTION OF A SOLITON

As was mentioned above, a soliton is a steady-state wave solution propagating with a constant speed M in a plasma containing macroparticles with a constant charge. Under assumption (vi) of Section 2, the soliton solution in such a plasma can exist for the Mach numbers obeying the inequalities

$$M^2 > 1 + Z_{d0}d, \tag{6}$$

and

$$\exp(M^2/2) + M^2 Z_{d0}d/2 \le 1 + (1 + Z_{d0}d)M^2. \tag{7}$$

Comparing inequalities (5) and (6), we can easily see that the soliton velocities are higher than the velocities of steady-state shocks (of course, we should remember that steady-state solutions in the form of solitons and shocks exist in plasmas containing macroparticles with constant and variable charges, respectively).

Here, we consider the problem of the evolution of an initial soliton (which is a steady-state wave solution in a plasma containing macroparticles with a constant charge) and its transformation into a nonlinear wave structure in a charge-varying dusty plasma. We consider the situation when, in the absence of wave perturbations, the initial dust grain charge is in equilibrium. We use the normalization $x/\lambda_D \longrightarrow x$ for the spatial variable and $tc_s/\lambda_D \longrightarrow t$ for time. The results of calculations describing the evolution of an initial soliton in a dusty plasma with $Z_{d0}d = 2$, $T_e/T_i = 10$, and $a/\lambda_D = 0.01$ are presented in Fig. 3. The initial Mach number is $M_{in} = 1.8$. The initial normalized dust grain charge number is $z_0 \approx 1.23$ [4]. Figure 3 shows the profiles of the potential $\varphi(x)$; the electric field $E = -d_x\varphi$; the normalized charge perturbation δz; and the ion density n_i, normalized to the unperturbed electron density n_{e0}, at the instants $t = 0$, 30, 60, 90, and 120 ($\delta z = 0$ at $t = 0$).

It can be seen in the figure that, in a charge-varying dusty plasma, the soliton (which is a steady-state solution in a plasma containing macroparticles with a constant charge) evolves into a nonsteady shocklike solution, whose amplitude decreases with time. The Mach number M of the perturbation also decreases down to the value $M_{fin} \approx 1.68$. Then, the velocity of the nonsteady shocklike solution remains almost constant. We note that, for the plasma parameters of Fig. 3, the value $M_{fin} \approx 1.68$ satisfies inequalities (5) for the Mach numbers of steady-state shocks. The oscillations in the profile of the shocklike solution are related to the charge separation effect. The front width of the shocklike structure Δx is on the order of 10 (or $10\lambda_D$ in dimensional variables). This value corresponds to the theoretical value of the front width $\Delta x \sim c_s/\nu_q$ of an ion-acous-

tic shock wave that exists because of efficient dissipation due to dust grain charging (here, $\nu_q = \omega_{pi}^2 a(1 + z_0 + T_i/T_e)/\sqrt{2\pi}\, v_{Ti}$ is the dust grain charging rate and $\omega_{pi} = (4\pi n_i e^2/m_i)^{1/2}$ is the ion plasma frequency). The reason for both the decrease in the amplitude of the shocklike solution and the fact that the steady-state shock wave solution similar to those shown in Figs. 1 and 2 is not formed under these conditions is the small intensity of the initial soliton.

5. EVOLUTION OF AN INITIALLY IMMOBILE PERTURBATION WITH A CONSTANT INCREASED ION DENSITY

Now, we consider the situation in which the initial perturbation can evolve into a shock wave structure that is close to a steady-state shock wave. For simplicity, we consider an initially immobile perturbation with a constant increased ion density. The intensity of the initial perturbation is chosen from the following considerations. In a frame of reference related to the wave, it follows from the momentum transfer equation that

$$\varphi + v_i^2/c_s^2 = \text{const}. \qquad (8)$$

In the region occupied by the initial perturbation, $v_i = 0$, but $\varphi - \varphi_0 \neq 0$, whereas ahead of the front of a steady-state shock, we have $\varphi = 0$ and $|v_i|/c_s \approx M$. Thus, we obtain $\varphi_0 \approx M^2/2$. The initial ion density is evaluated using the continuity equation.

The results of calculations describing the evolution of an initially immobile perturbation with a constant increased ion density that corresponds to the Mach number $M \approx 1.5$ (i.e., $\varphi_0 \approx M^2/2 \approx 1.125$) for the plasma parameters $Z_{d0}d = 2$, $T_e/T_i = 10$, and $a/\lambda_D = 0.01$ are presented in Fig. 4. It is assumed that the initial charge of the dust grains is in equilibrium in the absence of wave perturbations ($z_0 \approx 1.23$). Figure 4 shows the profiles of the potential $\varphi(x)$; the electric field $E = -d_x\varphi$; the normalized charge perturbation δz; and the ion density n_i, normalized to the unperturbed electron density n_{e0}, at the instants $t = 100$, 1000, and 1500. The initial profiles ($t = 0$) of the potential φ and the normalized ion density n_i/n_{e0} are presented by the light curves on the left of the corresponding plots. The light curves on the right of Fig. 4 show the corresponding profiles of the steady-state shock wave solution with $M = 1.49$.

It is seen from Fig. 4 that an intense, initially immobile perturbation with a constant increased ion density evolves into a shock wave solution similar to the exact steady-state solution with the Mach number $M = 1.49$. The difference between these two solutions is that, in the former, the compression region is accompanied by a rarefaction region (dilatation wave). During the evolution of the shock wave, the distance between the rarefaction and compression regions decreases. Finally,

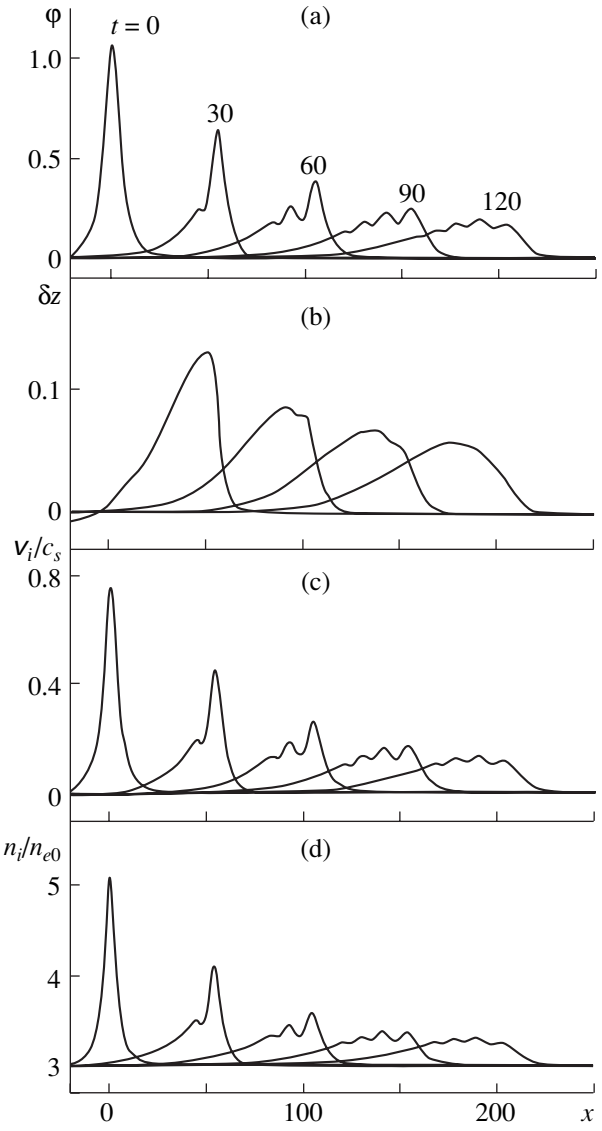

Fig. 3. Profiles of (a) $\varphi(x)$, (b) $E(x) = -d_x\varphi(x)$, (c) $\delta z(x)$, and (d) $n_i(x)/n_{e0}$ at $t = 0$, 30, 60, 90, and 120 ($\delta z = 0$ at $t = 0$) showing the evolution of an initial soliton. The parameters are $Z_{d0}d = 2$, $T_e/T_i = 10$, and $a/\lambda_D = 0.01$. The initial soliton Mach number is $M_{in} = 1.8$, and the initial normalized dust grain charge number is $z_0 \approx 1.23$.

the presence of the dilatation wave leads to the destruction of the shock structure.

We have studied the influence of the initial charge of dust grains on the evolution of an initially immobile perturbation with a constant increased ion density. In Fig. 5, the profiles of the potential φ at $t = 100$ are presented for the cases in which the initial dust grain charge is equal to zero (heavy line) and is in equilibrium in the absence of perturbations; i.e., $z_0 \approx 1.23$ (light line). The remaining parameters of Fig. 5 are the same as those of Fig. 4. In Fig. 6, the results of calculating the dust grain charging process are presented for

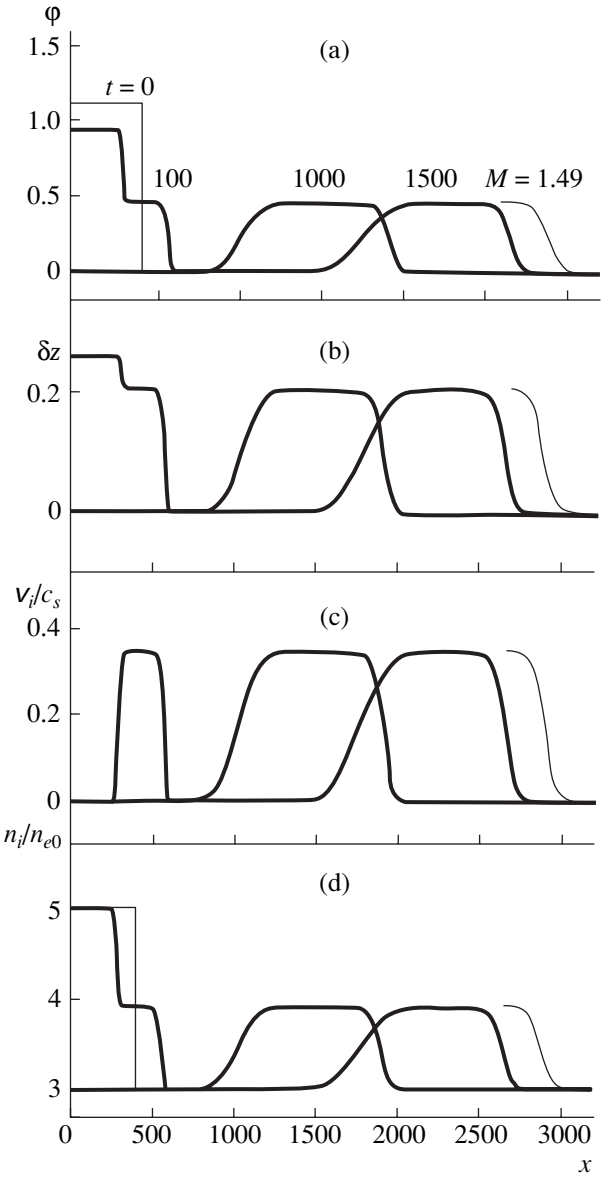

Fig. 4. Profiles of (a) $\varphi(x)$, (b) $E(x) = -d_x\varphi(x)$, (c) $\delta z(x)$, and (d) $n_i(x)/n_{e0}$ at $t = 100$, 1000, and 1500 showing the evolution of an initially immobile perturbation with a constant increased ion density. The parameters are $Z_{d0}d = 2$, $T_e/T_i = 10$, and $a/\lambda_D = 0.01$. The initial normalized dust grain charge number is $z_0 \approx 1.23$. The initial profiles ($t = 0$) of φ and n_i/n_{e0} are presented by the light curves on the left of the plots. The light curves on the right of the plots show the profiles of the steady-state shock wave solution with $M = 1.49$.

two initial values of z ($z = 0$ and $z = 1.5z_0$) and for $Z_{d0}d = 2$, $T_e/T_i = 10$, $a/\lambda_D = 0.01$, and $n_i = 1.66 \times 10^{11}$ cm^{-3}. Saturation ($z_0 = 1.23$) is reached at a time on the order of $\nu_q^{-1} \sim 10$ (here, ν_q^{-1} is normalized as $\nu_q^{-1}c_s/\lambda_D \longrightarrow \nu_q^{-1}$). In both cases (in which the initial dust grain charge equals zero and in which it is in equilibrium in the absence of perturbations) at $t = 100$ (and the more so at

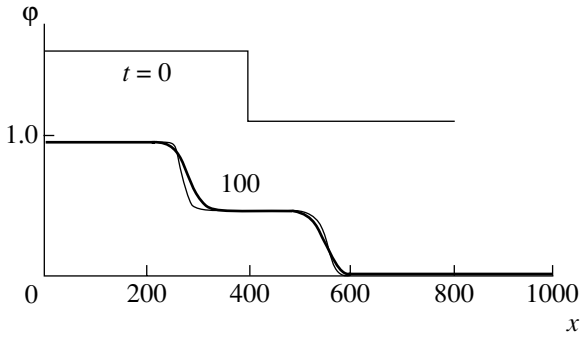

Fig. 5. Profiles of $\varphi(x)$ at $t = 100$ for the zero initial dust grain charge (heavy curve) and for the initial dimensionless dust grain charge equal to $z_0 \approx 1.23$ (light curve). The remaining parameters are the same as in Fig. 4. The upper curve shows $\varphi(x)$ at $t = 0$.

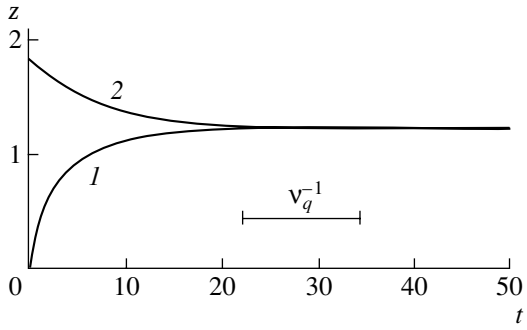

Fig. 6. Dimensionless dust grain charge z as a function of time t for two initial values of z: (*1*) $z = 0$ and (*2*) $z = 1.5z_0$. The parameters are $Z_{d0}d = 2$, $T_e/T_i = 10$, $a/\lambda_D = 0.01$, and $n_i = 1.66 \times 10^{11}$ cm^{-3}.

$t > 100$), the evolution of the initial perturbation leads to almost the same results (see Fig. 5). This is related to the fact that the characteristic charging time ν_q^{-1} is far less than the time during which the structure similar to the steady-state solution is established (see Figs. 4, 6).

6. SUMMARY

To summarize, we have considered a plasma with variable-charge dust grains, Boltzmann electrons, and inertial ions. We have studied the influence of electron and ion charge separation on steady-state ion-acoustic shock structures that are associated with an anomalous dissipation originating from dust grain charging. The charge separation effect manifests itself in the appearance of oscillations in the shock wave profile. This effect increases as the shock wave propagation velocity increases.

We have considered the problem of the evolution of a perturbation and its transformation into a nonlinear wave structure. For this purpose, we have developed a computational method that allows us to numerically

solve the set of equations describing the evolution of a nonlinear structure in a charge-varying dusty plasma. We have investigated the evolutions of both an initial soliton (which is a steady-state wave solution in a plasma containing macroparticles with a constant charge) and an intense, initially immobile perturbation with a constant increased ion density.

It is shown that a soliton in a charge-varying dusty plasma evolves into a nonsteady shocklike structure that propagates at a constant speed and whose amplitude decreases with time. The Mach number of this structure satisfies inequalities (5) for the Mach numbers of steady-state shocks. The charge separation effect manifests itself in the appearance of oscillations in the profile of the shocklike structure. The width of its front corresponds to the theoretical value of the front width of an ion-acoustic shock wave that exists because of efficient dissipation due to dust grain charging. The reason for the decrease in the amplitude of the shocklike structure is the low intensity of the initial soliton.

An intense, initially immobile perturbation with a constant increased ion density evolves into a shock wave solution that is similar to a steady-state shock wave. The difference between these two solutions is that, in the former, the compression region is accompanied by a rarefaction region (dilatation wave). Finally, the presence of the dilatation wave leads to the destruction of the shock structure. These shocks are also related to the efficient dissipation due to dust grain charging. However, the influence of the initial dust grain charge on the evolution of an initially immobile perturbation with a constant increased ion density is insignificant. This is related to the fact that the characteristic charging time of dust grains is far less than the time during which the structure similar to the steady-state shocklike solution is established.

The solution of the problem of the evolution of a perturbation in a charge-varying dusty plasma and its transformation into a shock wave opens up the possibility of describing real phenomena (such as supernova explosions) and laboratory and active space experiments. Furthermore, the solution of this problem confirms that, in real dusty plasmas, shock structures are the main nonlinear wave structures.

ACKNOWLEDGMENTS

This work was supported by INTAS (grant no. 97-2149) and INTAS–RFBR (grant no. IR-97-775).

REFERENCES

1. V. N. Tsytovich, Usp. Fiz. Nauk **167**, 57 (1997) [Phys. Usp. **40**, 53 (1997)].
2. Ya. B. Zel'dovich and Yu. P. Raizer, *Physics of Shock Waves and High–Temperature Hydrodynamic Phenomena* (Nauka, Moscow, 1966; Academic, New York, 1967).
3. R. Z. Sagdeev, in *Reviews of Plasma Physics*, Ed. by M. A. Leontovich (Atomizdat, Moscow, 1964; Consultants Bureau, New York, 1966), Vol. 4, p. 20.
4. S. I. Popel, M. Y. Yu, and V. N. Tsytovich, Phys. Plasmas **3**, 4313 (1996).
5. S. I. Popel, V. N. Tsytovich, and M. Y. Yu, Astrophys. Space Sci. **256**, 107 (1998); in *Plasma Physics*, Ed. by P. Martin and J. Puerta (Kluwer, Dordrecht, 1998), p. 107.
6. S. I. Popel, A. A. Gisko, A. P. Golub', *et al.*, Phys. Plasmas **7**, 2410 (2000).
7. Y. Nakamura, H. Bailung, and P. K. Shukla, Phys. Rev. Lett. **83**, 1602 (1999).
8. Q.-Z. Luo, N. D'Angelo, and R. L. Merlino, Phys. Plasmas **6**, 3455 (1999).
9. S. A. Kaplan and S. B. Pikel'ner, *Physics of Interstellar Medium* (Nauka, Moscow, 1979; Harvard Univ. Press, Cambridge, 1982).
10. S. I. Popel and V. N. Tsytovich, Astrophys. Space Sci. **264**, 219 (1999).
11. S. I. Popel and M. Y. Yu, Contrib. Plasma Phys. **35**, 103 (1995).
12. F. F. Chen, in *Plasma Diagnostic Techniques*, Ed. by R. H. Huddlestone and S. L. Leonard (Academic, New York, 1965), Chap. 4.
13. M. S. Barnes, J. H. Keller, J. C. Forster, *et al.*, Phys. Rev. Lett. **68**, 313 (1992).
14. S. I. Popel and M. Y. Yu, Phys. Rev. E **50**, 3060 (1994).
15. V. N. Tsytovich and O. Havnes, Comments Plasma Phys. Controlled Fusion **15**, 267 (1993).
16. E. C. Whipple, Rep. Prog. Phys. **44**, 1198 (1981).
17. J. Goree, Plasma Sources Sci. Technol. **3**, 400 (1994).
18. E. S. Oran and J. P. Boris, *Numerical Simulation of Reactive Flow* (Elsevier, New York, 1987).
19. G. E. Forsythe, M. A. Malcolm, and G. B. Moler, *Computer Methods for Mathematical Computations* (Prentice-Hall, Englewood Cliffs, 1977).

Translated by the authors

Plasma Physics Reports, Vol. 27, No. 6, 2001, pp. 462–473. Translated from Fizika Plazmy, Vol. 27, No. 6, 2001, pp. 491–502.

PLASMA KINETICS

Characteristic Features of Electron–Ion Collisions in Strong Electric Fields

A. A. Balakin, V. A. Mironov, and G. M. Fraĭman

Institute of Applied Physics, Russian Academy of Sciences, ul. Ul'yanova 46, Nizhni Novgorod, 603600 Russia

Received April 20, 2000; in final form, October 3, 2000

Abstract—The classical motion of an electron in the Coulomb field of an ion and in a uniform external electric field is analyzed. A nondimensionalization method that makes it possible to study electron motion in arbitrarily strong electric fields is proposed. The possible electron trajectories in the plane of motion in a static field are classified. It is noted that, from a practical standpoint, the most interesting trajectories are snakelike trajectories, which are absent in the problem with a weak external field. An adiabatic approximation for transverse electron motions in quasistatic (strong) fields is constructed. A one-dimensional equation of motion is derived that accounts for transverse electron oscillations and the increase in the effective electron mass as an electron approaches an ion. An analytic model is used to calculate the spectra of bremsstrahlung generated by individual electrons. The calculated results are shown to agree well with the results of direct numerical integration of the basic equations. It is predicted that, at frequencies higher than the frequency of the incident light, pronounced peaks can appear in the spectrum of the transverse dipole moment of an electron; as a result, an electron is expected to effectively emit radiation at these frequencies in the direction of the external field. © *2001 MAIK "Nauka/Interperiodica".*

1. INTRODUCTION

In recent years, interest has grown in the electron dynamics in the field that is a superposition of a Coulomb field and an electromagnetic field of subatomic (and even relativistic) strength [1–12]. Investigations in this area have revealed not only the expected effects (such as self-focusing [2] and self-defocusing [3], the penetration of radiation into an overdense plasma [4], and harmonic generation [5]) but also a number of unexpected phenomena, among which we must, first of all, mention the effective cascading of the radiation energy to the ultraviolet spectral region [6], the generation of high harmonics of the incident light at targets and atomic clusters [7], and the production of accelerated electrons [8]. With this rich store of accumulated experimental data, it becomes relevant to investigate the expected effects theoretically in order to plan future experiments. That is why it is very important to study phenomena that occur in the interaction of ultraintense electromagnetic radiation with matter [9, 10]. The electron–ion (e–i) collisions, which may play a special role in these phenomena, were analyzed numerically in a number of interesting papers (see, e.g., [11]). So far, no adequate explanation of the above effects has been given; in some cases, they have not been discussed even at a qualitative level.

In [12], we showed that taking into account the focusing properties of the Coulomb potential when an electron repeatedly returns to the strong field region substantially modifies the traditional picture of the interaction of an electron with an ion (e.g., the effective interaction cross section and the energy exchange processes). Actually, the study presented here was carried out before that reported in [12]. Analyzing the known results on the scattering of charged particles in a Coulomb field and a uniform static field, we noticed that the problem of e–i interaction is a particular case of a more complicated three-body problem, specifically, the problem of a satellite that orbits a planet and experiences the gravitational force of a remote, very massive body. This problem has been thoroughly investigated in celestial mechanics (see, e.g., [13]). We found that the most striking were trajectories similar to those in Fig. 4 (see below), which we called snakelike trajectories. An important point here is that these are fundamentally (qualitatively) new trajectories in the problem of scattering in a purely Coulomb field: a charged particle that moves in the external decelerating field and is attracted by an ion oscillates with a certain characteristic frequency on one side of the region around the ion. Clearly, such motion can strongly influence the overall picture of scattering in an alternating field if the field amplitude is sufficiently large.

Here, we consider natural questions related to the effect of external, uniform, quasistatic fields on the electron dynamics. In Section 2, we show that the problem under consideration involves only two dimensionless parameters (the integrals of motion) and can be reduced to the problem for two noninteracting nonlinear oscillators by switching to the Levi-Civita variables. In Section 3, we classify the possible electron trajectories in the plane of these two parameters (the bifurcation diagram) and obtain analytic solutions in explicit form (in particular, the solutions describing the

1063-780X/01/2706-0462$21.00

above snakelike trajectories near the separatrix). In Section 4, we construct an adiabatic approximation by the method of averaging over fast transverse (with respect to the external field) electron oscillations. As a result, we arrive at the conclusion that the effective mass of an electron increases as it is attracted toward an ion. In Section 5, we consider the spectral properties of such e–i collisions and, in particular, the possible appearance of characteristic peaks in the spectra of bremsstrahlung generated by decelerated electrons. In Section 6, we discuss some of the consequences of the resulting picture of the electron dynamics.

2. FORMULATION OF THE PROBLEM

In order to consider the classical trajectories, we start with the equation

$$m\ddot{\mathbf{r}} = -\frac{Ze^2}{r^3}\mathbf{r} + e\mathbf{E}, \tag{1}$$

which describes the electron motion in the field of an ion with charge Ze and in a uniform electrostatic field $\mathbf{E}$. By analogy with [12], we nondimensionalize Eq. (1) as follows:

$$r_E = \sqrt{\frac{eZ}{E}}, \quad t_E = \frac{1}{\omega_E} = \sqrt[4]{\frac{m^2Z}{eE^3}}, \tag{2}$$

where r_E is the radius of the spherical surface around the ion at which the Coulomb field is equal to the uniform electrostatic field E and ω_E is the electron revolution frequency along a Keplerian orbit of radius r_E.

As a result, we obtain

$$\ddot{\mathbf{r}} = \frac{\mathbf{r}}{r^3} + \mathbf{n}, \tag{3}$$

where $\mathbf{n}$ is a unit field-aligned vector ($\mathbf{E} = E\mathbf{n}$).

With an alternating electric field $\mathbf{E}\cos\omega t$ varying at the frequency ω, the problem contains a dimensionless parameter—the dimensionless frequency Ω equal to

$$\Omega = \frac{\omega}{\omega_E} = \omega\left(\frac{m^2Z}{eE^3}\right)^{1/4} \approx 1.21\frac{Z^{1/4}}{\lambda\ [\mathrm{cm}]\ (E\ [\mathrm{V/cm}])^{3/4}}, \tag{4}$$

which includes the frequency of the field and its strength through the combination ω^4/E^3. This indicates that, in the limiting case of an infinitely strong field, the field can be considered static ($\Omega \longrightarrow 0$). In this limit, the problem allows separation of variables, thereby providing a way of classifying electron trajectories. In fact, the characteristic time scale of the electron motion in an electrostatic field is t_E; consequently, for $\omega t_E \equiv \Omega \ll 1$, the electron trajectories can be analyzed within the assumption of a static field.

In a more realistic situation with an electric field that changes slowly in time, we can investigate adiabatic variations of the electron trajectories. In this case, it is convenient to switch to the Levi-Civita variables [14], which are better suited than parabolic coordinates [15, 16] for the description of a Coulomb system in an external unsteady field, because an electron moving in a Coulomb field at small distances from an ion can abruptly change its direction of motion, in which case calculations by means of perturbation theory or numerical computations lose accuracy. On the other hand, the shapes of electron trajectories at short distances from an ion are important in following the long-term motion of an electron. Consequently, the problem arises of how to transform the coordinates and time in such a way as to regularize the equation of electron motion (i.e., to eliminate the singularity at the position of the ion). The equation of motion is regularized in two steps. For simplicity, we consider the electron motion in the (x, z) plane, which contains the electric field vector $\mathbf{E}(0, 0, E)$ and passes through the center of the Coulomb field.

First, we introduce a new (fictitious) time s through the equation

$$\frac{dt}{ds} = r, \tag{5}$$

where $r = \sqrt{x^2 + z^2}$ is the distance from the center of the Coulomb field. This transformation acts to slow down the e–i interaction in real time t: the closer the electron is to the ion (to the Coulomb singularity), the larger the slowing-down factor. As a result, the equation of motion (3) takes the form

$$r\frac{d^2\mathbf{r}}{ds^2} - \frac{dr}{ds}\frac{d\mathbf{r}}{ds} = -\mathbf{r} + r^3\mathbf{n}. \tag{6}$$

Then, in place of the position vector $\mathbf{r}$, it is convenient to introduce an equivalent vector in the complex plane:

$$q = x + iz, \tag{7}$$

in which case we have

$$r\frac{d^2q}{ds^2} - \frac{dr}{ds}\frac{dq}{ds} = -q + r^3, \tag{8}$$

where $r = |q|$. Following the Levi-Civita approach, we introduce the new function

$$q = \eta^2, \quad \eta = u + iv. \tag{9}$$

In the variables u and v, we have

$$r = u^2 + v^2, \quad z = u^2 - v^2, \quad x = 2uv. \tag{10}$$

The equation for η,

$$2|\eta|^2\frac{d^2\eta}{ds^2} - 2\eta\left|\frac{d\eta}{ds}\right|^2 = -\eta + |\eta|^4\eta^* \tag{11}$$

can be substantially simplified by expressing $|d\eta/ds|$ in terms of the energy $W = \frac{1}{r} - \frac{1}{2}\left|\frac{dr}{dt}\right|^2$ of the Coulomb system, in which case we readily obtain $|d\eta/ds|^2 =$

$(|\eta|^2 W - 1)/2$ and thus arrive at the following regularized equation describing nonlinear electron oscillations:

$$\eta'' + \frac{W\eta}{2} = \frac{|\eta|^2\eta^*}{2}. \quad (12)$$

Equation (12) should be supplemented with the equation for real time:

$$t' = |\eta|^2. \quad (13)$$

The desired set of equations will become especially simple if we introduce the electron energy in the external field,

$$h = W + z = \text{const}. \quad (14)$$

This allows us to separate the variables in the equation of motion (12):

$$\begin{cases} u'' + \dfrac{h}{2}u = u^3 \\ v'' + \dfrac{h}{2}v = -v^3 \\ t' = u^2 + v^2. \end{cases} \quad (15)$$

The transformation from the Levi-Civita variables to the physical coordinates **r** and *t* has the form

$$\begin{cases} z = u^2 - v^2, \quad \dot{z} = \dfrac{2}{r}(uu' - vv') \\ x = 2uv \\ r = u^2 + v^2, \quad \dot{x} = \dfrac{2}{r}(vu' + uv') \end{cases} \quad (16)$$

the inverse transformation being

$$\begin{cases} u = \sqrt{\dfrac{r+z}{2}}, \quad P_u \equiv u' = \dfrac{1}{2}(u\dot{z} + v\dot{x}) \\ v = \dfrac{xu}{r+z}, \quad P_v \equiv v' = \dfrac{1}{2}(u\dot{x} - v\dot{z}). \end{cases} \quad (17)$$

We also write down the expression for the Hamiltonian *h* of the system:

$$h = \frac{1}{r} - \frac{|\dot{r}|^2}{2} + z = \frac{1 - 2(u'^2 + v'^2)}{u^2 + v^2} + u^2 - v^2, \quad (18)$$

which may be used to control the results of the numerical solution of the problem.

The transformation to the Levi-Civita variables is analogous to the transition to parabolic coordinates (which are traditionally used to analyze the problems with a spatially uniform field) and, for a static field, reduces our problem to that of two anharmonic oscillators.

One of the most interesting features of Eqs. (15) is that they differ only in the sign of the nonlinear terms. Consequently, changing the sign of the field converts the equations for *u* and *v* into each other. For a positive direction of the field, the variables *u* and *v* play the roles of "longitudinal" and "transverse" coordinates, respectively, and vice versa. This property of Eqs. (15) can be used to qualitatively analyze the long-term motion of an electron, in particular, to search for periodic electron trajectories.

Hence, passing over to the Levi-Civita variables makes it possible to remove the singularity at the center of the Coulomb field and to separate the variables in the equation of motion, as is the case with the parabolic coordinates used to analyze problems with a static field. Problems with an alternating field would involve a larger number of equations of motion. Although the resulting equations are more complicated in comparison with the basic equations, they are better suited for both numerical simulations and the application of perturbation theory.

Now, we proceed to the classification of electron trajectories in a static field.

3. CLASSIFICATION OF TRAJECTORIES

We have derived two independent equations describing nonlinear electron oscillations. Taking the product of the first two equations in (15) with *u*' and *v*', respectively, we arrive at the two integrals of motion,

$$\frac{u'^2}{2} + \frac{hu^2}{4} - \frac{u^4}{4} = c_u, \quad \frac{v'^2}{2} + \frac{hv^2}{4} + \frac{v^4}{4} = c_v. \quad (19)$$

That the constants c_u and c_v are not independent can be easily verified by multiplying the Hamiltonian *h* for Eqs. (15) by $(u^2 + u^2)/4$ and by collecting all like terms with *u* and *v*. After some trivial manipulations, we find

$$c_u = \frac{1+\beta}{8}, \quad c_v = \frac{1-\beta}{8}. \quad (20)$$

In Cartesian coordinates, the quantity β is the familiar integral obtained in [15] by transforming the Hamilton–Jacobi equation to parabolic coordinates and by separating the variables:

$$\beta = \frac{z}{r} + \dot{x}(x\dot{z} - z\dot{x}) - \frac{x^2}{2}. \quad (21)$$

Figure 1 illustrates possible types of the phase trajectories of anharmonic oscillators described by Eqs. (19), and Fig. 2 presents the parameter plane and the representative trajectories for a static field aligned with the *z*-axis.

An analysis of the phase portraits of the system leads to the following conclusions.

(i) Region $\beta < -1$ is characterized by unbounded (infinite) self-intersecting trajectories that do not encircle the center of the attracting Coulomb field. In the (u, p_u) phase plane, the trajectories are found to be only on one side of the separatrix. In the (x, z) plane, there exist unusual "self-recovering" trajectories: an electron

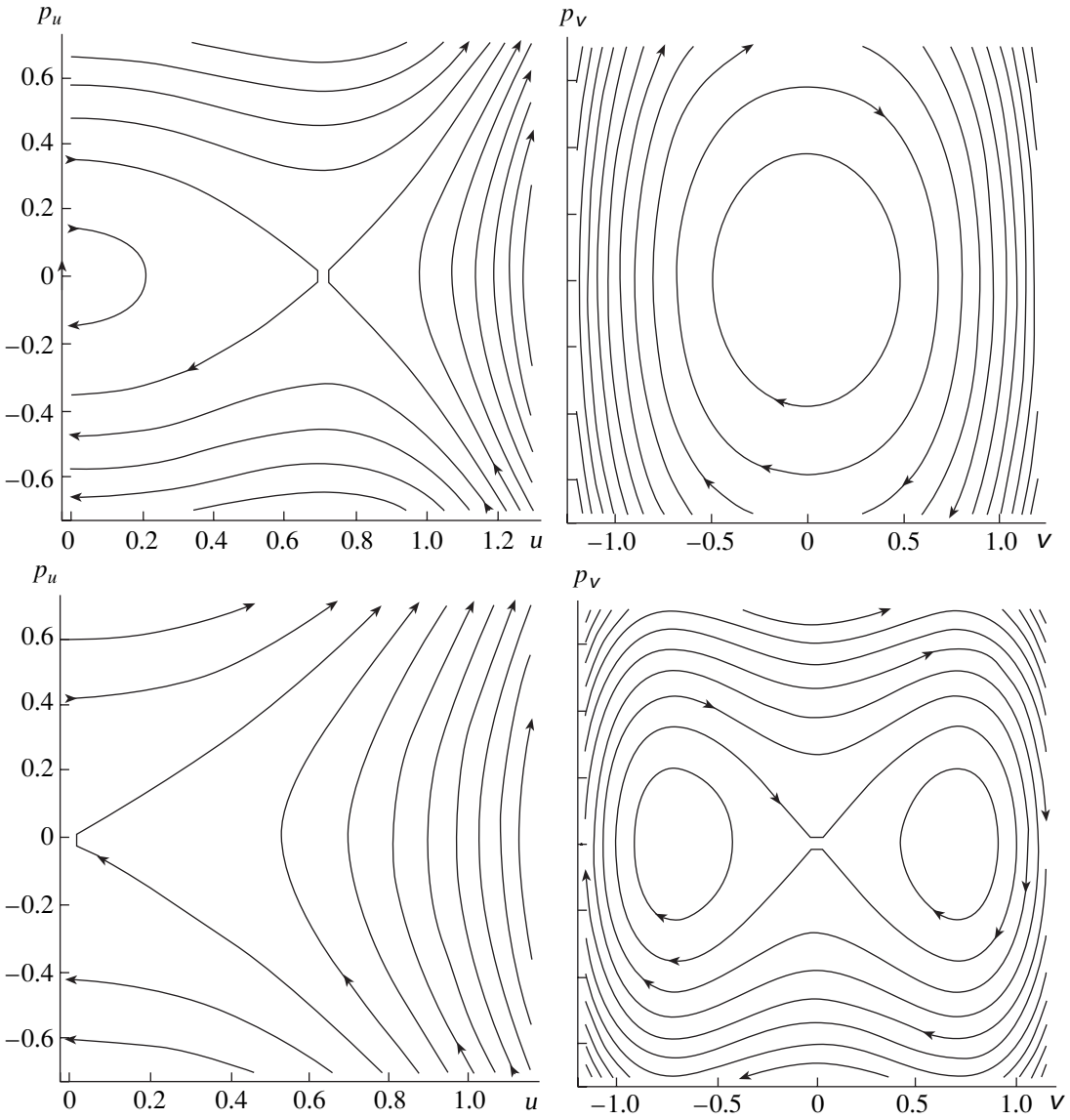

Fig. 1. Phase planes (u, p_u) and (v, p_v) for $h > 0$ (top) and $h < 0$ (bottom).

moves until its velocity vanishes; then, it starts moving along the same trajectory but in the opposite direction. Near the boundary, the electrons can move along snakelike trajectories, which, however, are not characteristic of this region and will be considered below in more detail.

(ii) Region $-1 \le \beta \le 1$, $h < \sqrt{2(\beta + 1)}$ is characterized by infinite self-intersecting trajectories that encircle the center of the attracting Coulomb field. In the (u, p_u) phase plane, the trajectories are found to be both above and below the separatrix. The most interesting trajectories are snakelike trajectories, which occur in the vicinity of one of the saddle points in the (u, p_u) phase plane for $h > 0$ (Fig. 1). This type of trajectories will be examined below.

(iii) Region $-1 \le \beta \le 1$, $h > \sqrt{2(\beta + 1)}$ is the only region where the finite trajectories, which are characteristic of an electron trapped by an ion, are possible. Infinite trajectories in this region are similar to those in region (ii). In the vicinity of one of the saddle points in the (u, p_u) phase plane (Fig. 1), the electrons can move along snakelike trajectories, as in region (ii). Among the finite trajectories, there are self-recovering trajectories, which are similar to those in region (i).

(iv) Region $\beta > 1$, $h < -\sqrt{2(\beta - 1)}$ is primarily characterized by infinite non-self-intersecting trajectories that smoothly encircle the center of the Coulomb field.

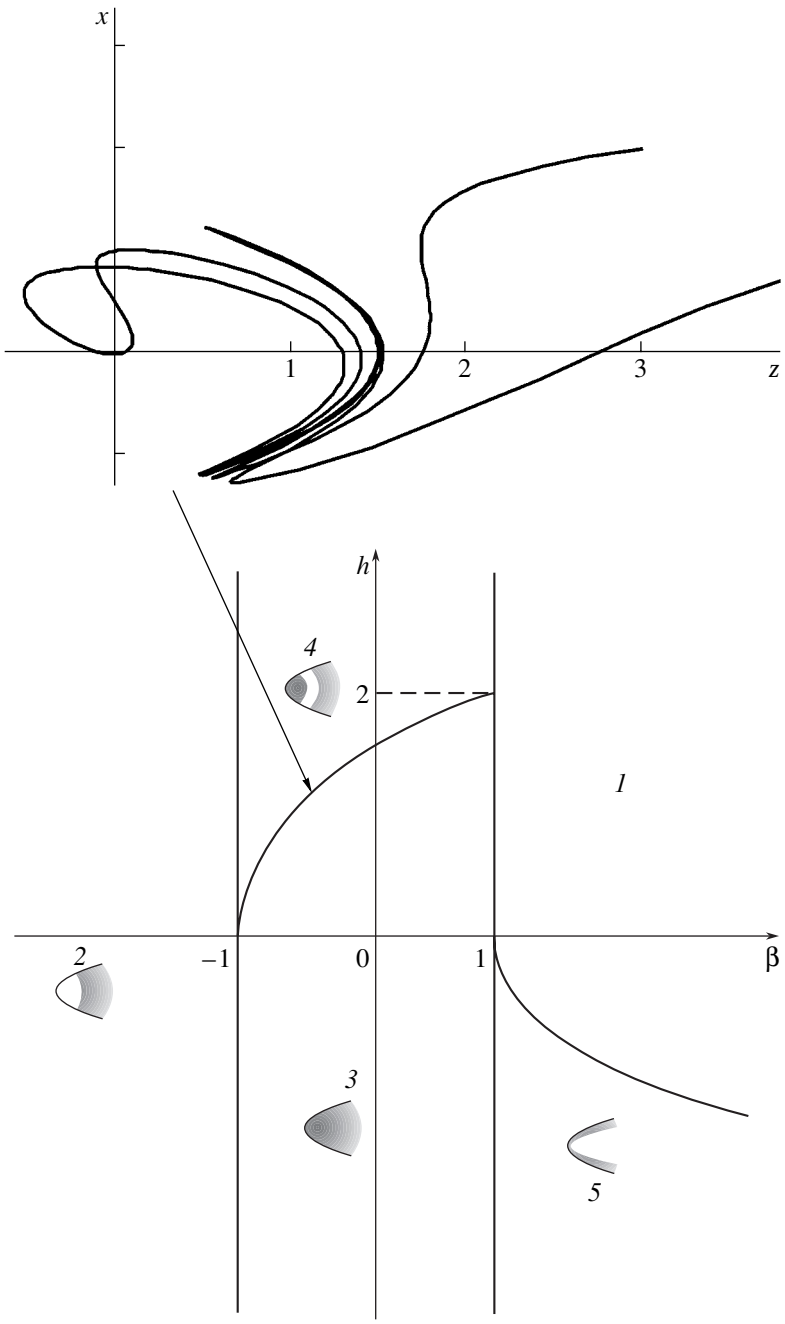

Fig. 2. Parameter plane for an electrostatic field. The regions of possible electron motion in the (x, z) plane are hatched (see text for details). The snakelike trajectory is presented in a separate frame, and the region where the snakelike trajectories can exist is indicated by an arrow.

(v) In region $\beta > 1$, $h > -\sqrt{2(\beta - 1)}$, electron motion is forbidden.

We stress that the division of the phase plane in Fig. 2 into five regions remains the same regardless of the field direction. Note also that, in an analogous problem of celestial mechanics, the trajectories were classified by analyzing the integrals of motion (see, e.g., [13]).

Equations (15) do not include the centrifugal force arising in the three-dimensional problem. In the case of nonplanar motion, Eqs. (15) contain the term $-M/u^3$ and, accordingly, the term $-M/v^3$, which reflect the angular momentum conservation. We can show that, in quasi-planar geometry ($M \ll 1$), the electron trajectories differ from planar only slightly. Taking into account the angular momentum does not lead to new

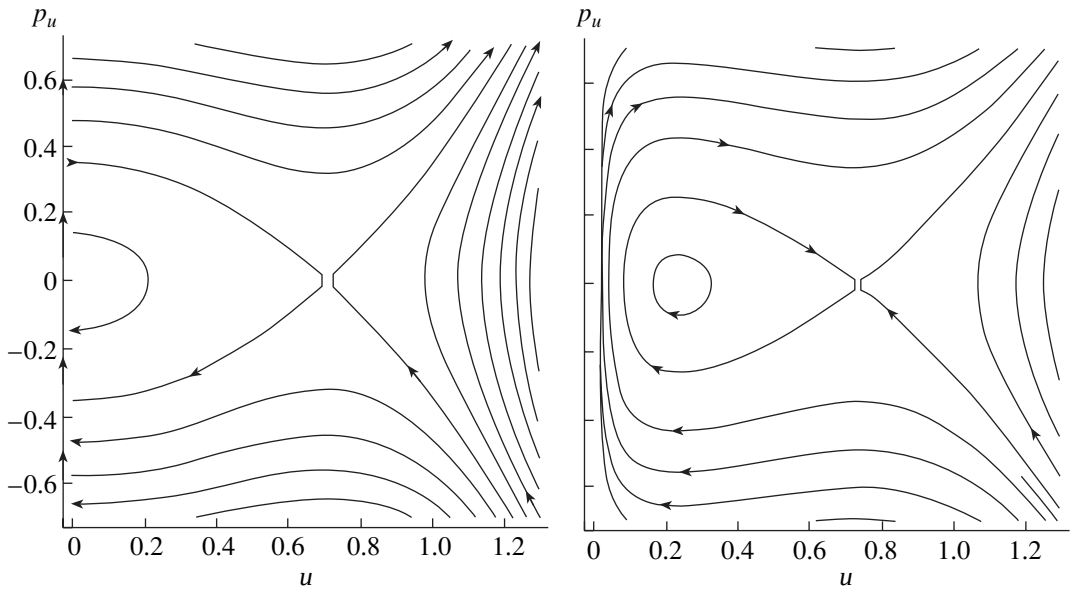

Fig. 3. Phase planes (u, p_u) without (left) and with (right) allowance for the centrifugal force.

physical effects. In this case, the phase planes for the coordinates u and v are each divided into two similar regions (cf. Figs. 1, 3), which are "confined" to the $u = 0$ and $v = 0$ axes, provided that the field is sufficiently strong. Calculations show that, in the general case, the situation is essentially the same.

To conclude this section, we present the exact solutions $u(s)$ and $v(s)$ in terms of Jacobian elliptic functions:

$$u_{\text{fin}}(s) = \sqrt{\frac{-H}{4}\left(2 - \frac{\gamma}{1-\sqrt{1-\gamma}}\right)} \times \text{cd}\left(\frac{s}{2}\sqrt{-H\frac{\gamma}{1-\sqrt{1-\gamma}}}, \frac{2-\gamma-2\sqrt{1-\gamma}}{\gamma}\right),$$

$$u_{\text{inf}}(s) = \sqrt{H\sqrt{1-\gamma}}\,\text{ds}\left(\frac{s}{2}\sqrt{\frac{H\sqrt{1-\gamma}}{2}}, \frac{1}{2}\left(1 + \frac{1}{\sqrt{1-\gamma}}\right)\right),$$

$$v(s) = \sqrt{\frac{H + \sqrt{H^2 + 2(1-\beta)}}{2}} \times \text{cn}\left(\frac{s}{2}\sqrt{\frac{\sqrt{H^2 + 2(1-\beta)}}{2}} + \varphi, \frac{H\sqrt{H^2 + 2(1-\beta)} + H^2 + 2(1-\beta)}{2H^2 + 4(1-\beta)}\right), \quad (22)$$

where $\gamma = 2(1 + \beta)/H^2$ and $H = -h$ is the Hamiltonian of the system. The first solution, $u_{\text{fin}}(s)$, describes electron trajectories that are localized about the center of the Coulomb field and are modified Keplerian elliptic orbits. The characteristic feature of these trajectories is that they do not close upon themselves because of the different periods of electron oscillations in the u and v directions. The second solution describes unbounded trajectories of the electrons that come from and go to infinity. These trajectories contain snakelike paths, which indicates that the electron may remain near the ion for a long time.

Let us examine these trajectories in more detail. An analysis of the phase portraits in Fig. 1 shows that the trajectories pass near a saddle point in the (u, p_u) phase plane. In other words, such "resonant" electrons are characterized by the parameters (Fig. 4)

$$\begin{aligned} &(1)\ h < 0, \quad \beta \approx -1, \\ &(2)\ h > 0, \quad h^2 \approx 2(\beta + 1). \end{aligned} \quad (23)$$

Along the separatrices in the phase plane for the u-coordinate, the $v(s)$ coordinate oscillates according to the law

$$v_1(s) = \sqrt{\frac{H + \sqrt{H^2 + 4}}{2}} \times \text{cn}\left(\frac{s}{2}\sqrt{\frac{\sqrt{H^2 + 4}}{2}} + \varphi, \frac{H + \sqrt{H^2 + 4}}{2\sqrt{H^2 + 4}}\right), \quad (24)$$

$$v_2(s) = \sqrt{1 - \frac{h}{2}}\,\text{cn}\left(\frac{s}{2} + \varphi, \frac{2-h}{4}\right).$$

Since the parameter of the Jacobian elliptic functions is smaller than 1/2, these oscillations can be regarded as

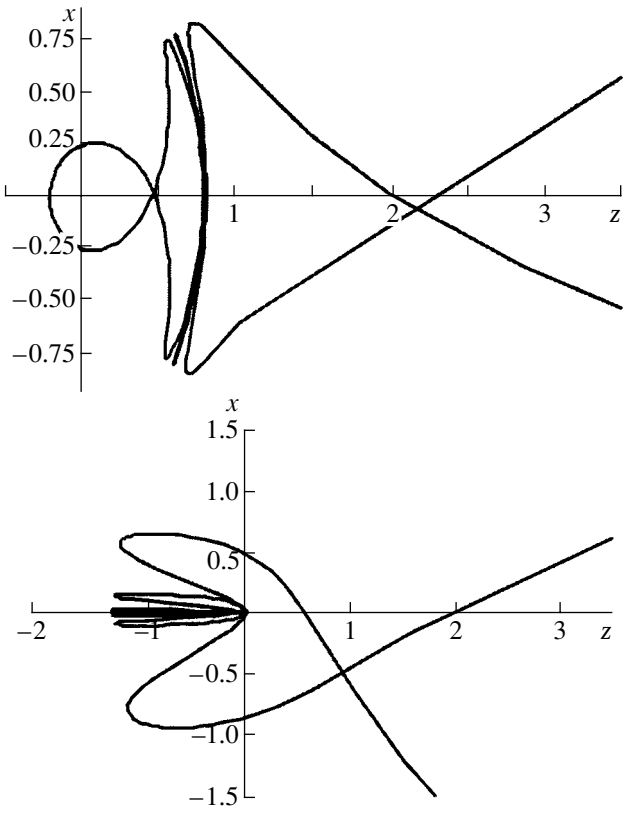

Fig. 4. Electron trajectories near the saddle point in Cartesian coordinates.

being almost harmonic. Below, this circumstance will be used to construct the adiabatic approximation.

The behavior of the u coordinate is qualitatively different. When approaching the saddle point in the phase plane (Fig. 1), the electron velocity decreases, so that the electron remains near the saddle point with the coordinates

$$u_1(s) = \sqrt{H}\sinh\left(\sqrt{\frac{H}{2}}s\right)^{-1},$$
$$u_2(s) = -\sqrt{\frac{h}{2}}\tanh\left(\frac{s\sqrt{h}}{2}\right)^{-1} \quad (25)$$

for quite a long time s_0, which can be estimated from the known formula as

$$s_0 \approx 2\sqrt{\frac{1}{h}}\ln\delta, \quad (26)$$

where δ is the minimum distance between the electron trajectory and the saddle point in the (u, p_u) phase plane (Fig. 1). For an alternating electric field, this time cannot be longer than the half-period of the electric field.

As a result of transverse oscillations, an electron acquires a dipole moment that is perpendicular to the external field. The dipole moment governs the characteristic features of the bremsstrahlung spectrum (see Section 5 for details).

Note that the snakelike trajectories satisfy the condition

$$s_0 \gg 1, \quad (27)$$

which implies that the electron has enough time to experience many oscillations in the v direction before its u coordinate changes substantially. This circumstance enables us to predict that the bremsstrahlung spectrum will be peaked at frequencies that are multiples of the frequency ω_E! Such factors as intense radiation emitted by an electron moving along a snakelike trajectory and low electron energy raise the hope that an alternating electric field will act to enhance recombination and bond an electron to an ion.

4. ADIABATIC APPROXIMATION

Above, we have analyzed electron motion in a static external electric field. For a slowly changing external field, we can use an adiabatic approximation. Recall that, in the most interesting case of snakelike trajectories, the electron motion in the v direction is periodic in the fictitious time s and is weakly sensitive to changes in the external field. These circumstances enable us to introduce the action variable I_v and the phase variable associated with the v coordinate and to construct the desired adiabatic approximation.

In Cartesian coordinates, an electron moving along a snakelike trajectory experiences oscillations along the arc of a parabola, which itself moves slowly along the external field (see Fig. 5, which is a model representation of the snakelike trajectories shown in Fig. 4).

The adiabatic description actually implies that the characteristic frequency of the external field is much lower than the frequency of fast electron oscillations:

$$\omega \lll \omega_E = \frac{1}{t_E} = \sqrt[4]{\frac{eE^3}{m^2Z}}. \quad (28)$$

Inequality (28) corresponds to the condition for an electron to interact with an ion for a short time in comparison with the external field period. This permits us to describe the e–i interaction in the same way as in the case of a static field. We can see that the adiabaticity condition (28) fails to hold as $E \longrightarrow 0$, where E is the instantaneous external field at the time when a collision event occurs. However, the above considerations do not imply that this approach can be used to describe the global parameters of the electron distribution in the plasma, because, in [12], we showed that, in an alternating field, it is important to take into account the electrons that repeatedly return to an ion.

In the adiabatic approach, we can find an adiabatic invariant for the periodic motion in the v direction:

$$J = \oint p_v dv = \frac{2}{3}\frac{\sqrt[4]{h^2 + 4fc_v}}{\sqrt{2f}} \times \left(\frac{E(m)}{(\sqrt{h^2 + 4fc_v} - h)} + \frac{K(m)}{h}\right), \quad (29)$$

$$m = 1 + \frac{h}{\sqrt{h^2 + 4fc_v}},$$

where $E(m)$ and $K(m)$ are complete elliptic integrals of the first and second kind, respectively.

Let us convert the integrals of motion (19) to a form convenient for interpreting the results obtained. Note that the equation for v describes a nonlinear oscillator. Consequently, we can introduce the action–phase variables J and Θ such that

$$c_v = c_v(J, h, f), \quad (30)$$

in which case the constant c_u for u satisfies the equation

$$\frac{2u'^2}{u^2} - fu^2 - \frac{1 - 4c_v(J, h, f)}{u^2} = h. \quad (31)$$

Introducing the new time

$$d\tau = u^2 ds \quad (32)$$

and the new coordinate

$$\xi = u^2, \quad (33)$$

we obtain

$$\frac{1}{2}\xi'^2_\tau - f\xi - \frac{1 - 4c_v}{\xi} = h. \quad (34)$$

Hence, we reduce the problem to that of describing one-dimensional motion in both the external field f and the Coulomb field that is produced by an effective charge $1 - 4c_v$, distributed over a paraboloid with a vertex at the point $z = \xi$. The condition $c_v = 1/4$ corresponds to an electron that comes from infinity and becomes trapped near the center of the Coulomb field. For $c_v \approx 1/4$, the electron remains trapped by an ion for a finite time. The relevant electron trajectories are described by the analytic formulas (24) and (25).

The smallness of c_v along the snakelike trajectories under consideration allows us to simplify expression (29). To first order in the small parameter fc_v/h^2, we find

$$J \approx 4c_v\sqrt{h} = -\xi\sqrt{h}(h + H_0), \quad (35)$$

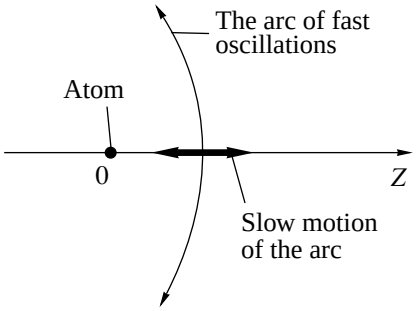

Fig. 5. Explanation of the motion along snakelike trajectories.

where $H_0 = \frac{2p_u^2}{u^2} - \frac{1}{u^2} - fu^2 = \left(\frac{\xi + J}{\xi}\right)^2 \frac{\dot{\xi}^2}{2} - \frac{1}{\xi} - f\xi =$ $m_{\text{eff}}\frac{\dot{\xi}^2}{2} - \frac{1}{\xi} - f\xi$ and m_{eff} has the form

$$m_{\text{eff}} = \left(1 + \frac{J}{\xi}\right)^2. \quad (36)$$

According to formula (35), the first-order Hamiltonian $H = -h$ is

$$H \approx \left(1 + \frac{J}{|\xi|}\right)^2 \frac{\dot{\xi}^2}{2} - \frac{1 - 4c_v}{|\xi|} - f\xi. \quad (37)$$

We emphasize that, in contrast to the problem that is originally formulated in four-dimensional phase space, Hamiltonian (37) describes one-dimensional electron motions, which allows a significant amount of progress in the qualitative analysis of the problem. Expression (37) implies that, when an electron approaches an ion, its effective mass increases. This effect is attributed to the conversion of the longitudinal energy of an electron into its transverse energy; as a result, an electron is reflected at a large distance from the ion.

Note that the coordinate ξ introduced in the above manner is positive. In other words, in Hamiltonian (37), the transition of ξ through zero is forbidden (one can readily see that the velocity $\dot{\xi}$ vanishes as $\xi \longrightarrow 0$). Nevertheless, Hamiltonian (37) also describes periodic electron motions.

Qualitatively, electron motions at small ($\xi < 1$) and large ($\xi \gg 1$) distances from the ion are well described by Hamiltonian (37). At large distances, the electron motion is a superposition of fast oscillations along the radial coordinate $r_\sim$ and a slow drift in the Coulomb field of an ion with renormalized charge. When approaching the region $\xi \leq 1$ (or, in dimensional variables, $r \leq r_E$), an electron sharply changes its direction of propagation on a very short time scale. This change

is very similar to the jumplike transition of a slow electron from one trajectory to another.

Now, we apply the adiabatic approximation constructed above in order to determine the radiation spectrum of an electron.

5. RADIATION SPECTRUM

The radiation spectral intensity I_ω is related to the dipole moment spectrum d_ω by the well-known expression $I_\omega = \omega^2 d_\omega$. In order to determine the spectrum d_ω, we turn to the adiabatic approximation. In Levi-Civita variables, we have

$$\mathbf{d}_\omega = e\int_{-\infty}^{\infty} \mathbf{r} e^{i\omega\int r ds} r ds. \quad (38)$$

The spectrum of the transverse component of the dipole moment is of the greatest interest for our study, because the spectrum of the longitudinal component corresponds to the bremsstrahlung spectrum that was analyzed in detail when solving the one-dimensional problem. This is related to the fact that, for small-angle scattering, the longitudinal oscillating component of v is small. As a result, the bremsstrahlung spectrum is determined by the spectrum of ξ.

Let us analyze the qualitative features of the dipole moment spectrum (39). For a portion of the trajectory along which the variable u changes gradually over the period of oscillations in the v direction, we arrive at the approximate dependence $t = \int r ds \approx r_0 s$ (where $r_0 = \langle r \rangle$). Consequently, we can expect that the spectrum will be peaked at frequencies that are multiples of the frequency $\omega = \tilde{\omega}/r_0$, where $\tilde{\omega} \approx 1$ is the frequency of oscillations in the v direction. Note that, under condition (27), an electron will emit radiation at frequencies that are multiples of the frequency equal to unity (or, in dimensional variables, to ω_E) for a long time. This effect significantly increases the efficiency of emission at higher harmonics. The above conditions are well satisfied for snakelike trajectories, i.e., for electrons that remain near the ion for a long time. In the (u, p_u) phase plane, the corresponding trajectories pass near the saddle point.

Let us estimate the shape of the spectrum of the transverse dipole moment. In the adiabatic approximation, the variable v changes harmonically in the fictitious time:

$$v = v_0 \cos(\tilde{\omega} s). \quad (39)$$

We also assume that $u \approx u_0 = \text{const}$, which corresponds to electron motion near the saddle point in the phase plane. In this case, we can make simple estimates to obtain

$$u_0 \approx \sqrt{\frac{h}{2}}, \quad \tilde{\omega} \approx 1, \quad u v_0 \approx \sqrt{J/\sqrt{h}} \ll 1, u_0. \quad (40)$$

As a result, the spectrum of the transverse dipole moment in dimensionless variables has the form

$$d_{\omega\perp} = e\sqrt{2J\sqrt{h}} \sum_n J_n\left(\frac{\omega J}{2\sqrt{h}}\right)\delta\left(\omega\frac{h}{2} + 1 + 2n\right). \quad (41)$$

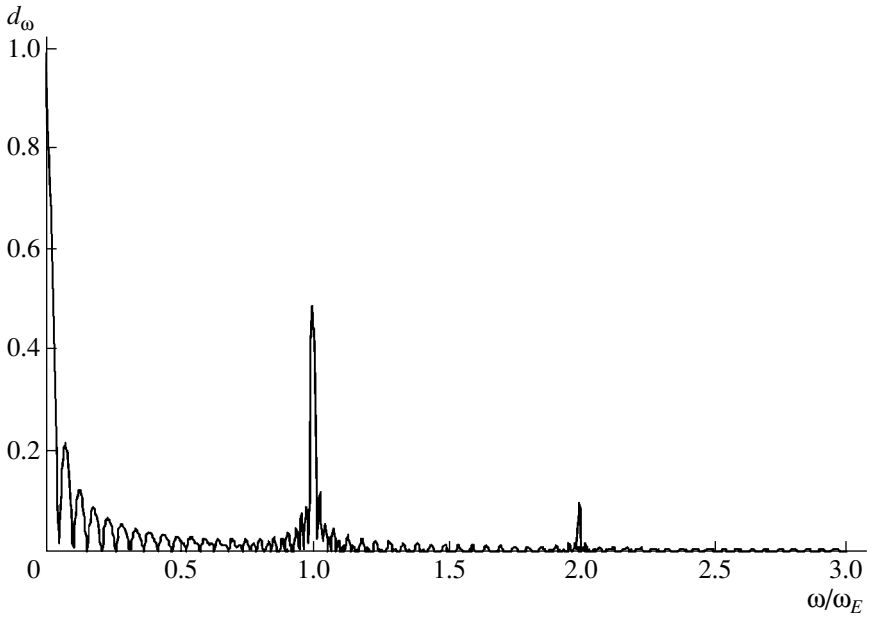

Fig. 6. Analytic spectrum of the normalized transverse dipole moment.

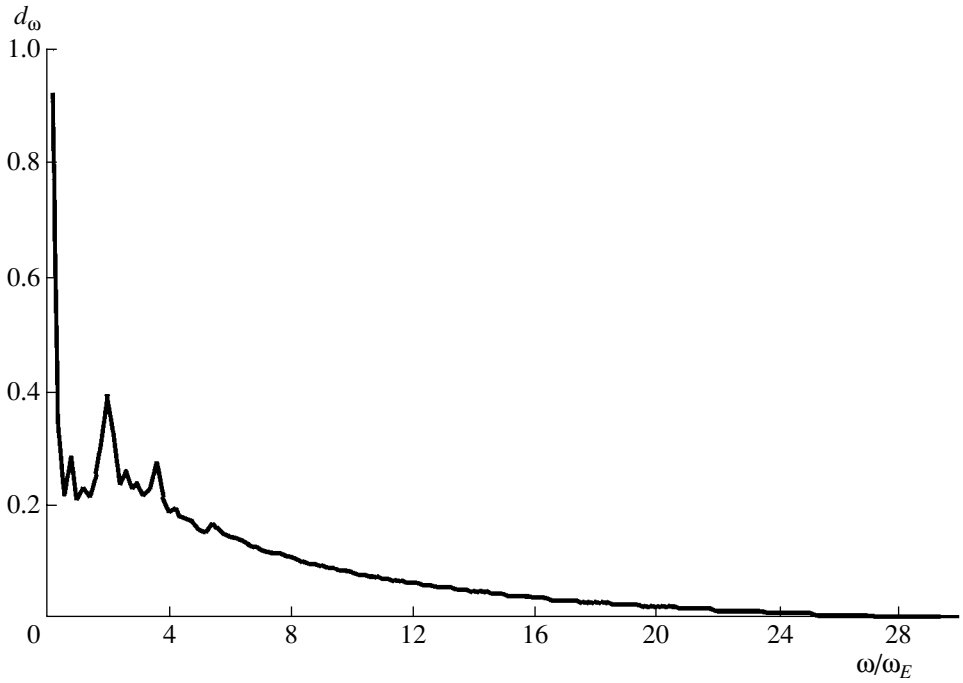

Fig. 7. Numerical spectrum of the normalized total dipole moment.

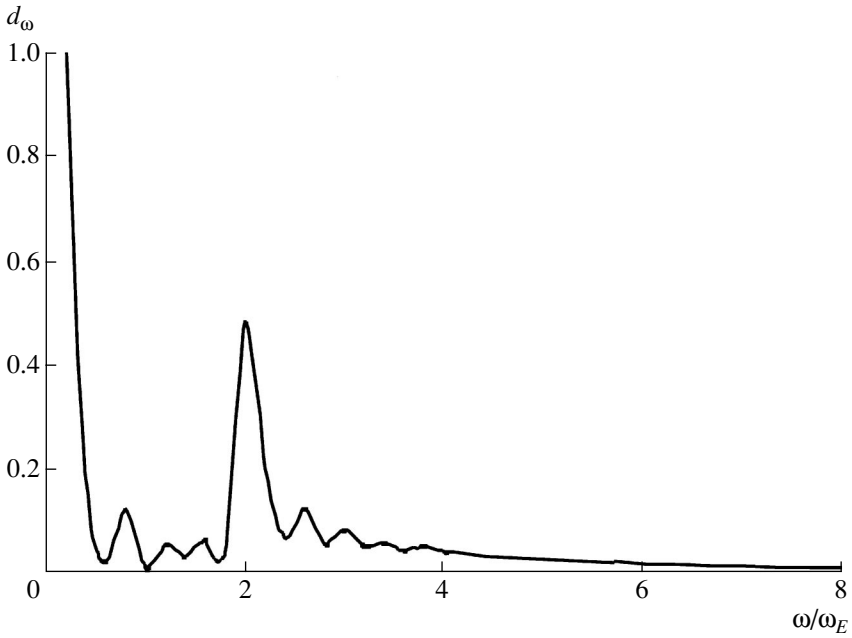

Fig. 8. Numerical spectrum of the normalized transverse dipole moment.

In dimensional variables, the Hamiltonian h is close to unity, so that the spectrum has the form of a set of delta-functions at frequencies equal to $2\omega_E(2n + 1)$.

To conclude this section, note that formula (41) does not account for the effects associated with the change in the longitudinal coordinate u, in which case the bremsstrahlung generated by an electron broadens the spectral lines to a width of about $1/\tau$, where τ is the time scale on which an electron remains near the saddle point (Fig. 1). Note also that the appearance of a narrow peak at low frequencies ($\omega \approx 0$) is associated with the conventional bremsstrahlung. As a result, we arrive at the spectrum shown in Fig. 6.

Integrating the basic equations numerically yields analogous spectra (see Figs. 7, 8). We can see that the numerical spectra are also peaked at frequencies that are multiples of the frequency ω_E. The higher the frequency of the emitted electromagnetic wave, the wider the peaks in the radiation spectrum.

Note that the peaks in the spectrum of the transverse dipole moment (Fig. 8) are more pronounced compared to those in the spectrum of the total dipole moment (Fig. 7). Individual electrons emit radiation preferentially in the direction of the external field. The total radiation emitted by an ensemble of electrons is quadrupole in character, because the center of mass of the ensemble is not accelerated in the transverse direction, in which case, however, the shape of the frequency spectrum of the dipole moment remains the same.

In accordance with the simplest analytic approximation (41), the main difference between the spectrum shown in Fig. 6 and the spectrum in a weak external field is in the presence of two additional peaks in the intensity of radiation emitted by an electron. It is important to note that the height of the second peak, which is associated with fast transverse electron oscillations, is equal in order of magnitude to the height of the main peak. For this reason, we can expect that the electromagnetic waves will be efficiently excited at the corresponding frequencies.

6. DISCUSSION OF THE RESULTS

We have carried out an analytic investigation of the characteristic features of the scattering of an electron by an ion with a Coulomb potential in the presence of an external electrostatic field. The most interesting result is that we have revealed the existence of snakelike trajectories. The other results can be summarized as follows.

(i) The equation of electron motion in the Coulomb field of an ion has been regularized by switching to the Levi-Civita variables [14]. The regularization procedure makes it possible not only to simplify analytic calculations of the electron trajectories in a prescribed static field but also to increase both the accuracy and rate of numerical computations of the electron motion in an alternating electric field and in the Coulomb field of an ion. A slightly modified version of this regularization method was also applied in our paper [12].

(ii) The electron motions in a static field have been classified, and an explicit time-dependent solution has been derived. It should be noted that the explicit expression for the time-dependent electron coordinates, which has been obtained here for the first time, will make it possible to clarify possible applications of our results and, in particular, to determine all of the parameters of electron scattering by an ion in a uniform electrostatic field. This will be done in subsequent papers.

(iii) The equations of the adiabatic approximation developed here enabled us to formulate the problem in three-dimensional phase space. Using the adiabatic approximation, we have shown that snakelike trajectories, which are most interesting in the problem under investigation, can substantially modify the spectra of radiation emitted by electrons during stimulated scattering in a strong field. In accordance with expression (41), the spectrum of the dipole moment of the "optimum" electrons (Figs. 6, 8) is peaked at frequencies that are multiples of the frequency $2\omega_E$. We emphasize that the spectra of the dipole moment of the trapped particles are peaked in an analogous manner. Of course, in this case, the equations of the problem should be quantized. However, the atoms in Rydberg states are obviously subject to the transverse focusing effect that stems from the large asymmetry of the classical trajectories of trapped electrons (as well as to the longitudinal polarization effect). These questions will be analyzed in a separate paper.

ACKNOWLEDGMENTS

This work was supported in part by the Russian Foundation for Basic Research, project nos. 99-02-16443 and 98-02-17205.

REFERENCES

1. M. H. Mittleman, *Introduction to the Theory of Laser-Atom Interactions* (Plenum, New York, 1993); V. P. Silin, Zh. Éksp. Teor. Fiz. **47**, 2254 (1964) [Sov. Phys. JETP **20**, 1510 (1964)]; G. J. Pert, Phys. Rev. E **51**, 4778 (1995); G. Shvets and N. J. Fisch, Phys. Plasmas **4**, 428 (1997); J. M. Rax and J. Yu. Kostyukov, Phys. Rev. E **59**, 1122 (1999).
2. A. B. Borisov, X. Shi, V. B. Karpov, *et al.*, J. Opt. Soc. Am. B **11**, 1941 (1994); P. Monot, T. Auguste, P. Gibbon, *et al.*, Phys. Rev. Lett. **74**, 2953 (1995); P. E. Young and P. R. Bolton, Phys. Rev. Lett. **77**, 4556 (1996).
3. M. Dunne, T. Asshav-Rad, J. Edwards, *et al.*, Phys. Rev. Lett. **72**, 1024 (1994); A. J. Mackinnon, M. Borghesi, A. Iwase, *et al.*, Phys. Rev. Lett. **76**, 1473 (1996).
4. R. Kodama, K. Takahashi, K. A. Tonaka, *et al.*, Phys. Rev. Lett. **77**, 4906 (1996).
5. V. P. Silin, Kvantovaya Élektron. (Moscow) **26**, 11 (1999); V. P. Silin, Kvantovaya Élektron. (Moscow) **26**, 49 (1999); P. A. Norreys, M. Zepf, S. Monstaizis, *et al.*, Phys. Rev. Lett. **76**, 1832 (1996).
6. H. Nishioka, M. Odajima, K. Ueda, *et al.*, Opt. Lett. **20**, 2505 (1995).
7. E. M. Shydev, S. A. Buzza, and A. W. Castleman, Phys. Rev. Lett. **77**, 3347 (1996); T. D. Donnelly, T. Ditmire, K. Neiman, *et al.*, Phys. Rev. Lett. **76**, 2472 (1996).
8. Y. L. Shao, T. Ditmire, J. W. Tisch, *et al.*, Phys. Rev. Lett. **77**, 3343 (1996).
9. P. B. Corcum, Phys. Rev. Lett. **71**, 1994 (1993); V. D. Gildenburg, A. V. Kim, and A. M. Sergeev, Pis'ma Zh. Éksp. Teor. Fiz. **51**, 91 (1990) [JETP Lett. **51**, 104 (1990)]; N. D. Delone and V. P. Krainov, *Multiphoton Process in Atoms* (Springer-Verlag, Berlin, 1994); N. B. Delone and V. P. Kraĭnov, Usp. Fiz. Nauk **165**, 1295 (1995) [Phys. Usp. **38**, 1247 (1995)].

10. M. V. Fedorov, *Electron in a Strong Light Field* (Nauka, Moscow, 1991).
11. L. Wiesenfeld, Phys. Lett. A **144**, 467 (1990); C. D. Decker, W. B. Mori, J. M. Dawson, and T. Katsouleas, Phys. Plasmas **1**, 4043 (1994); S. Pfalzner and P. Gibbon, Phys. Rev. E **57**, 4698 (1998).
12. G. M. Fraiman, V. A. Mironov, and A. A. Balakin, Phys. Rev. Lett. **82**, 319 (1999); G. M. Fraĭman, V. A. Mironov, and A. A. Balakin, Zh. Éksp. Teor. Fiz. **115**, 463 (1999) [JETP **88**, 254 (1999)].
13. V. V. Beletskiĭ, *Essays about Motion of Cosmic Bodies* (Nauka, Moscow, 1972).
14. E. Stiefel and G. Scheifele, *Linear and Regular Celestial Mechanics* (Springer-Verlag, Berlin, 1971; Nauka, Moscow, 1975).
15. L. D. Landau and E. M. Lifshitz, *Mechanics* (Nauka, Moscow, 1988; Pergamon, New York, 1988).
16. L. D. Landau and E. M. Lifshitz, *The Classical Theory of Fields* (Nauka, Moscow, 1973; Pergamon, Oxford, 1975).

Translated by I. A. Kalabalyk

Plasma Physics Reports, Vol. 27, No. 6, 2001, pp. 474–479. Translated from Fizika Plazmy, Vol. 27, No. 6, 2001, pp. 503–508.

PLASMA KINETICS

Theory of the Polarization Bremsstrahlung from Thermal Electrons Scattered by the Debye Sphere of an Ion in a Plasma

V. A. Astapenko

Moscow Institute of Physics and Technology, Institutskiĭ proezd 9, Dolgoprudnyĭ, Moscow oblast, 141700 Russia
e-mail: astval@hotmail.com

Received October 11, 2000

Abstract—The polarization bremsstrahlung from thermal electrons scattered by the Debye sphere of an ion in a plasma is studied in the quasiclassical approximation. The model of the local plasma frequency is used to check the validity of the asymptotic expression for the polarizability of the electron cloud of an ion in the high-frequency range. This asymptotic expression is then used to derive a formula for the intensity of the total effective polarization bremsstrahlung. The *R* factor (the ratio of the contribution from the polarization bremsstrahlung to the contribution from conventional static bremsstrahlung) is obtained as a function of the plasma coupling parameter and electron density in order to analyze the role of the polarization bremsstrahlung in the total bremsstrahlung of the thermal plasma electrons. The spectral intensity of the effective polarization bremsstrahlung is calculated in the rotational approximation, which was previously employed in the theory of conventional static bremsstrahlung. It is shown that the spectral intensity of the polarization bremsstrahlung from thermal electrons scattered by the Debye sphere around an ion, as compared with the polarization bremsstrahlung by fast superthermal electrons, decreases more gradually with increasing frequency. *© 2001 MAIK "Nauka/Interperiodica".*

1. INTRODUCTION

The polarization bremsstrahlung from the Debye clouds surrounding colliding charged particles in a plasma is associated with the emission of a photon as a result of scattering of the incident particle by the polarization charge. Previously, the polarization bremsstrahlung (the transition bremsstrahlung in the terminology introduced originally by Akopyan and Tsytovich [1, 2]) was studied in the context of superthermal charged particles in the Born approximation. This approach makes it possible to describe the interaction of a photon-emitting charged particle with the scattering center by perturbation theory [3]. Then, the spectral intensity of the polarization bremsstrahlung can be calculated by the method of nonlinear current [1] or the method of the dynamic form factor of the plasma components [3].

The study of transition bremsstrahlung in the Born approximation is certainly of much physical interest. In fact, the higher the particle energy, the larger the relative contribution of the transition bremsstrahlung to the total bremsstrahlung generated by charged particles in a plasma, because the frequency range $\omega < \gamma\omega_{pe}$ (where $\gamma = (1 - v^2/c^2)^{-1/2}$ is the relativistic factor, ω_{pe} is the electron plasma frequency, and v is the velocity of the incident particle), in which the conventional bremsstrahlung is suppressed by a density effect, broadens with the particle energy.

On the other hand, the Born parameter $\eta = Z_i e^2/\hbar v$ for thermal plasma electrons is, as a rule, larger than or on the order of unity; consequently, for most of the plasma electrons, the bremsstrahlung intensity should be calculated in the opposite (quasiclassical) approximation ($\eta > 1$). In fact, the semiclassical approach developed by V.I. Kogan and his collaborators [4, 5] on the basis of the quasiclassical approximation (in particular, the methods of the so-called Kramers electrodynamics [6], which are aimed at investigating collision and emission processes during the motion of charged particles along strongly curved trajectories) proved to be very efficient when calculating conventional static bremsstrahlung in the Coulomb field as well as in the atomic field. The relative error in using the semiclassical approach to calculate bremsstrahlung is no larger than several percent, as compared to the consistent quantum-mechanical approach [5].

Accordingly, it is natural to expect that the semiclassical approach can also be used to determine the contribution of the polarization bremsstrahlung to the total bremsstrahlung intensity. For the polarization bremsstrahlung of the bound electrons, this problem was solved in [7, 8] by using the Brandt–Lundqvist plasma model [9] for the polarizability of the electron shell of the target atom (ion).

Our purpose here is to apply the methods of the Kramers electrodynamics in order to calculate the total and spectral intensities of bremsstrahlung from thermal

1063-780X/01/2706-0474$21.00 © 2001 MAIK "Nauka/Interperiodica"

plasma electrons by the Debye clouds around the ions in a plasma.

2. METHOD OF CALCULATION

The method of calculation used here is based on both the semiclassical approach mentioned in the Introduction and the local plasma model of the polarizability of the Debye sphere around an ion in a plasma (the Brandt–Lundqvist model). This model was originally developed in order to describe the photoionization of atoms [9] in the frequency range in which the main contribution to the photoeffect comes from such distances from the nucleus that are on the order of the corresponding Thomas–Fermi radius.

In the Brandt–Lundqvist model, the polarizability of the electron subsystem of the target (the Debye cloud) at the frequency ω has the form

$$\alpha^{\mathrm{BL}}(\omega) = \int_0^{R_0} \frac{\omega_p^2(r) r^2 dr}{\omega_p^2(r) - \omega^2 - i\delta} = \int \beta^{\mathrm{BL}}(r, \omega) d\mathbf{r}. \quad (1)$$

Here, the local plasma frequency $\omega_{pe}(r) = \sqrt{4\pi(e^2/m_e)n_e(r)}$ depends on the electron density at a given point in the plasma and $\beta^{\mathrm{BL}}(r, \omega)$ is the dynamic polarizability of a spherical layer of unit radius (the spatial density of the target polarizability).

In [7, 8], it was shown that the local approach to describing the target polarizability (1) makes it possible to introduce the nondipolar polarization potential of the interaction of an incident particle with the target,

$$V_{\mathrm{pol}}(\mathbf{R}, \omega) = \frac{\mathbf{R}\mathbf{E}(\omega)}{R^3} \int_0^R \beta(r, \omega) 4\pi r^2 dr \quad (2)$$

and the related induced dipole moment of the electron shell of the target,

$$\mathbf{D}_{\mathrm{pol}}(\mathbf{R}, \omega) = -\frac{\mathbf{R}}{R^3} \int_0^R \beta(r, \omega) 4\pi r^2 dr, \quad (3)$$

which determines the effective spectral intensity of the polarization bremsstrahlung:

$$\frac{d\kappa_{\mathrm{pol}}(\omega)}{d\omega} = \frac{4\omega^4}{3c^3} \int_0^\infty \left| \mathbf{D}_{\mathrm{pol}}^{\omega}(\omega, \rho) \right|^2 \rho d\rho; \quad (4)$$

where the Fourier transformed polarization dipole moment (3) of the Debye sphere at the frequency $\mathbf{D}_{\mathrm{pol}}^{\omega}(\omega, \rho)$ is calculated along the trajectory of the incident particle with the impact parameter ρ.

It is worth noting that, from a physical standpoint, the Brandt–Lundqvist model is even better suited for the problem under consideration than for the problem of the polarization bremsstrahlung from bound electrons [7, 8]. In fact, the motion of plasma electrons that occur inside the Debye sphere and emit polarization bremsstrahlung photons is only slightly affected by quantum-mechanical effects.

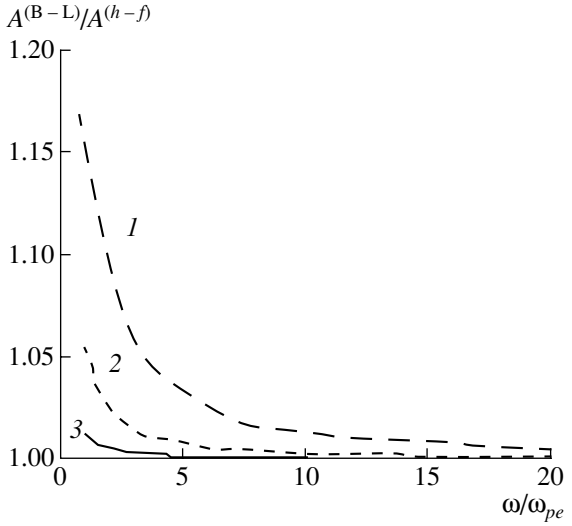

Fig. 1. Ratio of the polarization bremsstrahlung intensity in the Brandt–Lundqvist plasma model for the polarizability of the Debye sphere to that in the high-frequency limit vs. the ratio of the polarization bremsstrahlung photon frequency to the plasma frequency. The profiles were calculated in the rotational approximation for $T = 1$ eV and for different electron plasma densities n_e = (*1*) 10^{-8}, (*2*) 10^{-10}, and (*3*) 10^{-12} atomic density units (one atomic density unit is equal to $\sim 8 \times 10^{24}$ cm^{-3}).

On the other hand, from Fig. 1, we can see that, in the Brandt–Lundqvist model, the polarizability of the Debye sphere in the frequency range $\omega > \omega_{pe}$ essentially coincides with its value in the high-frequency limit, in which the spatial polarizability density has the following form (here and below, we use atomic units):

$$\beta_\infty(\omega, r) = -\frac{\omega_{pe}^2(r)}{4\pi\omega^2} = -\frac{n_e(r)}{\omega^2}. \quad (5)$$

Inside the Debye sphere, the electron density is equal to

$$n_e(r) = \frac{Z_i}{4\pi r_{\mathrm{D}e}^2} \frac{\exp(-r/r_{\mathrm{D}e})}{r}, \quad (6)$$

where $r_{\mathrm{D}e}$ is the electron Debye radius. With this expression, the induced dipole moment (3) becomes

$$\mathbf{D}_{\mathrm{pol}}^{(\mathrm{D})}(\omega, \mathbf{R}) = \frac{1}{\omega^2} \frac{\mathbf{R}}{R^3} N_e(R); \quad (7)$$

where the number $N_e(R)$ of plasma electrons within a sphere of radius R is equal to

$$N_e(R) = \int_0^R 4\pi n_e(r) r^2 dr = Z_i[1 - e^{-R/r_{De}}(1 + R/r_{De})]. \quad (8)$$

3. TOTAL BREMSSTRAHLUNG LOSSES

In order to calculate the intensity of the total (integrated over the impact parameter and frequency) effective bremsstrahlung generated by an electron with energy T scattered by the Debye sphere of an ion, we start with the expression

$$\kappa_{\rm pol} = \int_{\omega_{pe}}^{T/\hbar} d\kappa_{\rm pol}(\omega). \quad (9)$$

Substituting formulas (4) and (7) into expression (9), we obtain

$$\kappa_{\rm pol}^{(\rm D)}(T) = \frac{4}{3c^3}\int_0^\infty \rho d\rho \iint dt dt' \times \int_0^{T/\hbar} e^{i\omega(t-t')} \frac{\mathbf{R}(t)\mathbf{R}(t')}{R^3(t)R^3(t')} N[R(t)]N[R(t')] d\omega. \quad (10)$$

Here, the lower limit of integration over frequency is set equal to zero. However, in reality, the transverse photons are known to propagate in a plasma only under the condition $\omega > \omega_{pe}$. Consequently, this choice of the lower limit of integration corresponds to an ideal plasma, in which the characteristic correlation time scale for the motion of the scattered electrons is smaller than the inverse plasma frequency.

Then, we turn to the equality $\int_0^\infty e^{i\omega(t-t')} d\omega = \pi\delta(t - t')$, in which, in accordance with the quasiclassical condition $\hbar \longrightarrow 0$, we extend the upper limit of integration to infinity. In formula (10), we pass over to the new integration variables R, in which case the lower limit of integration becomes equal to the minimum impact parameter $r_{\min}(\rho)$ (or, equivalently, the minimum distance between the incident electron and the ion) and the integral itself should be doubled, because the integrand in formula (10) is an even function of time. We also integrate over the impact parameter ρ in the same way as was done in [4]. As a result, we obtain

$$\kappa_{\rm pol}^{(\rm D)} = \frac{8\pi}{3c^3\sqrt{2T}}\int_0^\infty f_{\rm pol}^2(r)\sqrt{1 - \frac{U_{\rm D}(r)}{T}} r^2 dr. \quad (11)$$

Here, $U_{\rm D}(r) = -Z_i \exp(-r/r_{De})/r$ is the Debye screening potential of an ion in a plasma and the polarization force $f_{\rm pol}(r)$ has the form

$$f_{\rm pol}(r) = \frac{N_e(r)}{r^2}. \quad (12)$$

The repulsive force (12) is exerted by electrons that are inside a sphere of radius R on the incident electron. According to Newton's third law, the incident electron exerts an equal force on the electrons inside the sphere, thereby accelerating a negatively charged electron cloud around an ion as a single entity and driving the polarization bremsstrahlung.

We also present the expression for the intensity of the total effective static bremsstrahlung [4]:

$$\kappa_{\rm st}^{(\rm D)} = \frac{8\pi}{3c^3\sqrt{2T}}\int_0^\infty f_{\rm st}^2(r)\sqrt{1 - \frac{U_{\rm D}(r)}{T}} r^2 dr; \quad (13)$$

where $f_{\rm st}(r) = -dU_{\rm D}/dr$ is the ordinary "static" force, which governs the trajectory of the incident particle.

Note that, although formulas (11) and (13) are very similar in structure, there is an important difference: the integral in expression (13) diverges at the lower limit (in the quasiclassical approximation, as $\int_0 r^{-5/2} dr$) and should be truncated, whereas, in formula (11), the integral at the lower limit is converging. The latter is explained by the fact that, according to formula (8), the charge $N_e(R)$ of the plasma electrons that emit polarization bremsstrahlung photons approaches zero as R decreases.

Using relationships (8), (11), and (12) and the above formula for the Debye potential, we arrive at the following expression for the intensity of the total effective polarization bremsstrahlung:

$$\kappa_{\rm pol}^{(D)} = \frac{8\pi}{3c^3\sqrt{2T}}\frac{Z_i^2}{r_{De}}\Phi\left(\frac{2a_T}{r_{De}}\right), \quad (14)$$

where we introduce the function

$$\Phi(x) = \int_0^\infty [1 - (1 + r)e^{-r}]^2 \sqrt{1 + (x/r)e^{-x}}\, dr/r^2. \quad (15)$$

The parameter $a_T = Z_i/2T$ is the length of Coulomb scattering of an electron with energy T by the Debye cloud of an ion of charge Z_i.

Note that the ratio $2a_T/r_{De}$ is inversely proportional to the plasma coupling parameter. For an ideal plasma, we have $2a_T/r_{De} \ll 1$.

The plot of the function $\Phi(x)$ is shown in Fig. 2. We can see that the function is gradually increasing, so that,

for an ideal plasma, we can set $\Phi(\xi) = 0.5$, in which case expression (14) becomes

$$\kappa_{\rm pol}^{(\rm D)} = \frac{4\pi}{3c^3\sqrt{2T}}\frac{Z_i^2}{r_{\rm De}}. \qquad (14a)$$

When applied to one ion, formula (14a), which is valid for quasiclassical motion of the incident particle, coincides with the corresponding formula derived by Tsytovich [10] for the intensity of the total polarization bremsstrahlung generated by superthermal electrons moving along straight trajectories.

Hence, we can conclude that, in an ideal plasma, the total effective polarization bremsstrahlung generated by an incident particle is weakly sensitive to the shape of the particle trajectory.

For effective static bremsstrahlung in the Coulomb field of an ion, expression (13) with the integral truncated at the lower limit takes the form

$$\kappa_{\rm st} = \frac{8\pi Z_i\sqrt{2T}}{9c^3}\left[\left(\frac{x_m+2}{x_m}\right)^{3/2}-1\right]; \qquad (16)$$

where $x_m = (2\sqrt{2T}/Z_i)^{2/3}$.

For $x_m \ll 1$, formula (16) simplifies to

$$\kappa_{\rm st} = \frac{8\sqrt{2}\pi}{9c^3}Z_i^2. \qquad (16a)$$

Formula (16a) differs from the Kramers formula only in a numerical coefficient of about 0.8, because the radius at which the integral in expression (13) is truncated is taken with an approximate numerical factor.

Using the familiar expression for the Debye radius, we obtain from formulas (16a) and (14a) the ratio of the contribution of the polarization bremsstrahlung to that of static bremsstrahlung:

$$R^{\rm D}(n_e, T) = \frac{\kappa_{\rm pol}^{\rm D}}{\kappa_{\rm st}} \simeq 3\frac{\sqrt{n_e}}{T}. \qquad (17)$$

This relationship implies that, in order for the polarization effects to make a significant contribution to the total bremsstrahlung of an incident electron scattered by the Debye screening cloud around an ion, the plasma should be sufficiently dense and cold.

For a laser plasma with the parameters $n_e \approx 7 \times 10^{18}$ cm^{-3} and $T \approx 1$ eV, the ratio $R^{\rm D}$ is estimated as $R^{\rm D} \approx 0.1$.

For $n_e \approx 7 \times 10^{20}$ cm^{-3}, we have $R^{\rm D} \approx 1$, in which case, however, the plasma is nonideal, because the plasma coupling parameter is smaller than unity.

It is of interest to estimate the contribution of the polarization bremsstrahlung for a plasma in the solar interior, where $n_e \approx 5.7 \times 10^{25}$ cm^{-3} and $T \approx 1550$ eV. With these parameter values, formula (17) gives $R^{\rm D} \approx 0.15$.

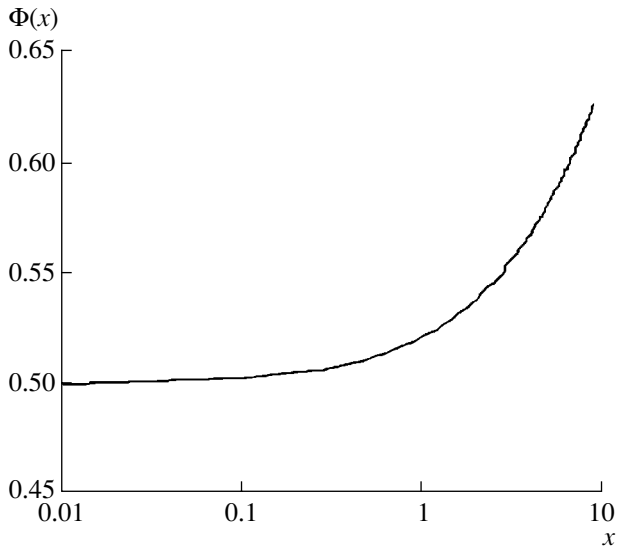

Fig. 2. Plot of the function $\Phi(x)$, which is defined by formula (15) and enters expression (14) for the intensity of the total effective polarization bremsstrahlung from a thermal electron scattered by the Debye cloud of an ion in a plasma.

In terms of the plasma coupling parameter $\zeta = (4\pi/3)r_{\rm D}^3 n_e$, the ratio $R^{\rm D}$ has the form

$$R^{\rm D}(n, \zeta) \approx 1.24\frac{n^{1/6}}{\zeta^{2/3}}. \qquad (17a)$$

One can see that, for a fixed coupling parameter ζ, the ratio $R^{\rm D}$ is almost insensitive to the density of the plasma electrons.

The above analysis shows that the contribution of the polarization effects to the total bremsstrahlung losses suffered by the thermal plasma electrons scattered by the Debye cloud around an ion in a nondegenerate plasma may be comparable with that of conventional static bremsstrahlung only when the plasma is sufficiently cold and dense, such that the coupling parameter ζ is on the order of unity. Otherwise, the ratio of these contributions is no larger than 10–15%.

4. SPECTRAL BREMSSTRAHLUNG LOSSES IN THE ROTATIONAL APPROXIMATION

Here, we calculate the spectral intensity of the effective polarization bremsstrahlung (the spectral bremsstrahlung losses) in the rotational approximation, which was previously used to determine the spectral intensity of the conventional static bremsstrahlung [4–6]. Formally, this approximation implies that expression (11) should be supplemented with the delta function of the frequency difference $\omega - \omega_{\rm rot}(r)$, where the angular

frequency $\omega_{rot}(r)$ of rotation of the incident particle at a given point in the plasma has the form

$$\omega_{rot}(r) = \sqrt{\frac{2(T + |U(r)|)}{r^2}}. \quad (18)$$

Then, we arrive at the following expression for the spectral intensity of the effective polarization bremsstrahlung:

$$\frac{d\kappa_{pol}^{(rot)}(\omega)}{d\omega} = \frac{8\pi}{3c^3\sqrt{2T}}\int_0^\infty f_{pol}^2(r)\sqrt{1-\frac{U_D(r)}{T}}\delta[\omega-\omega_{rot}(r)]r^2dr. \quad (19)$$

Taking the integral in this expression, we find

$$\frac{d\kappa_{pol}^{(rot)}(\omega)}{d\omega} = \frac{8\pi f_{pol}^2(r_\omega)}{3c^3\sqrt{2T}}\frac{r_\omega^4}{1+\left|U_r'(r_\omega)\right|/(\omega^2 r_\omega)}; \quad (19a)$$

where the quantity r_ω satisfies the equation

$$\omega = \omega_{rot}(r). \quad (20)$$

The expression for the spectral intensity of the effective static bremsstrahlung is analogous to expression (19a):

$$\frac{d\kappa_{st}^{(rot)}(\omega)}{d\omega} = \frac{8\pi f_{st}^2(r_\omega)}{3c^3\sqrt{2T}}\frac{r_\omega^4}{1+\left|U_r'(r_\omega)\right|/(\omega^2 r_\omega)}. \quad (21)$$

Formula (21) differs from formula (19a) only in that it contains an ordinary static force exerted by a plasma ion on the incident electron instead of the polarization force (12).

As a result, using formulas (19a) and (21), we obtain the following expression for the spectral R factor in the rotational approximation:

$$R^{(rot)}(\omega) \equiv \frac{d\kappa_{pol}^{(rot)}(\omega)}{d\kappa_{st}^{(rot)}(\omega)} = \left[\frac{f_{pol}(r_\omega)}{f_{st}(r_\omega)}\right]^2 = \left[\frac{N_e(r_\omega)}{r_\omega^2 U_r'(r_\omega)}\right]^2. \quad (22)$$

With the above formulas for $N_e(r)$ and $U(r)$, expression (22) becomes

$$R^{(rot)}(\omega) = \left[1-\frac{\exp(r_\omega/r_{De})}{1+r_\omega/r_{De}}\right]^2 \approx (r_\omega < r_{De}) \approx \frac{1}{4}\left(\frac{r_\omega}{r_{De}}\right)^4. \quad (22a)$$

When deriving expression (22a), we used the inequality $r_\omega < r_{De}$, which applies to an ideal plasma and is valid in the frequency range $\omega \approx \omega_C = v^3/Z_i$, i.e., for frequencies that are on the order of (or higher than) the characteristic Coulomb frequency.

From expression (22a), we can see that, in the rotational approximation, the polarization bremsstrahlung at frequencies $\omega > \omega_{pe}$ makes only a small contribution to the spectral cross section for bremsstrahlung from thermal electrons scattered by the Debye sphere of an ion. Estimates show that $R^{(rot)}(\omega) \le 0.01$ in this case.

For a Coulomb field, the quantity r_ω has the form $r_\omega^C \approx \sqrt[3]{2Z_i/\omega^2}$. From this expression and from formula (22a), the law according to which the factor $R^{(rot)}(\omega)$ decreases can be obtained in an explicit form:

$$R_D^{rot}(\omega) \approx \frac{1}{4r_D^4}\frac{(2Z_i)^{4/3}}{\omega^{8/3}}. \quad (23)$$

In the frequency range under consideration, the spectral intensity of the static bremsstrahlung depends weakly on the frequency. Consequently, in the rotational approximation, formula (23) can be used to determine the frequency dependence of the spectral intensity of the effective polarization bremsstrahlung from thermal plasma electrons scattered by the Debye sphere around an ion:

$$\frac{d\kappa_{pol}^{(rot)}(\omega)}{d\omega} \propto \omega^{-\frac{8}{3}}. \quad (24)$$

The frequency dependence (24) is somewhat different from the dependence [10]

$$d\kappa_{pol}^{(rot)}(\omega)/d\omega \propto \omega^{-4}. \quad (25)$$

which describes a decrease in the spectral cross section for bremsstrahlung from superthermal electrons in the frequency range $\omega > (v/v_{Te})\omega_{pe}$.

5. CONCLUSION

The polarization bremsstrahlung from thermal plasma electrons scattered by the Debye sphere around an ion in a plasma has been studied in the quasiclassical approximation. This work complements papers [1–3], in which a related problem was solved for fast superthermal electrons. The total polarization bremsstrahlung losses have been determined as functions of the plasma coupling parameter and electron plasma density. It is shown that the R factor (the ratio of the contribution of the polarization bremsstrahlung to that of static bremsstrahlung) increases gradually with increasing the density of the thermal electrons and is usually no larger than 10–15%.

The spectral intensity of the effective polarization bremsstrahlung generated by the thermal electrons has been calculated using the rotational approximation, which was previously applied in the theory of static bremsstrahlung [4–6]. Analysis has revealed that, in the frequency range $\omega > \omega_{pe}$, the polarization bremsstrahl-

ung from the thermal electrons makes only a small contribution to the total bremsstrahlung. A comparison between the asymptotic expressions (24) and (25) shows that the spectral intensity of the effective polarization bremsstrahlung decreases more gradually than that of the transition bremsstrahlung in the Born approximation (see [2]).

ACKNOWLEDGMENTS

I am grateful to V.I. Gervids, V.I. Kogan, A.B. Kukushkin, and V.S. Lisitsa for their attention to this work and fruitful discussions. This work was supported by the Russian Foundation for Basic Research, project no. 98-02-16763.

REFERENCES

1. A. A. Akopyan and V. N. Tsytovich, Fiz. Plazmy **1**, 673 (1975) [Sov. J. Plasma Phys. **1**, 371 (1975)].
2. A. A. Akopyan and V. N. Tsytovich, Zh. Éksp. Teor. Fiz. **71**, 166 (1976) [Sov. Phys. JETP **44**, 87 (1976)].
3. V. A. Astapenko, V. M. Buĭmistrov, Yu. A. Krotov, and V. N. Tsytovich, Fiz. Plazmy **15**, 202 (1989) [Sov. J. Plasma Phys. **15**, 116 (1989)].
4. V. I. Gervids and V. I. Kogan, Pis'ma Zh. Éksp. Teor. Fiz. **22**, 308 (1975) [JETP Lett. **22**, 142 (1975)].
5. V. I. Kogan and A. B. Kukushkin, Zh. Éksp. Teor. Fiz. **87**, 1164 (1984) [Sov. Phys. JETP **60**, 665 (1984)].
6. V. I. Kogan, A. B. Kukushkin, and V. S. Lisitsa, Phys. Rep. **213**, 1 (1992).
7. V. A. Astapenko, L. A. Bureyeva, and V. S. Lisitsa, Phys. Scr. T **T86**, 62 (2000).
8. V. A. Astapenko, L. A. Bureeva, and V. S. Lisitsa, Zh. Éksp. Teor. Fiz. **117**, 496 (2000) [JETP **90**, 434 (2000)].
9. W. Brandt and S. Lundqvist, Phys. Rev. **139**, A612 (1965).
10. V. N. Tsytovich, in *Polarization Bremsstrahlung from Atoms and Particles*, Ed. by V. N. Tsytovich and I. M. Oĭringel' (Nauka, Moscow, 1987), Sec. 2.3.

Translated by O. E. Khadin

Plasma Physics Reports, Vol. 27, No. 6, 2001, pp. 480–489. Translated from Fizika Plazmy, Vol. 27, No. 6, 2001, pp. 509–518.

PLASMA OSCILLATIONS AND WAVES

Microwave Amplification in a Coaxial Slow-Wave Plasma Transmission Line

G. V. Sotnikov

Kharkov Institute of Physics and Technology, National Science Center, Akademicheskaya ul. 1, Kharkov, 61108 Ukraine

e-mail: sotnikov@kipt.kharkov.ua

Received June 19, 2000; in final form, November 22, 2000

Abstract—Microwave generation by an electron beam in a coaxial transmission line in which the inner and outer conductors are both corrugated is studied theoretically. An annular electron beam propagates in a transport channel filled entirely with plasma. The eigenmodes of the plasma-filled coaxial line are studied, as well as how they are affected by the plasma density. It is shown that, in the presence of a plasma, the microwaves are amplified to a significantly greater extent and the spectrum of the generated microwaves is broader. The nonlinear amplification regime is analyzed. The maximum possible amplitude of the longitudinal electric field and the interaction efficiency are determined as functions of the plasma density. A comparison between the results obtained and the analogous parameters of a vacuum structure shows that plasma-filled hybrid structures are more promising than vacuum sources. © *2001 MAIK "Nauka/Interperiodica".*

1. INTRODUCTION

A vacuum slow-wave structure acquires the well-known hybrid properties when its interaction chamber (the transport channel, where an electron beam propagates) is filled with a plasma. The principles of operation of hybrid plasma-filled slow-wave structures were first described in [1–3]. Filling the transport channel with a plasma makes it possible to substantially enhance the longitudinal electric field, so that the coupling constant increases and, accordingly, the amplification coefficient of the generated microwaves becomes larger. Under proper conditions, the beam interacts with the natural waves of a vacuum structure, thereby generating intense microwave power fluxes. Experimental investigations [4–6] confirm the theoretical predictions that hybrid slow-wave structures provide a basis for the creation of high-power oscillators and amplifiers.

Recall that, in research on hybrid plasma structures, the first experiments were carried out with vacuum slow-wave structures in the form of a chain of coupled cavity resonators. In such hybrid plasma structures, generation is most efficient when the frequency of the synchronously excited microwaves is equal to the plasma frequency. As a result, in a waveguide with a given plasma density, the spectrum of the excited microwaves is narrow (on the order of the instability growth rate). Kornilov *et al.* [7] suggested that filling a vacuum structure in which a broadband cable wave can propagate with a plasma makes it possible to increase the amplification coefficient, while maintaining the broadband amplification.

This paper is aimed at investigating the amplitude–frequency characteristics of an amplifier based on a coaxial transmission line in which the inner and outer conductors are both corrugated and the transport channel is filled entirely with a plasma. The linear and nonlinear theories of an amplifier based on an analogous vacuum structure were reported at the Seventh Crimea Conference on Microwave Techniques and Telecommunication Technology (Sevastopol, Ukraine) and the Twelfth International Conference on High-Power Particle Beams (Haifa, Israel) and were also published in the proceedings of these conferences ([8] and [9], respectively) and in [10]. It was shown that, in such a waveguide structure, microwaves are actually generated in a broad frequency band. The objective of our paper is to investigate how the dispersion properties, amplification coefficients, and microwave amplitude change in a coaxial slow-wave transmission line in which the transport channel is filled with a plasma. It should be noted that Kornilov *et al.* [7] carried out preliminary calculations of the amplification coefficients and coupling impedances in a plasma-filled coaxial line in which only the inner conductor is corrugated. They showed that the presence of a plasma can substantially alter the electrodynamic parameters of the waveguide structure if the radius of the transport channel is comparable with or larger than the wavelength of the amplified microwaves. This effect is attributed to the surface nature of the resonant wave (in [7], the electron beam was assumed to interact with the zeroth spatial mode of the cable wave). The overall picture of the microwave amplification changes substantially only if the plasma density is very high.

1063-780X/01/2706-0480$21.00

2. LINEAR REGIME

The slow-wave structure under consideration (Fig. 1) is a coaxial transmission line in which the inner and outer cylindrical conductors (of radii ρ and b, respectively) are both corrugated. The transport channel with an inner radius σ and outer radius a is filled entirely with a plasma of density n_p. The microwaves in the transport channel are generated by a thin annular electron beam with a radius r_b, velocity v_0, and current I_b. Let the period of the structure be D and let the resonators be the same width equal to d. The inner conductor can be displaced with respect to the outer conductor by an arbitrary distance l.

In the linear approximation, the dispersion relation describing the generation of a monochromatic wave by an electron beam can be obtained by the method of separate regions. We conditionally divide the slow-wave structure into four regions: (**I**) $a \le r \le b$, (**II**$_<$) $\sigma \le r \le r_b$, (**II**$_>$) $r_b \le r \le a$, and (**III**) $\rho \le r \le \sigma$. For each of these regions, we must solve Maxwell's equations and match the solutions (with arbitrary constants) at the boundaries. The periodicity of the slow-wave structure enables us to represent the perturbations of all of the quantities in the transport channel in the same manner:

$$X = \sum_{m=-\infty}^{m=\infty} X_m \exp(i\beta_m z - i\omega t), \tag{1}$$

where $\beta_m = \beta_0 + 2\pi m/D$, ω is the wave frequency, and the z-axis is directed along the symmetry axis of the structure. Inside the resonators, we restrict ourselves to considering the fundamental spatial mode of a standing wave. The boundary conditions imply that, first, the tangential components of the electric field should vanish at the metal surfaces and, second, the tangential components of the electric and magnetic fields should be continuous at the boundaries between the transport channel and the resonators. The jump in the components E_r and H_φ of the electric and magnetic fields at the beam surface is proportional to the beam current

$$H^{\mathrm{II}_>}_{\varphi,m} - H^{\mathrm{II}_<}_{\varphi,m} = i\frac{2e\omega I_b}{(\omega-\beta_m v_0)^2\gamma_0^3 mc v_0 r_b} E_{z,m}(r_b), \tag{2}$$

where $\gamma_0 = 1/\sqrt{1 - v_0^2/c^2}$.

For better convergence of the numerical method, we take into account a quasistatic singularity of the tangential electric field at the steps of the corrugations [11, 12]:

$$E_z^{\mathrm{I}} = E_z^{\mathrm{II}_>}\Big|_{r=a} = \begin{cases} M_1, & |z+nD| < d/2 \\ 0, & d/2 < |z+nD| < D/2 \end{cases}, \tag{3}$$

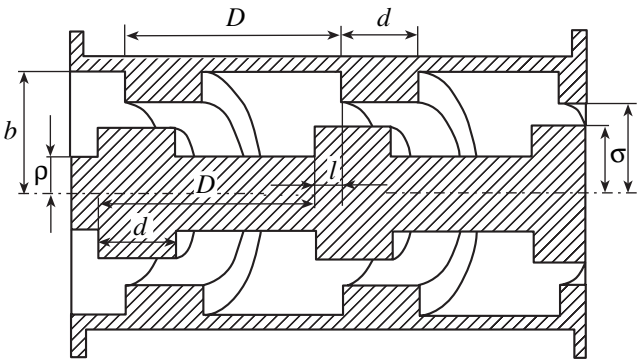

Fig. 1. Configuration of a coaxial slow-wave structure.

$$E_z^{\mathrm{III}} = E_z^{\mathrm{II}_<}\Big|_{r=\sigma} = \begin{cases} M_2\exp(i\beta_0 l), & |z-l+nD| < d/2 \\ 0, & d/2 < |z-l+nD| < D/2 \end{cases}, \tag{4}$$

where M_1 and M_2 are arbitrary constants, the integer n is the number of the resonator, and the origin $z = 0$ of the longitudinal coordinate is in the middle of the inner resonator.

Taking into account conditions (2) at the beam surface and conditions (3) and (4), we match the longitudinal components of the electric field at the boundaries $r = \sigma$ and $r = a$. As a result, we obtain the following expressions for the components of the electromagnetic field of the E-wave in each of the above four regions:

$$E_z^{\mathrm{I}} = M_1\frac{F_0(k,r,b)}{F_0(k,a,b)}, \quad H_\varphi^{\mathrm{I}} = -iM_1\frac{F_1(k,r,b)}{F_0(k,a,b)}, \tag{5}$$

$$E_z^{\mathrm{III}} = M_2 e^{i\beta_0 l}\frac{F_0(k,r,\rho)}{F_0(k,\sigma,\rho)}, \qquad H_\varphi^{\mathrm{III}} = -iM_2 e^{i\beta_0 l}\frac{F_1(k,r,\rho)}{F_0(k,\sigma,\rho)}, \tag{6}$$

$$E_z^{\mathrm{II}_>} = \frac{d}{D}\sum_{m=-\infty}^{\infty}\frac{\psi_m}{\Delta_m}e^{i\beta_m z}\left\{M_2 e^{-im\varphi_0}\frac{F_0(k_{\perp m},r,a)}{F_0(k_{\perp m},\sigma,a)} + M_1\left[\frac{F_0(k_{\perp m},r,\sigma)}{F_0(k_{\perp m},a,\sigma)} - \frac{\alpha_m^2 F_0(k_{\perp m},r,r_b)}{(\omega-\beta_m v_0)^2}\frac{F_0(k_{\perp m},r_b,\sigma)}{F_0(k_{\perp m},a,\sigma)}\right]\right\},$$

$$H_\varphi^{\mathrm{II}_>} = \frac{d}{D}\sum_{m=-\infty}^{\infty}\frac{-ik\varepsilon_3}{k_{\perp m}}\frac{\psi_m}{\Delta_m}e^{i\beta_m z}$$

$$\times\left\{M_2 e^{-im\varphi_0}\frac{F_1(k_{\perp m}, r, a)}{F_0(k_{\perp m}, \sigma, a)} + M_1\left[\frac{F_1(k_{\perp m}, r, \sigma)}{F_0(k_{\perp m}, a, \sigma)}\right.\right.$$

$$\left.\left. - \frac{\alpha_m^2 F_1(k_{\perp m}, r, r_b)}{(\omega - \beta_m v_0)^2}\frac{F_0(k_{\perp m}, r_b, \sigma)}{F_0(k_{\perp m}, a, \sigma)}\right]\right\}, \quad (7)$$

$$E_r^{\text{II}_>} = \frac{d}{D}\sum_{m=-\infty}^{\infty}\frac{-i\beta_m\varepsilon_3}{k_{\perp m}}\frac{\psi_m}{\Delta_m}e^{i\beta_m z}$$

$$\times\left\{M_2 e^{-im\varphi_0}\frac{F_1(k_{\perp m}, r, a)}{F_0(k_{\perp m}, \sigma, a)} + M_1\left[\frac{F_1(k_{\perp m}, r, \sigma)}{F_0(k_{\perp m}, a, \sigma)}\right.\right.$$

$$\left.\left. - \frac{\alpha_m^2 F_1(k_{\perp m}, r, r_b)}{(\omega - \beta_m v_0)^2}\frac{F_0(k_{\perp m}, r_b, \sigma)}{F_0(k_{\perp m}, a, \sigma)}\right]\right\},$$

$$E_z^{\text{II}_<} = \frac{d}{D}\sum_{m=-\infty}^{\infty}\frac{\psi_m}{\Delta_m}e^{i\beta_m z}$$

$$\times\left\{M_1\frac{F_0(k_{\perp m}, r, \sigma)}{F_0(k_{\perp m}, a, \sigma)} + M_2 e^{-im\varphi_0}\left[\frac{F_0(k_{\perp m}, r, a)}{F_0(k_{\perp m}, \sigma, a)}\right.\right.$$

$$\left.\left. - \frac{\alpha_m^2 F_0(k_{\perp m}, r, r_b)}{(\omega - \beta_m v_0)^2}\frac{F_0(k_{\perp m}, r_b, a)}{F_0(k_{\perp m}, a, \sigma)}\right]\right\},$$

$$H_\varphi^{\text{II}_<} = \frac{d}{D}\sum_{m=-\infty}^{\infty}\frac{-ik\varepsilon_3}{k_{\perp m}}\frac{\psi_m}{\Delta_m}e^{i\beta_m z}$$

$$\times\left\{M_1\frac{F_1(k_{\perp m}, r, \sigma)}{F_0(k_{\perp m}, a, \sigma)} + M_2 e^{-im\varphi_0}\left[\frac{F_1(k_{\perp m}, r, a)}{F_0(k_{\perp m}, \sigma, a)}\right.\right. \quad (8)$$

$$\left.\left. - \frac{\alpha_m^2 F_1(k_{\perp m}, r, r_b)}{(\omega - \beta_m v_0)^2}\frac{F_0(k_{\perp m}, r_b, a)}{F_0(k_{\perp m}, a, \sigma)}\right]\right\},$$

$$E_r^{\text{II}_<} = \frac{d}{D}\sum_{m=-\infty}^{\infty}\frac{-i\beta_m\varepsilon_3}{k_{\perp m}}\frac{\psi_m}{\Delta_m}e^{i\beta_m z}$$

$$\times\left\{M_1\frac{F_1(k_{\perp m}, r, \sigma)}{F_0(k_{\perp m}, a, \sigma)} + M_2 e^{-im\varphi_0}\left[\frac{F_1(k_{\perp m}, r, a)}{F_0(k_{\perp m}, \sigma, a)}\right.\right.$$

$$\left.\left. - \frac{\alpha_m^2 F_1(k_{\perp m}, r, r_b)}{(\omega - \beta_m v_0)^2}\frac{F_0(k_{\perp m}, r_b, a)}{F_0(k_{\perp m}, a, \sigma)}\right]\right\}.$$

In formulas (7) and (8), the expressions for the electromagnetic field components symbolized by ">" and "<" are valid in the regions $r > r_b$ and $r < r_b$, respectively. The rest of the notation is as follows:

$$F_n(q, x, y) = J_n(qx)Y_0(qy) - Y_n(qx)J_0(qy),$$

$$\varepsilon_3 = 1 - \omega_p^2/\omega^2, \quad \omega_p^2 = 4\pi e^2 n_p/m,$$

$$k_{\perp m} = \sqrt{(k^2 - \beta_m^2)\varepsilon_3}, \quad k = \omega/c,$$

$$\varphi_0 = 2\pi l/D, \quad \psi_m = \sin(\beta_m d/2)/(\beta_m d/2),$$

$$\Delta_m = 1 + \frac{\alpha_m^2 F_0(k_{\perp m}, r_b, a)}{(\omega - \beta_m v_0)^2}\frac{F_0(k_{\perp m}, r_b, \sigma)}{F_0(k_{\perp m}, a, \sigma)},$$

$$\alpha_m^2 = \frac{I_b}{I_A}\frac{\pi c^3(k^2 - \beta_m^2)}{\gamma_0^3 v_0}, \quad I_A = 17\ \text{kA},$$

where J_n and Y_n are nth order Bessel and Weber functions.

The condition that the radial microwave fluxes be continuous at the surfaces of the transport channel, $r = a$ and $r = \sigma$, yields the desired dispersion relation

$$Y_{12}Y_{32} - Y_{11}Y_{33} = 0, \quad (9)$$

$$Y_{12} = \frac{d}{D}\sum_{m=-\infty}^{\infty}\frac{k\varepsilon_3}{k_{\perp m}}\frac{\psi_m^2}{\Delta_m}\left[\frac{F_1(k_{\perp m}, a, \sigma)}{F_0(k_{\perp m}, a, \sigma)} - \frac{\alpha_m^2}{(\omega - \beta_m v_0)^2}\right.$$

$$\left.\times F_1(k_{\perp m}, a, r_b)\frac{F_0(k_{\perp m}, r_b, \sigma)}{F_0(k_{\perp m}, a, \sigma)}\right] - \frac{F_1(k, a, b)}{F_0(k, a, b)},$$

$$Y_{32} = \frac{d}{D}\sum_{m=-\infty}^{\infty}\frac{k\varepsilon_3}{k_{\perp m}}\frac{\psi_m^2}{\Delta_m}\left[\frac{F_1(k_{\perp m}, \sigma, a)}{F_0(k_{\perp m}, \sigma, a)} - \frac{\alpha_m^2}{(\omega - \beta_m v_0)^2}\right. \quad (10)$$

$$\left.\times F_1(k_{\perp m}, \sigma, r_b)\frac{F_0(k_{\perp m}, r_b, a)}{F_0(k_{\perp m}, a, \sigma)}\right] - \frac{F_1(k, \sigma, \rho)}{F_0(k, \sigma, \rho)},$$

$$Y_{11} = \frac{d}{D}\sum_{m=-\infty}^{\infty}\frac{k\varepsilon_3}{k_{\perp m}}\frac{\psi_m^2}{\Delta_m}e^{im\phi_0}\frac{F_1(k_{\perp m}, a, a)}{F_0(k_{\perp m}, \sigma, a)},$$

$$Y_{33} = \frac{d}{D}\sum_{m=-\infty}^{\infty}\frac{k\varepsilon_3}{k_{\perp m}}\frac{\psi_m^2}{\Delta_m}e^{-im\phi_0}\frac{F_1(k_{\perp m}, \sigma, \sigma)}{F_0(k_{\perp m}, a, \sigma)}.$$

The quantities Y_{12} and Y_{32} have a clear physical meaning: they describe the eigenmodes of a slow-wave structure whose outer ($Y_{12} = 0$) and inner ($Y_{32} = 0$) conductors are both corrugated. The way in which the dispersion relation is derived gives the following relationship between the arbitrary constants M_1 and M_2:

$$M_2 = -M_1 Y_{12}/Y_{11} \text{ or } M_2 = -M_1 Y_{33}/Y_{32}. \quad (11)$$

In order to investigate the microwave amplification coefficient, we reduce the dispersion relation (9) to the characteristic equation for a traveling-wave tube (TWT) [13]. To do this, we transform expressions (10) to the identities

$$\begin{aligned}
Y_{12} &= Z_1 - \frac{d}{D}\sum_{m=-\infty}^{\infty}\frac{k\varepsilon_3}{k_{\perp m}}\psi_m^2\frac{1-\Delta_m}{\Delta_m}\\
&\times\frac{F_1(k_{\perp m}, a, a)}{F_0(k_{\perp m}, \sigma, a)}\frac{F_0(k_{\perp m}, r_b, \sigma)}{F_0(k_{\perp m}, r_b, a)},\\
Y_{32} &= Z_2 - \frac{d}{D}\sum_{m=-\infty}^{\infty}\frac{k\varepsilon_3}{k_{\perp m}}\psi_m^2\frac{1-\Delta_m}{\Delta_m}\\
&\times\frac{F_1(k_{\perp m}, \sigma, \sigma)}{F_0(k_{\perp m}, a, \sigma)}\frac{F_0(k_{\perp m}, r_b, a)}{F_0(k_{\perp m}, r_b, \sigma)},\\
Y_{11} &= Z_{11} + \frac{d}{D}\sum_{m=-\infty}^{\infty}\frac{k\varepsilon_3}{k_{\perp m}}\psi_m^2\frac{1-\Delta_m}{\Delta_m}\frac{F_1(k_{\perp m}, a, a)}{F_0(k_{\perp m}, \sigma, a)}e^{im\phi_0},\\
Y_{33} &= Z_{33} + \frac{d}{D}\sum_{m=-\infty}^{\infty}\frac{k\varepsilon_3}{k_{\perp m}}\psi_m^2\frac{1-\Delta_m}{\Delta_m}\frac{F_1(k_{\perp m}, \sigma, \sigma)}{F_0(k_{\perp m}, a, \sigma)}e^{-im\phi_0}.
\end{aligned} \tag{12}$$

Here, the quantities Z_1, Z_2, Z_{11}, and Z_{33} are independent of the beam current and are defined as

$$\begin{aligned}
Z_1 &= \frac{d}{D}\sum_{m=-\infty}^{\infty}\frac{k\varepsilon_3}{k_{\perp m}}\frac{\psi_m^2}{\Delta_m}\frac{F_1(k_{\perp m}, a, \sigma)}{F_0(k_{\perp m}, a, \sigma)} - \frac{F_1(k, a, b)}{F_0(k, a, b)},\\
Z_2 &= \frac{d}{D}\sum_{m=-\infty}^{\infty}\frac{k\varepsilon_3}{k_{\perp m}}\frac{\psi_m^2}{\Delta_m}\frac{F_1(k_{\perp m}, \sigma, a)}{F_0(k_{\perp m}, \sigma, a)} - \frac{F_1(k, \sigma, \rho)}{F_0(k, \sigma, \rho)},\\
Z_{11} &= \frac{d}{D}\sum_{m=-\infty}^{\infty}\frac{k\varepsilon_3}{k_{\perp m}}\psi_m^2\frac{F_1(k_{\perp m}, a, a)}{F_0(k_{\perp m}, \sigma, a)}e^{im\phi_0},\\
Z_{33} &= \frac{d}{D}\sum_{m=-\infty}^{\infty}\frac{k\varepsilon_3}{k_{\perp m}}\psi_m^2\frac{F_1(k_{\perp m}, \sigma, a)}{F_0(k_{\perp m}, a, \sigma)}e^{-im\phi_0}.
\end{aligned} \tag{13}$$

The form of expressions (12) implies that the contributions of the beam current to the functions Y_{12}, Y_{32}, Y_{11}, and Y_{33} are important near the resonance $\omega = \beta_N v_0$. To be specific, we set $N = 0$; i.e., we take into account only the zeroth spatial mode of the perturbed beam current. It is this case for which the nonlinear analysis of microwave amplification will be carried out. We substitute expressions (12) into Eq. (9) and perform the necessary manipulations in order to arrive at the following dispersion relation in which the terms proportional to the beam current are singled out in explicit form:

$$\begin{aligned}
&(Z_1Z_2 - Z_{11}Z_{33})[(\omega - \beta_0 v_0)^2 - \Gamma\Omega_b^2]\\
&\quad = \frac{d}{D}\frac{k}{a}\psi_0^2(a^2 - \sigma^2)Z_2\\
&\times\left|\frac{F_0(k_{\perp 0}, r_b, \sigma)}{F_0(k_{\perp 0}, a, \sigma)} - \frac{Z_{33}}{Z_2}\frac{F_0(k_{\perp 0}, r_b, a)}{F_0(k_{\perp 0}, \sigma, a)}\right|^2\Omega_b^2,
\end{aligned} \tag{14}$$

where $\Omega_b^2 = \dfrac{4I_b}{I_A(a^2 - \sigma^2)}\dfrac{c^3}{\gamma_0^3 v_0}$ and the depression coefficient Γ is defined as

$$\begin{aligned}
\Gamma &= \frac{\pi}{4}(k^2 - \beta_0^2)(a^2 - \sigma^2)F_0(k_{\perp 0}, a, r_b)\\
&\times F_0(k_{\perp 0}, r_b, \sigma)/F_0(k_{\perp 0}, a, \sigma).
\end{aligned} \tag{15}$$

When deriving the dispersion relation (14), we used the approximate equality $Z_{11} \approx -\sigma Z_{33}/a$, which is satisfied exactly for $\phi_0 = 0$ and π and holds with an ample margin in the remaining cases, because the functions $F_0(k_{\perp m}, a, \sigma)$ and $F_0(k_{\perp m}, \sigma, a)$ in the denominators of Z_{11} and Z_{33} increase exponentially with the mode number $m \neq 0$.

In the absence of a beam ($\Omega_b = 0$), dispersion relation (14) determines the wavenumbers β_0^0 of the eigenmodes of the waveguide structure:

$$Z(\omega, \beta_0^0) \equiv Z_1Z_2 - Z_{11}Z_{33} = 0. \tag{16}$$

The expansion $Z(\omega, \beta_0) \approx (\beta_0 - \beta_0^0)\left.\dfrac{\partial Z(\omega, \beta_0)}{\partial\beta_0}\right|_{\beta_0 = \beta_0^0}$ near the wavenumbers of the eigenmodes converts dispersion relation (14) to the characteristic equation for a TWT:

$$\begin{aligned}
&(\beta_0 - \beta_0^0)[(\omega - \beta_0 v_0)^2 - \Gamma\Omega_b^2]\\
&\quad = -\frac{\omega}{4}\Omega_b^2(a^2 - \sigma^2)(\beta_0^0)^2R_c^0.
\end{aligned} \tag{17}$$

Here, the coupling impedance R_c^0 has the form

$$\begin{aligned}
R_c^0 &= \left(\frac{d}{D}\right)^2\psi_0^2\left|\frac{F_0(k_{\perp 0}, r_b, \sigma)}{F_0(k_{\perp 0}, a, \sigma)} - \frac{Z_{33}}{Z_2}\frac{F_0(k_{\perp 0}, r_b, a)}{F_0(k_{\perp 0}, \sigma, a)}\right|^2\\
&\times\left\{\frac{c}{2\pi}(\beta_0^0)^2\left(\frac{d}{D}\right)^2\sum_{m=-\infty}^{\infty}\frac{k\varepsilon_3\beta_m}{2k_{\perp m}^2}\psi_m^2\right.\\
&\times\left[a^2\left(1 + \frac{F_1^2(k_{\perp m}, a, \sigma)}{F_0^2(k_{\perp m}, a, \sigma)}\right) - \frac{2a}{k_{\perp m}}\frac{F_1(k_{\perp m}, a, \sigma)}{F_0(k_{\perp m}, a, \sigma)}\right.\\
&\left.\left. - \sigma^2\frac{F_1^2(k_{\perp m}, \sigma, \sigma)}{F_0^2(k_{\perp m}, a, \sigma)} + \left|\frac{Z_{33}}{Z_2}\right|^2\left[a^2\frac{F_1^2(k_{\perp m}, a, a)}{F_0^2(k_{\perp m}, \sigma, a)}\right.\right.\right.
\end{aligned} \tag{18}$$

$$-\sigma^2\left(1+\frac{F_1^2(k_{\perp m},\sigma,a)}{F_0^2(k_{\perp m},\sigma,a)}\right)+\frac{2\sigma}{k_{\perp m}}\frac{F_1(k_{\perp m},\sigma,a)}{F_0(k_{\perp m},\sigma,a)}\Bigg]$$

$$-2\frac{\mathrm{Re}(Z_{33}\exp(im\phi_0))}{Z_2}\frac{F_1(k_{\perp m},a,a)}{F_0(k_{\perp m},\sigma,a)}$$

$$\times\left[a^2\frac{F_1(k_{\perp m},a,\sigma)}{F_0(k_{\perp m},a,\sigma)}+a\sigma\frac{F_1(k_{\perp m},\sigma,a)}{F_0(k_{\perp m},\sigma,a)}-\frac{2a}{k_{\perp m}}\right]\Bigg]\Bigg\}^{-1},$$

where all of the quantities that depend on β_0 are calculated at $\beta_0=\beta_0^0$.

From expressions (7) and (8) for the field components and relationship (11) between the constants M_1 and M_2, we can see that, for $I_b = 0$, the expression in braces in formula (18) is proportional to the energy flux averaged over the period of the structure. The numerator in formula (18) is the squared absolute value of the longitudinal electric field of the zeroth spatial mode, which interacts with the beam electrons. As a result, the coupling impedance R_c^0 is seen to be described by the standard expression used in theoretical research on microwave electronics [13, 14].

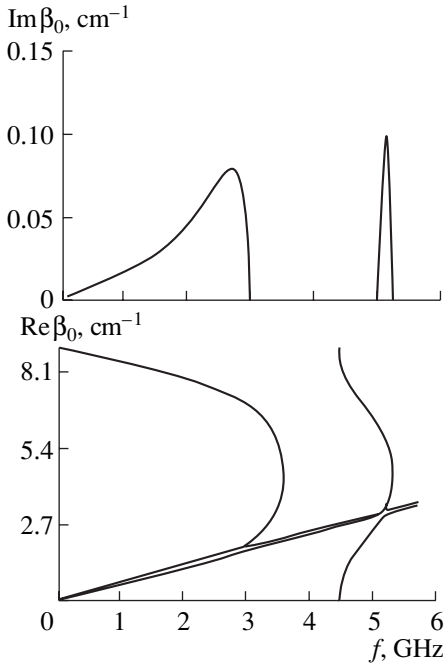

Fig. 2. Real ($\mathrm{Re}\,\beta_0$) and imaginary ($\mathrm{Im}\,\beta_0$) parts of the longitudinal wavenumber of the eigenmode of a coaxial vacuum slow-wave structure with a beam vs. frequency for b = 5.3 cm, a = 4.0 cm, σ = 3.5 cm, ρ = 1.9 cm, D = 0.7 cm, d = 0.5 cm, $\varphi_0 = 0$, and r_b = 3.6 cm; the beam current and beam energy are I_b = 5.0 A and W_b = 35 keV, respectively.

Dispersion relation (9) was solved for the following parameters of the electron beams and the hybrid structure used in the experiments at the Kharkov Institute of Physics and Technology, National Academy of Sciences of Ukraine [15]: b = 5.3 cm, a = 4.0 cm, σ = 3.5 cm, ρ = 1.9 cm, D = 0.7 cm, d = 0.5 cm, $\varphi_0 = 0$, r_b = 3.6 cm, I_b = 5.0 A, and W_b = 35 keV. For comparison, in Fig. 2, we also present the dispersion curves for a vacuum slow-wave structure. The plots in Fig. 2 reflect the dependence of the real and imaginary parts, $\mathrm{Re}\,\beta_0$ and $\mathrm{Im}\,\beta_0$, of the longitudinal wavenumber on the frequency $f = \omega/2\pi$. In the frequency band f = 0–5.3 GHz, the hybrid slow-wave structure provides two passbands: first, the lower frequency passband f = 0–3.6 GHz, in which the dispersion properties of microwaves are analogous to those in a spiral slow-wave structure [16, 17] and the microwave phase velocity is equal to $v_{ph}/c = \sqrt{\ln(a/\sigma)/[\ln(a/\sigma) + d\ln(b\sigma/a\rho)/D]}$, and, second, the higher frequency passband f = 4.5–5.3 GHz. The lower cutoff frequency is determined by the inner, more corrugated, conductor, and the upper cutoff frequency is governed by the outer, less corrugated, conductor. This circumstance should be kept in mind when the eigenmodes of the structure are excited by a thin-walled electron beam that does not completely fill the transport channel. The beam should be confined to the conductor that governs the eigenmode of the structure. It is worth noting that the two frequency passbands can exist simultaneously only in a slow-wave transmission line in which both the inner and outer conductors are corrugated. In a slow-wave structure in which only one (outer or inner) conductor is corrugated, there exists only a coaxial wave with an upper cutoff frequency, which is determined by the resonator radius. The frequency dependence of the imaginary part of the longitudinal wavenumber, $\mathrm{Im}\,\beta_0$, is also characterized by two different ranges. In the first range (f = 0–3 GHz), the slowed coaxial wave is amplified (the amplification band is narrower than the passband). The frequency profile of the amplification coefficient is peaked at the resonance of the beam with the eigenmode of the structure. The low-frequency portion of the profile goes to zero almost linearly, while the high-frequency portion falls off to zero in a jumplike manner. In the second, very narrow, range, the frequency profile of the amplification coefficient has a sharp peak, which reflects the resonance of the beam with the eigenmode of the structure in the higher frequency passband. Since the group velocity of this eigenmode is substantially lower than that of the slowed coaxial wave, the maximum amplification coefficient in the higher frequency passband is about three times larger than that in the lower frequency passband, while the resonance width is much narrower.

Figure 3 shows the dispersion curves for a slow-wave structure filled entirely with a plasma of density $n_p = 1.8 \times 10^{11}$ cm^{-3}, in which case the plasma frequency $f_p = \omega_p/2\pi$ is higher than the upper cutoff fre-

quency of the coaxial mode. In addition to the waves that exist in the structure in the absence of plasma, there are many waves associated with the radial modes as well as with the Floquet modes of the natural waves of the coaxial plasma column. If the electron beam velocity is close to the phase velocity of the wave corresponding to the intersection point of the dispersion curves of a pair of eigenmodes of the plasma-filled structure, then a narrow pronounced peak appears in the frequency profile of the imaginary part of the longitudinal wavenumber, because, at this point, the group velocity of the waves, which usually determines the amplification coefficient, vanishes. In this case, the spatial growth rate is determined by the higher order derivatives of the wave frequency with respect to the longitudinal wavenumber. A comparison between Figs. 2 and 3 shows that, in a plasma-filled transport channel, the amplification band broadens by 10%, while the amplification coefficient increases simultaneously by the same amount, 10%.

Figure 4 shows the plots of the maximum amplification coefficient and the frequency at which the amplification coefficient is maximum as functions of the plasma density. In the frequency band under investigation, the amplification coefficient is almost linearly proportional to the plasma density. Presumably, such behavior of the amplification coefficient can be explained by the fact that, as the plasma density increases, the frequency of the wave that resonates with the beam grows linearly and its group velocity decreases.

Expressions (7) and (8) imply an antisymmetric spatial structure of the longitudinal electric field of the zeroth spatial mode of the cable wave, which is in resonance with the beam. Consequently, the amplification coefficient should become zero for a beam whose radius is chosen to be equal to the radius of the cylindrical surface at which the longitudinal electric field vanishes. This situation is illustrated in Fig. 5, which shows how the maximum amplification coefficients in the lower and higher frequency passbands depend on the beam radius. In the higher frequency passband, the amplification coefficient increases monotonically when the beam radius increases from the radius of the inner conductor to the radius of the outer conductor.

An important parameter inherent in a slow-wave structure is the wave impedance. In theoretical research on microwave electronics, it is usually defined as [12]

$$\rho_w = \left|\int_1^2 \mathbf{E}\,d\mathbf{l}\right|^2 / 2P_z, \qquad (19)$$

where the line integral is calculated along a straight path between two points lying on the conducting surface in the same transverse cross section of the slow-wave system and P_z is the longitudinal energy flux in

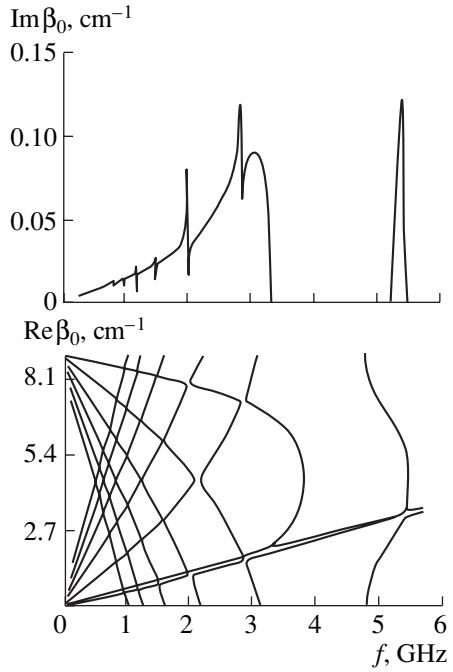

Fig. 3. Real ($\mathrm{Re}\beta_0$) and imaginary ($\mathrm{Im}\beta_0$) parts of the longitudinal wavenumber of the eigenmode of a coaxial plasma-filled slow-wave structure with a beam vs. frequency for the same parameters of the structure and beam as in Fig. 2; the plasma density is $n_p = 1.8 \times 10^{11}$ cm^{-3}.

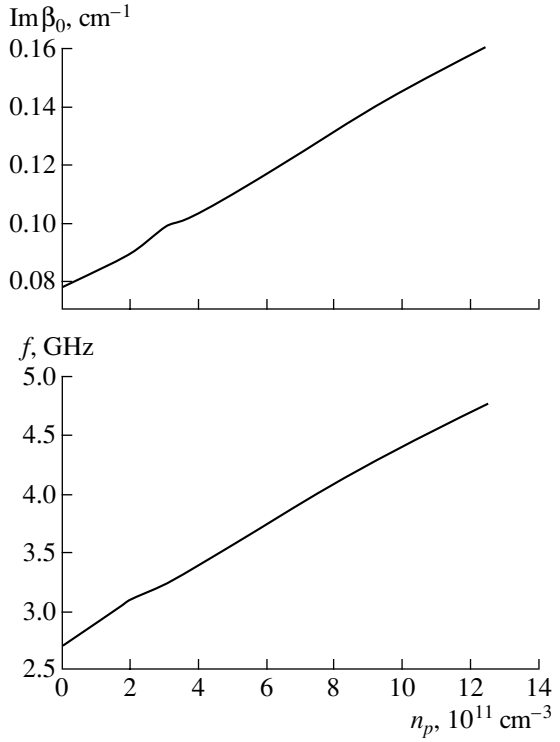

Fig. 4. Maximum amplification coefficient and the frequency at which the amplification coefficient is maximum vs. plasma density for the same parameters of the structure and beam as in Fig. 2.

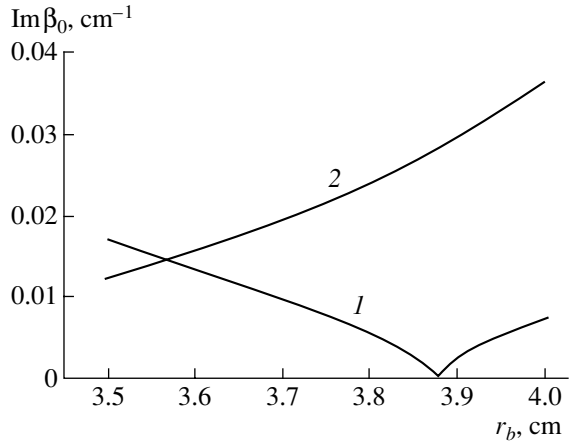

Fig. 5. Maximum amplification coefficients in the (*1*) lower and (*2*) higher frequency passbands vs. beam radius for the same parameters of the structure and beam as in Fig. 2, except for the beam current, which is equal to $I_b = 0.01$ A.

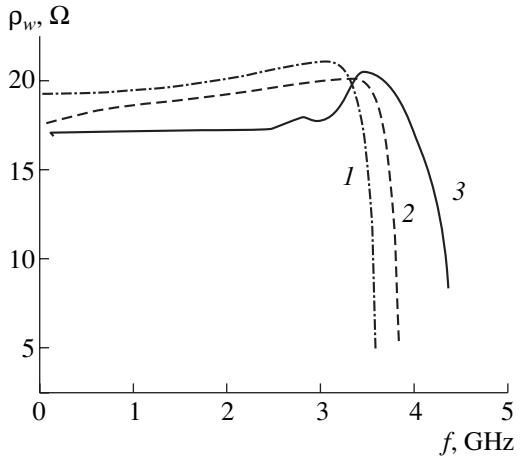

Fig. 6. Wave impedance of the coaxial slow-wave structure vs. frequency for the same parameters of the structure and beam as in Fig. 2 and different plasma densities: n_p = (*1*) 0, (*2*) 1.8×10^{11}, and (*3*) 7.2×10^{11} cm^{-3}.

the system. For the slow-wave structure under consideration, the wave impedance (in Ω) is equal to

$$\rho_w = 60\left|\int_\sigma^a E_r^{\mathrm{II}} dr\right|^2 / \int_\sigma^a E_r^{\mathrm{II}} H_\varphi^{\mathrm{II}*} r dr. \qquad (20)$$

Figure 6 displays the wave impedance of a coaxial slow-wave structure calculated as a function of frequency for different plasma densities. We can see that, in the presence of a plasma, the wave impedance changes insignificantly; i.e., it remains nearly constant over almost the entire main passband. Since the dispersion curves for a plasma-filled structure exhibit linear behavior over a broader frequency interval in comparison with those in the absence of a plasma, the frequency interval over which the wave impedance remains essentially unchanged is also broader. Hence, we can conclude that, as vacuum structures, plasma-filled slow-wave hybrid transmission lines also provide the possibility of achieving good matching of the slow-wave structure with devices for inputting and extracting microwave power in a broad frequency band.

3. NONLINEAR REGIME

In order to investigate the nonlinear stage of the interaction between an electron beam and the natural waves of a coaxial slow-wave transmission line, we start with the equation for the averaged (over the cross section of the transport channel) amplitude E of the longitudinal electric field [13],

$$\frac{dE}{dz} + i(\beta_e - \beta_0^0)E = (\beta_0^0)^2 I_b R_c^0 \frac{1}{2\pi}\int_0^{2\pi} e^{i\theta} d\theta_0 \qquad (21)$$

and the equations of motion of the beam electrons,

$$\frac{dv(z)}{dz} = \frac{e}{mv(z)}\left(1 - \frac{v^2(z)}{c^2}\right)^{3/2} \mathrm{Re}(Ee^{-i\theta}),$$
$$\frac{d\theta}{dz} = \beta_e\left(\frac{v_0}{v(z)} - 1\right). \qquad (22)$$

In Eqs. (21) and (22), we introduce the following notation: $\beta_e = \omega/v_0$, ω and β_0^0 are the frequency and longitudinal wavenumber of the eigenmode of the structure that satisfy the dispersion relation (9) with $I_b = 0$; I_b is the beam current; and $v(z)$ is the beam electron velocity. The coupling impedance R_c^0 is defined as

$$R_c^0 = \frac{E_{z,0}^{\mathrm{II}2}(r_b)}{\frac{c}{2\pi}(\beta_0^0)^2 \sum_{m=-\infty}^{\infty} \int_S E_{r,m}^{\mathrm{II}} H_{\varphi,m}^{\mathrm{II}*} dS}, \qquad (23)$$

where S is the cross-sectional area of the transport channel; r_b is the beam radius; and $E_{z,m}^{\mathrm{II}}$, $E_{r,m}^{\mathrm{II}}$, and $H_{\varphi,m}^{\mathrm{II}}$ are the electromagnetic field components (7) and (8) of the eigenmode of the hybrid structure in the absence of a beam ($\alpha_m = 0$).

Expression (23) for the coupling impedance is the standard formula used in theoretical research on microwave electronics [13, 14]. For a vacuum coaxial slow-wave transmission line, the related explicit expression is presented in [11]. If we substitute the electromagnetic field components (7) and (8) with $\alpha_m = 0$ into expression (23) and take the relevant integrals, then we arrive at the explicit expression (18) for the coupling impedance of a coaxial plasma-filled slow-wave transmission line.

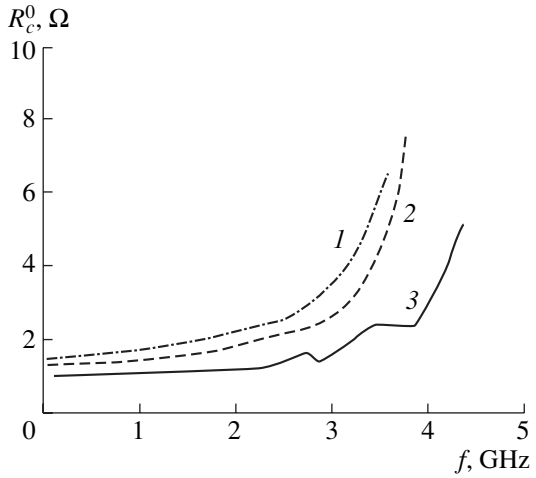

Fig. 7. Coupling impedance of the coaxial slow-wave structure vs. frequency for the same parameters of the structure and beam as in Fig. 2 and different plasma densities: n_p = (*1*) 0, (*2*) 1.8×10^{11}, and (*3*) 7.2×10^{11} cm^{-3}.

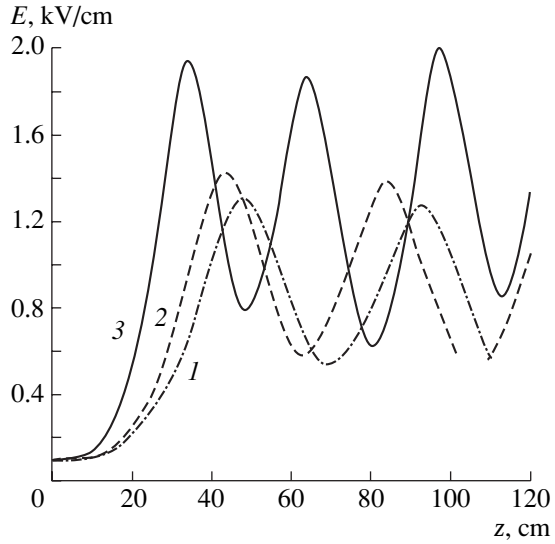

Fig. 8. Amplitude of the longitudinal electric field vs. the length of the structure for the same parameters of the structure and beam as in Fig. 2 and different plasma densities: n_p = (*1*) 0, (*2*) 1.8×10^{11}, and (*3*) 7.2×10^{11} cm^{-3}.

In the equations of motion (22), we assume that the beam electrons are affected only by the synchronous harmonic of the total electric field; in other words, we neglect the space-charge effect on both the beam dynamics and the electromagnetic field structure. This approach is quite justified because we are interested in beam currents far below the vacuum limiting current [2, 18].

In the linear approximation, Eqs. (21)–(23) yield the characteristic equation (17) for a TWT. In accordance with the above analysis, Eq. (17) should be taken with $\Gamma = 0$. This equation makes it possible to determine the amplification coefficients of the generated microwaves. The standard nonlinear theory of microwave generation and amplification in waveguides [14] is constructed, in particular, on the basis of the known dispersion properties of a "cold" slow-wave structure (i.e., the structure without a beam). At present, the theory of transversely nonuniform beam–plasma amplifiers is being actively developed (see [2, 19]), which allows one to derive the linear dispersion relation for a cold structure from the nonlinear equations of microwave generation.

Figures 7–10 illustrate the results of a numerical solution of Eqs. (21)–(23) for the above parameters of the experimental device [15]. The beam current and electron beam energy are equal to $I_b = 5.0$ A and $W_b = 35$ keV, respectively. Figure 7 shows the frequency profiles of the coupling impedance calculated for the plasma densities $n_p = 0$, 1.8×10^{11}, and 7.2×10^{11} cm^{-3}. In comparison with the vacuum case, the coupling impedance of a plasma-filled slow-wave structure is somewhat lower over most of the frequency passband, but the maximum coupling impedance in the presence of a plasma is higher than the vacuum one. As a function of frequency, the coupling impedance behaves in essentially the same manner as the amplification coefficient (Figs. 2, 3). For a plasma-filled slow-wave structure, the amplification coefficient is also somewhat smaller over most of the frequency passband, but the passband itself is broader and the maximum amplification coefficient is larger than those in the vacuum case.

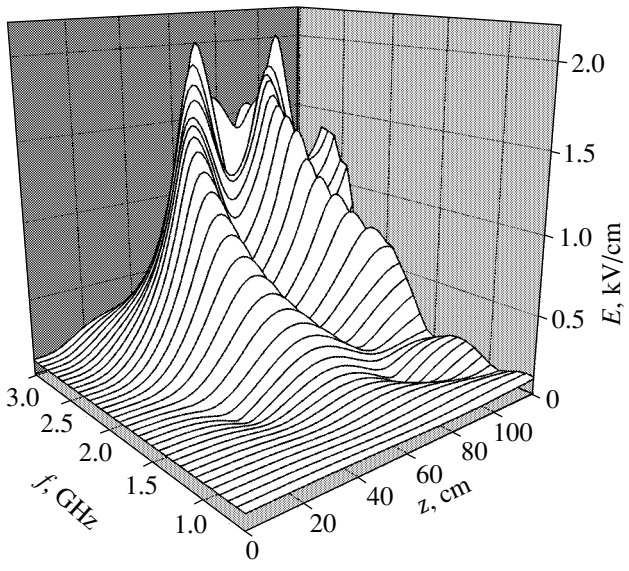

Fig. 9. Amplitude of the longitudinal electric field vs. the wave frequency and the length of a coaxial vacuum structure for the same parameters of the structure and beam as in Fig. 2.

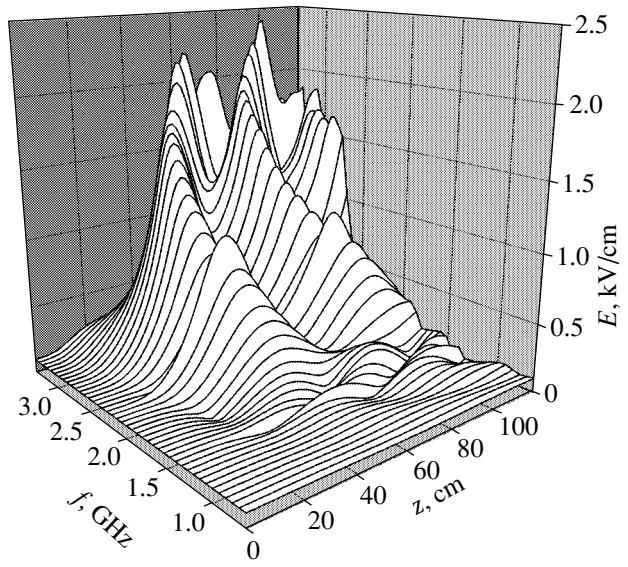

Fig. 10. Amplitude of the longitudinal electric field vs. the wave frequency and the length of a coaxial plasma-filled structure for the same parameters of the structure and beam as in Fig. 2 and the plasma density $n_p = 1.8 \times 10^{11}$ cm^{-3}.

Figure 8 shows how the amplitude of the longitudinal electric field depends on the length of the slow-wave structure. Each of the profiles was calculated for the frequency and wave vector corresponding to the maximum amplification coefficient in the linear regime. For a plasma density of 1.8×10^{11} cm^{-3}, the longitudinal electric field saturates at 1.42 kV/cm, the optimum length of a hybrid structure being 43.6 cm. For a plasma density of 7.2×10^{11} cm^{-3}, the saturation level is 1.93 kV/cm and the optimum length of the structure is 34.8 cm. For the vacuum case, the relevant parameters are equal to 1.3 kV/cm and 48 cm. The profiles of the interaction efficiency indicate that the maximum losses in the energy of the electron beam are nearly the same (about 24–26%) for both vacuum and plasma-filled coaxial slow-wave structures. For the maximum energy losses, the plasma-filled structure is significantly shorter in length than the vacuum structure. Hence, our nonlinear analysis confirms the assumption that filling the structure with a plasma results primarily in an increase in the frequency at which resonant interaction occurs. Of course, this conclusion refers specifically to the problem as formulated; i.e., in contrast to the analyses carried out in [3, 7] for other hybrid structures, we do not fix the frequency at which microwaves are generated but study the microwave amplification over the entire frequency passband. Naturally, in this case, the resonant frequency of interaction increases with the plasma density.

We note that the above dependences of the optimum interaction length and the energy losses by the beam electrons through radiation on the plasma density agree qualitatively with the results obtained by Krasil'nikov *et al.* [2] for a plasma-filled dielectric waveguide. The most important effect of the plasma is a substantial shortening of the optimum amplification length, in which case, however, the amplification efficiency changes insignificantly. This is the main difference from the case of microwave generation in a hybrid slow-wave structure in the form of a chain of coupled cavity resonators [1, 3].

The amplitude of the longitudinal electric field, calculated as a function of the length of the structure for different eigenfrequencies, is shown in Fig. 9 for a vacuum structure and in Fig. 10 for a structure filled entirely with a plasma of density $n_p = 1.8 \times 10^{11}$ cm^{-3}. The frequency profile of the first maximum in the amplitude corresponds to the frequency dependence of the amplification coefficient in Figs. 2 and 3. We can see that, over the entire main frequency passband, the optimum length of the structure changes only slightly. The results of nonlinear numerical modeling validate the predictions made in linear theory about the broadening of the frequency band over which microwaves are generated and the increase in the amplification efficiency after the transport channel of a vacuum slow-wave structure is filled with a plasma.

4. CONCLUSION

Investigations of the electrodynamic parameters of a coaxial plasma-filled slow-wave transmission line have shown that it holds promise for creating high-power plasma-based microwave devices. The plasma waveguide, like the vacuum one, is characterized by a broad frequency passband. Moreover, in a plasma waveguide, the amplification efficiency is higher and the frequency amplification band is broader in comparison with the vacuum case. In the first (lower frequency) passband, the amplification coefficient depends linearly on the plasma density. The electron beam interacts most strongly with the T-wave. The generation efficiency of the plasma modes corresponding to the eigenmodes of an annular plasma column in which the electron beam propagates is low, and the frequency band over which the plasma modes are amplified is narrow. In the first passband, the wave impedance of the slow-wave structure is only weakly dependent on frequency; in a plasma-filled structure, the frequency interval over which the wave impedance is constant is even broader than in a vacuum structure. Nonlinear numerical modeling shows that, in a plasma-filled slow-wave structure, the maximum amplitudes of the saturated microwaves are larger than those in the vacuum case. The optimum length of a coaxial plasma-filled slow-wave transmission line is significantly shorter than that of a vacuum structure. As functions of frequency, the saturation amplitude and the interaction efficiency behave in the same manner as the amplification coefficient: they are both peaked near the resonance of the beam with the eigenmode of the plasma-

filled structure and the low-frequency portions of their profile decrease with frequency.

ACKNOWLEDGMENTS

I am grateful to E.A. Kornilov for discussing the results obtained and to P.I. Markov for his help in carrying out simulations. This work was supported in part by the Ukrainian Center for Science and Technology, project no. 256.

REFERENCES

1. Ya. B. Faĭnberg, Yu. P. Bliokh, E. A. Kornilov, *et al.*, Dokl. Akad. Nauk Ukr. SSR, Fiz.-Mat. Tekh. Nauki, No. 11, 55 (1990).
2. M. A. Krasil'nikov, M. V. Kuzelev, V. A. Panin, and D. S. Filippychev, Fiz. Plazmy **19**, 1061 (1993) [Plasma Phys. Rep. **19**, 554 (1993)].
3. Ya. B. Faĭnberg, Yu. P. Bliokh, M. G. Lyubarskiĭ, *et al.*, Fiz. Plazmy **20**, 757 (1994) [Plasma Phys. Rep. **20**, 681 (1994)].
4. A. N. Antonov, Yu. P. Bliokh, Yu. A. Degtyar', *et al.*, Fiz. Plazmy **20**, 777 (1994) [Plasma Phys. Rep. **20**, 699 (1994)].
5. M. A. Zav'yalov, V. O. Martynov, L. A. Mitin, *et al.*, in *Proceedings of the IX Symposium on High-Current Electronics, Russia, 1992*, p. 132.
6. Y. Carmel, K. Miami, R. A. Kohs, *et al.*, Phys. Rev. Lett. **62**, 2389 (1989).
7. E. O. Kornilov, O. M. Korostel'ov, O. V. Lodygin, *et al.*, Ukr. Fiz. Zh. **40**, 312 (1995).
8. E. A. Kornilov, P. I. Markov, and G. V. Sotnikov, in *Proceedings of the 7th International Crimean Conference "Microwave and Telecommunication Technologies"* (Veber, Sevastopol, 1997), Vol. 2, p. 427.
9. E. A. Kornilov, P. I. Markov, and G. V. Sotnikov, in *Proceedings of 12th International Conference on High Power Particle Beams, Haifa, 1998*, Vol. 1, p. 877.
10. G. V. Sotnikov, Élektromagn. Yavleniya **1**, 383 (1998).
11. M. F. Stel'makh and E. B. Ol'derogge, Radiotekh. Élektron. (Moscow) **4**, 980 (1959).
12. A. D. Grigor'ev and V. B. Yankevich, *Microwave Resonators and Resonant Slow-Wave Structures* (Radio i Svyaz', Moscow, 1984).
13. L. A. Vaĭnshteĭn and V. A. Solntsev, *Lectures on Microwave Electronics* (Sov. Radio, Moscow, 1973).
14. A. D. Grigor'ev, *Electrodynamics and Microwave Engineering* (Vysshaya Shkola, Moscow, 1990).
15. V. S. Antipov, V. I. Karpukhin, E. A. Kornilov, and L. A. Loginov, in *Proceedings of the 8th International Crimean Conference "Microwave Engineering and Telecommunication Technologies"* (Veber, Sevastopol, 1998), Vol. 2, p. 749.
16. R. A. Silin and V. P. Sazonov, *Slow-Wave Structures* (Sov. Radio, Moscow, 1966).
17. H. P. Freud, E. G. Zaidman, and T. M. Antonsen, Phys. Plasmas **3**, 3145 (1996).
18. V. A. Balakirev, N. I. Karbushev, and G. V. Sotnikov, Radiotekh. Élektron. (Moscow) **37**, 1729 (1992).
19. M. V. Kuzelev, V. A. Panin, A. P. Plotnikov, and A. A. Rukhadze, Zh. Éksp. Teor. Fiz. **101**, 460 (1992) [Sov. Phys. JETP **74**, 242 (1992)].

Translated by G. V. Shepekina

Plasma Physics Reports, Vol. 27, No. 6, 2001, pp. 490–496. Translated from Fizika Plazmy, Vol. 27, No. 6, 2001, pp. 519–525.

PLASMA OSCILLATIONS AND WAVES

Quasilinear Theory of the Ion Weibel Instability in the Earth's Magnetospheric Tail

A. M. Sadovskiĭ and A. A. Galeev

Institute for Space Research, Russian Academy of Sciences, Profsoyuznaya ul. 84/32, Moscow, 117810 Russia

Received October 1, 2000; in final form, January 24, 2001

Abstract—The quasilinear equation for the ion Weibel instability is solved for waves propagating along the magnetic field. The energy of the excited waves is estimated and the moments of the ion distribution function in the saturation stage are determined as functions of the current velocity for parameters characteristic of the neutral sheet of the Earth's magnetotail. The question is studied of whether the current disruption at the beginning of the explosive phase of a substorm can be explained as being due to the onset of the ion Weibel instability.

1. INTRODUCTION

Instabilities associated with the current flowing perpendicular to the magnetic field (the cross-field current) in a plasma have been actively studied for many years. Interest in these instabilities stems primarily from investigations of collisionless shock waves in laboratory and space plasmas and from research on the Earth's magnetospheric tail. Under such conditions, the ions are usually assumed to be essentially unmagnetized, while electrons are regarded as strongly magnetized. In studies of related instabilities, special attention has been paid to the modified two-stream instability and to the lower hybrid drift instability. Previously, these instabilities were described assuming that ions play a negligible role because their mass is large. However, Chang *et al.* [1] found that ions respond to electromagnetic perturbations propagating strictly (or nearly so) along the magnetic field by giving rise to an aperiodic electromagnetic mode. This mode was called the ion Weibel instability [1], because its properties are analogous to those of the classical Weibel instability, which is excited by an electron flow in a plasma without a magnetic field [2]. Numerical solution of the dispersion relation for the purely growing mode [3] showed that the ion Weibel instability occurs in a plasma with high values of the parameter $\beta = 8\pi nT/B_0^2$ (the ratio of the gas-kinetic plasma pressure to the magnetic field pressure) and grows at a rate comparable with the ion gyrofrequency. This circumstance gave rise to the idea that the ion Weibel instability may play an important role in the initiation of a magnetospheric substorm and, in particular, in the observed decrease of the transverse current density in the magnetotail (current disruption) [3–6].

It is not surprising that the study of the mechanism for current disruption has been, and will continue to be, one of the main problems in magnetospheric physics. Among the numerous models developed to describe this phenomenon (see, e.g., [4, 6]), we can mention those based on the tearing instability, the ballooning instability, thermal catastrophe, and the crossfield current instabilities. The latter mechanism for current disruption was analyzed quite thoroughly by Lui *et al.* [6] for waves propagating parallel to the magnetic field. In the model developed in that paper, the ion Weibel instability plays an important role. First of all, it increases the anomalous resistance to a level high enough to substantially change the current density. In addition, it was estimated that the ion Weibel instability can ensure the energy level required to initiate fast magnetic reconnection or, at least, to trigger another kind of instability (e.g., unstable tearing modes) [4].

The nonlinear stage of the ion Weibel instability was considered in [1, 7] for a quasi-perpendicular collisionless wave. The nonlinear stage of the evolution of the ion Weibel instability in different regions of the neutral sheet of the magnetotail was studied in [3, 5]. In all of the papers cited, the kinetic equation was solved numerically in order to obtain the moments of the electron and ion velocity distribution functions. The authors assumed that the electron and ion temperatures and the drift velocity were all time-dependent, while the initial shape of the distribution functions remained unchanged.

Here, we show that the quasilinear equation for the ion Weibel instability admits an analytic solution. We also determine how the ion distribution function changes in time and derive equations for its moments. Having done this, we then obtain the steady-state plasma parameters in the saturation stage of the instability and find the maximum possible energy of the magnetic field generated during the collective interactions in a plasma.

1063-780X/01/2706-0490$21.00

2. FORMULATION OF THE PROBLEM AND THE LINEAR THEORY OF THE INSTABILITY

The coordinate system and the geometry of the problem are presented in Fig. 1. Unmagnetized ions move at a mean velocity $\mathbf{v}_0 = v_0\mathbf{y} \lesssim v_{Ti} = (2T_i/m_i)^{1/2}$ (where v_{Ti} is the ion thermal velocity) perpendicular to the external magnetic field $\mathbf{B}_0 = B_0\mathbf{z}$. Here, $\mathbf{x}$, $\mathbf{y}$, and $\mathbf{z}$ stand for unit basis vectors in a right-handed Cartesian coordinate system: the x-axis points from the Earth to the Sun and the z-axis is directed from the south to the north pole. The electron component is assumed to be magnetized and immobile. Hence, we are working under the conditions

$$\begin{aligned} |kv_{Te}| &\ll |\omega_{ce}|, \\ |kv_{Ti}| &\gg \omega_{ci}, \\ \omega_{ci}^2 \ll |\omega|^2 &\ll \omega_{ce}^2, \end{aligned} \tag{1}$$

where $\omega_{cj} = e_jB_0/m_jc$ is the cyclotron frequency of the particles of species j and k is the wave vector.

We also assume that the plasma is homogeneous and the initial electron and ion temperatures are both isotropic. We are interested in the waves propagating along the external magnetic field; i.e., we set $\mathbf{k} = k\mathbf{z}$. In our model, the electrons obey a Maxwellian distribution, while the ions are described by a Maxwellian distribution shifted by the magnitude of the current velocity:

$$f_i(\mathbf{v}) = \frac{n}{\pi^{3/2}v_{Ti}^3}\exp\left\{-\frac{v_x^2 + (v_y - v_0)^2 + v_z^2}{v_{Ti}^2}\right\}. \tag{2}$$

The dispersion relation for waves propagating along the external magnetic field was derived and thoroughly investigated in [5, 7, 8]. Under conditions (1), the dispersion relation without allowance for the displacement current has the form [3, 7]

$$\begin{aligned} &-1 - \frac{k^2c^2}{\omega_{pi}^2} - \frac{T_{i\perp}}{T_{i\parallel}}\frac{Z'(\xi_i)}{2} + \frac{\omega^2}{1 + \dfrac{k^2c^2}{\omega_{pi}^2} + \dfrac{T_{i\perp}}{T_{i\parallel}}\dfrac{Z'(\xi_i)}{2}} \\ &\quad - \frac{v_0^2}{v_{Ti}^2}\frac{T_iZ'(\xi_i)Z'(\xi_e)}{T_eZ'(\xi_i) + T_iZ'(\xi_e)} = 0, \end{aligned} \tag{3}$$

where ω_{pi} is the ion plasma frequency. The function Z is defined as

$$Z(\xi_j) = \frac{v_{Tj}}{n}\int d\mathbf{v}\frac{f(\mathbf{v})}{v_z - \xi_j}, \tag{4}$$

where the prime denotes the first derivative of the function with respect to its argument ξ_j, which is defined as $\xi_j = \omega/kv_{Tj}$. For a Maxwellian plasma, this function coincides with the familiar plasma dispersion function.

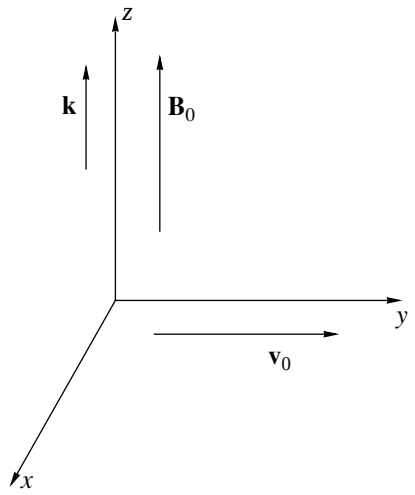

Fig. 1. Schematic representation of the coordinate system and the directions of the magnetic field, wave vector, and ion velocity.

By analogy with [5], we consider the ion Weibel instability for two sets of parameter values, typical of the inner and middle regions of the neutral sheet of the Earth's magnetotail [9]. The parameters of the inner part ($\sim 10R_E$) of the tail are as follows: $T_i/T_e = 4$, $T_i = 12$ keV, $n_e = n_i = n = 0.6$ cm^{-3}, and $B_0 = 25$ nT [6, 10]. The midtail neutral sheet ($\sim 40R_E$) is characterized by the parameter values $T_i/T_e = 10$, $T_i = 2$ keV, $n_e = n_i = n = 0.3$ cm^{-3}, and $B_0 = 5$ nT [6, 10, 11]. Since the inequality $T_e \ll T_i$ holds for both cases, we will neglect small terms on the order of T_e/T_i in further analysis.

The above dispersion relation has a solution describing a purely growing mode (for which the real part of the mode frequency vanishes). For aperiodic instabilities, the quasilinear theory can be applied only under the condition $\gamma_k \ll kv_{Ti}$ [12–14], in which case the instability growth rate γ_k can be obtained by expanding the function $Z(\xi_j)$ in a power series in the limit $|\xi_j| \ll 1$:

$$\begin{aligned} \gamma_k = \frac{kv_{T_{i\parallel}}}{\sqrt{\pi}}&\left\{\frac{Z'_{0i}}{2} + T_{i\parallel}\frac{1 + \dfrac{k^2c^2}{\omega_{pi}^2}}{mv_0^2 + T_{i\perp}}\right\} \\ &\times\left(\frac{v_{T_{i\parallel}}^3\sqrt{\pi}}{2n}\int\frac{\partial^2 f(\mathbf{v})}{\partial v_z^2}\delta(v_z)d\mathbf{v}\right)^{-1}, \end{aligned} \tag{5}$$

where m is the mass of an ion and $Z'_{0i} = \dfrac{v_{T_{i\parallel}}^2}{2n}\int\dfrac{\partial f(\mathbf{v})}{v_z\partial v_z}d\mathbf{v}$ is the first term of the expansion of $Z'(\xi_i)$ in powers of ξ_i.

Since any function f having a maximum at $v_z = 0$ satisfies the inequality

$$\int \frac{\partial^2 f(\mathbf{v})}{\partial v_z^2} \delta(v_z) d\mathbf{v} < 0, \tag{6}$$

the condition for the onset of the instability has the form

$$-\frac{Z_{0i}'}{2} > \frac{T_{i\|}}{m v_0^2 + T_{i\perp}}. \tag{7}$$

In turn, the condition $\gamma_k \ll k v_{Ti}$ holds when

$$Y = 1 + \frac{2T_{i\|}}{Z_{0i}'(m v_0^2 + T_{i\perp})} \ll 1, \tag{8}$$

which is valid for the above parameter values of the neutral sheet of the magnetotail.

3. QUASILINEAR THEORY

The larger the wave amplitude, the stronger the influence of the nonlinear effects on the wave dynamics. Since the crossfield current is carried mainly by the ions, we can neglect the influence of magnetized electrons and write the quasilinear kinetic equation for the ion distribution function as

$$\frac{\partial f_i}{\partial t} = -\frac{e}{m} \int \frac{\partial}{\partial \mathbf{v}} \left\langle \left\{ \mathbf{E}_k + \frac{1}{c} \mathbf{v} \times \mathbf{B}_k \right\}^* \delta f_k \right\rangle dk. \tag{9}$$

Here, the angular brackets denote averaging over the random phases; the asterisk stands for complex conjugation; $\mathbf{E}_k$ and $\mathbf{B}_k$ are the Fourier harmonics of the electric and magnetic field fluctuations; and the Fourier component δf_k of the rapidly oscillating part of the ion distribution function is determined in terms of the integral along the unperturbed ion trajectories

$$\delta f_k = -\frac{e}{m} \int_{-\infty}^{0} \left\{ \mathbf{E}_k + \frac{1}{c} \mathbf{v}(t) \times \mathbf{B}_k \right\} \frac{\partial f}{\partial \mathbf{v}} e^{-i(\omega - k v_z)t} dt, \tag{10}$$

where $v_x(t) = v_\perp \sin(\theta - \omega_{ci} t)$, $v_y(t) = v_0 + v_\perp \cos(\theta - \omega_{ci} t)$, $v_z(t) = v_z$, $v_\perp^2 = v_x^2 + v_y^2$, and θ is the azimuthal angle in velocity space. The electric and magnetic fields are related by Maxwell's equations,

$$E_{xk} = \frac{\omega}{kc} B_{yk}, \qquad E_{yk} = -\frac{\omega}{kc} B_{xk}. \tag{11}$$

Taking the integral in Eq. (10), we obtain the perturbed ion distribution function:

$$\delta f_k = i \frac{e}{mc} \left\{ \sum_{\pm} \frac{\left[\left(\frac{\omega}{k} - v_z \right) \frac{\partial}{\partial v_\perp} + v_\perp \frac{\partial}{\partial v_z} \right] f_i}{\omega - k v_z \pm \omega_{ci} + i0} \right. \tag{12}$$

$$\left. \times (B_{yk} \cos\theta - B_{xk} \sin\theta) + \frac{v_0 B_{xk}}{\omega - k v_z + i0} \frac{\partial f_i}{\partial v_z} \right\}.$$

The differential operator in front of the function δf_k in Eq. (9) can be rewritten as

$$\frac{\partial}{\partial \mathbf{v}} \left\{ \mathbf{E}_k + \frac{1}{c} \mathbf{v} \times \mathbf{B}_k \right\}^*$$

$$= \frac{1}{c} \left[\left(\frac{\omega^*}{k} - v_z \right) \frac{\partial}{v_\perp \partial v_\perp} v_\perp + v_\perp \frac{\partial}{\partial v_z} \right] \tag{13}$$

$$\times (B_{yk} \cos\theta - B_{xk} \sin\theta) - \frac{1}{c} \left(\frac{\omega^*}{k} - v_z \right)$$

$$\times \frac{\partial}{v_\perp \partial \theta} (B_{yk} \sin\theta + B_{xk} \cos\theta) + \frac{v_0}{c} B_{xk} \frac{\partial}{\partial v_z}.$$

From expression (12) and Eq. (13), the quasilinear kinetic equation for the ion distribution function can be obtained by averaging over the azimuthal angle:

$$\frac{\partial f_i}{\partial t} = \frac{ie^2}{4m^2 c^2} \int dk \left\{ \left[\left(\frac{\omega^*}{k} - v_z \right) \frac{\partial}{v_\perp \partial v_\perp} v_\perp \right. \right.$$

$$\left. + v_\perp \frac{\partial}{\partial v_z} \right] \sum_{\pm} \frac{|B_{xk}|^2 + |B_{yk}|^2}{\omega - k v_z \pm \omega_{ci} + i0} \tag{14}$$

$$\times \left[\left(\frac{\omega}{k} - v_z \right) \frac{\partial}{\partial v_\perp} v_\perp + v_\perp \frac{\partial}{\partial v_z} \right] f_i$$

$$\left. + \frac{\partial}{\partial v_z} \frac{v_0^2 |B_{xk}|^2}{\omega - k v_z + i0} \frac{\partial f_i}{\partial v_z} \right\}.$$

When studying the linear dispersion relation, Wu *et al.* [3] arrived at the condition $|B_{xk}|^2/(|B_{yk}|^2 + |B_{xk}|^2) \approx C\xi_i^2 \ll 1$, which indicates that the wave polarization is almost linear. For this reason, we can neglect the squared Fourier amplitudes $|B_{xk}|^2$ of the magnetic field. Since the ions are unmagnetized, we can take the limit $B_0 \longrightarrow 0$, in which Eq. (14) reduces to

$$\frac{\partial f_i}{\partial t} = \frac{ie^2}{2m^2 c^2} \int dk \left\{ \left[\left(\frac{\omega^*}{k} - v_z \right) \frac{\partial}{v_\perp \partial v_\perp} v_\perp \right. \right.$$

$$+ v_\perp \frac{\partial}{\partial v_z}\Big]\frac{(i\gamma_k + kv_z)|B_{yk}|^2}{\gamma_k^2 + k^2 v_z^2},$$
$$\Big[\Big(\frac{\omega}{k} - v_z\Big)\frac{\partial}{\partial v_\perp} v_\perp + v_\perp \frac{\partial}{\partial v_z}\Big] f_i \qquad (15)$$
$$+ \frac{\partial}{\partial v_z}\frac{i\gamma_k v_0^2 |B_{xk}|^2}{\gamma_k^2 + k^2 v_z^2}\frac{\partial f_i}{\partial v_z}\Big\}.$$

The evolution of the electromagnetic field energy is described by the equation

$$\frac{\partial}{\partial t}|\mathbf{B}_k|^2 = 2\gamma_k |\mathbf{B}_k|^2. \qquad (16)$$

The kinetic equation (15) describes the adiabatic interaction of the waves with all plasma ions. However, the coefficient that accounts for the quasilinear diffusion is especially large for $v_z \ll v_{Ti}$. Consequently, in the range of low velocities v_z, the ion distribution function f_i varies most strongly [13, 14]. The above analysis shows that we can neglect the derivatives with respect to the transverse velocity component in Eq. (15). As a result, using Eq. (16), we obtain

$$\frac{df_i}{dt} = \frac{d}{dt}\Big[\frac{e^2}{2m_i^2 c^2}\int \frac{|B_{xk}|^2}{k^2} dk\Big]\frac{\partial}{\partial v_z}\Big(\frac{v_\perp^2}{2} + v_0^2\Big)\frac{\partial f_i}{v_z^2 \partial v_z}. \qquad (17)$$

Integrating Eq. (17) over $v_\perp$ and introducing the notation $h = \dfrac{e^2}{2m_i c^2}\displaystyle\int \frac{|B_{xk}|^2}{k^2} dk$, we arrive at the simple equation [13, 14]

$$\frac{\partial f_i}{\partial h} = \frac{\partial}{\partial v_z}\frac{v_0^2 + v_{T_{i\perp}}^2/2}{m_i v_z^2}\frac{\partial f_i}{\partial v_z}, \qquad (18)$$

which admits an analytic solution. For the initial ion distribution function (2), we obtain [13]

$$f(h) = n\frac{\Gamma(3/4)|v_z|^{3/2} 2^{1/4}}{\pi v_{T_{i\parallel}}^3}$$
$$\times \int_0^\infty \frac{e^{-4(v_0^2 + v_{T_{i\perp}}/2)\lambda^2 h/m}\lambda^{1/4} J_{-3/4}(\lambda v_z^2)}{\Big(\lambda^2 + \dfrac{1}{v_{T_{i\parallel}}^4}\Big)^{3/4}} d\lambda. \qquad (19)$$

This solution shows that, as the wave energy increases, a plateau appears in the ion distribution function in the vicinity of $v_z = 0$, indicating possible suppression of the ion Weibel instability.

4. MOMENTS OF THE ION DISTRIBUTION FUNCTION

The mechanism for the ion Weibel instability is unrelated to any specific group of resonant ions, and the instability growth rate is determined by the mean values of $T_\perp$, $T_\parallel$, and v_0 [12, 15]. Consequently, we can restrict ourselves to considering the quantities that are averaged over the velocity, specifically, the moments of the distribution function. Using Eqs. (9)–(13), we can readily obtain the equations [7]

$$\frac{dT_{i\perp}}{dt} = \frac{e^2}{m_i c^2}\int dk \frac{\gamma_k |B_{xk}|^2}{k^2}\Big(1 + \frac{T_{i\perp}}{T_{i\parallel}} Z'\Big),$$
$$\frac{dT_{i\parallel}}{dt} = -\frac{e^2}{m_i c^2}\int dk \frac{\gamma_k |B_{xk}|^2}{k^2}\Big(\frac{T_{i\perp}}{T_{i\parallel}} + \frac{2K}{T_{i\parallel}}\Big)Z', \qquad (20)$$
$$\frac{dK}{dt} = \frac{e^2}{m_i c^2}\int dk \frac{\gamma_k |B_{xk}|^2}{k^2}\frac{2K}{T_{i\parallel}} Z',$$

where $K = m_i v_0^2/2$ and Z' is defined by formula (4).

Taking the limit $\xi_i \ll 1$, we expand the function $Z'(\xi_i)$ in Eqs. (20) in a power series and retain the lowest order terms in order to arrive at the following set of differential equations describing the evolution of the moments of the ion distribution function in terms of h:

$$\frac{dT_{i\perp}}{dh} = 1 + \frac{T_{i\perp}}{T_{i\parallel}} Z'_{0i}(1 - Y),$$
$$\frac{dT_{i\parallel}}{dh} = \frac{T_{i\perp} + 2K}{T_{i\parallel}} Z'_{0i}(1 - Y), \qquad (21)$$
$$\frac{dK}{dh} = \frac{2K}{T_{i\parallel}} Z'_{0i}(1 - Y).$$

Here, for the solution obtained above, i.e., for the ion distribution function (19), the function $Z'_{0i}(h)$ has the form

$$Z'_{0i}(h) \approx -2\Big[1 - \alpha\Big(h\frac{T_{i\perp} + 2K}{T_{i\parallel}^2}\Big)^{1/4}\Big], \qquad (22)$$

where α is a constant on the order of unity.

On the other hand, in the saturation stage ($\gamma_k \longrightarrow 0$), condition (8) implies that

$$\frac{-Z'^f_{0i}(h)}{2} = \frac{T^f_{i\parallel}}{2K^f + T^f_{i\perp}}. \qquad (23)$$

We set $T^f_{i\parallel} = T_i + \delta T_{i\parallel}$, $T^f_{i\perp} = T_i + \delta T_{i\perp}$, and $K^f = K_0 + \delta K$ and assume, for simplicity, that the initial ion temperature is isotropic, $T_{i\parallel} = T_{i\perp} = T_i$. Obviously, the contributions of the terms $\delta T_{i\parallel}$, $\delta T_{i\perp}$, and δK to Eq. (23) are on the order of h and thus can be neglected in comparison

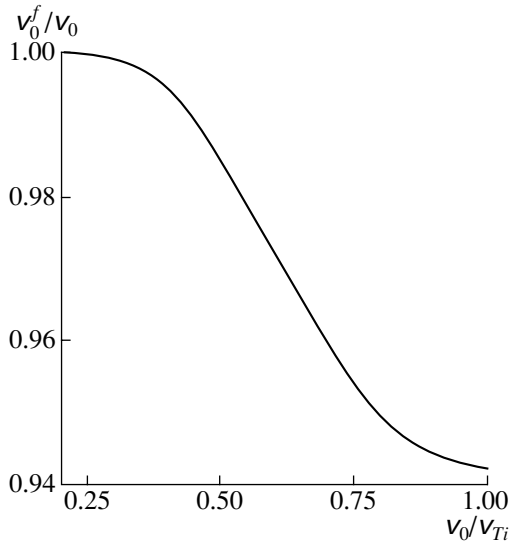

Fig. 2. Normalized ion current velocity v_0^f/v_0 vs. its initial value.

with the contribution of the term $Z'_{0i} \sim h^{1/4}$. As a result, it is an easy matter to obtain

$$h = \frac{Y^4}{\alpha^4}\frac{T_i^2}{T_i + 2K_0}. \tag{24}$$

We neglect the terms of the higher orders in Y and, on the right-hand sides of Eqs. (21), replace the quantities $T_{i\perp}$, $T_{i\parallel}$, and K by their initial values (this replacement also corresponds to neglecting the terms of the higher orders in Y). In addition, we change all of the differentials by δ to arrive at

$$\delta T_{i\perp} = \frac{2K_0 - T_i}{2K_0 + T_i}h,$$
$$\delta T_{i\parallel} = 2h, \tag{25}$$
$$\delta K = -\frac{4K_0}{2K_0 + T_i}h.$$

From Eq. (5) and the definition of h, one can see that the wave energy is a quantity of the next higher order in Y. If we assume that the fastest growing waves are those whose wave vectors are close to the wave vector k_m at which the instability growth rate is maximum, then the energy gained by these waves, normalized to the energy of the external magnetic field, can be estimated as

$$\frac{\delta B^2}{B_0^2} = \int dk \frac{|B_k|^2}{B_0^2} \sim \beta \frac{h}{T_i}\frac{Y}{3}. \tag{26}$$

The steady-state moments of the ion distribution function in the saturation stage of the ion Weibel instability are illustrated in Figs. 2 and 3 as functions of the ratio v_0/v_{Ti}. The figures show the ion current velocity v_0^f and the longitudinal and transverse ion temperatures, $T_\parallel^f$ and $T_\perp^f$, all normalized to their initial values. Within the accuracy of calculations, the relative varia-

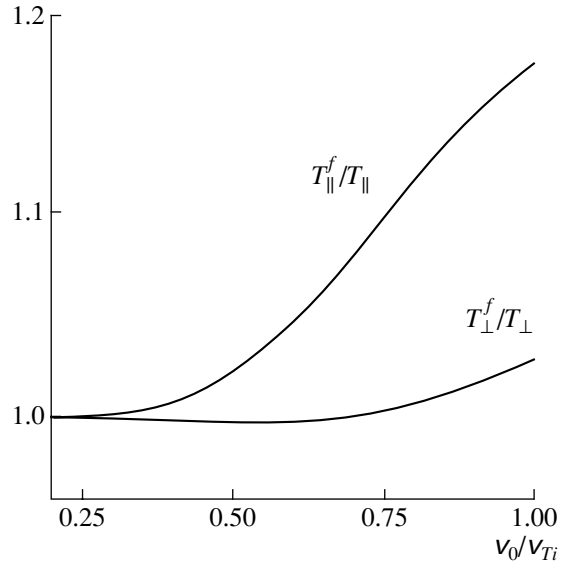

Fig. 3. Transverse and longitudinal ion temperatures, $T_\parallel^f$ and $T_\perp^f$, vs. current velocity.

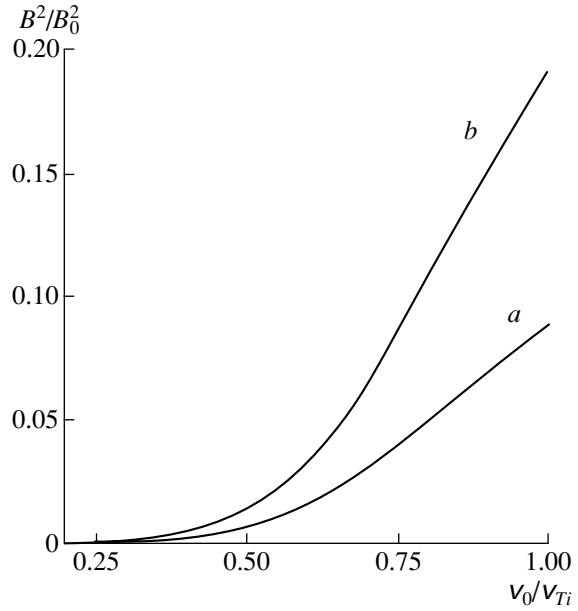

Fig. 4. Total wave energies δB^2 vs. current velocity.

tions in the current velocity and temperature do not differ between the inner and middle regions of the neutral sheet of the magnetotail. As expected, during the excitation of electromagnetic waves, the longitudinal ion thermal energy increases due to a decrease in the cross-field ion current, in which case the transverse ion temperature remains essentially unchanged.

Figure 4 shows the wave energy δB^2 in the inner (Fig. 4a) and middle (Fig. 4b) regions of the neutral sheet of the tail. In Fig. 4b, the amplitude of the fluctuating fields is seen to be substantially larger, because, in the midtail, the external magnetic field B_0 is weaker and the parameter β is larger than those in the central part.

5. CONCLUSIONS

We have investigated the evolution of the ion Weibel instability in the neutral sheet of the Earth's magnetotail. The results obtained show that the suppression of the instability is associated with the formation of a plateau in the ion distribution function. The ion Weibel instability is found to resemble (both formally and physically) the firehose instability described by Shapiro and Shevchenko [12]: the development of these instabilities is accompanied by an increase in the longitudinal thermal plasma energy at the expense of the transverse plasma energy.

The level at which the ion Weibel instability saturates depends on the cross-field current velocity and on the values of the plasma parameters. For parameters typical of the neutral sheet of the magnetotail, the moments of the ion distribution function and the amplitude of the magnetic field fluctuations in the saturation stage are all substantially smaller than those obtained by Lui *et al.* [5] by numerically solving the equations for the moments of the ion distribution function during the ion Weibel instability. Even for $v_0 = v_{Ti}$, the current velocity and longitudinal temperature change by approximately 5.8 and 17%, respectively. These values are smaller by a factor of approximately 4.5 than those obtained in [4, 5]. The reason for this is the following. When solving the equations for the moments of the ion distribution function numerically in the quasilinear approximation, the authors of [4, 5] assumed that the shape of the distribution function remains unchanged, and, at each time step, they varied only the global parameters such as v_{Ti} and v_0. Mathematically, this procedure implies that the function Z'_{0i} in conditions (8) and (23) is constant, in which case the instability saturates at a much higher level (at substantially larger values of the moments of the distribution function), because the dependence of $Z'_{0i}(h)$ on h makes the largest contribution to condition (23). Although our analysis deals only with longitudinal waves, there is no reason to suggest that transverse waves could substantially affect the saturation level (cf. [12]). However, obliquely propagating waves may be the subject of ongoing investigations, although, with the transverse component of the wave vector taken into account, the calculations become much lengthier.

The calculated change in the current velocity is smaller than that obtained by processing the data from observations made by the IMP 6 and ISEE 1 satellites (which was estimated to be about 25%) [5]. Thus, we can conclude that, in our model, the ion Weibel instability cannot increase the anomalous resistance to a level required to initiate magnetic reconnection. Nevertheless, the ion Weibel instability can trigger another kind of instability, e.g., the tearing instability, which, in turn, can ensure the required level of anomalous resistance.

Since our analysis is very preliminary, we cannot assert that the ion Weibel instability is completely useless for describing the substorm onset and current disruption. In order to investigate the ion Weibel instability more completely, it is necessary to take into account the magnetic field nonuniformity in the Earth's magnetotail. The relevant analysis for a cold plasma was carried out by Yoon and Lui [16], who described the magnetic field using the Harris model of a plane neutral sheet. Their calculations showed that the threshold for the ion Weibel instability is higher than that in a homogeneous plasma. However, they neglected kinetic effects, which can substantially alter the dispersion relation. Another important point is that the ion distribution function may be non-Maxwellian. In particular, an analysis of the experimental data obtained when the Galileo spacecraft traveled near the current sheet of the Earth's magnetotail confirmed the non-Maxwellian nature of the ion distribution function [17]. The problem of the excitation of low-frequency electromagnetic waves by ions obeying a non-Maxwellian distribution requires a separate analysis, and the question of whether non-Maxwellian ions are stable against these waves remains open.

ACKNOWLEDGMENTS

This work was supported in part by the Russian Foundation for Basic Research (project nos. 00-15-96631, 00-02-17127) and INTAS/ESA (grant no. 99-1006).

REFERENCES

1. C.-L. Chang, H. K. Wong, and C. S. Wu, Phys. Rev. Lett. **65**, 1104 (1990).
2. E. S. Weibel, Phys. Rev. Lett. **2**, 83 (1959).
3. C. S. Wu, P. H. Yoon, L. F. Ziebell, *et al.*, J. Geophys. Res. **97**, 141 (1992).
4. A. T. Y. Lui, J. Geophys. Res. **101**, 13067 (1996).
5. A. T. Y. Lui, P. H. Yoon, and C.-L. Chang, J. Geophys. Res. **98**, 153 (1993).
6. A. T. Y. Lui, C.-L. Chang, A. Mankofsky, *et al.*, J. Geophys. Res. **96**, 11389 (1991).
7. P. H. Yoon, Phys. Fluids B **3**, 3074 (1991).

8. P. H. Yoon, C. S. Wu, and M. E. Mandt, Phys. Fluids B **4**, 719 (1992).
9. A. T. Y. Lui, Geophys. Monogr., AM. Geophys. Union **64**, 43 (1991); **64**, 1104 (1991).
10. A. T. Y. Lui, R. E. Lopez, B. J. Anderson, *et al.*, J. Geophys. Res. **97**, 1461 (1992).
11. W. Baumjohann, Space Sci. Rev. **64**, 141 (1993).
12. V. D. Shapiro and V. I. Shevchenko, Zh. Éksp. Teor. Fiz. **45**, 1612 (1963) [Sov. Phys. JETP **18**, 1109 (1964)].
13. D. Biskamp, R. Z. Sagdeev, and K. Schindler, Cosmic Electrodyn. **1**, 297 (1970).
14. A. A. Galeev and R. Z. Sagdeev, in *Reviews of Plasma Physics*, Ed. by M. A. Leontovich (Atomizdat, Moscow, 1973; Consultants Bureau, New York, 1979), Vol. 7.
15. R. C. Davidson, D. A. Hammer, I. Haber, and C. E. Wagner, Phys. Fluids **15**, 317 (1972).
16. P. H. Yoon and A. T. Y. Lui, J. Geophys. Res. **101**, 4899 (1996).
17. T. M. Burinskaya and E. M. Indenbom, Fiz. Plazmy **26**, 49 (2000) [Plasma Phys. Rep. **26**, 46 (2000)].

Translated by O. E. Khadin

Plasma Physics Reports, Vol. 27, No. 6, 2001, pp. 497–506. Translated from Fizika Plazmy, Vol. 27, No. 6, 2001, pp. 526–535.

PLASMA DIAGNOSTICS

Analytic Approximations for the Broadening of the Spectral Lines of Hydrogen-Like Ions

I. O. Golosnoy

Institute of Mathematical Modeling, Russian Academy of Sciences, Miusskaya pl. 4a, Moscow, 125047 Russia

Received October 17, 2000

Abstract—Broadband approximate expressions for calculating the broadening of the spectral lines of hydrogen-like ions in a multicomponent plasma are derived taking into account both the influence of the interaction between plasma particles on the distribution function of the plasma microfield and the effect of the microfield dynamics on the broadening of the central component of the spectral line. With the approximate expressions proposed, the calculation of the shape of a given spectral line of a certain ion in a plasma with a given ion composition requires only a few seconds of computer time. The approximate expressions provide a good computational accuracy not only for the central component of the spectral line but also for the spectral line wings.

1. INTRODUCTION

The development of a new alternative electric energy source—an inertial confinement fusion (ICF) reactor—is a problem of current interest. ICF targets should be designed with allowance for the absorption and reemission of light by the hot target material. In target computations, one of the most important problems is that of calculating the absorption spectral lines of plasma ions and atoms [1]. The shape of the spectral lines provides a tool for diagnosing the plasma temperature and density. Note also that microfield fluctuations affect the population of the energy levels of plasma ions and atoms and thus should be incorporated into the equation of state for the plasma [2].

The Stark broadening of the spectral lines of plasma ions and atoms occurs under the action of low-frequency ion electric fields and high-frequency electron electric fields. As a rule, the contribution of electrons to the Stark broadening is described using the impact model, while the contribution of ions is treated as quasistatic. These assumptions make it possible to describe a significant part of the spectral line; however, a comparison between the theoretical and experimental spectral-line profiles reveals a systematic discrepancy between the calculated and measured profiles of the central parts of the line. Thus, in the Lyman and Balmer series of spectral lines, the measured full widths at half-maximum (FWHMs) of the unshifted components are several times larger than the calculated ones [3, 4]. Demura *et al.* [5] showed that, near the line center, the effects associated with the rotation of ion microfields play a governing role. The corrections for the influence of electron thermal motion that were obtained in [5, 6] using perturbation theory refer to a low-temperature plasma. In a hot plasma, the effect of ion motion on the spectral line broadening is so strong that it cannot be treated perturbatively and the analytic corrections obtained in [5, 6] fail to be valid.

For practical calculations, it is necessary to develop models of spectral broadening that are simple and at the same time applicable to broad temperature and density ranges. Present-day broadband models of quasistatic plasma microfields [7] and dynamic microfields [8] are fairly involved, because they require solving integrodifferential equations. This paper is devoted to constructing simple approximate analytic expressions for the static distribution function of the ion microfield in a plasma with an arbitrary ion content. The approximate expressions proposed here, on the one hand, have almost the same accuracy and applicability range as those of the known models and, on the other hand, provide computations that are thousands of times faster. The approximate expressions were constructed using analytic expansions in the Coulomb coupling parameter for the distribution function of the microfield in the limiting cases of a slightly nonideal plasma (the Debye–Hückel model) and a highly compressed hot plasma (the model of harmonic oscillators). It is well known that the ranges of validity of these models do not overlap. In this paper, however, a universal approximate analytic expression is obtained that describes both of these limiting cases and the intermediate region between them. The physical accuracy and the range of validity of the approximate expressions are sufficient for most practical applications; moreover, with the approximate expressions proposed, the calculation of the distribution function of the microfield in a plasma with a prescribed ion composition requires several seconds of computer time.

This paper also presents a derivation of the universal semiempirical analytic model of the ion motion–related broadening over the entire intermediate region between the impact broadening and quasistatic broadening. The

1063-780X/01/2706-0497$21.00

model is constructed in two steps: first, a qualitative functional dependence of the broadening on the plasma parameters is obtained using simplified physical models and, second, the free coefficients of the model are adjusted to achieve satisfactory agreement with both the experimental data and the results from computer simulations based on the molecular dynamic (MD) method.

2. INDIVIDUAL SPECTRAL-LINE COMPONENT APPROXIMATION

We consider a plasma containing k ion species with charge numbers Z_k and relative (normalized to the total density of the heavy particles) concentrations x_k:

$$\sum_k x_k = 1, \quad \sum_k Z_k x_k = x_e.$$

We assume that the plasma is in local thermodynamic equilibrium and apply a two-temperature model, in which the electron temperature T_e may differ from the ion temperature T. The plasma electrons may also be partially degenerate, in which case the related plasma state is described by introducing the parameter $\Theta = k_B T_e/\varepsilon_F$, where $\varepsilon_F = (3\pi^2)^{2/3}(\hbar^2/2m_e)N_e^{2/3}$. The mean radius R_e of the electron cell is determined from the relationship $(4\pi/3)R_e^3 N_e = 1$, where N_e is the electron plasma density. The ion microfield is expressed in units of $E_0 = e/R_e^2$, and the electron plasma parameter is $\Gamma = e^2/R_e k_B T$.

In order to calculate the intensity distribution $I_{ab}(\Delta\omega)$ in the spectral line resulting from the transition $a \longrightarrow b$, we express I_{ab} in terms of the correlation function $\Phi_{ab}(t)$ of the dipole moments of a radiating particle [9]

$$I_{ab}(\Delta\omega) = \frac{1}{\pi}\mathrm{Re}\int_0^\infty \Phi_{ab}(t)\exp(-i\Delta\omega t)dt.$$

Then, we use the model of the isolated Stark components $\alpha \longrightarrow \beta$, $\alpha \in a$, $\beta \in b$ with the Stark constant $C_{\alpha\beta}$ [10]. In this model, the correlation function has the form

$$\Phi_{ab}(t) = \left(\sum_{\substack{\alpha\in a\\ \beta\in b\\ C_{\alpha\beta}\geq 0}} \Phi_{\mathrm{ion}}^{\alpha\beta}(t)\Phi_{ei}^{\alpha\beta}(t)\right)\Phi_{\mathrm{dop}}(t), \qquad (1)$$

where $\Phi_{\mathrm{ion}}^{\alpha\beta}(t)$ and $\Phi_{ei}^{\alpha\beta}(t)$ are the normalized autocorrelation functions of the dipole moment of a radiating particle in the case of its interaction exclusively with plasma ions and exclusively with plasma electrons, respectively. For example, we have $\Phi_{el}^{\alpha\beta}(t) = \exp(-w_{\alpha\beta}t)$, where $w_{\alpha\beta}$ is the electron impact–related FWHM and the function $\Phi_{\mathrm{dop}}(t) = \exp\left(-\frac{\omega_0^2 u_i^2}{c^2}t^2\right)$ accounts for the Doppler broadening. The rest of the notation is as follows: ω_0 is the unperturbed transition rate, $u_i^2 = 2k_B T/m_0$ is the squared mean thermal velocity of a radiating particle, and c is the speed of light. In the quasistatic model of the ion-related broadening, we have

$$\Phi_{\mathrm{ion}}^{\alpha\beta}(t) = 2I_{\alpha\beta}[Q(C_{\alpha\beta}E_0 t) + C_{\alpha\beta}E_0 t Q'(C_{\alpha\beta}E_0 t)], \qquad (2)$$

where $I_{\alpha\beta}$ is the intensity of the Stark component under consideration and $Q(L)$ is the Fourier transformed distribution function of the plasma microfield [7],

$$E_0 p(E/E_0) = \frac{2E}{\pi E_0}\int_0^\infty dL \sin(LE/E_0)Q(L)L. \qquad (3)$$

In this expression, $p(E)$ is the probability density for the appearance of an instantaneous ion microfield of strength E at the point where a particle with charge number Z_0 occurs.

In expression (1), the summation is carried out over all Stark components of the spectral line with a positive Stark constant. For the unshifted component of the line in the quasistatic model of the ion-related broadening, we have $C_{\alpha_0\beta_0} = 0$ and $\Phi_{\mathrm{ion}}^{\alpha_0\beta_0}(t) \equiv 1$. In other words, in the quasistatic model, the central component broadens exclusively due to the Doppler effect and collisions with electrons.

Hence, in order to arrive at the desired broadband approximate expressions, we need to approximate the function $Q(L)$, which accounts for the static distribution of the microfield, and the function $\Phi_{\mathrm{ion}}^{\alpha_0\beta_0}(t)$, which describes the dynamics of the ion microfield. The influence of the microfield dynamics on the shifted component of the spectral line is less significant than on the central component and thus can be neglected in the first approximation.

3. APPROXIMATE EXPRESSION FOR THE QUASISTATIC MICROFIELD DISTRIBUTION IN THE MODEL OF NONINTERACTING PARTICLES

3.1. Basic Formulas

The models used to calculate various physical properties of the plasma were derived under additional assumptions regarding the influence of plasma electrons on the distribution function of the ion microfield. Among the most widely used models, we can mention,

first, the model of a homogeneous neutralizing electron background [the so-called one-component plasma (OCP) model, which is often used to describe a relatively cold dense plasma] and, second, the model of the ions surrounded by a polarization electron cloud [the so-called low-frequency plasma microfield component (LFMC) model, which is used to describe a hot plasma with multicharged ions]. It is well known that the microfield distribution functions calculated using these models for a nonideal plasma differ by several times. It turns out, however, that the microfield distribution functions in these models can be determined using the same mathematical apparatus. The models differ only in the approximate expressions for the effective interaction potentials and the effective ion fields in the plasma.

In the noninteracting quasi-particle approximation, which was originally developed for the OCP model, the function $Q(l)$ (such that $L = lE_0$) is approximated by [11]

$$\ln Q(l) = -\sum_k \frac{x_k}{x_e} 4\pi n_e \int_0^\infty dr r^2 g_{0k}(r) \frac{E_k(r)}{E_k^*(r)} \left\{ 1 - \frac{\sin[lE_k^*(r)]}{lE_k^*(r)} \right\}, \quad (4)$$

where $g_{0k}(r)$ is the pair distribution function of a test ion with charge number Z_0 and an ion with charge number Z_k, $E_k(r)$ is the field generated by an ion of species k in the vicinity of the test ion, and $E_k^*(r)$ is the effective field of an ion of species k in the plasma.

In the OCP model, we have $E_k(r) = Z_k e/r^2$, and, in the LFMC model, we have $E_k(r) = Z_k e(1 + q_e r)\exp(-q_e r)/r^2$ with

$$q_e^2 = (4/\pi)(2m_e k_B T_e)^{1/2} e\hbar^{-3} I'_{1/2}(\mu/k_B T_e).$$

Here, I_ν are Fermi–Dirac functions and the electron chemical potential μ is related to the electron density by

$$N_e = \sqrt{2}\pi^{-2}(m_e k_B T_e \hbar^{-2})^{1/2} I_{1/2}(\mu/k_B T_e).$$

The effective field $E_k^*(r)$ is chosen so that the function $p(E)$ determined from formulas (3) and (4) satisfies the second moment rule

$$\langle \mathbf{E}\mathbf{E} \rangle = \int_0^\infty E^2 p(E) dE, \quad (5)$$

where $\mathbf{E} = \sum_k \frac{Z_k \mathbf{r}_k}{r_k^3}$ is the ion microfield vector, which is not averaged over directions, and the angular brackets denote statistical averaging, i.e., averaging over all possible configurations of charges with allowance for the Boltzmann probability of the given distribution of charged particles. Note that, up to this point, the shape of $E_k^*(r)$ has been arbitrary. The following approximate expression for $E_k^*(r)$ appears to be the most convenient:

$$E_k^*(r) = Z_k(1 + \alpha_k r)\exp(-\alpha_k r)/r^2. \quad (6)$$

Here and below, r is in units of R_e, the parameters α_k are in units of R_e^{-1}, and the electric microfield is in units of E_0. Let us determine the explicit expressions for α_k that we will use to approximate the function $Q(L)$.

3.2. OCP Model

Theoretically, the case of an OCP has been studied in most detail. For $\Gamma \ll 1$, all of the parameters α_k are the same and have the form $(3\Gamma)^{1/2} Z_s$, where $Z_s = (\sum_k x_k Z_k^2/x_e)^{1/2}$.

In the limit $\Gamma \longrightarrow \infty$ (when the interaction between the charges is very strong), we can apply the model of simple harmonic oscillators [12], which can be readily extended to include ions with different charges:

$$\ln Q(L) = -\sum_k x_k Z_k L^2/2Z_0\Gamma x_e. \quad (7)$$

For $Z_0 = 0$, the parameters $\alpha_k = \alpha$ with arbitrary values of k are expressed in terms of the energy ΔE_c of the Coulomb interaction between charged particles in an arbitrarily nonideal plasma [13]:

$$\alpha = -2\Delta E_c (Z_s^2 \Gamma N_e T)^{-1}. \quad (8)$$

These expressions will be used to construct an analytic approximation for $Q(l)$ in the OCP model with an arbitrary temperature, density, and ion composition of the plasma.

Let us expand the function $Q(L)$ in powers of L in the case of a weakly nonideal plasma such that $\alpha \longrightarrow 0$ and $g_{0k}(r) = \exp(-Z_0 Z_k \Gamma \exp(-\alpha r)/r)$. To do this, we introduce the notation

$$\Theta(x, y) = \int_0^\infty \frac{dz}{t(z, x)} \exp(-ye^{-xz}/z) \left\{ 1 - \frac{\sin[t(z, x)]}{t(z, x)} \right\}, \quad (9)$$

where $t(z, x) = (1 + xz)\exp(-xz)/z^2$. Then, in the OCP model, formula (4) takes the form

$$\ln Q(L) = -\sum_k 3x_k/x_e (Z_k L)^{3/2} \Theta\{\alpha(Z_k L)^{1/2}, Z_0 Z_k \Gamma (Z_k L)^{-1/2}\}. \quad (10)$$

The argument x in function (9) approaches zero as $\Gamma \longrightarrow 0$. Consequently, to the first order in x, we obtain

$$\Theta(x, y) \approx (1 + xy)\Theta(0, y) - x/6, \quad x \longrightarrow 0. \quad (11)$$

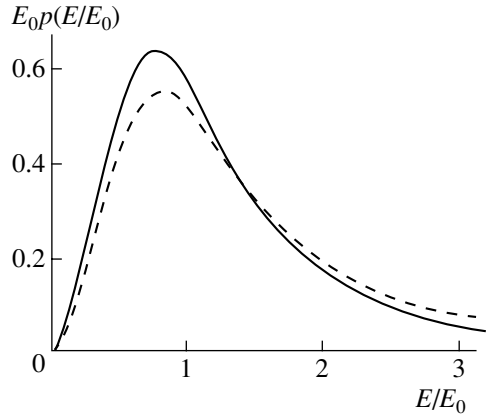

Fig. 1. Distribution function of the ion microfield $p(E)$ in a plasma with singly charged ions ($x_1 = 1$, $Z_1 = 1$) for $Z_0 = 0$ and $\Gamma = 10$ in the OCP model. The profiles obtained from MC [13] (solid curve) and MAPEX (dashed curve) calculations are shown.

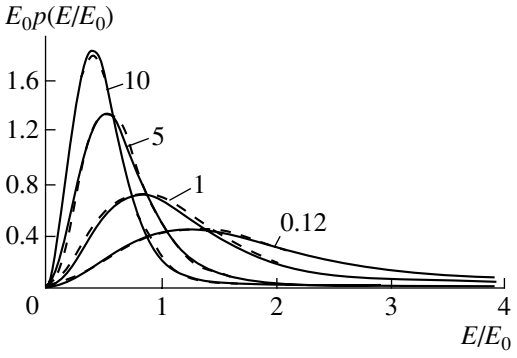

Fig. 2. Microfield distribution function obtained using the OCP model of a plasma with singly charged ions ($x_1 = 1$, $Z_1 = 1$) for $Z_0 = 1$ and for different values of the coupling parameter (numerals near the curves show the Γ values). The profiles obtained from MC [11] (solid curve) and MAPEX (dashed curve) calculations are shown.

Using this expression, we easily arrive at the relationships

$$\Theta(x, y) \approx 1/3 - \pi y/8 - x/6, \quad x \longrightarrow 0, \quad y \longrightarrow 0,$$
$$\Theta(x, y) \approx 1/(6y), \quad x \longrightarrow 0, \quad y \longrightarrow \infty,$$

which permit us to approximate the function $\Theta(x, y)$ by

$$\Theta(x, y) \approx (1/3)[1 + x/2 + 1.2y + 0.8y^2(1 + y^{1/2})^{-2}]^{-1}. \quad (12)$$

Note that, for $Z_0Z_k\Gamma \longrightarrow \infty$, the mean term in this approximate expression corresponds to expression (7) in the model of harmonic oscillators; consequently, formula (12) also applies to a dense plasma such that $Z_0Z_k\Gamma \longrightarrow \infty$.

For $Z_0 = 0$, the parameter α_k in the approximate expression (6) is determined by expression (8). The energy ΔE_c in expression (8) can be calculated using one of the many simple approximations proposed previously. We chose the following approximate formula, which is valid within an accuracy of about 10%:

$$\alpha = 2(3\Gamma)^{1/2}Z_s\pi^{-1}\arctan(2.418(3\Gamma)^{-1/2}Z_s^{-1}x_e^{-1/3}) + 0.64\Gamma Z_s^2 x_e^{1/3}(1 + 2.5\Gamma Z_s^2 x_e^{2/3})^{-1}.$$

For $Z_s^2\Gamma \leq 1$, this formula was derived using the method of collective variables [14] and was continued into the region $Z_s^2\Gamma \gg 1$ with the help of the familiar relationship

$$\Delta E_c/N_eT \approx -0.9\Gamma\sum_k Z_k^{5/2}x_k/x_e \approx -0.9\Gamma Z_s^2 x_e^{-1/3}.$$

The above formula is also valid for $Z_0 \neq 0$, because, for $\Gamma \ll 1$, it is subject to the regular Debye limit and, for $\Gamma \gg 1$ and $Z_0 \neq 0$, the coefficient α is unimportant [see formula (12) for $y \longrightarrow \infty$].

For $Z_s^2\Gamma \sim 1$, the parameter α is on the order of unity and expansion (11) applies only to small values of L. For $L \gg 1$, we can apply the method of steepest descent [15] to the approximate expressions (4) and (6) in order to obtain the first term of the asymptotic expansion of the function $Q(L)$ at infinity for $Z_0 \neq 0$:

$$\ln Q(L) = -\sum_k (x_k/x_e)Z_kL\alpha^{-1}(7/6 - (3\sin 1 + \cos 1)/10) \approx -1.5\sum_k (x_k/x_e)Z_kL\alpha^{-1}. \quad (13)$$

Hence, for $L \gg 1$, the main term in formula (13) differs from that in the approximate expression (12) only in the coefficient (1.5 in place of 2). Since this difference is insignificant, formula (12) yields fairly good results even for $Z_s^2\Gamma = 10$ (Fig. 1).

Below, the approximate expression (10) with formula (12) will be referred to as the modified adjustable parameter exponential (MAPEX) approximation. Recall that the MAPEX approximation provides a good description of a weakly nonideal plasma and highly compressed, hot, ionized fluid. Let us compare the MAPEX results with the results from test Monte Carlo (MC) calculations of the distribution function $p(E)$ for intermediate values of the coupling parameter Γ, i.e., for $Z_s^2\Gamma \sim 1$.

Figure 2 shows the microfield distributions in the vicinity of a test ion calculated for different Γ values in

a plasma with singly charged ions. Figures 3 and 4 compare the MAPEX and MC results on the microfield distribution $p(E)$ against the homogeneous electron background in a plasma with two ion species. We can see that, even in the most unfavorable cases, the accuracy of the MAPEX approximation is no worse than 10%.

3.3. Low-Frequency Microfield Component (LFMC) Model

The LFMC model is often used to calculate the optical plasma properties in order to determine the shape and intensity of the spectral lines.

In the LFMC model, the electric fields are assumed to be generated not by the point ions but by charged spheres centered on the point ion and filled with electrons correlated with the ion. The electron–ion correlations are, as a rule, treated in the random phase approximation, which applies to a weakly nonideal plasma and yields the familiar Debye expression for the static dielectric constant of an electron gas:

$$\varepsilon(q, 0) = 1 + q_e^2/q^2.$$

In this case, the effective field produced by an ion with charge number Z_k at the position of the ith ion has the form

$$E_k(r_{ik}) = Z_k(1 + q_e r_{ik})\exp(-q_e r_{ik})/r_{ik}^2. \qquad (14)$$

Formula (14) can be used for weak electron–electron and electron–ion interactions (such that the conditions $\Gamma < 1$ and $Z_k\Gamma < 1$ hold for all ion species k). The corresponding calculations show that, under the above restrictions, the distribution function $p(E)$ in the LFMC model can be obtained with an accuracy of 20% by treating the ion–ion correlations in the Debye approximation, in which case, in formulas (4) and (6), we can set

$$\alpha_k \equiv \alpha = (q_e^2 + q_i^2)^{1/2},$$
$$g_{0k}(r) = \exp\{-(Z_0 Z_k \Gamma/r)\exp(-\alpha r)\}.$$

Hence, in the LFMC model, the desired approximate expressions can be constructed in the same way as in the OCP model. We set

$$\Theta_e(x, y) = \int_0^\infty \frac{dz}{t(z, x)}(1 + \varphi xz)\exp(-\varphi xz) \times \exp(-ye^{-xz}/z)\left\{1 - \frac{\sin[t(z, x)]}{t(z, x)}\right\}, \qquad (15)$$

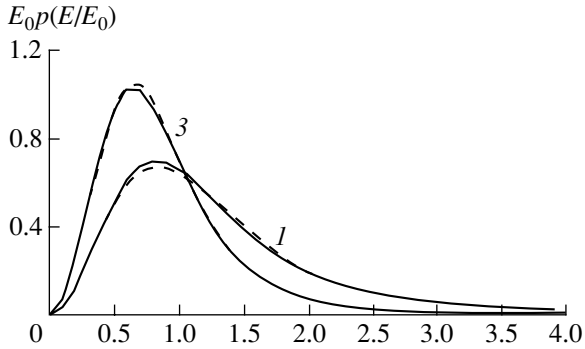

Fig. 3. Microfield distribution function obtained using the OCP model of a plasma with two ion species ($x_1 = 0.97$, $Z_1 = 1$, $x_2 = 0.03$, $Z_2 = 3$) for $\Gamma = 1$ (numerals near the curves show the Z_0 values).

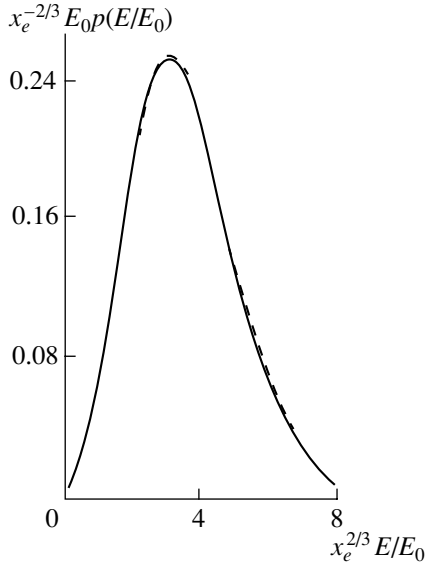

Fig. 4. Microfield distribution function obtained using the OCP model of a plasma with two ion species ($x_1 = 0.5$, $Z_1 = 1$, $x_2 = 0.5$, $Z_2 = 17$) for $x_e^{-1/3}\Gamma = 1$ and $Z_0 = 17$.

where $t(z, x) = (1 + xz)\exp(-xz)/z^2$ and $\varphi = q_e/\alpha$. Then, in the LFMC model, formula (4) can be written as

$$\ln Q(L) = -\sum_k 3x_k/x_e(Z_k L)^{3/2}\Theta_e\{\alpha(Z_k L)^{1/2}, Z_0 Z_k \Gamma(Z_k L)^{-1/2}\}. \qquad (16)$$

In the case at hand, we have $\alpha \ll 1$; consequently, to arrive at the desired approximate expression, it is sufficient to consider the limit $x \longrightarrow 0$ in relationship (15). Retaining only the first-order term in the expansion in x, we obtain

$$\Theta_e(x, y) \approx (1 + xy)\Theta_e(0, y) - (1 + \varphi + \varphi^2)x/(6 + 6\varphi), \quad x \longrightarrow 0, \qquad (17)$$

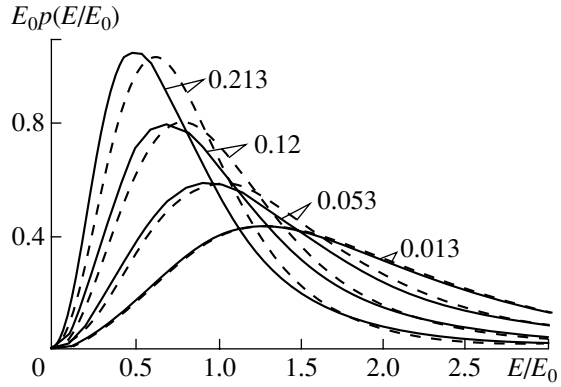

Fig. 5. Microfield distribution function obtained using the LFMC model of a plasma with singly charged ions ($x_1 = 1$, $Z_1 = 1$) for the charge number $Z_0 = 9$ of a test ion (numerals near the curves show the Γ values). The profiles obtained from the approximate expression (21) (dashed curve) and more exact APEX calculations (solid curve) are shown.

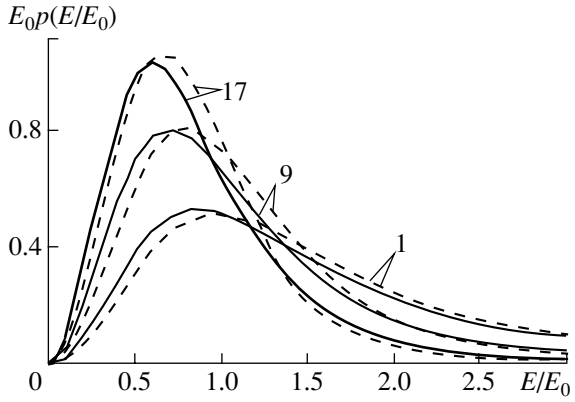

Fig. 6. Microfield distribution function obtained using the LFMC model of a plasma with singly charged ions ($x_1 = 1$, $Z_1 = 1$) for $\Gamma = 0.12$ (numerals near the curves show the Z_0 values). The profiles obtained from the approximate expression (21) (dashed curve) and more exact APEX calculations (solid curve) are shown.

which gives

$$\Theta_e(x, y) \approx 1/3 - \pi y/8 - (1 + \varphi + \varphi^2)x/(6 + 6\varphi), \quad x \longrightarrow 0, \quad y \longrightarrow 0, \tag{18}$$

$$\Theta_e(x, y) \approx (1 + xy)/(6y) - (1 + \varphi + \varphi^2)x/(6 + 6\varphi) = 1/(6y) - \varphi^2 x/(6 + 6\varphi), \quad x \longrightarrow 0, \quad y \longrightarrow \infty, \tag{19}$$

$$\Theta_e(0, y) \approx 1/(6y), \quad y \longrightarrow \infty.$$

We consider a slightly nonideal ($Z_s^2\Gamma \leq 1$) plasma with $Z_0 \sim 10$, in which case we have $\Lambda_k = Z_0Z_k\Gamma\alpha \geq 1$ (this situation is encountered in diagnosing the spectral lines from a small population of noble-gas impurity ions in a hydrogen plasma). For such a plasma, the quantity xy in expansion (17) is larger than unity, so that the expansion itself no longer holds. Consequently, in order to obtain the desired approximate expression, it is sufficient to analyze the region $Z_k\alpha^2L \ll \Lambda_k$. In this region, we can expand the expression in braces in formula (15) in powers of L and replace the lower limit of integration by $z_{ab} = (\ln\Lambda_k - \ln\ln\Lambda_k)/\alpha$, setting $y = 0$. As a result, we obtain

$$\ln Q(L) \approx -\sum_k (3L^2Z_k^2x_k\alpha/x_e) \int_{\alpha z_{ab}}^{\infty} \frac{dz(1 + \varphi z)(1 + z)}{6z^2\exp(z + z\varphi)}$$

$$\approx -\sum_k (L^2Z_k^2x_k)/(2Z_0Z_k\Gamma x_e) \tag{20}$$

$$\times [1 + \varphi\ln\Lambda_k/(1 + \varphi)]\left\{\frac{\ln\Lambda_k}{\Lambda_k}\right\}^{\varphi}.$$

Using relationships (15)–(20), we can construct the following approximate expression for $Q(L)$ in the LFMC model:

$$\ln Q(L) = -\sum_k (x_k/x_e)(Z_kL)^{3/2}G^{-1},$$

$$G = 1 + 0.5\alpha(Z_kL)^{1/2}(1 + \varphi + \varphi^2)/(1 + \varphi) + 1.2y_k[1 + 2y_kf_k](1 + 1.2y_k)^{-1}, \tag{21}$$

$$y_k = Z_0Z_k\Gamma(Z_kL)^{-1/2},$$

$$f_k = \left\{\frac{\Lambda_k}{\ln\Psi_k}\right\}^{\varphi}[1 + \varphi\ln\Psi_k/(1 + \varphi)]^{-1},$$

$$\Psi_k = \Lambda_k + (1 + 0.5\Lambda_k^2)^{-1}.$$

Figure 5 compares the distribution functions $p(E)$ calculated from formula (21) and those calculated from the more exact adjustable parameter exponential (APEX) approximation in the LFMC model for a plasma with singly charged ions and with different coupling parameters. Figure 6 presents the distribution functions $p(E)$ calculated from formula (21) and from the APEX approximation for different charge numbers Z_0 of the test ion and for $\Gamma = 0.12$. The accuracy of approximate expression (21) is seen to be about 15%, which is quite sufficient for most applications.

4. SEMIEMPIRICAL ANALYTIC MODEL OF THE DYNAMIC ION-RELATED BROADENING

In order to construct the desired broadband approximate expression, we apply perturbation theory to the

autocorrelation function of the central component of the spectral line. In [5, 6], it was shown that

$$\Phi_{\text{ion}}^{\alpha_0\beta_0}(t) \simeq \exp(-w_0 t)[1 - s_{pt}t^2 + \ldots]. \quad (22)$$

According to [16], the coefficient s_{pt} for a multicomponent plasma can be readily written as

$$s_{pt} \approx 4.156\frac{k_B T N^{2/3}}{w_0^3}\frac{\sum_k x_k Z_k^{1/2}\mu_k^{-1}}{\left(\sum_k x_k Z_k^{3/2}\right)^{1/3}}, \quad (23)$$

where $\mu_k^{-1} = m_k^{-1} + m_0^{-1}$ is the reduced mass of a radiating–perturbing pair of particles and $N = N_e/x_e$ is the total ion plasma density.

In a hot plasma, the ion spectral lines can be described in terms of the impact broadening with the FWHM $w_{\text{dyn}} \sim \sum_k N x_k C_k^2/v_k$, where $v_k^2 = 2k_B T/\mu_k$ and C_k is the mean splitting of the Stark components under the action of the ion of species k. For simplicity, we will approximate a real system of the Stark energy sublevels by a system of $n = 2$ levels of a hydrogen atom; in other words, we will describe the dynamic effects of the ion microfield in terms of the Ly_α line with the effective Stark constant

$$C_k = 1.5n[n_1 - n_2]_{\text{eff}}\frac{Z_k\hbar}{m_e(Z_0+1)},$$

$$[n_1 - n_2]_{\text{eff}}^2 = \frac{\sum_{\alpha,\beta,n_1>n_2} I_{\alpha\beta}(n_1-n_2)^2}{\sum_{\alpha,\beta,n_1>n_2} I_{\alpha\beta}}.$$

Here, n, n_1, and n_2 are the principal and parabolic quantum numbers and $Z_0 + 1$ is the nuclear charge number of the emitting particle.

Hence, we have derived approximate expressions for all of the limiting cases. In order to construct the desired approximations in the intermediate region, it is necessary to know the functional dependence of the FWHM of the spectral line on the plasma parameters. This dependence can be established using the simplified physical model developed by Lisitsa and Sholin [17], who showed that, in the single-particle approximation, the profile of the hydrogen spectral line can be described in terms of the quadratures of the Bateman functions [18] without any assumptions regarding the character of binary collisions. An analysis of these quadratures for the central component of the Ly_α line yields the following profile:

$$I(\Delta\omega) \simeq \frac{w_{\text{dyn}}}{\Delta\omega^2} \text{ for } \Delta\omega \le \sum_k \frac{x_k v_k^2}{C_k},$$
$$w_{\text{dyn}} \sim \sum_k \frac{N x_k C_k^2}{v_k}\ln\left[\frac{v_k^2 R_k^2 + C_k^2}{C_k^2}\right], \quad (24)$$

where $\frac{4\pi}{3}N x_k R_k^3 = 1$. Consequently, the quantity w_{dyn} can be interpreted as the ion dynamic FWHM. Note that the FWHM w_{dyn} in formula (24) represents (to within a numerical factor) both the impact-related FWHM of the ion spectral lines and the dynamic corrections to the static profile. Using formula (24) for w_{dyn} and formulas (22) and (23), which were obtained perturbatively, we can approximate the autocorrelation function for the ions by

$$\Phi_{\text{ion}}^{\alpha_0\beta_0}(t) = \exp(-st^2),$$
$$s = \sum_k \frac{\xi_k^{1/2} N x_k C_k^2}{v_k}\ln\left[\frac{K v_k^2 R_k^2 + C_k^2}{C_k^2}\right]. \quad (25)$$

Here, the coefficient K incorporates the multicomponent nature of the plasma,

$$K = \frac{\left(\sum_k x_k Z_k^{1/2}\mu_k^{-1}\right)^{1/2}}{\left(\sum_k x_k Z_k^{3/2}\right)^{1/6}\left(\sum_k x_k \mu_k^{-1/2}\right)}, \quad (26)$$

and the coefficient ξ_k is introduced in order to take into account multiparticle effects in a relatively cold plasma (in [17], these effects were neglected) and to ensure a smooth transition from the impact-related corrections to dynamic corrections to the static profile. Here, it is proposed to approximate the coefficient ξ_k by

$$\xi_k = \left(\eta + 22x\log\left[\frac{C_k}{v_k R_k} + 1\right]\right)\left(1 + x\log\left[\frac{C_k}{v_k R_k} + 1\right]\right)^{-1}, \quad (27)$$

where η corresponds to the impact broadening limit. For example, for the Ly_α line, we have $\eta = 2$ and $C_k = 3Z_k\hbar(Z_0+1)^{-1}m_e^{-1}$, and, for the Ly_γ line, we have $\eta = 2.74$ and $C_k = 14.7Z_k\hbar(Z_0+1)^{-1}m_e^{-1}$. The empirical coefficient x in the approximate expression (27) is adjusted to achieve the best agreement of the calculated line profiles with the experimental data [3] or with the basic MD results on spectral line broadening [4]. This coefficient, which was specially chosen for each of the lines (Ly_α, Ly_γ, H_α, etc.) is independent of the radiating-particle charge number Z_0, the ion composition, and the

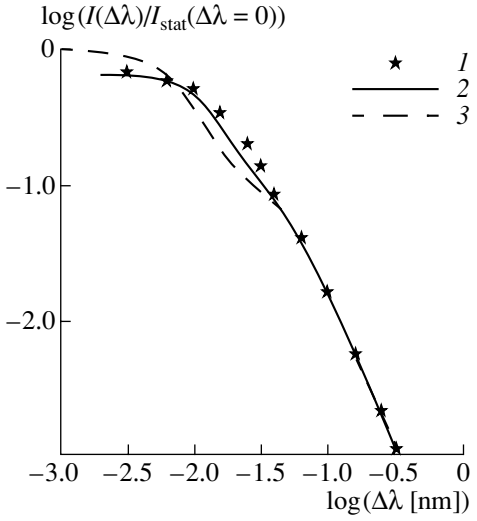

Fig. 7. Comparison between the experimental and theoretical profiles of the Ly_α line of hydrogen in a plasma with singly charged argon ions and with $T = 13200$ K and $N_e = 2 \times 10^{17}$ cm^{-3}: (*1*) the measured profile and the approximate profiles calculated (*2*) with and (*3*) without allowance for the ion microfield dynamics. The emission intensity on a logarithmic scale is normalized to the spectral line intensity calculated using the quasistatic model of the ion-related broadening for $\Delta\lambda = 0$.

plasma parameters. For example, we have $x = 0.4$ for the Ly_α line and $x = 0.6$ for the Ly_γ line.

5. COMPARISON WITH THE EXPERIMENT

In [3], the experiments were carried out with a plasma containing singly charged argon ions and a small hydrogen admixture, the ion temperature and electron density being $T \sim 10^4$ K and $N_e \sim 10^{17}$ cm^{-3}. These experimental conditions made it possible to avoid strong absorption at the frequencies of the hydrogen lines under investigation: the plasma was optically thin even for the Ly_α line emission. The difference between the spectral line profiles measured experimentally and those calculated from the approximate expressions (2) and (21) in the quasistatic model and with allowance for the dynamic ion autocorrelation function (25)–(27) is illustrated in Fig. 7. In order to compare both the central component of the line and the farthest components of the line wings, the profiles in Fig. 7 are plotted on a logarithmic scale. We see that the results obtained from the approximate expressions (1), (2), (21), and (25)–(27) agree well with the experimental data. At the same time, the quasistatic model of the ion-related broadening underestimates the FWHM of the spectral line by a factor of 2.

The results of experiments carried out in [3] are summarized in the table. One can see that the results obtained from the approximate expressions proposed here lie within the measurement errors and are close to the experimental data, while the quasistatic model of the ion-related broadening underestimates the FWHM of the line by a factor of approximately 2. Hence, we can conclude that, in plasma diagnostics, it is important to take into account the ion microfield dynamics. The approximate expressions (25)–(27) provide a way of doing this with an expenditure of only a small amount of computer time.

The effect of the reduced mass on the approximation accuracy has also been investigated. Thus, the ratio of the intensities of the central components of the Ly_α lines of deuterium and hydrogen was measured in the experiments of [20]. At $T = 15500$ K and $N_e = 2 \times 10^{17}$ cm^{-3}, this ratio was found to be 1.17. The above approximate expressions yield essentially the same result: 1.18; this value differs from the experimental one by less than 1%.

Stamm *et al.* [4] calculated the spectral lines of the hydrogen-like ions Al^{+12} and Ar^{+17} at $T \sim 10^6$ K and $N_e \sim 10^{22}$ cm^{-3} and the spectral lines of hydrogen for the experimental conditions of [3]. The results obtained for hydrogen turned out to be close to the experimental data. This supports the conclusion on the reliability of the assumptions underlying MD simulations. In [4], the calculations were performed without allowance for the fine structure splitting and Doppler effect. Consequently, the MD results obtained in [4] (especially, those on the Ly_α line of Ar^{+17}) are likely to be regarded as test (rather than practical) results. However, these test results can be used to check particular models of the spectral line broadening due to the plasma influence on the emitting ion.

Figures 8–10 compare the results calculated for the Lyman series of spectral lines from the Al^{+12} and Ar^{+17} ions by the MD method, the standard spectral-line

FWHM of the Ly_α line (in nm) in an Ar^+ plasma. The measurement errors are $\Delta N_e/N_e < \pm 0.1$ and $\Delta T/T < \pm 0.03$

N_e, 10^{17} cm^{-3}	T, K	Calculated		Measurements (±0.002)
		quasistatic model [19]	proposed approximation	
1	12700	0.014	0.021	0.023
2	13200	0.016	0.028	0.030
3	13200	0.019	0.034	0.036
4	14000	0.022	0.040	0.042

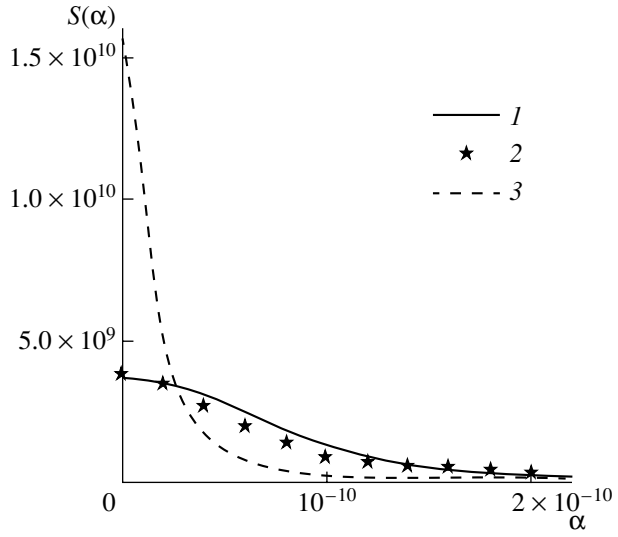

Fig. 8. Ly_α line of Ar^{+17} ions in a 100% Ar^{+17} plasma with $T = 10^7$ K and $N_e = 1.5 \times 10^{23}$ cm^{-3}. The profiles are obtained from (*1*) the approximate expressions (25)–(27), (*2*) MD simulations, and (*3*) the quasistatic model. The abscissa is the parameter $\alpha = \Delta\lambda/E_0$ with $\Delta\lambda$ given in angstroms.

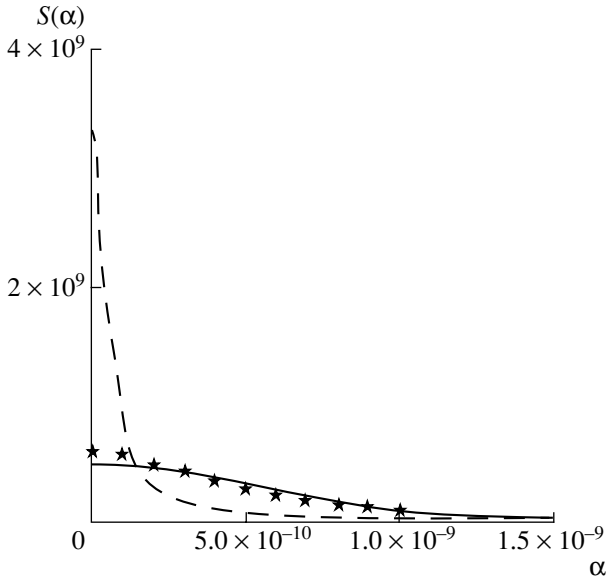

Fig. 9. Ly_α line of Al^{+12} ions in a 100% Al^{+12} plasma with $T = 2.7 \times 10^6$ K and $N_e = 4 \times 10^{21}$ cm^{-3}. Notation is analogous to that in Fig. 8.

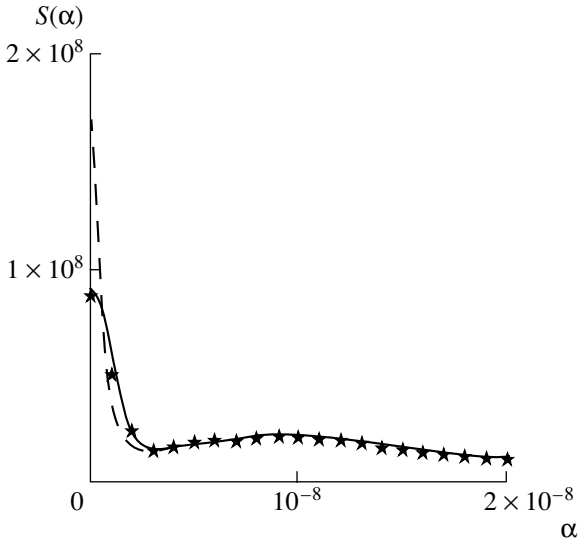

Fig. 10. Ly_γ line of Al^{+12} ions in a 100% Al^{+12} plasma with $T = 10^7$ K and $N_e = 4 \times 10^{21}$ cm^{-3}. Notation is analogous to that in Fig. 8.

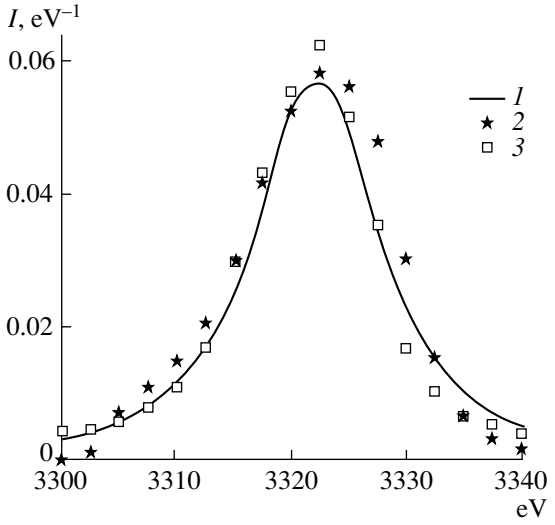

Fig. 11. Ly_α line of Ar^{+17} ions in a hydrogen plasma with the ion temperature $T = 10^7$ K and electron density $N_e = 5 \times 10^{24}$ cm^{-3}. The profiles are obtained from (*1*) the approximate expressions (25)–(27), (*2*) MD simulations [21], and (*3*) MD simulations [22].

broadening model, and the approximate expressions (25)–(27). Note that, in accordance with theoretical predictions, the wings of the lines are well described by the quasistatic model of the ion-related broadening. However, the results obtained for the central part of the lines disagree considerably with computer simulations. On the other hand, the approximate expressions proposed here give reliable results for both the central parts and the line wings and thus can be applied to a broad range of plasma parameters (the plasma parameters in the experiments of [3] and the MD simulations of [4] differ by several orders of magnitude).

In order to determine the actual applicability range of the approximate expressions, it is necessary to compare the results calculated from formulas (25)–(27)

with the MC results obtained for the Ly_α line with allowance for the fine structure components [21, 22]. In [21, 22], it was shown that, for Ar^{+17} ions in a hydrogen plasma, the Stark mixing of the $2s_{1/2}$, $2p_{1/2}$, and $2p_{3/2}$ levels occurs at the electron density $N_e = 5 \times 10^{24}$ cm^{-3} and higher. At such densities, nonlinear interference effects are unimportant [21], which makes it possible to assume that, for the Ly_α line of Ar^{+17} ions, the approximate formulas (25)–(27) apply to the density range $N_e > 5 \times 10^{24}$ cm^{-3}. In fact, under these conditions, the approximate results agree fairly well with the MD results (Fig. 11). Hence, it is possible to conclude that the approximate expressions (25)–(27) are valid when the calculated FWHM of the line exceeds the separation between the fine structure components by a factor of more than 2.

ACKNOWLEDGMENTS

I am grateful to N.N. Kalitkin and A.N. Starostin for fruitful discussions and valuable remarks. This work was supported in part by the Russian Foundation for Basic Research, project nos. 99-01-00082 and 00-01-00151.

REFERENCES

1. H. R. Griem, *Spectral Line Broadening by Plasmas* (Academic, New York, 1974; Mir, Moscow, 1978).
2. V. S. Volokitin, I. O. Golosnoĭ, and N. N. Kalitkin, Izv. Vyssh. Uchebn. Zaved., Fiz., No. 4, 11 (1995).
3. K. Grutzmacher and B. Wende, Phys. Rev. A **16**, 243 (1977).
4. R. Stamm, B. Talin, E. L. Pollock, and C. A. Iglesias, Phys. Rev. A **34**, 4144 (1986).
5. A. V. Demura, V. S. Lisitsa, and G. V. Sholin, Zh. Éksp. Teor. Fiz. **73**, 400 (1977) [Sov. Phys. JETP **46**, 209 (1977)].
6. R. Gauble and H. R. Griem, Phys. Rev. A **27**, 3187 (1983).
7. J. W. Dufty, *Strongly Coupled Plasma Physics* (Plenum, New York, 1987).
8. D. B. Boercker, C. A. Iglesias, and J. W. Dufty, Phys. Rev. A **36**, 2254 (1987).
9. I. I. Sobelman, *Atomic Spectra and Radiative Transitions* (Fizmatgiz, Moscow, 1963; Springer-Verlag, Berlin, 1979).
10. G. V. Sholin, A. V. Demura, and V. S. Lisitsa, Zh. Éksp. Teor. Fiz. **64**, 2097 (1973) [Sov. Phys. JETP **37**, 1057 (1973)].
11. C. A. Iglesias and J. L. Lebowitz, Phys. Rev. A **30**, 2001 (1984).
12. A. D. Selidovkin, Teplofiz. Vys. Temp. **6**, 10 (1968).
13. J. W. Dufty, D. B. Boercker, and C. A. Iglesias, Phys. Rev. A **31**, 1681 (1985).
14. A. A. Broyles, Phys. Rev. A **100**, 1181 (1955).
15. V. I. Smirnov, in *A Course of Higher Mathematics* (Nauka, Moscow, 1974; Addison-Wesley, Reading, 1964), Vol. 3, Part 2.
16. S. Chandrasekhar, *Stochastic Problems in Physics and Astronomy* (American Inst. of Physics, New York, 1943; Inostrannaya Literatura, Moscow, 1947).
17. V. S. Lisitsa and G. V. Sholin, Zh. Éksp. Teor. Fiz. **61**, 912 (1971) [Sov. Phys. JETP **34**, 484 (1972)].
18. *Higher Transcendental Functions (Bateman Manuscript Project)*, Ed. by A. Erdelyi (McGraw-Hill, New York, 1953, 1953, 1955; Nauka, Moscow, 1965, 1966, 1967), Vols. 1–3.
19. C. R. Vidal, J. Cooper, and E. W. Smith, Astrophys. J., Suppl. Ser. **25**, 37 (1973).
20. M. Geisler, K. Grutzmacher, and B. Wende, in *Spectral Line Shapes*, Ed. by K. Burnett (de Gruyter, Berlin, 1983), Vol. 2, p. 37.
21. A. V. Anufrienko, A. E. Bulyshev, A. L. Godunov, *et al.*, Zh. Éksp. Teor. Fiz. **103**, 417 (1993) [JETP **76**, 219 (1993)].
22. F. Khelfaoui, Ph.D.Thesis (Univ. de Provence, Marseille, 1991).

Translated by O. E. Khadin

Plasma Physics Reports, Vol. 27, No. 6, 2001, pp. 507–510. Translated from Fizika Plazmy, Vol. 27, No. 6, 2001, pp. 536–539.

BEAMS IN PLASMA

Coherent Interaction of a Relativistic Electron Beam with a Plasma

G. G. Oksuzyan, M. I. Ivanyan, and A. S. Vardanyan

Yerevan Physical Institute, Yerevan, 375036 Armenia

e-mail: oksuzyan@moon.yerphi.am

Received July 21, 2000; in final form, November 20, 2000

Abstract—Results are presented from experimental studies of the interaction of a modulated relativistic electron beam with a plasma. The electron energy spectra at the exit from the interaction chamber are measured for electron beams with energies of about 50 and 20 MeV. The coherent interaction of an electron beam with a microwave-driven plasma is studied. It is shown that, in strong electric fields that can be generated in the coherent interaction, the beam current is very sensitive to the phase of the microwave field. © *2001 MAIK "Nauka/Interperiodica".*

At present, plasma methods for the acceleration of charged particles are being actively developed (see, e.g., [1], the reviews by Ya.B. Faĭnberg [2–4], and the literature cited therein). Theoretical and experimental papers aimed at investigating the mechanisms for the generation of strong wakefields show that one of the main directions in this area—the wakefield excitation by relativistic electron bunches—has many useful applications (see, e.g., [5–11]), in particular, in creating the conditions for the coherent interaction of a relativistic electron beam with a plasma. These conditions can be achieved, e.g., in the interaction of a modulated electron beam with a plasma driven by a microwave pulse at the frequency of the accelerating field in an accelerator.

We carried out experiments with a decaying plasma and a microwave-driven plasma. The experimental device consists of a four-stage linear accelerator (linac), a plasma chamber, magnetic analyzers, and other elements shown in Fig. 1. The parameters of the electron beam are as follows: the peak value of the beam current is 0.1–0.15 A, the modulation frequency is f_m = 2797.3 MHz, the beam diameter is about 1 cm, and the length of electron bunches is about 1 cm. The plasma chamber is an 8-cm-diameter glass tube with the electrodes separated by a distance of about 40 cm. The plasma is created by applying a dc voltage to the hollow electrodes of the discharge chamber through a high-voltage modulator, which is switched on synchronously with the linac operating in the pulsed mode. During the pulse, the peak plasma current is 100–150 A. The plasma density is measured both with a radio interferometer at a wavelength of 3 cm and from the cutoff of the probing signal. The optimum plasma density is chosen by delaying the current pulse of an electron beam with respect to the plasma current pulse. Our experiments were conducted in the absence of an external magnetic field.

We begin by describing experiments with a decaying plasma. The electron energy spectra were measured over times much longer than the repetition period of the current pulses; i.e., we measured the integral spectra. In order to improve the measurement accuracy, a magnetic analyzer installed behind the interaction chamber was equipped with an additional solenoid (*23*) (Fig. 1) in which the number of coils was two orders of magnitude smaller than that in the main magnet. Both the magnets and solenoids were powered by a dc source with an instability of about 0.03%, the instability of the voltage source that supplied the linac being about 0.1%. The current of the electrons that traversed the entire plasma region was measured with an accuracy of about 10%, the accuracy of the measurements of the electron energy being about 0.3%.

Figures 2 and 3 show the electron energy spectra of a beam with the maximum current before and after the interaction with the plasma. The energy spectra of the beam electrons are incomplete (the wings of the spectrum are absent) because, at the exit from the interaction chamber, the average electron beam current was too low ($I_b \ll 0.1$ μA) to be measured reliably when the field of the magnetic analyzer changed substantially. For this reason, the measurements were aimed at revealing the largest displacement of the energy spectrum toward high energies. In a plasma with a density of about $\sim 4 \times 10^{11}$ cm^{-3}, the increment in the energy of the beam electrons injected at energies of about 50 MeV was found to be 0.6 MeV. For an injection energy of about 20 MeV and a plasma density of about $\sim 10^{11}$ cm^{-3} (which corresponds to the electron plasma frequency close to the modulation frequency of the beam), the peak in the energy spectrum was observed to be displaced toward higher energies by approximately

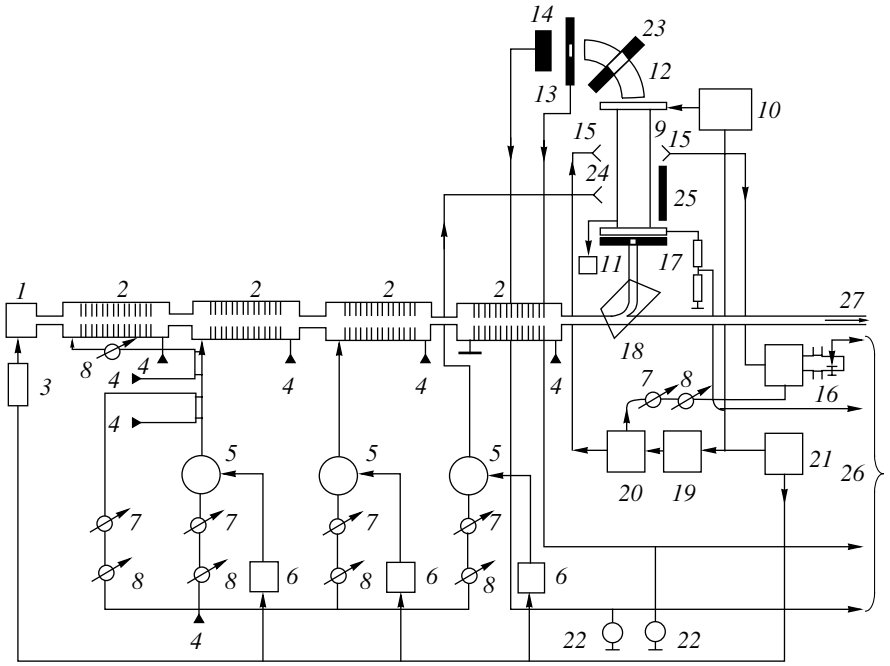

Fig. 1. Experimental scheme of the device: (*1*) electron source, (*2*) diaphragmatic waveguide, (*3*) electron source modulator, (*4*) matched microwave load, (*5*) high-power klystron ($P_{puls} \approx 20$ MW), (*6*) klystron modulator, (*7*) attenuator, (*8*) phase shifter, (*9*) plasma chamber, (*10*) modulator supplying the plasma chamber, (*11*) forevacuum pump, (*12*) magnetic analyzer, (*13*) collimator, (*14*) Faraday cup, (*15*) emitting and receiving antennas, (*16*) radio interferometer, (*17*) load resistor, (*18*) beam-deflecting magnet, (*19*) microwave oscillator, (*20*) microwave amplifier, (*21*) synchronization unit, (*22*) microammeter, (*23*) additional solenoid, (*24*) antenna emitting a high-power microwave signal, (*25*) reflector, (*26*) signals fed to an oscilloscope, and (*27*) electron beam escaping from the linac.

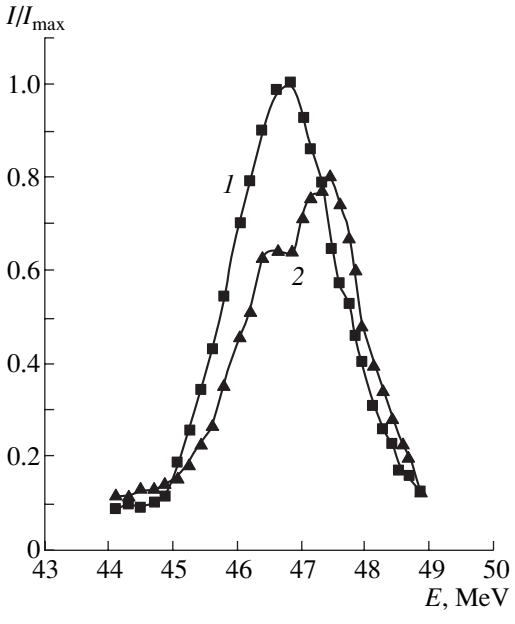

Fig. 2. Energy spectra of the beam electrons (*1*) in the absence of a plasma and (*2*) in the presence of a plasma of density $n_p \sim 4 \times 10^{11}$ cm^{-3}.

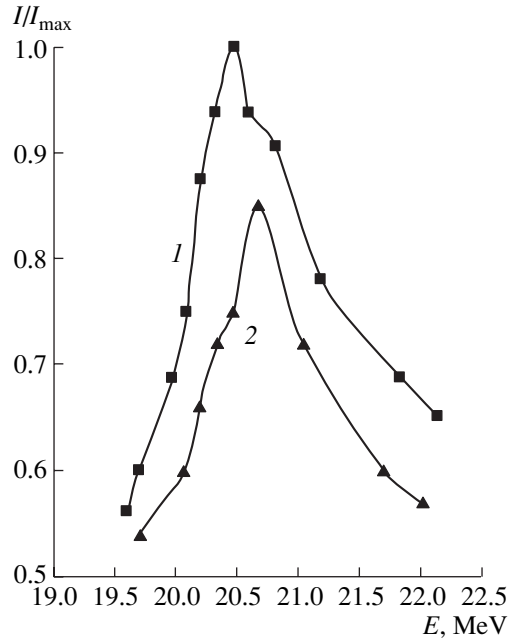

Fig. 3. Energy spectra of the beam electrons (*1*) in the absence of a plasma and (*2*) in the presence of a plasma of density $n_p \sim 10^{11}$ cm^{-3}.

0.2 MeV. This result agrees with the conclusion drawn in [6]: the higher the energy of the injected electron beam, the higher the beam–plasma interaction efficiency.

The second series of experiments was carried out with a plasma created by a microwave pulse in an open resonator (Fig. 1). The electric field vector **E** of the microwave field was oriented along the plasma chamber, i.e., in the propagation direction of the electron bunches. In order for the plasma to be produced most intensively, the distance d ($d \sim \lambda = 10.72$ cm, where λ is the radiation wavelength) between reflector (*25*) and the emitting open end of the waveguide was chosen in such a way that the antinode of the standing wave of microwave oscillations occurred at the symmetry axis of the plasma chamber. Microwave radiation was fed into the plasma chamber from the accelerator microwave power supply system (klystron *5*). As a result, the plasma was created by the same microwave field that was used to form electron bunches and to accelerate them to an energy of 20 MeV. Consequently, the interaction of electron bunches with a plasma whose density n_p was constant during the microwave pulse was coherent in character. This is illustrated in Fig. 4, which shows the current of the electrons accelerated to an energy of 20 MeV after they passed through the entire plasma region versus the microwave field phase, which was biased with respect to the phase of a periodic sequence of electron bunches. Unfortunately, with a klystron whose nominal microwave power was about 20 MW, the maximum microwave power did not exceed ~100 kW because of the low electric strength of the waveguide. Also, the intense scattering of electromagnetic waves in the open resonator did not allow us to concentrate the microwave energy and to achieve strong microwave fields at the axis of the plasma chamber. For this reason, the plasma density in our experiments was too low to achieve resonance interaction conditions. That is why our measurements of the electron energy spectrum at different beam currents (see Fig. 4) revealed no significant difference in the spectral distribution of the beam electrons.

By increasing the plasma density at the expense of the constant voltage component of a pulsed modulator while simultaneously feeding microwave and high-voltage pulses, we observed that the electron beam current became completely independent of the wave phase. This effect can be explained as being due to the high voltages and high currents generated by a pulsed modulator: after switching on the modulator, the microwave discharge was observed to decay, because the constant component of the plasma current destroyed the spatial periodicity of the distribution of the electron plasma density; as a result, the electron beam current became independent of the wave phase. This phenomenon can be used to obtain indirect estimates of the amplitude of the microwave field generated in the plasma. Under the coherent interaction conditions (Fig. 4), the fraction of the scattered (absorbed) beam

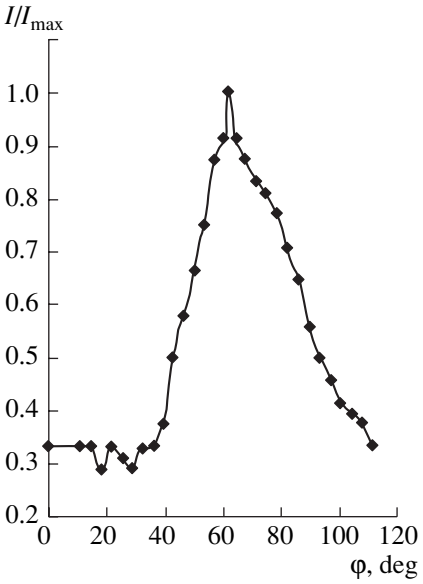

Fig. 4. Current of the electrons of an injected 20-MeV beam that pass through the plasma vs. the phase of the microwave field. The plasma was produced by a microwave pulse with a power of about $P_{puls} \sim 100$ kW. The phase of the microwave field was biased with respect to the phase of a periodic sequence of electron bunches that were formed and accelerated to 20 MeV by the same microwave pulse in the accelerating sections of the linac.

current in a microwave field with a comparatively small amplitude (<0.05 of the amplitude of the microwave field that was used to accelerate the beam) amounted to 70–80%. In this case, the relative increase in the current can attain 10% per degree of the phase of the microwave field. This effect can find applications, in particular, in fusion devices in which the plasma is heated by high-current relativistic electron beams [3]. In closed electrodynamic systems, varying the amplitude of the microwave field and biasing its phase with respect to the phase of a periodic sequence of electron bunches provides more efficient control of the generation of potential waves without energy losses due to the excitation of radiation at the combination frequencies. The strong coupling of the phase of the oscillations at the combination frequencies to the phase of the original microwave field can provide optimum interaction conditions (the polarization losses change sign [12, 13]) for raising the wakefield amplitude. Also, under the coherent interaction conditions, the so-called zero method makes it possible to find the relation between the beam and plasma parameters, i.e., to estimate the beam–plasma interaction efficiency. In our experiments, a 20-MeV electron beam was completely scattered (absorbed) over a distance of about 10–20 cm (with allowance for the nonuniform character of ionization) in the plasma chamber, thereby providing evidence of the possible onset of strong microwave fields (both transverse and longitudinal). Hence, the plasma experi-

enced both internal and external forces exerted by the electron beam and microwave pulse, respectively.

The revealed strong coherent dependence of the current of a relativistic electron beam on the phase of the microwave field holds promise for increasing the electron acceleration rate through the direct excitation of high-power parametric oscillations [14]. The pump frequency ω_{pump} (the same as the frequency of the plasma-producing microwave field) can generally be higher than (or equal to) $n\omega_m$, where ω_m is the frequency of the accelerating field or, equivalently, the modulation frequency of an electron beam. This relationship between the frequencies can play an important role at high plasma densities. It is well known that the most stable parametric resonance occurs under the condition $\omega_{pump} = 2\omega_m$. This condition is especially important because the difference combination frequency is equal to the frequency of the accelerating field, $\omega_{comb} = \omega_{pump} - \omega_m = \omega_m$ [15]. The plasma excitation by high-power microwaves at the second harmonic of the accelerating field can be achieved through frequency multiplication followed by the amplification of the input signal power. Controlling the amplitude of the microwave field under the coherent interaction conditions makes it possible to equate the frequencies, $\omega_m = \omega_p$ (where ω_p is the plasma frequency), i.e., to achieve the resonant interaction conditions. For higher plasma densities (e.g., those corresponding to the optical range), the coherent interaction condition $\omega_{pump} = 2\omega_m$ can be achieved by using the free electron laser (FEL) scheme [3, 16]. Hence, in the three-wave approximation, the energy of Langmuir oscillations, the wakefield of a periodic sequence of electron bunches, and the pump field can act to enhance the wake potential (provided that the waves are properly phased) and thus increase the electron acceleration rate.

ACKNOWLEDGMENTS

We are grateful to V.S. Airapetyan and other collaborators from the synchrotron linear accelerator for their help in carrying out the experiments and to A.G. Khachatryan for fruitful remarks in discussing the experimental results. This work was supported in part by the International Science and Technology Center, project no. A-13.

REFERENCES

1. Ya. B. Fainberg, Proc. Symp. CERN **1**, 84 (1956).
2. Ya. B. Faĭnberg, Fiz. Plazmy **13**, 607 (1987) [Sov. J. Plasma Phys. **13**, 350 (1987)].
3. Ya. B. Faĭnberg, Fiz. Plazmy **20**, 613 (1994) [Plasma Phys. Rep. **20**, 549 (1994)].
4. Ya. B. Faĭnberg, Fiz. Plazmy **23**, 275 (1997) [Plasma Phys. Rep. **23**, 251 (1997)].
5. A. Ts. Amatuni, M. R. Magometov, É. V. Sekhposyan, and S. S. Élbakyan, Fiz. Plazmy **5**, 85 (1979) [Sov. J. Plasma Phys. **5**, 49 (1979)].
6. A. Ts. Amatuni, É. V. Sekhposyan, and S. S. Élbakyan, Fiz. Plazmy **12**, 1145 (1986) [Sov. J. Plasma Phys. **12**, 662 (1986)].
7. A. K. Berezin, Ya. B. Faĭnberg, L. I. Bolotin, *et al.*, Zh. Éksp. Teor. Fiz. **63**, 861 (1972) [Sov. Phys. JETP **36**, 453 (1973)].
8. P. Chen, J. M. Dawson, R. W. Huff, and T. Katsouleas, Phys. Rev. Lett. **54**, 693 (1985).
9. J. B. Rosenzweig, D. B. Cline, B. Cole, *et al.*, Phys. Rev. Lett. **61**, 98 (1988).
10. A. K. Berezin, Ya. B. Faĭnberg, V. A. Kiselev, *et al.*, Fiz. Plazmy **20**, 663 (1994) [Plasma Phys. Rep. **20**, 596 (1994)].
11. Ya. B. Fainberg, N. I. Aizatskii, V. A. Balakirev, *et al.*, in *Proceedings of the XV International Workshop on Charged-Particle Accelerators, Alushta, 1997.*
12. Yu. M. Aliev, L. M. Gorbunov, and R. R. Ramazashvili, Zh. Éksp. Teor. Fiz. **61**, 1477 (1971) [Sov. Phys. JETP **34**, 785 (1972)].
13. É. A. Akopyan and G. G. Matevosyan, Fiz. Plazmy **10**, 648 (1984) [Sov. J. Plasma Phys. **10**, 378 (1984)].
14. V. P. Silin, *Parametric Influence of High Power Radiation on Plasma* (Nauka, Moscow, 1973).
15. V. M. Lopukhin and A. S. Roshal', *Electron-beam Parametric Amplifiers* (Sov. Radio, Moscow, 1968).
16. V. I. Miroshnichenko, Ya. B. Faĭnberg, and A. E. Volkov, Fiz. Plazmy **20**, 620 (1994) [Plasma Phys. Rep. **20**, 555 (1994)].

Translated by G. V. Shepekina

Plasma Physics Reports, Vol. 27, No. 6, 2001, pp. 511–519. Translated from Fizika Plazmy, Vol. 27, No. 6, 2001, pp. 540–549.

BEAMS IN PLASMA

Calculation and Optimization of Plasma-Optic Focusing Devices

V. I. Butenko and B. I. Ivanov

Kharkov Institute of Physics and Technology, National Science Center, Akademicheskaya ul. 1, Kharkov, 61108 Ukraine
e-mail: ivanovbi@kipt.kharkov.ua

Received August 16, 2000

Abstract—(i) The focusing of an ion beam by a Morozov lens formed by a current ring in a plasma is calculated using an exact expression for the magnetic field and taking into account the nonparaxial character of the focused beam. The possible ways of optimizing such a lens are considered. (ii) Different versions of extended plasma-optic devices in which spherical aberrations are minimized are analyzed. It is proposed to optimize extended plasma-optic devices by changing the magnetic field from the entrance end to the exit end of the solenoid in such a way that the boundary magnetic surface always coincides with the boundary surface of the focused beam. It is shown that, under the same conditions, the focusing power of the optimized devices is one to two orders of magnitude higher than that of traditional thin plasma lenses. (iii) The problem of creating a magnetic field whose strength is optimized as a function of the longitudinal coordinate is solved by the Tikhonov regularization method. (iv) An extended plasma-optic device with an optimized solenoid for focusing 1-MeV ion beams is calculated, and the ion trajectories in the device are traced. (v) It is proved expedient to develop special-purpose computer codes aimed at modeling and optimizing the existing and planned experimental plasma-optic focusing devices. © *2001 MAIK "Nauka/Interperiodica".*

1. INTRODUCTION

Investigations on focusing intense ion beams of moderate and high energies play an important role in plasma physics and controlled fusion. These investigations are related, in particular, to the problems of inertial light- and heavy-ion confinement fusion, colliding-beam fusion reactors, examination of the resistance of the first wall of a reactor to radiation damage, and study of plasma heating in a reactor by injecting neutral beams produced by the charge exchange of intense ion beams. The problems of focusing intense ion beams are also important for nuclear physics, high-energy physics, accelerator physics and designs, and beam technologies. An essential feature of the focusing of intense ion beams is that, in order for the beam to be indestructible, it should be completely charge-neutralized. For these purposes, it is expedient to use plasma-optic focusing devices (lenses) whose development was initiated by A.I. Morozov *et al.* [1–3] and is now being successfully continued by A.A. Goncharov *et al.* [4–7]. At present, the main problem in this area is that of optimizing such lenses, i.e., minimizing spherical aberrations and maximizing the focusing power.

Here, we continue to study these optimization problems. In Section 2, we calculate the focusing of an ion beam in a Morozov lens formed by a current loop in a plasma and by a set of external ring electrodes. Since this problem is very important for calculating electrostatic plasma lenses, we investigate it more thoroughly than in [3] by taking into account the nonparaxial character of the focused beam and by using an exact expression for the magnetic field.

In Sections 3 and 4, we propose and analyze different versions of extended plasma-optic devices in which the ring electrodes are placed at the side cylindrical surface near the two ends of the device, i.e., in the regions where the magnetic field lines enter and leave the solenoid. In this case, the spherical aberrations are the lowest. For a uniform solenoid (which is considered in Section 3), the focusing length is independent of the radius of the injected beam; this provides the possibility of focusing large-aperture beams. In Section 4, we propose to optimize extended plasma-optic devices by changing the magnetic field from the entrance end to the exit end of the solenoid in such a way that the radius of the boundary magnetic surface always coincides with the radius of the focused beam: as the magnetic surfaces converge, the focusing field becomes stronger, thereby increasing the focusing power of the device. We solve the problem analytically in the paraxial approximation. We show that, under the same conditions, the focusing power of extended plasma-optic devices is one to two orders of magnitude higher than that of traditional thin plasma lenses.

In order to calculate the parameters of the solenoid and trace ion trajectories, we developed special-purpose computer codes. This is the subject of Section 5. The problem of generating nonuniform axisymmetric magnetic fields with a prescribed dependence on the longitudinal coordinate belongs to the class of the so-called ill-posed problems in the sense that, for a given

1063-780X/01/2706-0511$21.00

accuracy, it has an infinite number of solutions. We solve the problem by the Tikhonov regularization method, which implies that, among the possible solutions, it is necessary to choose the solution optimized for a certain criterion. Specifically, we optimize the solution with respect to the thickness of solenoidal coils of rectangular cross section. We calculate an extended plasma-optic device with an optimized magnetic field for focusing a 1-MeV ion beam and follow the ion trajectories. Since, in any cross section of such a device, the focusing force acting on an ion is proportional to its distance from the axis, there are no spherical aberrations.

2. MOROZOV LENS FORMED BY A CURRENT RING

In a Morozov plasma electrostatic lens, the magnetic surfaces are equipotential surfaces of the electric field [1, 3]. Usually, Morozov lenses are treated in axisymmetric geometry under the assumption that there is no current transverse to the magnetic field and that the strength of the electric field and its spatial distribution in a plasma are governed completely by the magnetic field geometry and the boundary condition on the externally defined electric potential Φ in the form of a continuous function $\Phi(R, z)$, where R is the radius of a cylindrical surface. In practice, the electric potentials are generated by discrete ring electrodes, which thus give rise to a system of charged magnetic surfaces in the plasma. Although the experimental investigations [2–7] on the whole confirm the theoretical model developed in [1, 3], they leave unanswered certain questions (in particular, the reasons for fairly significant spherical aberrations and how to remove them). The experimental experience gained in this area allows us to suppose that the possible corrections to the theory can be taken into account in the form of additional aberrations.

Different plasma-optic problems were studied theoretically in a paper by Morozov and Lebedev [3]. In particular, they considered axisymmetric electrostatic plasma lenses. Among other things, they estimated the focal length of the simplest plasma lens formed by a current-carrying ring. Since this problem is very important for practical calculations of electrostatic plasma lenses, we analyze it in more detail by taking into account the nonparaxial character of the focused beam and by using an exact expression for the magnetic field.

The azimuthal component of the vector potential of the magnetic field of a ring with radius a_c and current J has the form (see, e.g., [8])

$$A_\varphi = \frac{4J}{ck}\sqrt{\frac{a_c}{r}}\left[\left(1-\frac{k^2}{2}\right)K(k)-E(k)\right],$$
$$k^2 = \frac{4a_c r}{(a_c+r)^2+(z-l)^2}, \quad (1)$$

where l is the coordinate along the z-axis, c is the speed of light, and K and E are complete elliptic integrals of the first and second kind. Following [3], we introduce the magnetic flux function $\psi = rA_\varphi$, so that the equation $\psi(r, z) = \text{const}$ serves as an equation for the magnetic surfaces and also an equation for the magnetic field lines in the (r, z) plane. (The calculated families of the magnetic field lines will be presented below in the corresponding figures.) In a Morozov lens, the equipotential magnetic surfaces are described by the relationship [3] $\Phi = \Phi(\psi)$, where Φ is the electric field potential.

We express the components of the electric and magnetic fields in terms of ψ and A_φ:

$$E_r = -\frac{d\Phi}{d\psi}\frac{d\psi}{dr}, \quad E_z = -\frac{d\Phi}{d\psi}\frac{d\psi}{dz} = -\frac{d\Phi}{d\psi}r\frac{dA_\varphi}{dz},$$
$$H_r = -\frac{dA_\varphi}{dz}, \quad H_z = \frac{1}{r}\frac{d}{dr}rA_\varphi, \quad (2)$$

which gives

$$E_z = \frac{d\Phi}{d\psi}H_r r, \quad E_r = -\frac{d\Phi}{d\psi}H_z r. \quad (3)$$

Let us consider a number of practically important profiles of the electric potential Φ as a function of the magnetic flux ψ.

2.1. Case 1

Let the radial electric field in the plane $z = z_0$ of the current ring be specified by the normalized linear distribution

$$E_r(r, z_0) = E_r(r_1, z_0)\frac{r}{r_1} = E_{r1}\frac{r}{r_1}. \quad (4)$$

In practice, this distribution can be achieved directly by specifying the electric potential distribution at the electrodes adjacent to the plasma boundary and by measuring the distribution of the electric field strength in the plasma. (The method of local contactless measurements of the electric field strength was proposed and justified experimentally by Ivanov *et al.* [9].)

In this paper, the electric field in the plasma is obtained by calculation. The functions $\Phi = \Phi(\psi)$ and $d\Phi/d\psi$ are specified parametrically,

$$\begin{cases}\Phi(\psi(r, z_0)) = \dfrac{1}{2}\dfrac{E_{r1}}{r_1}r^2,\\ \psi(r, z_0) = rA_\varphi(r, z_0)\end{cases}$$
$$\begin{cases}\dfrac{d\Phi(\psi(r, z_0))}{d\psi} = -\dfrac{E_{r1}}{r_1 H_z(r, z_0)},\\ \psi(r, z_0) = rA_\varphi(r, z_0)\end{cases} \quad (5)$$

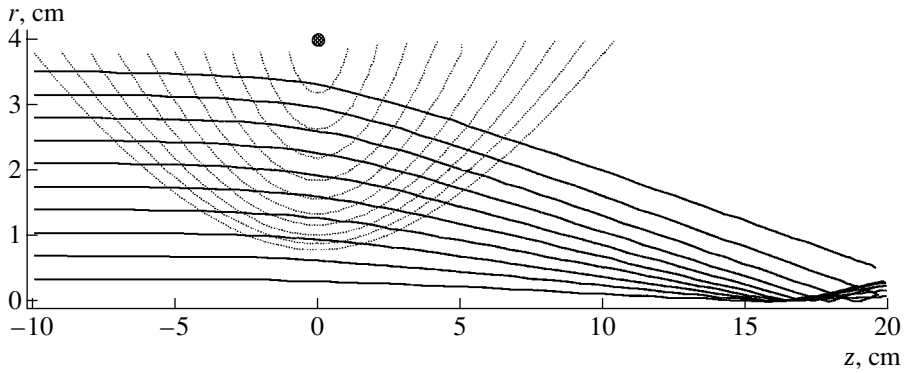

Fig. 1. Proton trajectories during the focusing of a 20-keV proton beam with an initial radius of 3.5 cm in a Morozov lens with a 4-cm-radius current ring at $z = 0$ and with 4-cm-radius electrodes. The radial distribution of the electric field strength at $z = 0$ is $E_r = A_1 r$, where $A_1 = 285$ V/cm^2.

On the cylindrical surface of radius R_{e1}, we impose the following boundary condition on the electric potential distribution (in practice, this condition can be achieved with a set of ring electrodes [4–7]):

$$\Phi(\psi(R_{e1}, z)) = \Phi(R_{e1} A_\varphi(R_{e1}, z)). \quad (6)$$

The motion of beam ions with mass M and charge q is described by the equations

$$M\frac{d^2 r}{dt^2} = -qE_r, \quad M\frac{d^2 z}{dt^2} = -qE_z. \quad (7)$$

In the case at hand ($H_r \sim H_z$), the magnetic field effects can be neglected in an energy range of about 10 keV/nucleon and, for the paraxial ions, in an energy range of about 1 MeV/nucleon.

The initial conditions at $t = 0$ are as follows:

$$z = z_0, \quad v_r = 0, \quad v_z = v_0, \quad r = r_0, \quad (8)$$

where the beam injection radius r_0 is changed from zero to a value smaller than the radius of the electrodes; $z_0 = -10$ cm; and v_r and v_z are the radial and longitudinal components of the ion velocity, respectively.

The ion trajectories can be followed by using relationships (4)–(6) with the electric field found from formulas (3) and by solving the equations of motion (7) with the initial conditions (8).

Figure 1 shows the ion trajectories computed in the case at hand. We can see that the best-focused ions are the paraxial ones. The nonparaxial ions (which dominate the beam because their number is proportional to the injection radius) are focused to a much lesser extent (i.e., underfocused); moreover, the larger the radius at which the nonparaxial ions are injected, the farther away the point of intersection of their trajectories with the z-axis from the origin of the coordinates. This stems from the fact that, due to the curvature of the magnetic surfaces, the nonparaxial ions injected at large radii experience strong focusing forces over an insufficiently long time. (In Section 3, we show that, in a magnetic field whose surfaces are concentric cylinders and in an electric field such that $E_r \propto r$, the ion focusing is free of spherical aberrations.)

Case 1 can be optimized as follows. Formula (4) for the radial electric field is supplemented with the second- and third-order (in r) terms. At this point, the coefficients of these terms were merely adjusted by the trial and error method. With the radial electric field optimized in such a manner, the focusing is seen to be much better (Figs. 2, 3): for the injection current $I = 1$ A, the maximum current density is $j = 170$ A/cm^2, the half-width of the focal spot is $\delta r = 0.03$ cm, and the relative fraction of the beam ions focused to the half-width of the spot is about 30%.

In principle, the problem of optimizing the electric field distribution can be solved by using a specially developed algorithm.

2.2. Case 2

In [3], Morozov and Lebedev very briefly considered a plasma lens formed by a current ring in an electric field with the potential distribution

$$\Phi = b\psi = brA_\varphi, \quad \text{where} \quad b = \text{const}. \quad (9)$$

They estimated the focal length of this lens to be $F = a_c W/2q\Phi_0\theta$, where W is the ion kinetic energy, Φ_0 is the ring potential, and the dimensionless parameter $\theta \approx 1$ depends on the geometry of the system.

Here, we consider this problem (with linearly related Φ and ψ) in more detail by applying computer modeling. We impose the boundary condition by specifying the potential distribution over a cylindrical surface of radius R_{e2}:

$$\Phi(R_{e2}, z) = bR_{e2} A_\varphi(R_{e2}, z). \quad (10)$$

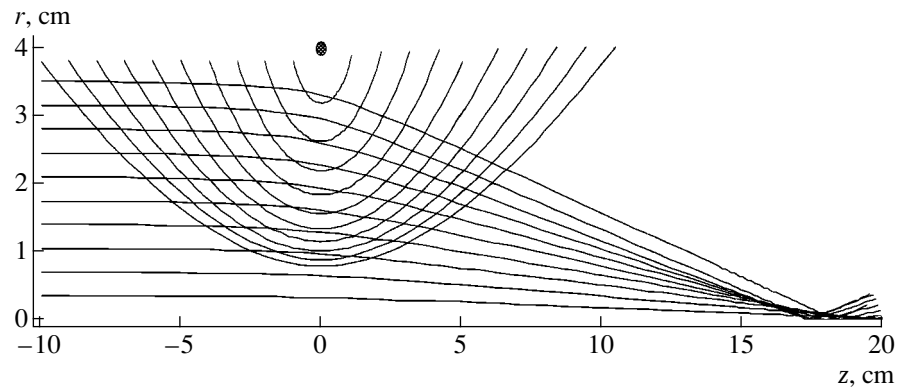

Fig. 2. Proton trajectories for the same conditions as in Fig. 1 but for an optimized radial distribution of the electric field strength (in V/cm) at $z = 0$: $E_r = A_1 r + A_2 r^2 + A_3 r^3$ with $A_1 = 210$ V/cm^2, $A_2 = 10.5$ V/cm^3, and $A_3 = 19.5$ V/cm^4.

According to formulas (3) and (9), the electric and magnetic fields are related by

$$E_z = brH_r, \quad E_r = -brH_z. \tag{11}$$

The constant b, which governs the focusing power of the lens, is determined by the given electric field strength E_{r2} produced by the electrodes at the point (r_2, z_0):

$$b = -E_{r2}/r_2 H_z(r_2, z_0). \tag{12}$$

These relationships are supplemented with the equations of motion (7) and the initial conditions (8).

The ion trajectories computed in case 2 are presented in Fig. 4, which shows that (as in case 1) the best-focused ions are the paraxial ones. However, in case 2, the nonparaxial ions are over-focused; moreover, the larger the radius at which they are injected, the closer the point of intersection of their trajectories with the z-axis is to the origin of the coordinates. This stems from the fact that the potential Φ, which is proportional to rA_φ, increases sharply when approaching the current loop surface.

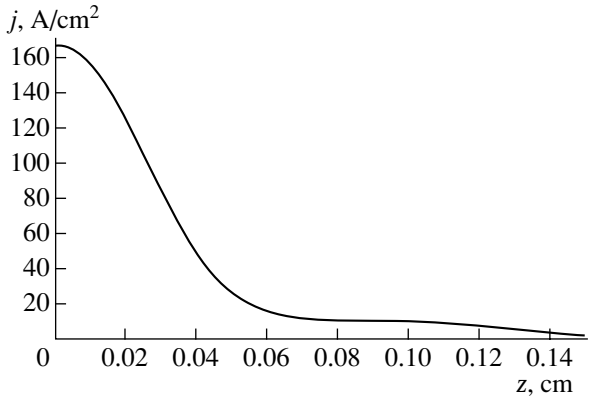

Fig. 3. Radial profile of the proton current density in the cross section in which the radius of the focused beam is the smallest (for the same conditions as in Fig. 2).

Case 2 can be optimized as follows. The condition for the focusing to be ideal is the requirement that the focusing force be proportional to the deviation of an ion from the symmetry axis in any cross section of the lens, i.e., $E_r \propto r$. Formula (11) converts this requirement into the equality $H_z(r) = \text{const}$, which holds for long solenoids (see Sections 3, 4). In case 2, the focusing can be optimized by reducing the relative role of the immediate vicinity of the current ring, or, equivalently, by increasing the radius of the ring (while keeping the radius of the electrodes equal to the initial beam radius) and the focusing length (by decreasing the constant b). The corresponding simulations show that, for $I = 1.3$ A, $j = 135$ A/cm^2, and $\delta r = 0.045$ cm, the relative fraction of the beam ions focused to the half-width of the focal spot is about 40% (Figs. 5, 6).

It should be noted that the field superposition principle makes it possible to readily generalize the problem with a single current ring to the problem with an arbitrary solenoid, in which case one can devise a special computer model for a particular experimental lens in order to optimize its parameters and modes of operation.

3. EXTENDED PLASMA-OPTIC LENS IN A UNIFORM MAGNETIC FIELD

In order to increase the focusing power and to lower the spherical aberrations, it is expedient to use extended plasma-optic devices (which will also be referred to as lenses for the sake of brevity). In an extended focusing device (a device in which the length of the solenoid is much larger than its diameter and the end solenoidal fields have an insignificant impact on the ion focusing), the ring electrodes can be installed at the side cylindrical surface near the two ends, i.e., in the regions where the magnetic field lines enter and leave the solenoid. In order for the end regions where

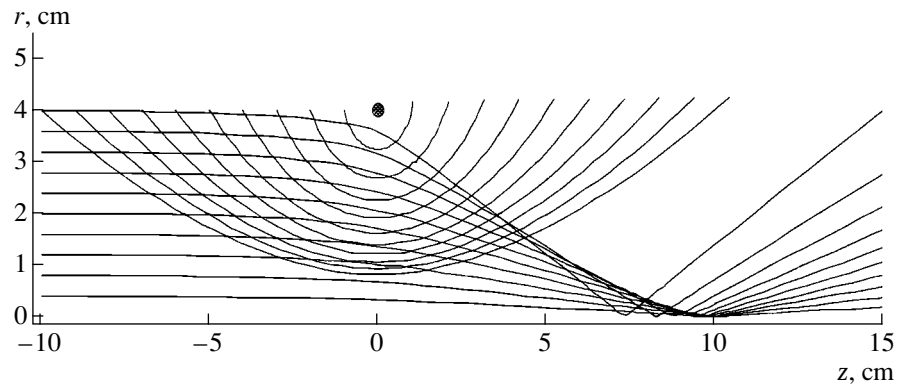

Fig. 4. Proton trajectories during the focusing of a 20-keV proton beam with an initial radius of 3.9 cm in a Morozov lens with a 4-cm-radius current ring at $z = 0$ and with 4-cm-radius electrodes. The beam is focused in the electric field with the given potential distribution Φ [V] = brA_φ with $b = 6$ V/Oe cm^2.

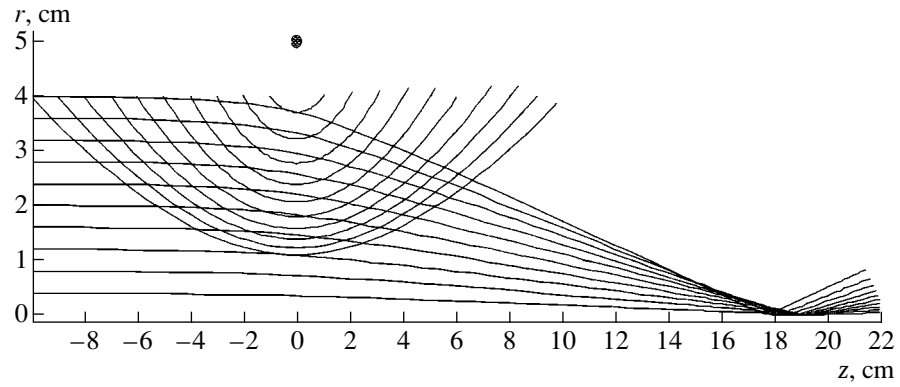

Fig. 5. Proton trajectories for the same conditions as in Fig. 4 but for a current ring of radius 5 cm and for the optimized radial distribution of the electric potential (in V): $\Phi = brA_\varphi$ with $b = 3$ V/Oe cm^2.

the ring electrodes are to be installed to be as small as possible, it is expedient to use oppositely directed coils [5–7], thereby increasing the deviation of the magnetic field lines from the symmetry axis. In order to minimize the spherical aberrations (e.g., when focusing a large-aperture beam onto a small spot), it is expedient to consider whether it is possible to install a set of thin concentric electrodes in the planes orthogonal to the symmetry axis near the entrance and exit ends of the device in the regions where the magnetic field is uniform. In this case, it is desirable for an array of beam-forming electrodes of an ion injector (e.g., of the MEVVA type [10]) to be geometrically similar to a set of lens electrodes and to shield the ring electrodes from the ion flux. It should be noted that ion implantation technologies allow no thermal damage of the samples, so that the lens electrodes will not be destroyed. However, when studying the thermal effects of the focused beam on the sample, one should keep in mind that the density of the ion flux onto the electrodes is lower than that onto the sample.

The focusing power of a plasma-optic lens has the form

$$F_e = qE_r = -q\frac{\partial\varphi(r,z)}{\partial r}. \quad (13)$$

With the electrodes placed at the ends of the solenoid (or near the ends), it is possible to create an electric

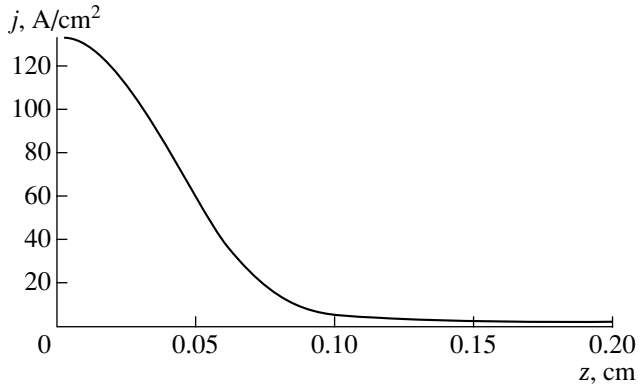

Fig. 6. Radial profile of the proton current density in the cross section in which the radius of the focused beam is the smallest (for the same conditions as in Fig. 5).

field with the radial potential profile $\varphi = \varphi_0 r^2/a_0^2$ (where the initial radius a_0 of the boundary magnetic surface is equal to the initial beam radius and φ_0 is the potential at the boundary surface) over almost the entire extended uniform lens. In this case, the motion of the focused ions is described by the equation

$$\frac{d^2r}{dz^2} + k_M^2 r = 0, \quad r = r_0 \cos k_M z, \tag{14}$$

where $k_M^2 = 2q\varphi_0/(Mv^2a_0^2)$ and r_0 is the beam injection radius, so that the focusing length is equal to

$$L_f = \pi(2k_M)^{-1} = \frac{\pi v a_0}{2}\sqrt{\frac{M}{2q\varphi_0}}. \tag{15}$$

If the length of a lens is such that $l < L_f$, then we have $l_f = l + k_M^{-1}\cot k_M l$; for $k_M l \ll 1$ (e.g., when the potential of the injector is much higher than the potential of the lens), we arrive at the focusing length $l_f = (k_M^2 l)^{-1}$ of a thin lens. Note that the above expressions for the focusing length are independent of the injection radius, thereby providing the possibility of focusing large-aperture beams.

4. EXTENDED PLASMA-OPTIC LENS IN AN OPTIMIZED MAGNETIC FIELD

An extended plasma-optic lens can be optimized by increasing the magnetic field strength from the entrance end to the exit end of the lens in such a way that the boundary magnetic surface always coincides with the boundary surface of the beam, provided that, at the entrance end, the radius of the boundary magnetic surface is equal to the beam radius. As the magnetic surfaces converge, the focusing electric field strength increases, thereby increasing the resulting efficiency and focusing power of the lens.

When solving the related optimization problem, we treat both the beam ions and magnetic field in the paraxial approximation. The equation for the paraxial magnetic surfaces has the form

$$a^2(z) = \frac{a_0^2 B(0)}{B(z)}, \tag{16}$$

where $a(z)$ is the varying radius of a magnetic surface and $B(z)$ is the longitudinal magnetic field at the axis of the lens. The quantities $B(0)$ and a_0 are determined from the boundary conditions at $z = 0$.

Clearly, Eq. (16) implies that, if some of the magnetic surfaces are equidistant at a certain cross section of the lens, they will remain equidistant everywhere, but the distance between them may change. Consequently, the parabolic radial potential profile specified at the entrance to the solenoid (at $z = 0$) will also remain parabolic everywhere, thereby providing the possibility of creating a lens free of spherical aberrations, because, in this case, the electric force that directs an ion toward the axis is proportional to the distance between the ion and the axis. As a result, for the parabolic radial potential profile $\varphi = \varphi_0 r^2/a_0^2$ of the electric field produced by the electrodes (here, a_0 is the radius of the boundary magnetic surface at $z = 0$ and φ_0 is the potential at the boundary surface), we can use Eq. (16) to obtain the following equation for the motion of the focused beam ions:

$$\frac{d^2r}{dz^2} + \frac{B(z)}{B(0)}k_M^2 r = 0, \tag{17}$$

where $k_M^2 = \dfrac{2q\varphi_0}{Mv^2a_0^2}$.

Generally, the trajectories of the focused ions can be traced only by computer calculations.

In a magnetic field with a converging boundary surface, some of the ions (specifically, those that are injected at large distances from the lens axis) may fail to enter the focusing channel and thus will not be focused to a common focal spot. In order to focus all of the beam ions to a focal spot, it is necessary to optimize the shape of the magnetic surface bounding the focusing channel. Then, one needs to calculate the parameters of the solenoid that produces the optimum magnetic surface and to follow the trajectories of the focused ions. The desired magnetic surface is determined by the condition that its radius a be equal to the radius R of the focused beam. The function $R(z)$ and, by virtue of Eq. (16), the function $B(z)$ satisfy the equation

$$\frac{d^2R}{dz^2} + \frac{\kappa}{R} = 0, \tag{18}$$

where $\kappa = \dfrac{2q\varphi_0}{Mv^2}$.

Using the initial conditions $R = R_0$ and $R' = R_0'$ at $z = 0$ and making the replacement $t^2 = (R_0'^2/\kappa) - 2\ln R/R_0$, we arrive at the following solution to Eq. (18):

$$z = \pm\sqrt{\frac{\pi}{2\kappa}}R_0 \exp\left(\frac{R_0'^2}{2\kappa}\right) \times \left[\Phi_p\left(\sqrt{\frac{R_0'^2}{\kappa} - 2\ln\frac{R}{R_0}}\right) - \Phi_p\left(\frac{R_0'}{\sqrt{\kappa}}\right)\right], \tag{19}$$

where Φ_p is the probability integral. The radius of the focusing channel decreases to a certain value R_g at the exit end z_g from the lens. Then, the charge-neutralized

beam ions leave the lens and continue to be focused by inertia. When all of the beam ions are injected parallel to the lens axis, the coordinate of the focal spot is equal to

$$z_f = \sqrt{\frac{\pi}{2\kappa}} R_0 \Phi_p(\sqrt{2\ln R_0/R_g}) + \frac{R_g}{\sqrt{2\kappa \ln R_0/R_g}}. \quad (20)$$

As a numerical example, we consider the focusing of a 1-MeV beam of radius $R_0 = 3$ cm. Let the potential φ_0 at the boundary magnetic surface be equal to 5 kV. Then, we have $\kappa = 2q\varphi_0/(Mv^2) = \varphi_0/U = 0.005$, where U is the accelerating potential. As a result of focusing in converging magnetic surfaces, we arrive at the ratio $R_0/R_g = 2.72$. Inserting this ratio into formula (20) yields the focusing length $z_f = 56$ cm, which is substantially shorter than that in a uniform lens. The shortening is especially pronounced for the focusing of diverging beams. The corresponding parameters of the solenoid and the associated ion trajectories were computed numerically (see below).

To conclude this section, we note that, as was mentioned in many papers (see, e.g., [1, 11]), the focusing length $L_f \propto (U/\varphi_0)^2$ in thin electron-plasma lenses is much shorter than $L_f \propto (U/\varphi_0)$ in vacuum electrostatic lenses. Our formulas (15) and (20) show that, in extended electron-plasma lenses, the focusing length obeys the dependence $L_f \propto (U/\varphi_0)^{1/2}$ and thus is even shorter.

5. CALCULATION OF A SOLENOID GENERATING THE DESIRED PREFORMED MAGNETIC FIELD

5.1. The creation of axisymmetric magnetic fields with the given dependence on the longitudinal coordinate is important for some applications in plasma physics, the physics of charged-particle beams, etc. One significant problem is the so-called reverse (or reconstruction) problem, which implies the reconstruction of the original solenoid configuration from the known profile of the magnetic field along the z-axis. Similar problems belong to the class of ill-posed problems in the sense that, for a given accuracy, each of them has an infinite number of solutions. We solve the problem by the Tikhonov regularization method [12], which implies that, among the possible solutions, it is necessary to choose the solution that satisfies certain criteria.

As a rule, magnetic fields with the above longitudinal profile are created by sectioned solenoids, i.e., solenoids composed of discrete coaxial sections (coils). In the literature devoted to this problem (see, e.g., [13]), the sought-for parameters were the current densities in the solenoidal coils. This is the simplest formulation of the problem, because the equation for the strength of the solenoidal magnetic field is linear in the current density. However, for a solenoid with a sufficiently large number of coils, the problem reduces to that of solving a set of nonlinear equations and thus may turn out to be ill-posed, which may lead to some loss of computational accuracy. This approach also does not hold promise from a technical viewpoint because each solenoidal coil requires its own power supply.

Here, we turn to the Tikhonov regularization method in order to solve a more general problem, specifically, we look for the parameters of the solenoidal coils in which the magnetic field strength is nonlinear, e.g., the coil thicknesses, the lengths of the coils, and their inner radii.

5.2. We consider a discrete (sectioned) solenoid consisting of n coaxial coils with arbitrary cross sections. Let the solenoid create a magnetic field whose strength over the interval $[a, b]$ on the solenoid axis is described by the function $f(z)$ with a given accuracy δ.

Let the magnetic field strength created by the ith solenoidal coil at the point z be described by the function $H_i(N_i, z)$, which depends on the geometric shape of this coil as well as on its dimensions and its position relative to this point through the parameter N_i. Then, the total magnetic field strength at the solenoid axis can be written as

$$B(z) = \sum_{i=1}^{n} H_i(N_i, z). \quad (21)$$

We define the deviation of $B(z)$ from $f(z)$ as

$$\rho(B, f) = \left\{\int_a^b [B(z) - f(z)]^2 dz\right\}^{1/2}. \quad (22)$$

For a given accuracy, the problem of searching for the desired set of coils has an infinite number of solutions; for a sufficiently large number of coils, the solutions are unstable against small variations in the initial parameters. Consequently, among all of the solutions satisfying the condition $\rho(B, f) \le \delta$, where δ is a given number, it is necessary to choose the solution optimized in a certain criterion (e.g., in the volume of the solenoidal coils or the power consumption). The problem at hand can be formulated as follows [12]: it is necessary to find the parameter set $(N_1, N_2, \ldots, N_n)$ that minimizes the functional

$$F(N_1, \ldots, N_n, \beta) = \int_a^b \left[\sum_{i=1}^{n} H_i(N_i, z) - f(z)\right]^2 dz + \beta\Omega(N_1, \ldots, N_n). \quad (23)$$

Here, $\Omega(N_1, \ldots, N_n)$ is the stabilizing functional, which is determined by the optimization criterion, and β is the regularization parameter. The conditions for functional (23) to be minimum, $\frac{\partial F(N_1, \ldots, N_n, \beta)}{\partial N_k} = 0$, yield the set of nonlinear equations

$$\int_a^b \left[\sum_{i=1}^{n} H_i(N_i, z) - f(z)\right] \frac{\partial H_k}{\partial N_k} dz + \beta \frac{\partial \Omega}{\partial N_k} = 0, \quad (24)$$

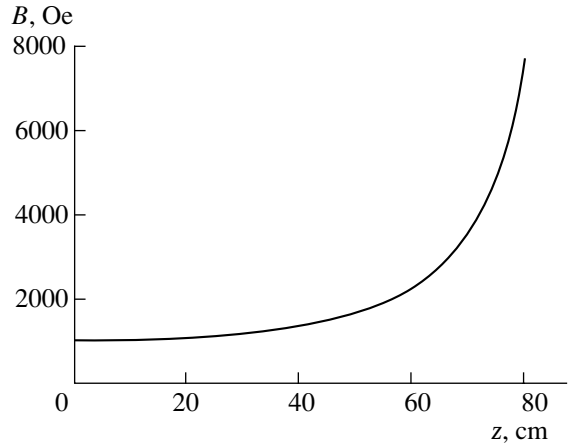

Fig. 7. Optimized longitudinal profile of the magnetic field strength at the solenoid axis in an extended plasma-optic lens.

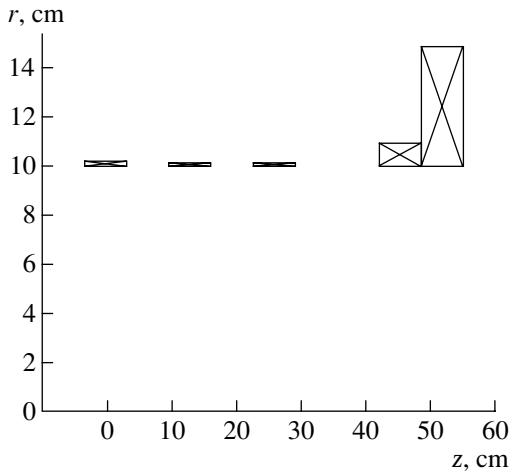

Fig. 8. Configuration of the solenoid creating a magnetic field with the desired profile $B(z)$.

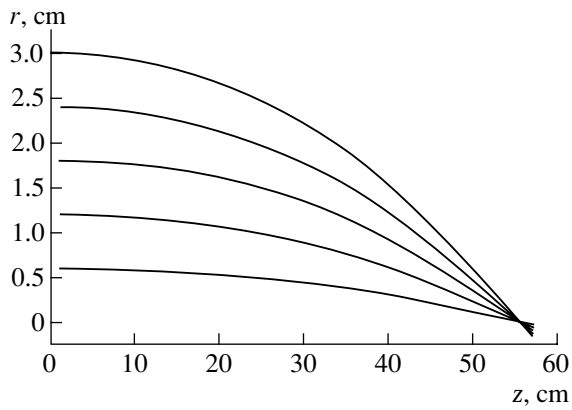

Fig. 9. Ion trajectories in an extended lens with an optimized magnetic field.

which can be solved by one of the gradient methods (see, e.g., [14]).

5.3. The method for solving the problem of calculating the solenoid consists of the following steps: the choice of the quantities governed by the parameters of the physical device; the choice of the initial approximation N_i^0 and the regularization parameter β in such a way that the iterative procedure converges; the solution of Eqs. (24) by iteration with a given accuracy; the adjustment of both the initial approximation (it is set equal to the current value of the sought-for parameter) and the regularization parameter β (if the iterative procedure converges too slowly, the parameter β is decreased); the reiteration of Eqs. (24); and so on until the desired solution is achieved.

We applied the above method to calculate a solenoid that is composed of coils with rectangular cross sections and creates a magnetic field shaped in a desired fashion. As the sought-for parameters N_i, we adopted the coil thicknesses $d_i = R_i - r_i$, in which case the approximating functions $H_i(d_i, z)$ and their first derivatives (in a Gauss system of units) have the form [15]

$$H_i(z) = \frac{2\pi J_i}{c}\left[(z-\zeta_i)\ln\frac{R_i+\sqrt{R_i^2+(z-\zeta_i)^2}}{r_i+\sqrt{r_i^2+(z-\zeta_i)^2}} - (z-a_i-\zeta_i)\ln\frac{R_i+\sqrt{R_i^2+(z-a_i-\zeta_i)^2}}{r_i+\sqrt{r_i^2+(z-a_i-\zeta_i)^2}}\right], \quad (25)$$

$$\frac{\partial H_i}{\partial d_i} = \frac{2\pi J_i}{c}\left[\frac{z-\zeta_i}{\sqrt{R_i^2+(z-\zeta_i)^2}} - \frac{z-a_i-\zeta_i}{\sqrt{R_i^2+(z-a_i-\zeta_i)^2}}\right]. \quad (26)$$

Here, J_i is the current density; ζ_i is the smallest coordinate of the cross sections of the coil; r_i and R_i are the inner and outer radii of the coil, respectively; and a_i is the coil length along the solenoid axis.

As the stabilizing functional, we adopted the squared Euclidean norm of the solution: $\Omega(d_1, \ldots, d_n) = \sum_{j=1}^{n}(d_j - d_j^0)^2$, where d_i^0 is the initial value of the sought-for parameter of the ith coil. This choice corresponds to the criterion of minimizing the total volume of the solenoidal coils. In each of the coils, the current density was taken to be the same in order to economize the wire for coils and to lower the power consumption in comparison with the solenoid in which the magnetic field with the desired longitudinal profile is created by redistributing the current between the coils. Also, the solenoid under consideration is easier to supply with power: the coils carrying the same currents can be connected in series and supplied from a common power source. All of the above factors will ultimately affect

the dimensions, weight, and cost of the resulting solenoid.

5.4. Here, we describe the computation of a solenoid aimed at creating a magnetic field with the desired longitudinal profile in the extended plasma-optic lens whose parameters were given in Section 4, in which we also presented the results of theoretical analysis and numerical calculation of this lens. The desired magnetic surface is determined from the condition that its radius a be everywhere equal to the radius R of the focused beam. In turn, the beam radius is found from Eq. (18) at $\kappa = 0.005$ with allowance for the initial conditions $R = R_0$, $R' = R_0' = 0$, and $B(0) = 1$ kOe at $z = 0$. In the paraxial approximation, the magnetic surface satisfies Eq. (16). From this equation and the corresponding initial conditions, we find the longitudinal profile of the magnetic field at the solenoid axis. For the lens under consideration, the magnetic-field profile is presented in Fig. 7. Then, we apply the above approach in order to determine the configuration of the solenoid that produces the magnetic field with the desired longitudinal profile $B(z)$ (Fig. 8). The main parameters of the solenoid (which is assumed to be supplied by power from a pulsed source) are as follows: the length is about 65 cm, the number of coils is equal to five, the inner coil radii are all equal to 10 cm, the length of each coil is 6.5 cm, and the mean current density over the cross section of each coil is 100 A/mm^2 (the coils are assumed to be made of a 65-mm-wide metal strip). The thicknesses of the coils (from the first to fifth) are 0.18, 0.12, 0.13, 0.95, and 4.92 cm. Over the entire solenoid, the relative error in approximating the magnetic field is no worse than $\Delta = 4 \times 10^{-2}$ (such an accuracy is quite sufficient for our purposes in the example at hand). Further optimization assumes the use of the solenoidal coils whose radii decrease as the radius of the focused beam decreases.

Figure 9 shows ion trajectories in a plasma-optic lens with an optimized magnetic field. In accordance with Sections 3 and 4, the ions are focused to the same point, because, in each cross section of the lens, the focusing force acting on each ion is proportional to the distance between the ion and the axis. Note that the focusing length $L_f = 56$ cm, which was calculated analytically in the previous section, is exactly equal to that obtained in this section by tracing the ion trajectories numerically.

In conclusion, we will say a few words about the usefulness of computer modeling of plasma-optic focusing devices. Our study demonstrates that, in this way, one inevitably will be faced with fairly involved computations, which include a preliminary choice of the geometric and electric parameters of the device, the analysis and reconstruction of two-dimensional magnetic and electric fields, tracing of the trajectories of charged particles in these fields, and the variations of these fields (and possibly other parameters) in order to minimize aberrations and to achieve the desired output characteristics of the focused beam. Such simulations require the development of special-purpose computer codes aimed at modeling particular plasma-optic configurations. Such numerical codes will make it possible to efficiently optimize the existing and planned experimental devices.

ACKNOWLEDGMENTS

We are grateful to A.A. Goncharov for fruitful discussions and useful remarks.

REFERENCES

1. A. I. Morozov, Dokl. Akad. Nauk SSSR **163**, 1363 (1965) [Sov. Phys. Dokl. **10**, 775 (1966)].
2. V. V. Zhukov, A. I. Morozov, and G. Ya. Shchepkin, Pis'ma Zh. Éksp. Teor. Fiz. **9**, 14 (1969) [JETP Lett. **9**, 9 (1969)].
3. A. I. Morozov and S. V. Lebedev, in *Reviews of Plasma Physics*, Ed. by M. A. Leontovich (Atomizdat, Moscow, 1974; Consultants Bureau, New York, 1980), Vol. 8.
4. A. A. Goncharov, A. N. Dobrovol'skiĭ, A. N. Kotsarenko, *et al.*, Fiz. Plazmy **20**, 499 (1994) [Plasma Phys. Rep. **20**, 449 (1994)].
5. A. A. Goncharov, I. M. Protsenko, and A. Zatuagan, IEEE Trans. Plasma Sci. **21**, 573 (1993).
6. A. A. Goncharov, A. N. Dobrovolskiy, I. Litovko, *et al.*, IEEE Trans. Plasma Sci. **25**, 709 (1997).
7. A. A. Goncharov, I. M. Protsenko, G. Yu. Yushkov, and I. G. Brown, Appl. Phys. Lett. **75**, 911 (1999).
8. A. I. Morozov and L. S. Solov'ev, in *Reviews of Plasma Physics*, Ed. by M. A. Leontovich (Gosatomizdat, Moscow, 1963; Consultants Bureau, New York, 1966), Vol. 2.
9. B. I. Ivanov, V. P. Prishchepov, and V. M. Kodyakov, in *Proceedings of the 13th International Conference on High Energy Accelerators* (Nauka, Novosibirsk, 1987), Vol. 2, p. 229.
10. I. G. Brown, Rev. Sci. Instrum. **65**, 3061 (1994).
11. J. D. Lawson, in *The Physics of Charged-Particle Beams* (Clarendon Press, Oxford, 1977; Mir, Moscow, 1980), Chap. 2.
12. A. N. Tikhonov and V. Ya. Arsenin, *Solutions of Ill-Posed Problems* (Nauka, Moscow, 1986; Halsted Press, New York, 1977).
13. L. B. Luganskiĭ, Zh. Tekh. Fiz. **55**, 1263 (1985) [Sov. Phys. Tech. Phys. **30**, 731 (1985)].
14. G. A. Korn and T. M. Korn, *Mathematical Handbook for Scientists and Engineers* (McGraw-Hill, New York, 1968; Nauka, Moscow, 1984).
15. V. I. Butenko, Zh. Tekh. Fiz. **62** (7), 157 (1992) [Sov. Phys. Tech. Phys. **37**, 697 (1992)].

Translated by G. V. Shepekina

Plasma Physics Reports, Vol. 27, No. 6, 2001, pp. 520–531. Translated from Fizika Plazmy, Vol. 27, No. 6, 2001, pp. 550–562.

LOW-TEMPERATURE PLASMA

Pulsed Mode of a Negative Corona in Nitrogen: I. Experiment

Yu. S. Akishev, M. E. Grushin, V. B. Karal'nik, and N. I. Trushkin

Troitsk Institute for Innovation and Thermonuclear Research, Troitsk, Moscow oblast, 142190 Russia

Received September 28, 2000

Abstract—The pulsed mode of a negative corona discharge in air has long been known; however, in electropositive gases, this mode has not been previously observed. This paper presents the results from a systematic study of a newly discovered pulsed mode of a negative corona in nitrogen over a wide range of experimental parameters. The conditions under which the pulsed mode is realized are described in detail. The dynamic characteristics of current pulses are determined. The shapes and parameters of current pulses in nitrogen and air are compared. © *2001 MAIK "Nauka/Interperiodica".*

1. INTRODUCTION

A low-current discharge in a strongly inhomogeneous electric field (corona) has a variety of forms and current modes, which depend on the geometry of the electrodes, the gas type and pressure, and the polarity and amplitude of the applied voltage. The time averaged current–voltage (*I–V*) characteristic of a corona discharge is its generalized characteristic. A more detailed classification of corona modes requires a comparison of the *I–V* characteristic with the visual picture of a discharge glow and the time behavior of the discharge current.

Regular current pulses at a constant value of the applied voltage are one of the interesting features of a corona discharge. The pulsed mode of a negative corona in air was discovered by Trichel as early as 1938 [1]. The pulsed mode corresponds to initial corona currents of $I \leq 130$ μA. In this mode, the majority of the discharge gap remains dark and the glow is concentrated in a region of about 1 mm near the cathode point. The tip of the point is covered by a wide glow, which is overlain by a diffuse lilac aureole (corona), strongly diverging toward the anode.

Later (see, e.g., [2, 3]), it was found that the current pulses are due to the instability (and, accordingly, the nonsteady behavior) of the glow cathode sheath of a corona discharge at low currents, so that negative ions play a secondary role in the generation of Trichel pulses.

Unlike in air, the pulsed mode of a corona discharge in electropositive gases (nitrogen, helium, etc.) can be realized only through a certain experimental procedure that is not necessarily employed in usual gas-discharge experiments. For this reason, in the well-known work by Veksler (1943) [4], in which the same approach was used to study corona discharges in both air and nitrogen, no regular current pulses were observed in nitrogen. Based on the results of those experiments, it was concluded (see, e.g., [5, 6]) that the pulsed mode of a negative corona does not exist in electropositive gases.

We have observed the pulsed mode of a negative corona in nitrogen in the needle–plane electrode configuration, investigated the dynamic characteristics of the discharge, and compared them with Trichel pulses in a corona discharge in air under similar conditions.

To explain the essence of our experimental approach, we briefly revisit the general features of a negative corona in air and note its important distinctions from a negative corona in nitrogen.

It is well known [5–7] that the averaged *I–V* characteristic of a negative corona in air can be approximated with reasonable accuracy by the parabolic dependence

$$I = kU(U - U_0), \tag{1}$$

where I is the corona current; U is the applied voltage; k is a dimensional factor dependent on both the geometrical parameters of the electrodes and the mobility of charge carriers in the drift region of the corona; and U_0 is the so-called initial corona voltage, which is usually determined experimentally as the point at which the straight line representing the reduced current I/U intersects the voltage axis (in the literature, the dependence of I/U on U is referred to as the reduced *I–V* characteristic). Expression (1) also reflects the fact that the current of a negative corona in air is nonzero only for $U > U_0$ (here, we will not consider subnanoampere currents corresponding to voltages below U_0; detailed measurements of the *I–V* characteristic of a corona discharge at very low currents within this voltage range were carried out in [4, 8]).

In the literature, the initial corona voltage is often identified with the ignition voltage, i.e., the voltage at which the generating sheath (glow cathode sheath) sustained by electron avalanche processes is formed near the corona electrode (see, e.g., [5, 6]). The physical rea-

1063-780X/01/2706-0520$21.00

sons for such an identification are not quite clear, although, for centimeter interelectrode gaps, the value of U_0 in air coincides fairly well with the ignition voltage calculated from the condition for the existence of a self-sustained steady-state electron avalanche for the vacuum configuration of the electric field in the gap (this condition is analogous to the condition for the existence of a self-sustained steady-state cathode sheath of a glow discharge):

$$\int_0^d (\alpha_i - \alpha_a)dx \simeq \ln\frac{1}{\gamma}, \qquad (2)$$

where $\alpha_i - \alpha_a$ is the resultant electron avalanche gain factor, which is governed by ionization (α_i) and attachment (α_a) processes; d is the size of the region near the corona electrode in which $\alpha_i \geq \alpha_a$; and γ is the effective positive feedback factor for electron avalanches, which is determined by electron emission from the cathode surface bombarded by photons, positive ions, and excited particles.

At high electric fields, the ionization coefficients α_i in nitrogen and air are close to each other. Because of the sharp exponential dependence of α_i on the field strength, the corona ignition voltage in nitrogen, according to Eq. (2), differs slightly from the ignition voltage in air (the corresponding experimental data are presented in Fig. 1). The values of the voltage drop across the cathode sheath also differ insignificantly for these coronas. The potential drop U_c across the glow cathode sheath is usually equal to several hundred volts (i.e., $U_c < U_0$), whereas, in air, it contributes insignificantly to the total voltage drop across the corona.

In a negative corona in nitrogen, the main current carriers are electrons rather than positive ions. Consequently, the voltage across the drift region required for carrying the same current in nitrogen is substantially less than that in air. Thus, after ignition, the corona in nitrogen occurs under overvoltage conditions and its current abruptly increases to a fairly high value I_{ign} determined by the *I–V* characteristic of the corona and the load resistance in the external circuit. This is qualitatively illustrated in Fig. 2.

At atmospheric pressure, centimeter-scale interelectrode distances, and a resistance in the external circuit of $R \simeq 1$–10 MΩ, the corona current in nitrogen is usually established at a steady level of about 100 μA. At such currents, the visual picture of the corona glow near the cathode point differs significantly from that in air. In nitrogen, a small bright spot is observed on the cathode point [4] instead of a broad and diffuse glow, characteristic of a corona in air.

We note another experimental observation that is important from a methodological standpoint. When studying a corona discharge and measuring its *I–V* characteristic, the measurement procedure is usually the following. After the corona ignition, we gradually

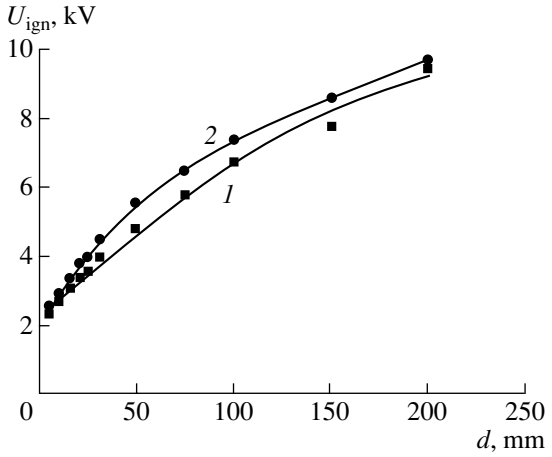

Fig. 1. Ignition voltage of a negative corona in (*1*) nitrogen and (*2*) air as a function of the interelectrode distance. The cathode-point radius is $r_c = 0.06$ mm, and the gas pressure is $P = 760$ torr.

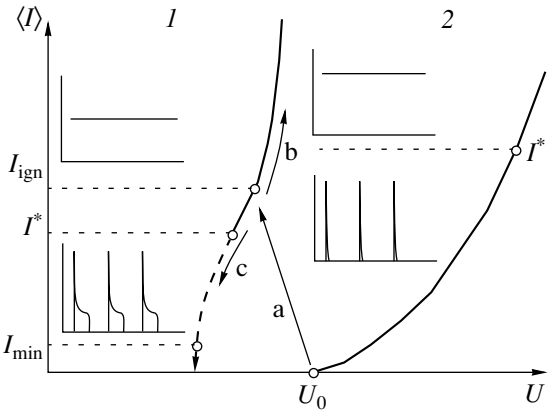

Fig. 2. Qualitative time-averaged *I–V* characteristics of negative coronas in (*1*) nitrogen and (*2*) air. The critical currents are the following: I_{ign} is the discharge current that is rapidly established after corona ignition, I_{min} is the minimum corona current below which the corona is quenched, and I^* is the current separating the steady-state mode of a corona discharge from the pulsed mode; U_0 is the corona ignition voltage. Characteristic current waveforms in the steady-state and pulsed modes are shown in insets. The characteristic period of current pulses is 3 μms for nitrogen and 30 μs for air. The hysteresis region of the corona is shown by the dashed line.

increased the power-source voltage, thereby moving upward along the *I–V* characteristic (Fig. 2, path a–b). In this case, the pulsed mode of a negative corona in nitrogen does not occur.

We have found that, if the applied voltage is decreased after igniting the corona (Fig. 2, path a–c), then the corona exists even at currents below I_{ign}. In other words, a corona discharge in nitrogen is characterized by hysteresis in a certain range of parameters. In

our experiments, we studied the corona at currents I both higher and lower than I_{ign}. This allowed us to observe the pulsed mode of a negative corona in nitrogen, because under most experimental conditions ($P \simeq$ 1 atm, $R < 10$ MΩ, and $d \simeq 3$ cm), regular current pulses can only be observed in the hysteresis region at currents $I < I_{ign}$.

2. EXPERIMENTAL TECHNIQUE

Corona experiments were carried out in the needle–plane electrode configuration within wide ranges of interelectrode distances (d = 0.1–21 cm) and cathode point radii (r_c = 0.06–5 mm). To avoid the edge effects due to the limitation of the transverse size of the corona, the diameter of the anode disk was always larger than the interelectrode distance by at least a factor of 3 (in special experiments, it was established that the edge effects are unimportant at this ratio between the anode diameter and the interelectrode distance).

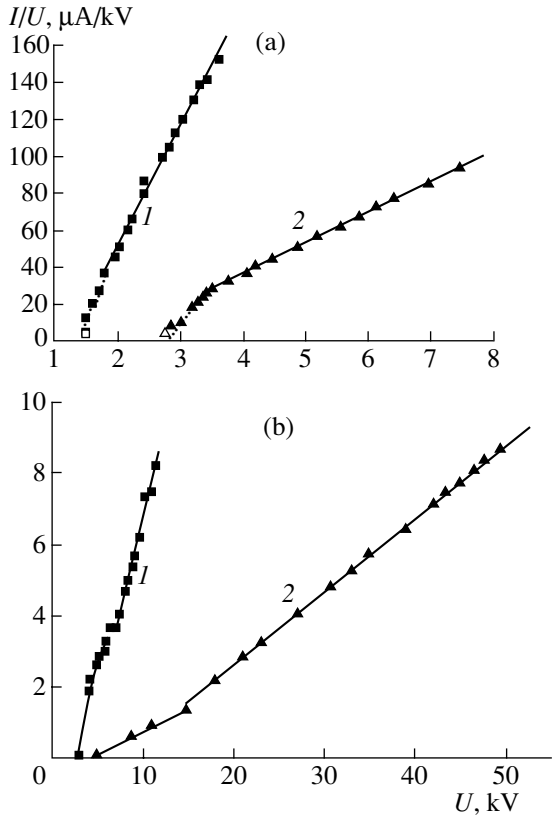

Fig. 3. (a) Time-averaged reduced *I–V* characteristic of a negative corona (a) in nitrogen at P = 1 atm, r_c = 0.06 mm, (*1*) d = 10 mm and $U_{ign} \approx$ 2.8 kV, and (*2*) d = 30 mm and $U_{ign} \approx$ 4 kV ($U_0 < U_{ign}$) and (b) in air at P = 1 atm, r_c = 0.06 mm, (*1*) d = 10 mm and $U_{ign} \approx$ 2.8 kV, and (*2*) d = 30 mm and $U_{ign} \approx$ 4.5 kV ($U_0 \simeq U_{ign}$). The hysteresis region in plot (a) is shown by the dashed curve; minimum corona currents of 3–5 μA are indicated by open symbols.

The anode was made of either stainless-steel or resistive-material plates. The thickness and resistivity of a resistive plate were chosen such that, at typical corona currents, the voltage drop across the plate was no higher than several tens of volts. To measure the current distribution over the anode, we used a sectioned anode consisting of ten nested metal rings separated by thin dielectric layers.

In experiments, we used chemically pure (99.999%) nitrogen. To maintain the certified purity of nitrogen and remove possible products of plasmochemical reactions from the discharge, the gas flowed continuously through the discharge chamber. The gas flow rate was set sufficiently low in order to avoid any perceptible gas-dynamic effect on the corona. The nitrogen pressure was from 1 torr to 25 atm. Pressures below atmospheric were measured by an M110 aneroid barometer; pressures above atmospheric were measured by an MO (model 1120) reference manometer.

The power supply was a stabilized high-voltage source ($\delta U/U \le 10^{-6}$) with a voltage of up to 60 kV. The voltage at the interelectrode gap was measured by either an S-196 electrostatic voltmeter or a calibrated high-voltage divider with an arm ratio of 1 : 10 000. The ballast resistance in the external circuit was from 1 MΩ to 1.5 GΩ. The averaged corona current was measured with a Ts4311 pointer instrument. The corona current pulses were recorded with an S1-104 analog oscillograph and a Tektronix TDS 520 digital oscillograph with a 500-MHz passband and 0.7-ns signal rise time. Some measurements in the low-frequency range were carried out with an S8-17 oscillograph.

3. EXPERIMENTAL RESULTS

3.1. Specific Features of the I–V Characteristic, Critical Currents, and the Visual Picture of the Glow of a Corona Discharge in Nitrogen

First, we describe the general properties of a corona with a metal anode. Figure 3a shows the time-averaged reduced *I–V* characteristic of a negative corona in nitrogen for two values of the interelectrode distance, d = 10 and 30 mm. The hysteresis regions in the *I–V* characteristics are indicated by the dashed lines. For comparison, Fig. 3b shows the reduced *I–V* characteristic of a corona discharge in air for the same interelectrode distances and point radii.

It is seen that, in the current range in which pulses are absent, the *I–V* characteristic of a corona in both nitrogen and air can be approximated by expression (1). We note that, in nitrogen (unlike in air), the voltage U_0 at which the straight line I/U intersects the voltage axis does not coincide with the corona ignition voltage. At nitrogen pressures of $P \le 1$ atm and centimeter interelectrode distances, the initial voltage U_0 determined from the *I–V* characteristic is always lower than the ignition voltage, $U_0 < U_{ign}$. However, as the interelectrode distance and the nitrogen pressure increase, the

voltage U_0 approaches U_{ign}. For example, at $P = 1$ atm and $d > 20$ cm or $P = 7$ atm and $d > 1.0$ cm, the initial voltage almost coincides with the ignition voltage.

A comparison of the slopes of the reduced I–V characteristic in nitrogen and air in the absence of pulses shows that their ratio (at the same values of P, r, and d) is about 60–80. This value is nearly four times smaller than the mobility ratio between electrons and negative ions, $\mu_e/\mu_i = 250$–300. This circumstance may be evidence of the difference between the effective current cross sections of nitrogen and air coronas.

Indeed, the effective cross section for an axisymmetric corona in air can be determined from the so-called Warburg distribution [9], according to which the current density at the metal anode falls monotonically with distance from the axis. It was found in [10] that a nitrogen corona had a nonmonotonic radial current profile with a deep and rather broad minimum in the center, which increased the effective current cross section of the corona.

Our experiments with a sectioned anode show that the nonmonotonic cross section is only typical of corona currents that lie outside the hysteresis region. In the hysteresis region, the radial current distribution over the anode is monotonic and resembles the Warburg distribution (Fig. 4). Hence, in the hysteresis region, the current cross section of a corona discharge in nitrogen is close to that in air, which reflects a steeper dependence of the reduced current on the voltage and a closer coincidence between the ratios of the slopes of the reduced I–V characteristics in nitrogen and air and the ratio μ_e/μ_i.

According to Fig. 2, several characteristic current values can be distinguished in the I–V characteristic of a negative corona: the initial current I_{ign}, which is rapidly established after igniting the corona; the minimum corona current I_{min}, below which the corona is quenched; and the critical current I^*, which separates the pulsed mode of the corona from the steady-state mode. Let us consider in more detail how each of these currents depends on the discharge parameters.

The value of the initial current I_{ign} depends on the dimensions of the electrode system (i.e., the point radius r and the interelectrode distance d), the nitrogen pressure P, and the ballast resistance R. By varying these parameters, it is possible to decrease the corona current, but not to an arbitrary small value. It turns out that, in the hysteresis region, the corona exists only when the current is above a certain level. In the experiment, this manifested itself in the fact that, as the applied voltage and, accordingly, the current slowly decreased, the corona was abruptly quenched at a certain threshold current $I = I_{min}$.

It was found that the minimum corona current I_{min} in nitrogen increases as the curvature radius of the cathode point increases. In contrast, as the interelectrode distance d and the ballast resistance R increase, the minimum corona current decreases. The corresponding experimental results are shown in Fig. 5. Increasing the pressure at fixed values of r and d also results in an increase in the current at which the corona is quenched. The experimental data obtained for a point radius of $r = 0.06$ mm, an interelectrode distance of $d = 0.4$ cm, and $R = 18$ MΩ are summarized in Table 1.

The hysteresis and the threshold current I_{min} were not observed in an air corona at atmospheric pressure. However, at low pressures $P \le 20$ torr, when the attach-

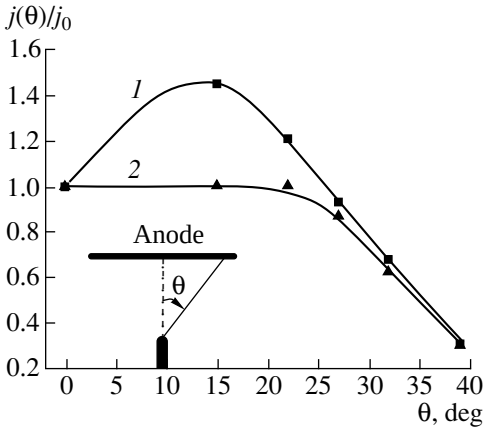

Fig. 4. Radial distribution of the current density over the anode in a negative corona in nitrogen at $P = 1$ atm, $r_c = 0.1$ mm, $d = 30$ mm, and $R = 7.8$ MΩ: (*1*) a steady-state corona mode at a current of $I = 108$ μA and $U = 3.05$ kV and (*2*) a pulsed corona mode at a mean current of $\langle I \rangle = 40$ μA and $U = 2.4$ kV; j_0 is the current density at the anode center ($\theta = 0$); θ is the angle (in degrees) measured from the discharge axis.

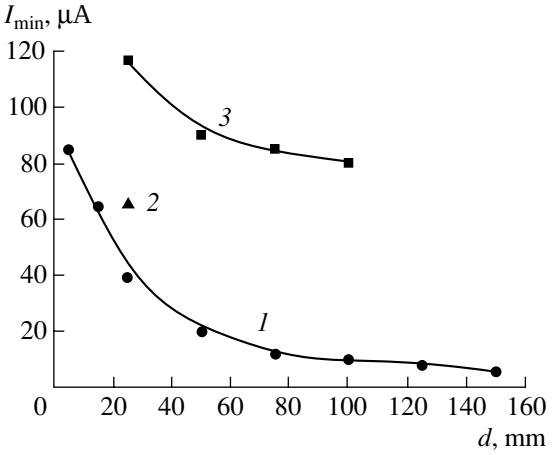

Fig. 5. Minimum current of a negative corona in nitrogen as a function of the interelectrode distance for different point radii: r_c = (*1*) 0.1, (*2*) 0.5, and (*3*) 1.1 mm. The gas pressure is $P = 750$ torr, and the ballast resistance is $R = 5$ MΩ.

Table 1

P, atm	1	2	3	7	10	18
I_{min}, μA	26	30	40	50	60	80

ment of electrons to oxygen was significantly weaker, the above effects were also observed in an air corona.

According to Fig. 2, regular current pulsations in nitrogen exist in the hysteresis region of the *I–V* characteristic at currents lower than a certain critical current I^*. The study of the evolution of the visual picture of the corona glow allowed us to reveal the key effect related to the appearance (or disappearance) of the pulsed mode.

At the current equal to I^*, the spatial structure of the glow near the cathode point rearranges abruptly. In the pulsed mode ($I < I^*$), the point is covered with a wide glow spot that is overlain by a diffuse corona glow diverging toward the anode. This structure of a corona glow in nitrogen is similar to that observed in air in the range of initial corona currents at which Trichel pulses exist.

For $I \geq I^*$ (steady-state corona), the transverse size of the steady-state cathode sheath is appreciably smaller to the eye than the average size of the pulsed sheath. The structure of the sheath and the surrounding glow depend on the nitrogen pressure. At higher pressures ($P \geq 0.5$ atm), the point glow is bright and is localized in one (or more) small current spots. Such a picture was usually observed in all of the known experiments with a nitrogen corona (see, e.g., [4, 5]).

At lower pressures ($P < 0.5$ atm), the contraction of the glow cathode sheath during the transition from the pulsed mode to the steady-state mode is less pronounced. After the transition, the steady-state glow cathode sheath appreciably reduces in diameter, but a small bright cathode spot on the point does not occur in this case (the spot can arise at higher currents). A similar structural rearrangement of the corona glow is observed in air when Trichel pulses disappear. The only difference is in the values of the currents I^*: the critical current in nitrogen is substantially lower than that in air, so the current range in which regular pulses exist is narrower for nitrogen.

At atmospheric pressure and centimeter gaps, the current boundary I^* between two visually different forms of the cathode sheath (a wide glow spot and a small bright spot) can vary approximately from 40 to 60 μA. This scatter in the currents is mainly due to the dependence I^* on the direction of motion ($\uparrow$ or $\downarrow$) along the hysteresis *I–V* characteristic ($\uparrow$ corresponds to the motion from lower to higher corona currents, and $\downarrow$ corresponds to the motion in the opposite direction). In other words, the transformation of the cathode sheath from one form to another is characterized by hysteresis. The current at which the glow disappears, $I^*\uparrow$, exceeds the current at which it arises $I^*\downarrow$. Thus, e.g., $I^*\downarrow = 42$ μA and $I^*\uparrow = 56$ μA for $d = 3.5$ cm. As the interelectrode distance increases, the I^* hysteresis becomes less pronounced and, for $d \geq 15$ cm, the difference between $I^*\uparrow$ and $I^*\downarrow$ disappears. At point radii larger than 0.1 mm, the value of the critical current I^* depends weakly on the radius.

At atmospheric pressure, centimeter gaps, small point radii ($r < 0.5$ mm), and small ballast resistances ($R < 10$ MΩ), the ignition current usually exceeds the critical current I^*. In this situation, the region in which regular current pulsations exist is determined by the condition $I^* > I_{min}$. This condition becomes invalid for large point radii and also small interelectrode distances because, in this case, the corona is spontaneously quenched even before the pulsed regime ($I^* < I_{min}$) occurs.

By significantly increasing the interelectrode distance (up to 20 centimeters or higher) and the ballast resistance (up to 100 MΩ or higher) or by decreasing the point radius and the nitrogen pressure, it is possible to reduce the current I_{min} at which the corona is quenched and to create conditions at which $I_{min} < I_{ign} < I^*$. In this case, the corona is ignited in the pulsed mode with a glow cathode sheath surrounded by a diffuse glow.

The parameters of the pulsed mode of a negative corona in nitrogen differ substantially for anodes made of different materials. For this reason, the results for coronas with metal and resistive anodes will be described individually.

3.2. Pulsed Mode of a Negative Corona with a Metal Anode

We studied the pulsed mode of a corona discharge at both atmospheric and reduced nitrogen pressures. The fact is that the current I_{min} at which the corona is quenched decreases rapidly as the pressure decreases. The magnitude of the current I^* corresponding to the upper boundary of the pulsed mode also decreases with decreasing pressure, but not as rapidly. Hence, the current range in which the pulsed mode exists ($I_{min} \leq I \leq I^*$) broadens as the pressure decreases, which facilitates the study of this mode. In addition, at low pressures, we can use lower ballast resistances in order to realize the pulsed mode of a corona discharge (the current I^* depends only slightly on the resistance). Thus, for $P \leq 100$ torr, we can use resistances about several MΩ. The corresponding experimental data are presented in Table 2.

First, we compare the shapes and characteristic parameters of oscillograms of the current pulses in nitrogen and room air, other conditions being the same. A comparative experiment was carried out at $P = 1$ atm, an interelectrode distance of $d = 30$ mm, a point radius of $r = 0.1$ mm, and a ballast resistance of $R = 750$ MΩ. The corresponding current oscillograms are shown in Figs. 6 and 7. It can be seen that the peak amplitudes of the pulses are close to each other and the durations of

Table 2

P, torr	750	300	100	100	100	100	750	750	750	750	750	300	100
R, MΩ	2	2	2	5.1	51	102	10	34	51	102	10	10	10
											100	100	100
d, mm	35	30	30	30	30	30	15	15	15	15	5	5	5
I^*, μA	42–56	38–26	13–16	15	15	15	–	40	40	40	–	–	–
											45	35	25
I_{min}, μA	40	40	25	10	<2	<1	45	11	10	9	45	40	30
											35	30	10

their steep (≈2 ns) leading edges are nearly the same (the equal amplitudes are observed for nitrogen and dry air); however, the duration of their trailing edges is markedly different.

A typical trailing edge duration of Trichel pulses in air is on the order of 100 ns; over this time, the current decreases to 1–3 μA. The trailing edge duration of current pulses in nitrogen lies in the millisecond range. Accordingly, the pulse periods are also different. Thus, for a mean corona current of $I \simeq 10$ μA, the period T of Trichel pulses is equal to 6 μs, whereas in nitrogen, it is $T = 2$ ms.

The shape of the pulse trailing edge in nitrogen is more complicated than that in air. During the first 70–80 ns after the pulse peak, the current falls as rapidly as it does in air. In this stage, the current falls rapidly from $A_1 = 1.6$ mA to $A_2 = 150$–300 μA (here, A_1 is the peak amplitude of the current pulse). Then, over about 6–7 μs, the current increases by several percent. The time it takes for the current to arrive at a gently sloping maximum (a hump) turned out to be linearly dependent on the interelectrode distance; at atmospheric pressure, we have t_{max} [μs] ≃ 0.2d [mm]. After the hump, the current falls monotonically to nearly 35 μA. After reaching this critical value, the current falls rapidly (over about several microseconds) to 1–3 μA and remains at this level until the next pulse begins. In some cases, the rapid fall of the current at the pulse trailing edge is also observed in air. Trichel pulses with such shapes were recorded in [11] and also in our experiments.

A monotonic decrease in the current at the pulse trailing edge after the current hump is characteristic of high pressures ($P \geq 0.5$ atm), when the pulse current approaches the critical value $I \simeq 35$ μA quite rapidly (the characteristic current-fall rate is $|dI/dt| \approx 1$ A/s). At lower pressures, there is a current quasi-plateau phase

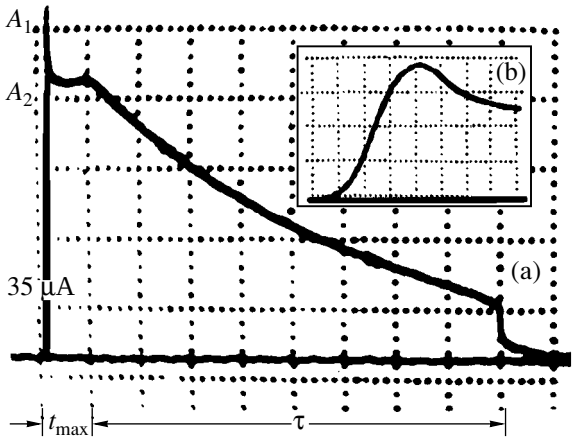

Fig. 6. Oscillogram of the current pulse of a negative corona with a metal anode in nitrogen at $P = 1$ atm, $R = 750$ MΩ, $d = 30$ mm, $r_c = 0.1$ mm, $\langle I \rangle = 8$ μA, and $U = 2.7$ kV: (a) a general structure of the current pulse (the pulse amplitude at the leading edge is depicted only roughly, the time scale is 20 μs/division, and the current scale is 40 μA/division); (b) a detailed structure of the leading edge of the current pulse (the time scale is 2 ns/division, and the current scale is 400 μA/division).

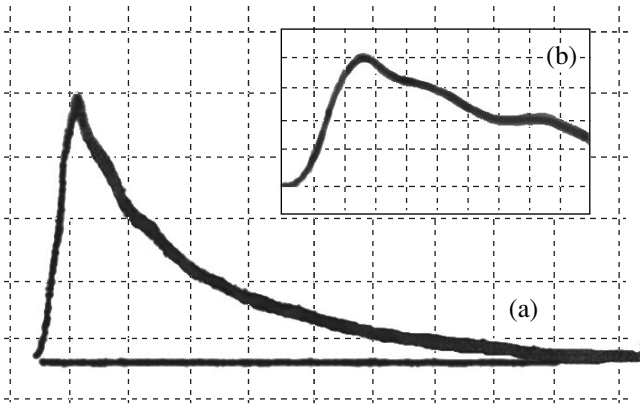

Fig. 7. Oscillogram of the current pulse of a negative corona with a metal anode in air (Trichel pulse) at $P = 1$ atm, $R = 750$ MΩ, $d = 30$ mm, $r_c = 0.1$ mm, $\langle I \rangle = 10$ μA, and $U = 11$ kV: (a) a general structure of the current pulse (the time scale is 10 ns/division, and the current scale is 400 μA/division); (b) a detailed structure of the leading edge of the current pulse (the time scale is 2 ns/division, and the current scale is 400 μA/division).

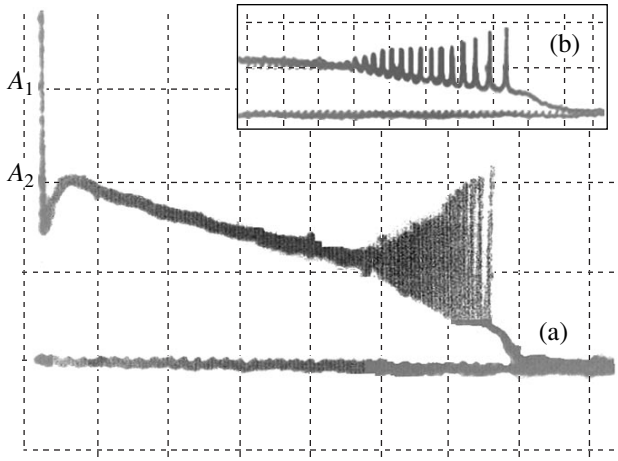

Fig. 8. High-frequency oscillations at the trailing edge of the current pulse of a negative corona with a metal anode in nitrogen at P = 120 torr, R = 34 MΩ, d = 30 mm, r_c = 0.1 mm, $\langle I \rangle$ = 10 μA, and U = 1.35 kV: (a) a general structure of the current pulse with high-frequency oscillations at the trailing edge (the time scale is 20 μs/division, and the current scale is 20 μA/division); (b) a detailed structure of high-frequency oscillations at the trailing edge of the current pulse (the time scale is 5 μs/division, and the current scale is 20 μA/division).

Fig. 9. High-frequency oscillations at the leading edge of the current pulse of a negative corona with a metal anode in nitrogen at P = 80 torr, R = 34 MΩ, d = 30 mm, r_c = 0.1 mm, $\langle I \rangle$ = 10 μA, and U = 1.0 kV: (a) a detailed structure of damping high-frequency oscillations that arise immediately after the leading edge of the current pulse (the time scale is 2 μs/division, and the current scale is 20 μA/division); (b) a general structure of low-frequency current oscillations (the interval *A*–*B* corresponds to high-frequency current oscillations shown in plot (a), the time scale is 100 μs/division, and the current scale is 20 μA/division).

at the pulse trailing edge, in which the current decreases rather slowly (the characteristic current-fall rate can be as low as $|dI/dt| \approx 0.01$ A/s). In this case, several tens of microseconds before the rapid fall, high-frequency oscillations with increasing amplitude and a period of 3–6 μs arise at the pulse trailing edge (Fig. 8).

As the nitrogen pressure decreases, both the amplitude and period of high-frequency oscillations increase, whereas the values of the critical currents at the trailing edge before and after the rapid fall become closer. Thus, at P = 100 torr, the critical current before the fall is equal to 20 μA, whereas after the fall, it is equal to 7–8 μA. At even lesser pressures $P \le 80$ torr, these oscillations arise not only at the pulse trailing edge, but also immediately after the current peak at the leading edge (Fig. 9). In this case, the oscillation amplitude decreases as the pulse current increases. The high-frequency oscillations observed in nitrogen with a metal anode are very similar to Trichel pulses in air with similar corona parameters.

As the interelectrode distance decreases, the two-humped shape of the pulse in nitrogen becomes more pronounced (e.g., at d = 3 mm, the hump height is nearly 50 times larger than the amplitude of a sharp peak at the leading edge). A decrease in the pressure leads to the same effect. As the mean current (or the applied voltage) increases, the hump progressively increases, and, finally, the corona transforms into a spark. If the interelectrode distance d and the point radius r decrease substantially, then the pulses in air also become two-humped in shape (provided that $P \le$ 1 atm and $r/d > 0.5$).

Table 3

T, ms	1.6	2	4
τ, μs	75	150	340
d, mm	5	30	150

Unlike the Trichel pulses in air, for which the repetition rate is always proportional to the mean current, the dependence of the pulse repetition rate f on the corona current in nitrogen is more complicated. In a certain range of initial currents, the pulse repetition rate varies linearly with the current. For example, at P = 1 atm, an interelectrode distance of d = 5 mm, and a point radius of r = 0.1 mm, the linear dependence takes place up to the mean current $I \simeq 15$ μA. At corona currents up to 30 μA, the repetition rate remains almost constant at a level of f = 1.5 kHz. Above 30 μA, the pulse repetition rate decreases with the current until the current reaches the value at which the glow cathode sheath transforms into a small bright spot.

Because of the complicated structure of the pulse trailing edge in nitrogen, it is necessary introduce (along with the period $T = 1/f$) one more parameter (Fig. 6), namely, the duration τ of the phase of slow decrease of the pulse current from A_2 (i.e., from several hundred microamperes) to several tens of microamperes (to 35 μA at P = 1 atm). Experiments show that the quantities T and τ depend differently on the current.

Table 4

P, torr	30–750	30–750	750	750	750	750	750
R, MΩ	≤18	100	18	3–5	18	18	≥750
d, mm	≤50	≥5	50 ($I \simeq 26$ μA)	100–200	210	210 ($I \simeq 17$ μA)	100–200
A_2, μA	No pulses	Pulses are present	150	150	150	150	180–200
τ, ms	($I_{min} \geq 10$ μA)		0.5	2	0.5	0.55	0.35
T, ms			1.25	17–20	4	2	4

At atmospheric pressure and d = const, the quantity τ remains constant in the range of corona currents corresponding to the linear growth of the repetition rate and begins to increase with the current outside this range. As the interelectrode distance increases (at a fixed current), the quantities τ and T increase (see Table 3 for P = 1 atm, r = 0.1 mm, $\langle I \rangle$ = 10 μA, and R = 750 MΩ).

We carried out experiments for different values of the ballast resistance R in the external circuit (from 1.0 MΩ to 1.5 GΩ). It was found that, for an air corona at atmospheric pressure, the value of R has little effect on the shape of Trichel pulses and their repetition rate. This is explained by the fact that a parasitic capacitance (on the order of several picofarads) rather than the ohmic resistance makes the main contribution to the total impedance of the external circuit at times on the order of the pulse period. In this case, the voltage across the gap remains constant throughout the pulse period and is independent of R.

In nitrogen, as for Trichel pulses, the value R has no effect on the shape of the short leading edge and the pulse amplitude A_1 (the pulse amplitude can be changed primarily by changing the point radius; A_1 increases with radius). At the same time, the structure of the trailing edge (i.e., the values of A_2, τ, and, accordingly, the pulse period T) varies when varying R. The results obtained at r = 0.1 mm and a mean current of $\langle I \rangle \simeq$ 10 μA are summarized in Table 4.

It is seen that, at low resistances (on the order of several MΩ), the values of τ and T substantially exceed analogous values for R > 10 MΩ. A plausible explanation is that the low R contributes significantly to the total impedance of the external circuit at times of about tens of milliseconds. At higher resistances, the pulse parameters depend only slightly on R (τ decreases slightly with R) because, at times on the order of or shorter than one millisecond, the impedance of the external circuit containing a large resistance is governed by its parasitic capacitance.

3.3. Pulsed Mode of a Negative Corona with a Resistive Anode

Experiments demonstrated that using a resistive anode stabilizes a nitrogen corona in the point glow mode. This also allows one to extend the existence domain of this mode toward smaller interelectrode distances and ballast resistances and larger point radii, including the use of flat-ended rods up to 5 mm in diameter. With a resistive anode, the upper current boundary I^* for the existence of a pulsed mode considerably exceeds the analogous value for a corona with a metal anode. With a resistive anode, the scenario of the disappearance of the pulsed mode in nitrogen at any pressure is similar to that of the disappearance of Trichel pulses in air; i.e., at $I = I^*$, a rapid and insignificant (by a factor of about 1.5–2) decrease in the diameter of the glow cathode sheath occurs instead of the formation of a bright small spot at the cathode point.

Experiments show that the anode resistivity substantially affects the shape of current pulses in nitrogen. With a resistive anode, the pulse leading edge is almost the same as that with a metal anode; however, the trailing edge no longer demonstrates a complicated and rather extended structure. The pulses significantly shorten and become very similar in shape to Trichel pulses in air for a corona with a resistive anode (Fig. 10).

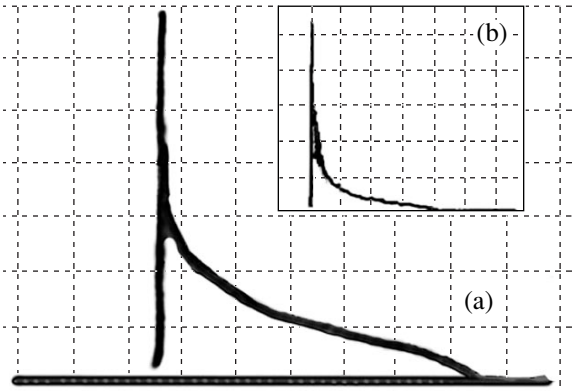

Fig. 10. Oscillograms of current pulses of a negative corona with a resistive anode at P = 100 torr, R = 15 MΩ, d = 30 mm, and r_c = 1 mm (a) in air for $\langle I \rangle$ = 40 μA and U = 1.1 kV (the time scale is 0.5 μs/division, and the current scale is 1.5 mA/division) and (b) in nitrogen for $\langle I \rangle$ = 38 μA and U = 0.9 kV (the time scale is 1 μs/division, and the current scale is 2 mA/division).

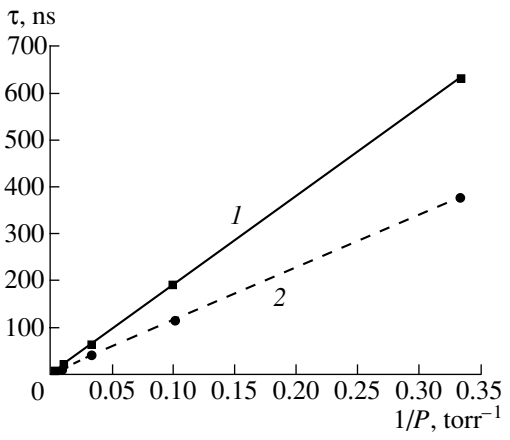

Fig. 11. Duration of the leading edge τ_1 of the current pulse of a negative corona with a resistive anode in (*1*) nitrogen ($p\tau_1 \simeq 2.5$ ns atm) and (*2*) air ($p\tau_1 \simeq 1.5$ ns atm) as a function of the gas pressure; the results presented refer to different interelectrode distances and cathode radii, because τ_1 depends only slightly on d and r_c.

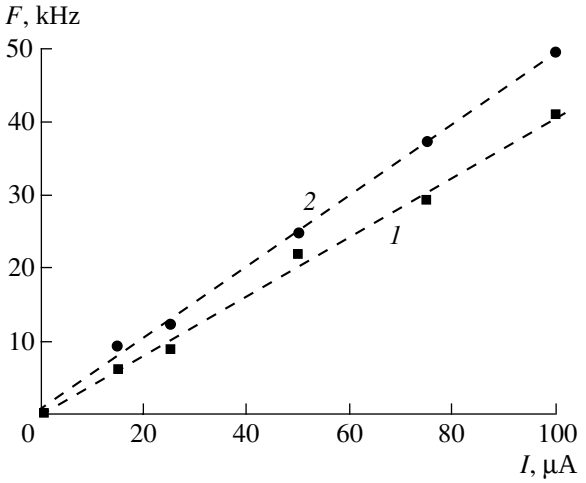

Fig. 12. Repetition rate of current pulses of a negative corona with a resistive anode in (*1*) nitrogen and (*2*) air as a function of the mean current for $d = 1$ mm, $r_c = 1$ mm, $P = 100$ torr, and $R = 15$ MΩ.

Comparing the Trichel pulses of air coronas with a metal and resistive anode, we can see that the anode resistivity has no effect on the structure of the leading edge, but it nearly doubles the duration of the trailing edge.

We compared the parameters of the leading edges of pulses in nitrogen and Trichel pulses in air under the same experimental conditions. Figure 11 shows the duration of the pulse leading edge τ_1 in nitrogen and air as a function of the pressure *P*. It was found that the value of the product $P\tau_1 \approx 2.5$ atm ns for nitrogen is close to the corresponding constant for air, $P\tau_1 \approx 1.5$ atm ns. The constant for air measured by us coincides with the corresponding constant presented in [12].

Figure 12 shows the repetition rates of the current pulses in nitrogen and air at $P = 100$ torr and $r = 1$ mm as functions of the mean corona current. It can be seen that, with a resistive anode, the region in which the repetition rate of pulses in nitrogen depends linearly on the current is significantly wider and the rate itself is close to the repetition rate of Trichel pulses. The latter circumstance indicates that the charges produced by individual current pulses are almost the same in nitrogen and air.

4. DISCUSSION OF EXPERIMENTAL RESULTS

4.1. Hysteresis in a Negative Corona in Nitrogen

The hysteresis effect in a negative corona in nitrogen is related to the difference between the voltages providing the self-maintenance condition (2) for electron avalanches in the gap before the corona ignition and after it. Before ignition, the avalanches develop in a relatively weak field at a large distance from the cathode point, which can occur only if a sufficiently high voltage is applied. After ignition, strong fields are localized near the point, so that the self-maintenance condition is satisfied at a very short length equal to the thickness of the glow cathode sheath. In this case, the voltage across the gap is lower. Let us discuss this in more detail.

The distribution of the electric field along the discharge axis before and after ignition is shown schematically in Fig. 13. It can be seen that the positive charge of the cathode sheath formed near the point shields and strongly reduces (in comparison with the initial vacuum electric field) the electric field E_c at the cathode boundary of the drift region. At the same time, the space electron charge in the drift region is small (in particular, at small initial corona currents and a centimeter-scale interelectrode distance); consequently, the configuration of the axial electric field $E(x)$ in this region remains very similar to the vacuum configuration.

To illustrate this, we consider the configuration of the vacuum field $E(x)$ between the paraboloidal point and the plane [5, 6]: $E(x) = E_0 r/(r + 2x)$, where E_0 is the field on the surface of the point of radius r before the corona ignition. According to the above discussion, the field distribution in the drift region after the corona ignition takes the form (Fig. 13) $E(x) = E_c r/(r + 2x)$ (the functional dependence $r/(r + 2x)$ remains the same because the cathode sheath thickness is usually much less than the point radius).

It is easy to ascertain that the initial voltage U_0 across the gap after the corona ignition is equal to $U = U_c + U_{ign}E_c/E_0$, where U_c is either the voltage across the glow cathode sheath of the corona (which is close in

magnitude to 0.5–1.0 kV [13]) or the voltage at the prearc cathode spot (which is close to 100 V [14]). Obviously, the initial voltage is lower than the ignition voltage. The voltage difference is equal to $\Delta U = U_{ign}(1 - E_c/E_0) - U_c$. Its upper boundary can be estimated at $\Delta U \approx U_{ign} - U_c$. In this case, the corona gap after the ignition turns out to be under the overvoltage conditions, which results in the current jump and the hysteresis of the *I–V* characteristic.

After igniting a corona in air, the interelectrode gap is rapidly (over the time during which the ions drift from the cathode toward the anode) filled with negative ions produced due to electron attachment. In this case, the electric field produced by the space charge of these ions in the drift region is much higher than the vacuum field and the total voltage drop across the cathode sheath and the drift region exceeds the ignition voltage; i.e., hysteresis at air pressures of tens of torr or higher is absent.

4.2. Contraction of the Diffuse Glow Cathode Sheath of a Negative Corona

The mechanism for the transition of the glow cathode sheath of a corona to the regime with a small bright current spot is similar to that for the contraction of the normal cathode sheath of a glow discharge to a prearc spot. This effect was revealed and studied in [14]. In that paper, the transformation into a spot is explained by the onset of the ionization instability in the glow sheath due to the accumulation of nitrogen metastables in the sheath up to the critical density at which their contribution to ionization becomes dominant. In this case, the voltage drop across the sheath decreases and the current density increases.

The critical currents corresponding to the transformation of the glow sheath into a prearc spot depend on the geometric parameters of the electrodes and the gas-mixture composition. The presence of efficient quenchers of metastable nitrogen states, such as oxygen and water vapor, increases the critical current considerably. This is why the regime with bright prearc spots at the corona electrode is easily realized in nitrogen but is hard to realize in a negative corona in air (particularly, in humid air).

4.3. Minimum Currents in a Negative Corona in Nitrogen

In our opinion, both of the threshold currents (the minimum mean current I_{min} below which the corona is quenched and the critical current at the pulse trailing edge below which the pulse current falls rapidly) are of the same nature. Indeed, as the corona current decreases, the transverse size of the glow cathode sheath at the point also decreases. Presumably, at sufficiently small transverse dimensions, diffusion comes into play and destroys the glow cathode sheath, which results in corona quenching. The stabilizing action of a large ballast resistance on the corona (i.e., the possibility of decreasing the current I_{min} by increasing R) does not contradict the aforesaid.

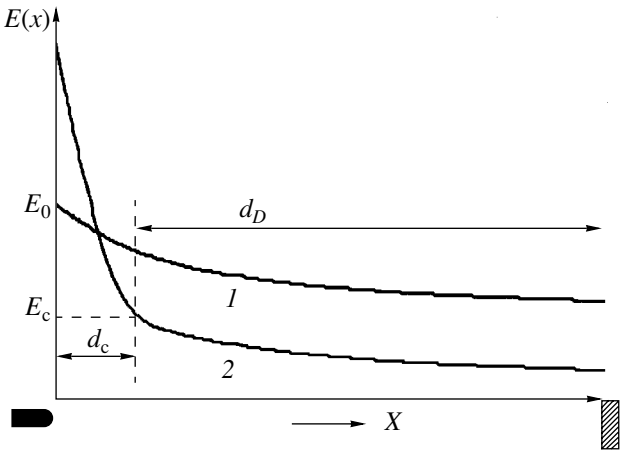

Fig. 13. Qualitative profile of the electric field along the discharge axis (*1*) before and (*2*) after the ignition of a negative corona in the needle–plane electrode configuration; E_0 is the field at the cathode point before the corona ignition; E_c is the field at the cathode boundary of the drift region after the corona ignition; d_c is the region of the positive space charge (the cathode sheath); d_D is the drift region.

4.4. Structure of the Trailing Edge of Current Pulses in the Negative Corona in Nitrogen

The two-humped shape of current pulses in nitrogen in the case of a metal anode is very similar to that observed when initiating the transformation of the corona into a spark [15, 16] and is associated with ionization processes, which strongly differ in their time scales. The first process (with a characteristic time on the order of 100 ns at atmospheric pressure) is related to electron-impact ionization and is identical to that occurring in Trichel pulses; i.e., it is related to the dynamics of the glow cathode sheath of a corona (see [2, 3, 15, 16]). The rapid decrease in the sheath thickness corresponds to the short leading edge of the pulse, whereas the slow growth in the sheath thickness corresponds to a current drop by nearly one order of magnitude from its maximum value.

The second process occurring on the millisecond time scale is reflected in the oscillogram as a rather flat hump and is probably related to the formation of a nonsteady plasma region in the corona. In this study, we did not examine the spatiotemporal evolution of the plasma region. Thus, we can only suppose two scenarios of this process: either the plasma region arises near the cathode sheath and then slowly expands toward the anode or the plasma is initiated near the axis in the vicinity of the anode due to the formation of the anode sheath (see

[17] and the literature cited therein) and then slowly expands toward the cathode.

In other words, the process occurring on the millisecond time scale is similar to the expansion of a slow anode- or cathode-directed streamer through the gap (which corresponds to the current growth up to the hump maximum); after passing a certain distance, the streamer decays (which corresponds to the current drop after the hump). We note that the term "streamer" is used here only by analogy. By virtue of the ionization mechanism for the processes maintaining the slow streamer, the latter may substantially differ from the well-known fast streamer by spatial, temporal, and current scales.

The above results demonstrating that the amplitude of the second hump increases monotonically with the applied voltage show that the second process is responsible for the formation of an expanding plasma region in the corona gap. In this case, when the plasma at a certain voltage bridges the interelectrode gap, the corona should transform into a spark, as was observed in experiments.

A resistive anode significantly modifies the current distributions both along the discharge and over the anode. The strong influence of the anode resistivity on the amplitude of a gently sloping current hump indirectly indicates that, at the beginning of the second process, the ionization and electrodynamic instabilities developing near the anode play a decisive role in the formation of a plasma region (or a slow streamer).

4.5. Comparison of the Results Obtained with the Published Data

Published experimental data on the dynamic characteristics of regular current pulses in a negative corona in nitrogen are lacking. We can only refer to papers [16, 18], which are devoted to studies of the structure of a current pulse (P = 50 and 100 torr) arising in nitrogen when a voltage pulse is applied across the needle–plane gap. The structure of this single pulse is also governed by ionization processes, but under the condition of the ignition of a corona discharge. Therefore, it is not obvious, first, that a regular pulsed mode will be established after the first pulse associated with the corona-ignition processes and, second, that the shape of the ignition pulse will coincide in shape with regular pulses in a steady-state corona.

The current pulse accompanying the corona ignition was studied in [16, 18] at a small value of the ballast resistance (R = 6 kΩ and in a rather narrow time interval 50 ns–1 μs. Thus, our results cannot be compared in full measure with data from those papers. Nevertheless, we note that, in the given time interval, the current oscillograms presented in [16, 18] also demonstrate the nonmonotonic behavior of the pulse current.

As was mentioned above, the resistive anode efficiently suppresses the development of the second process (i.e., the origination and expansion of a plasma region or a slow streamer). In this case, the parameters of current pulses in nitrogen are close to the parameters of Trichel pulses in air. In the literature, Trichel pulses are well studied over a sufficiently wide range of parameters, so we can compare our results in nitrogen at low pressures with the available data on Trichel pulses in air at the same pressures. The main effect from the lower voltage in the case of Trichel pulses reduces to an increase in the duration of the pulse trailing edge. Thus, in [19], the shape of the pulse in air at a pressure of P = 47 torr is presented, the duration of the trailing edge being 3.5–4 μs. Our experiment at the same nitrogen pressure gives close values.

4.6. Mechanism for the Current Pulse Generation in a Nitrogen Corona with a Resistive Anode

The results obtained indicate that, in the case of a resistive anode, the mechanisms for current pulse generation in negative coronas in nitrogen and air are the same and that the negative ions play a minor role in the pulse generation. The key point in this mechanism is the negative derivative of the dynamic I–V characteristic of a low-current glow cathode sheath sustained by electron avalanches. This problem is discussed in more detail in the second part of our paper [20], in which we present the results of numerical calculations.

ACKNOWLEDGMENTS

We thank A.P. Napartovich for fruitful discussions of the results obtained and É.M. Bazelyan for valuable remarks on the text of this paper. This work was supported in part by the International Science and Technology Center, project no. 439.

REFERENCES

1. G. W. Trichel, Phys. Rev. **54**, 1078 (1938).
2. R. Morrow, Phys. Rev. A **32**, 1799 (1985).
3. A. P. Napartovich, Yu. S. Akishev, A. A. Deryugin, *et al.*, J. Phys. D **30**, 2726 (1997).
4. G. L. Weissler, Phys. Rev. **63**, 96 (1943).
5. L. B. Leob, *Electrical Coronas* (Univ. of California Press, Berkeley, 1965).
6. Yu. P. Raizer, *Gas Discharge Physics* (Nauka, Moscow, 1987; Springer-Verlag, Berlin, 1991).
7. I. P. Vereshchagin, *Corona Discharge in Electronic and Ionic Technology Devices* (Énergoatomizdat, Moscow, 1985).
8. H. Korge, M. Laan, and P. Paris, J. Phys. D **26**, 231 (1993).
9. E. Warburg, Wied. Ann. **67**, 69 (1899).
10. A. Goldman, M. Goldman, J. E. Jones, and M. Yumoto, in *Proceedings of the IX International Conference on Gas Discharges and Their Applications, Venice, 1988*, p. 197.

11. R. Fieux and M. Boutteau, Bull. Dir. Etud. Rech., Electr. Fr., Ser. B **2**, 55 (1970).

12. R. Zentner, Z. Angew. Phys. **29**, 294 (1970).

13. Yu. S. Akishev, I. V. Kochetov, A. P. Napartovich, and N. I. Trushkin, Fiz. Plazmy **21**, 187 (1995) [Plasma Phys. Rep. **21**, 179 (1995)].

14. Yu. S. Akishev, A. P. Napartovich, V. V. Ponomarenko, and N. I. Trushkin, Zh. Tekh. Fiz. **55**, 655 (1985) [Sov. Phys. Tech. Phys. **30**, 388 (1985)].

15. E. Marode, A. Goldman, and M. Goldman, in *Nonthermal Plasma Techniques for Pollution Control*, Part A: *Overview, Fundamentals, and Supporting Technologies*, Ed. by B. M. Penetrante and S. E. Schulteis (Springer-Verlag, Berlin, 1993); NATO ASI Ser., Ser. G **34** (1993).

16. M. Cernak and T. Kaneda, J. Appl. Phys. **83**, 5678 (1998).

17. Yu. S. Akishev, A. M. Volchek, A. P. Napartovich, and N. I. Trushkin, Plasma Sources Sci. Technol. **1**, 190 (1992).

18. M. Cernak, T. Hosokava, and I. Odrobina, in *Proceedings of the X International Conference on Gas Discharges and Their Applications, Swansea, 1992*, Vol. II, p. 238.

19. R. S. Sigmond, J. Appl. Phys. **53**, 891 (1982).

20. Yu. S. Akishev, M. E. Grushin, V. B. Karal'nik, and N. I. Trushkin, Fiz. Plazmy **27**, 563 (2001) [Plasma Phys. Rep. **27**, 532 (2001)].

Translated by N. F. Larionova

Plasma Physics Reports, Vol. 27, No. 6, 2001, pp. 532–541. Translated from Fizika Plazmy, Vol. 27, No. 6, 2001, pp. 563–572.

LOW-TEMPERATURE PLASMA

Pulsed Mode of a Negative Corona in Nitrogen: II. Numerical Calculations

Yu. S. Akishev, M. E. Grushin, V. B. Karal'nik, and N. I. Trushkin

Troitsk Institute for Innovation and Thermonuclear Research, Troitsk, Moscow oblast, 142090 Russia

Received September 28, 2000

Abstract—A simplified model of a cathode sheath sustained by electron avalanches is presented. The model is used to calculate the pulsed mode of a negative corona in nitrogen in order to establish the physical picture of the processes occurring in a pulsed corona. The most important point is that, in the pulsed mode, both the averaged and dynamic current–voltage characteristics of a glow cathode sheath are found to have a negative slope. Lowering the degree to which the glow cathode sheath is subnormal (by sharply reducing the sheath area) or switching on additional ionization mechanisms (e.g., stepwise ionization) that force the cathode sheath to evolve into a prearc spot causes the negative slopes of the averaged and dynamic current–voltage characteristics of the sheath to become more gradual and even positive, thereby stabilizing the discharge current. © *2001 MAIK "Nauka/Interperiodica".*

1. INTRODUCTION

The development of a negative corona is usually attributed to the formation of a glow sheath at the cathode point. The so-called ignition voltage of the corona is determined from the condition for the avalanche processes in a vacuum electric field in the discharge gap to be steady and self-sustaining [1]. For nitrogen, this condition has the form

$$\int_0^d \alpha_i dx \simeq \ln\frac{1+\gamma}{\gamma}, \qquad (1)$$

where α_i is the gain factor of an electron avalanche caused by direct ionization processes; d is the distance between the electrodes; and γ is the effective positive feedback factor for electron avalanches, which is determined by electron emission from the cathode surface bombarded by photons, positive ions, and excited particles.

On the other hand, condition (1) is also the condition for a glow cathode sheath to be self-sustaining, in which case d stands for the sheath thickness. For a steady cathode sheath, condition (1) reflects the charge conservation in the sheath.

With regard to the cathode sheath, condition (1) can be understood not only as a steady-state condition but also as a condition that holds on average over certain time intervals:

$$\langle(1+\gamma)j_{ic}(t)\rangle \simeq \left\langle \gamma j_{ic}(t)\exp\left(\int_0^{d(t)}\alpha(x)dx\right)\right\rangle, \qquad (1')$$

where j_{ic} is the flux density of positive ions at the cathode.

The modified condition (1') implies that the time-averaged conduction currents at the left and right boundaries of the cathode sheath are equal to one another (or, in other words, the charge in the cathode sheath is conserved). Consequently, according to condition (1'), it is possible to achieve a steady discharge mode with an unsteady glow cathode sheath. The time-averaged parameters of such a sheath should correspond to the subnormal state, because it is the state that is unstable due to the negative slope of the current–voltage (I–V) characteristic of the sheath [1] and, consequently, can force the discharge to evolve into the pulsed mode.

The area of the cathode spot, which was determined from visual observations, allowed us to estimate the mean current density at the cathode point as $j \simeq 2$–6 A/cm^2. According to this estimate, the above situation is typical of negative coronas in air, which are unstable in the range of initial currents and exist in a pulsed mode (Trichel pulses [2]). In the experimental part of our work [3], an analogous situation was achieved for the first time in a corona in nitrogen.

The steady-state pulsations of a negative corona in air were calculated for the first time by Napartovich *et al.* [4]. The current pulse generated by a voltage pulse applied to a unionized gas in the gap between the point and plane electrodes was calculated in a number of earlier and subsequent papers (see [5, 6] and the literature cited therein). It should be noted that both the shape and the parameters of the initial current pulse during the discharge ignition (the pulse amplitude and the durations of the leading and trailing edges of the pulse) differ markedly from those of the regular pulses in a steady-state corona, because the conditions for the formation of these pulses are different [7–10].

1063-780X/01/2706-0532$21.00 © 2001 MAIK "Nauka/Interperiodica"

The difference is especially pronounced for a negative corona in nitrogen, in which case the *I–V* characteristic of the corona describes a hysteresis loop [3]. The hysteresis effect manifests itself in the fact that the voltage required to drive the ignition pulse is higher than that supplying regular pulses. As a result, the ignition and regular pulses differ substantially in shape, amplitude, and characteristic duration. This conclusion is confirmed by Fig. 1, which compares the experimental data on ignition and regular pulses.

However, it should be kept in mind that, after the ignition, a corona does not inevitably evolve into a pulsed mode; whether such a transition occurs depends on the sort of gas and discharge parameters [3]. The possibility of such evolution should be assessed in each particular experiment. Consequently, when analyzing steady-state pulsations, special care is needed in using the experimental data (see, e.g., [11, 12]) and numerical results [5, 6] on the ignition pulses.

In the first part of our work [3], we arrived at the conclusion that the current pulses in negative coronas in air and nitrogen are generated by identical mechanisms. The key factor in the generation of regular pulses is the negative slope of the dynamic *I–V* characteristic of the glow cathode sheath of a corona in the range of initial corona currents. In this paper, which is the second part of our study, we present the results of numerical calculations aimed at justifying this conclusion for a negative corona in nitrogen.

In [3], we established that the pulsed mode of a negative corona in nitrogen can be achieved over a broad range of experimental parameters, in particular, in long and short discharge gaps. Consequently, the physical nature of the pulsed mode is not governed by the distance between the electrodes. On the other hand, a negative corona in a short interelectrode gap is simpler to model than that in a long gap. For this reason, we will focus below on the calculation of steady-state pulsations of a corona in a short discharge gap.

The numerical results are tested against the experimental data for coronas with a resistive anode, which makes it possible to prevent plasma production in the corona, thereby avoiding current pulses with complicated double-humped profiles. In this case, current pulses in nitrogen are similar in shape to Trichel pulses in air. The scheme of the discharge circuit is presented in Fig. 2.

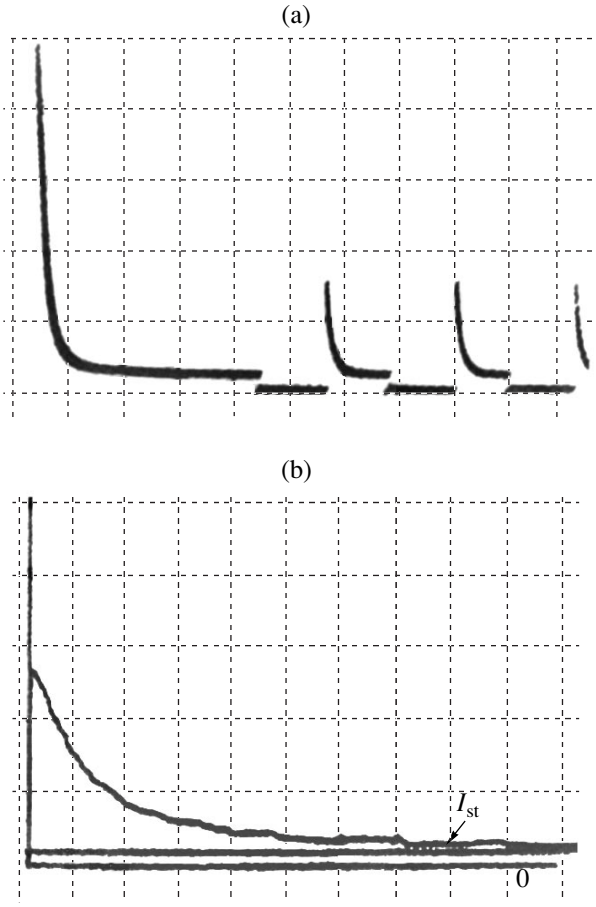

Fig. 1. (a) Sequence of the first four current pulses during the evolution of the cathode sheath to the pulsed mode in nitrogen for P = 760 torr, d = 15 mm, r_c = 0.1 mm, R = 51 MΩ, $\langle I\rangle$ = 15 μA, U = 2.3 kV, and U_{ign} = 3.1 kV. The amplitude of the first pulse is $I_A \approx 3.5$ mA. The time scale is 2 ms/division, and the current scale is 0.2 mA/division. (b) Current pulse igniting the corona during the evolution to the steady-state regime for P = 760 torr, d = 15 mm, r_c = 0.1 mm, R = 0.75 MΩ, $\langle I\rangle$ = 15 μA, U = 2.5 kV, and U_{ign} = 3.1 kV. The pulse amplitude is $I_A \approx 7$ mA. The time scale is 0.1 ms/division, and the current scale is 0.4 mA/division. The lower horizontal line corresponds to a zero current, and the upper horizontal line corresponds to the steady-state corona current I = 80 μA.

2. DESCRIPTION OF THE MODEL

The experimental results were obtained for discharges in short interelectrode gaps in which the effects of geometric expansion of the electric field lines are unimportant. Such discharges can be modeled under the assumption that the discharge-current cross section is constant. We are particularly justified in using this approach because the main discharge processes to be modeled occur in a comparatively thin cathode sheath, which is usually much shorter than the interelectrode gap. Without allowance for geometric effects, the problem can be reduced to that of modeling a one-dimensional unsteady glow discharge in a short interelectrode gap.

Our model is based on the familiar continuity equations describing the dynamics of the electron density n_e and positive ion density n_i:

$$\frac{\partial n_e}{\partial t} - \operatorname{div} \mathbf{j}_e = \alpha j_e + S^* - R, \tag{2}$$

$$\frac{\partial n_i}{\partial t} + \operatorname{div} \mathbf{j}_i = \alpha j_e + S^* - R, \tag{3}$$

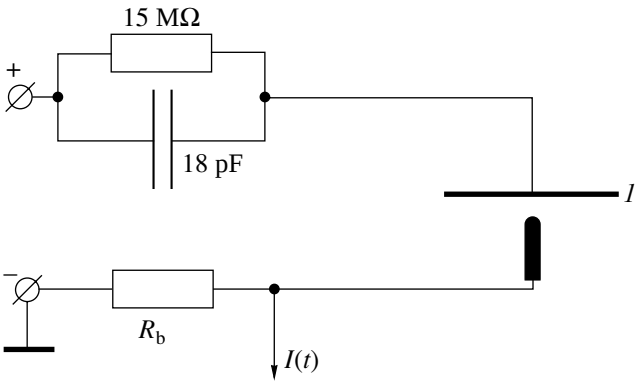

Fig. 2. Scheme of the discharge circuit: (*1*) discharge gap.

where $\mathbf{j}_e$ and $\mathbf{j}_i$ are the electron and ion flux densities, α is the Townsend coefficient for gas (N_2) ionization by direct electron impact, S^* is the power of the stepwise ionization source, and R is the power of charged-particle losses due to volumetric processes.

Equations (2) and (3) are supplemented with Poisson's equation, Kirchhoff's equation, and the boundary conditions at the electrodes:

$$\operatorname{div}\mathbf{E} = \frac{e(n_i - n_e)}{\varepsilon_0}, \tag{4}$$

$$U_0 = U_d + U_R, \tag{5}$$

$$\gamma j_{ic} = j_{ec}, \quad j_{ia} = 0. \tag{6}$$

Here, e is the electron charge, ε_0 is the permittivity of free space, $\mathbf{E}$ is the electric field strength in the discharge, U_0 is the amplitude of the applied voltage, U_d is the voltage drop across the discharge gap, U_R is the voltage drop at the ballast resistor, $\gamma \simeq 0.03$ is the coefficient of secondary electron emission from the cathode (the electron flux j_{ec}) caused by the ion flux j_{ic} (the electron emission due to metastable nitrogen atoms and photons is neglected), and j_{ia} is the ion flux emitted by the anode (which is assumed to emit no ions). The quantities U_d and U_R have the form

$$U_d = \int_0^d E dx, \quad U_R = RI_R = \frac{Q}{C}, \quad Q(t) = \int_0^t I dt, \tag{7}$$
$$I(t) = S(e\mu_e n_e E + e\mu_i n_i E + \varepsilon_0 \dot{E}),$$

where d is the length of the interelectrode gap, Q is the charge at the capacitor plates, C is the capacitance of the capacitor, S is the cross-sectional area of the discharge column, μ_e and μ_i are the electron and ion mobilities, and $I(t)$ is the total discharge current with allowance for the displacement current (the contribution of diffusive processes to the total current is ignored).

Equations (2)–(7) describe the longitudinal structure of a transversely homogeneous discharge over the entire interelectrode gap and make it possible to follow the discharge evolution. Unfortunately, these integrodifferential equations are fairly difficult to solve numerically: to calculate the steady-state discharge mode requires large amounts of computer time. Under certain simplifying assumptions regarding the longitudinal discharge structure, integration of Eqs. (2)–(7) over the interelectrode gap can result in a (formally) zero-dimensional set of the differential equations for a number of parameters. Numerical integration of the reduced equations requires far less computer time, thereby making it possible to calculate a large number of versions and to establish many parametric dependences characteristic of the discharges under investigation. In many cases, this advantage of reduced equations can compensate for the insufficient accuracy of the model.

We tried to simplify the mathematical model by taking into account the familiar features of the longitudinal structure of glow discharges and their kinetics at low currents corresponding to a negative corona:

(i) The main components of a glow discharge are the cathode and anode sheaths and the plasma column between them.

(ii) The potential drop across the anode sheath is usually small enough not to seriously influence the total voltage drop across the discharge and thus can be ignored.

(iii) The entire plasma column can be regarded as being homogeneous.

(iv) Because of the high mobility of the electrons, their dynamics can be treated in the quasisteady approximation, in which the term $\partial n_e/\partial t$ in Eq. (2) is omitted.

(v) In a glow cathode sheath, the processes of stepwise ionization and charged-particle recombination can be neglected.

Hence, we can model glow discharges by analyzing, first, a cathode sheath sustained by electron impact–driven avalanche ionization and, second, a quasineutral plasma column with a uniform electric field.

Let us discuss additional simplifying assumptions that can be made when modeling a cathode sheath at high pressures. It is worth noting that, in a steady discharge, the positive space charge is distributed almost uniformly within a normal glow cathode sheath [1], in which case the electric field decreases linearly with distance from the cathode. In an unsteady discharge, the cathode sheath may be thicker than the steady-state normal sheath; accordingly, the electric field within the sheath may be lower. As a result, the drifting positive ions do not have enough time to equalize the positive space charge distribution in the sheath, so that the electric field profile will progressively deviate from being linear.

One-and-a-half-dimensional simulations of an unsteady cathode sheath in air [4] clearly show that, during the sheath compression, the space charge in the cathode region is distributed nonuniformly: it is concentrated preferentially inside a narrow layer at a certain distance from the cathode, while the space charge density near the cathode is low (Fig. 3). In this case, the electric field decreases gradually in the region where the space charge is low and decreases sharply in the region where the space charge is high; moreover, the profile of the electric field that decreases with distance from the cathode can be approximated by a straight line.

The strong electric field region near the cathode (where the space charge density is low) makes the most important contribution to both the voltage drop across the cathode sheath and the intensity of ionization processes in the sheath. Consequently, the length of the strong field region can be regarded as the effective thickness of the cathode sheath. In order to estimate the sheath thickness, we turn to the idea originated by Cernak *et al.* [12], who suggested that the cathode sheath thickness d_c is close to the scale length on which the avalanche ionization power described by the source term $\alpha(E(x))j_e(x)$ reaches its maximum.

In the quasisteady approximation, the electron avalanche formation in the strong field region near the cathode can be described by the relationships

$$j_e(x) \simeq \gamma j_{ic} \exp \int_0^x \alpha(E(x))dx, \tag{8}$$

$$E(x) = E_c - \frac{j_{ic}}{\mu_i E_c}\frac{e}{\varepsilon_0}x, \tag{9}$$

where E_c is the electric field at the cathode surface and the field profile $E(x)$ in the region of a low space charge is formed by the drift flux j_{ic} of positive ions toward the cathode.

For the given field profile (9), the condition for the function $\alpha(E(x))j_e(x)$ to be maximum yields the following equation for the effective thickness d_c of the cathode sheath:

$$\alpha^2(E(d_c)) = \frac{j_c}{\mu_i E_c}\frac{e}{\varepsilon_0}\frac{\partial}{\partial E}\alpha(E(d_c)). \tag{10}$$

Taking into account the above characteristic features of the discharge, we can integrate the integrodifferential equations (2)–(7) over the x coordinate in order to arrive at a far simpler set of the formally zero-dimensional differential equations. The reduced set, which should be solved with allowance for relationship (10), consists of the balance equations for the components of the total discharge current $I(t)$ in four cross sections of the discharge column.

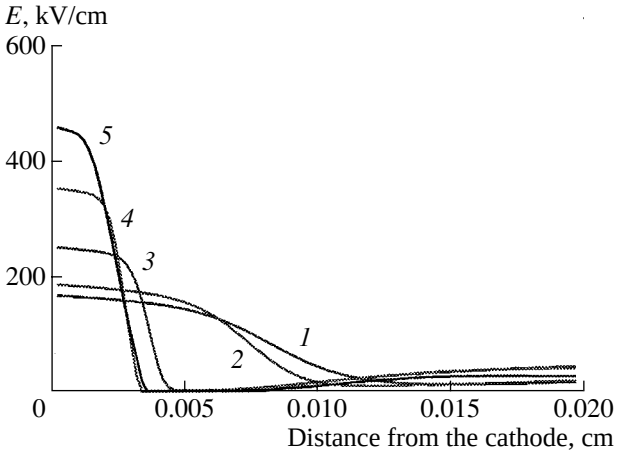

Fig. 3. Evolution of the electric field at the front of a Trichel pulse in the cathode sheath in air. The longitudinal field profiles were calculated in [4] at (*1*) 89999.07, (*2*) 89999.52, (*3*) 90000.00, (*4*) 90000.50, and (*5*) 90001.25 ns.

The first reduced equation is the condition that the total discharge current be continuous at the right and left boundaries of the cathode sheath:

$$\begin{aligned}&\varepsilon_0 S\dot{E}_c + eS(1+\gamma)j_{ic}\\ &= eS\gamma\exp(\alpha(E_c)d_c\theta)j_{ic} + eSn_p\dot{d}_c = I(t).\end{aligned} \tag{11}$$

Here, the area S of the current spot at the cathode surface serves as a free model parameter (this area was measured visually by observing the discharge and was used as an input parameter for each of the calculation versions) and the plasma density n_p in the discharge column serves as an adjustable parameter.

When deriving Eq. (11), we used the relationship $\int_0^d \alpha(E(x))dx \simeq \alpha(E_c)d_c\theta$ (where the parameter θ is close to unity) and took into account the fact that the total rate of change of the space charge in an unsteady cathode sheath depends on the time rate of change of the sheath thickness.

The second reduced equation is the condition that the total discharge current be continuous at the boundary between the cathode sheath and the plasma column:

$$I(t) = eS\mu_e n_p E_p + \varepsilon_0 S\dot{E}_p, \tag{12}$$

where E_p is the electric field in the plasma column.

The third equation implies that the total current at the cathode surface is equal to the total current in the external circuit:

$$I(t) = I_R + \dot{I}_R RC. \tag{13}$$

The fourth equation reflects the voltage balance in the circuit under investigation:

$$I_R = \frac{U_0 - (E_c d_c + E_p(d - d_c))}{R}, \tag{14}$$

where $E_p(d - d_c)$ is the voltage drop across the plasma column, $E_c d_c$ is the voltage drop across the cathode sheath, d is the interelectrode distance, C is the capacitance of a capacitor in the external circuit, and R is the ballast resistance of the discharge.

The dependence of the experimental ionization coefficient for nitrogen, $\alpha(E)$, on the electric field strength was taken from [13] and was approximated by the expression

$$\alpha(E) = \chi_1 \exp(-E_{cr1}/E) + \chi_2 \exp(-\sqrt{E_{cr2}/E}),$$

where the parameter values $\chi_1 = 7.3 \times 10^3$ cm^{-1}, $E_{cr1} = 2.1 \times 10^5$ V/cm, $\chi_2 = 3.1 \times 10^4$ cm^{-1}, and $E_{cr2} = 4.1 \times 10^6$ V/cm correspond to the nitrogen pressure $P = 750$ torr.

Below, we will present the results of calculations of the steady-state current pulsations in nitrogen at pressures of $10 \le P \le 100$ torr. The calculations were also carried out for lower and higher pressures. However, an analysis of the results obtained shows that our simplified model is valid only in the indicated pressure range.

For low pressures, our approach fails to correctly determine the cathode sheath thickness d_c. The reason for this is as follows. In the cathode sheath, the mean space charge density decreases with pressure as P^2. This indicates that, at low pressures, the electric field decreases very gradually with distance from the cathode, so that the ionization source term $\alpha(E(x))j_e(x)$ has a very flat peak. As a result, intense ionization processes will efficiently generate electron avalanches over a fairly long distance from the cross section at which the ionization source term is maximum. However, this situation contradicts the assertion that, near the cathode, the main contribution to both the intensity of ionization processes and the voltage drop across the cathode sheath comes from the strong field region whose length d_c is determined by the condition that the function $\alpha(E(x))j_e(x)$ be maximal.

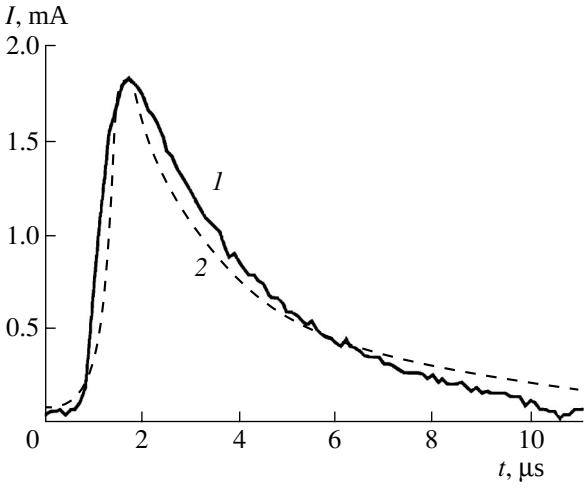

Fig. 4. (*1*) Experimental and (*2*) numerical waveforms of a current pulse in nitrogen for $P = 10$ torr, $d = 3$ mm, $\langle I \rangle = 60$ μA, and $U = 0.60$ kV (the cathode is a 10-mm-diameter rod with a flat end).

At high pressures, the cathode sheath evolves so rapidly that the calculated rise time of the pulse front becomes comparable to the time required for electrons to drift across the sheath. In this case, the quasisteady approximation fails to describe the electron dynamics.

Note that the above range of nitrogen pressures is merely the range in which the calculated results are expected to agree quantitatively with the experimental data. However, beyond this pressure range, the simulations based on the simplified model will yield a qualitatively correct picture of the physical mechanism for generating current pulses.

3. NUMERICAL RESULTS AND COMPARISON WITH THE EXPERIMENT

In the pressure range $10 \le P \le 100$ torr, the results obtained with the simplified model were found to agree quite well with the experimental data. Note that, in our experiments, an interelectrode gap of length $d = 3$ mm was filled with nitrogen at the pressure $P = 10$ torr. In this case, the cathode was a 10-mm-diameter rod with a flat end. In experiments with nitrogen at the pressures $P = 30$ and 100 torr, the interelectrode gap was as long as 1 mm and a 2-mm-diameter wire with a hemispherical end served as the cathode.

3.1. Calculation of the Waveforms of Current Pulses in a Negative Corona in Nitrogen

As an example, Figs. 4–6 show numerical waveforms and experimental oscilloscope traces obtained for the pressures $P = 10$, 30, and 100 torr. We can see that the calculated pulse amplitude and pulse front duration agree qualitatively with the experimental data. However, for the same discharge parameters, the calculated period of the current pulses is always longer than the measured one.

We attribute this discrepancy to the characteristic features of the dynamics of the cathode sheath at the trailing edge of the current pulse. These features were noticed in the first part of our study [3]: in experiments, the current at the trailing edge of the pulse was found to decrease sharply (in a jumplike manner) after reaching a certain critical value. A jumplike decrease in the current was accompanied by the decay of the cathode sheath due to diffusion; in turn, the decay of the sheath hastened the establishment of conditions favorable for the formation of the next current pulse. In our simulations, this effect was neglected, so that the current at the trailing edge of the pulse decreased gradually, thereby leading to a longer period of pulsations in comparison with the experimentally measured period. Nevertheless, the experimentally observed increase in the repe-

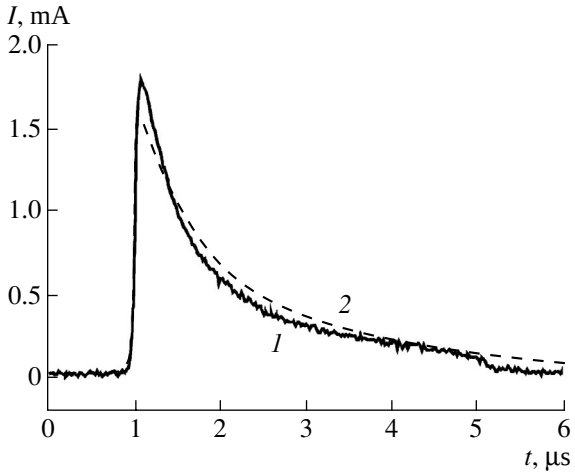

Fig. 5. (*1*) Experimental and (*2*) numerical waveforms of a current pulse in nitrogen for P = 30 torr, d = 1 mm, $\langle I\rangle$ = 15 μA, and U = 0.57 kV (the cathode is a 2-mm-diameter wire with a hemispherical end).

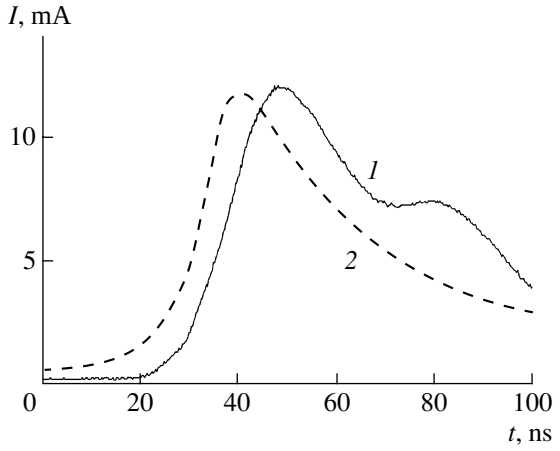

Fig. 6. (*1*) Experimental and (*2*) numerical waveforms of a current pulse in nitrogen for P = 100 torr, d = 1 mm, $\langle I\rangle$ = 38 μA, and U = 0.9 kV (the cathode is a 2-mm-diameter wire with a hemispherical end).

tition rate of the pulses with increasing mean current was captured qualitatively by our calculations.

In our model, the plasma density in the discharge column served as an adjustable parameter and was chosen in such a way that the calculated pulse parameters coincided with the experimental ones. We found that, the larger the pulse amplitude A and/or the higher the pressure P, the larger the adjustable plasma density n_p should be (see table). Adjusting the plasma density in such a fashion does not contradict the accepted views regarding the physical nature of glow discharges.

3.2. Parametric Dependences of the Voltage Drop across the Pulsed Cathode Sheath and the Sheath Thickness

Figures 7 and 8 present the thickness d_c of the cathode sheath and the voltage drop U_c across the sheath calculated as functions of the mean current. The vertical bars at the corresponding magnitudes of the current reflect the range of changes of the quantities d_c and U_c during pulsations. The horizontal dashes indicate the time-averaged values of the sheath thickness and the voltage drop across the sheath. We can see that, as the mean discharge current increases, the ranges over which the quantities d_c and U_c change become narrower and the time-averaged values of the sheath thickness and voltage drop across the sheath decrease. Figures 7 and 8 clearly demonstrate that the time-averaged parameters of a pulsed cathode sheath correspond to the subnormal state, in which the *I–V* characteristic of the sheath has a negative slope.

3.3. Calculation of the Currents at Which the Pulsed Mode Terminates

The pulsed mode of the discharge in nitrogen terminates above a certain value I^* of the mean current, as is the case with discharges in air. Observations show that, when the current approaches the critical value I^*, the amplitude of pulsations does not decrease gradually to zero; instead, the pulsations decay in a jumplike manner. During this jumplike transition from a pulsed mode to a steady-state discharge, the cathode spot is clearly seen to become smaller in size. Recall that, after the jumplike transition, the cathode sheath at low pressures (P < 0.5 atm) remains in the glow regime, whereas the cathode sheath at high pressures evolves into a prearc spot.

As was mentioned above, the area S of the glow cathode spot serves as a free parameter of the model; for each of the calculation versions, the value of S was taken from experiments. Calculations in which the area S was

Table

P, torr	10	10	10	30	30	100	100
$\langle I\rangle$, μA	13	30	60	15	35	38	108
A, mA	4	3.4	1.8	1.8	0.85	12	11
n_p, cm^{-3}	1.4×10^{12}	8.7×10^{11}	4.8×10^{11}	6×10^{12}	4×10^{12}	4.5×10^{13}	1.8×10^{13}

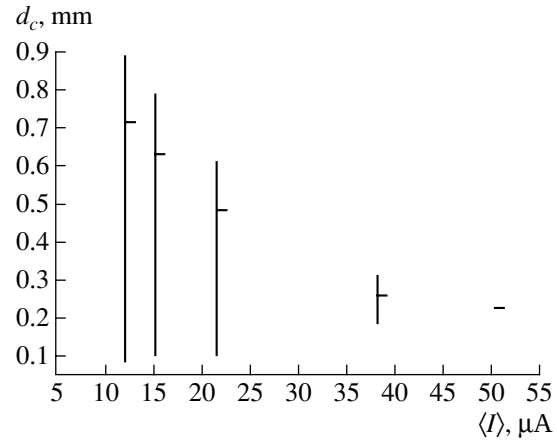

Fig. 7. Calculated cathode sheath thickness d_c vs. the mean discharge current for the pressure P = 30 torr, the cathode spot area S = 0.34 mm^2, and the interelectrode distance d = 1 cm. The vertical bars reflect the range of changes of the thickness d_c over the period of pulsations, and the horizontal dashes indicate the period-averaged sheath thickness.

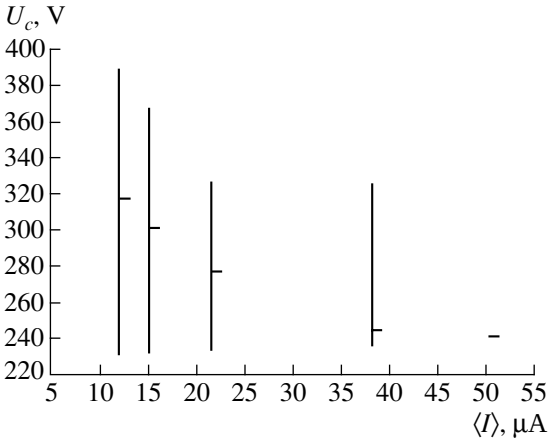

Fig. 8. Calculated voltage drop U_c across the cathode sheath vs. the mean discharge current for the pressure P = 30 torr, the cathode spot area S = 0.34 mm^2, and the interelectrode distance d = 1 cm. The vertical bars reflect the range of changes of the voltage drop U_c over the period of pulsations, and the horizontal dashes indicate the period-averaged voltage drop.

determined from visual observations of the cathode spot in the pulsed mode and was assumed to be independent of the mean current in a corona yielded much higher critical currents than the experimental ones. However, calculations in which the area S was assumed to decrease abruptly when the current approached the measured critical value I^* showed that the pulsations terminated when the critical current was reached, in agreement with the experimental data.

Note that, as the cathode spot area decreases at a constant mean current, the degree to which the glow cathode sheath is subnormal decreases and the negative slope of the I–V characteristic of the sheath becomes more gradual; in this case, the sheath itself becomes more stable. At the same time, it still remains unclear what the physical reasons are for such a sharp decrease in the area of the glow cathode sheath when the current approaches the critical value I^*.

Our simulations also show that switching on additional ionization mechanisms (e.g., stepwise ionization) that force the cathode sheath to evolve into a prearc spot causes the negative slopes of both the averaged and dynamic I–V characteristics of the sheath to become more gradual and even positive, thereby also stabilizing the discharge current.

3.4. Dynamics of the Parameters of a Pulsed Sheath

Figures 9–11 illustrate the dynamics of the total current in a pulse, the displacement current at the cathode, the cathode sheath thickness, the electric field at the cathode, and the electron-avalanche multiplication factor $\Phi = \frac{\gamma}{1+\gamma}\exp\int_0^{d_c}\alpha(x)dx$. The results of simulations make it possible to reconstruct a complete picture of the evolution of a discharge in the pulsed mode.

As the current in a pulse increases, the cathode sheath is compressed and the electric field at the cathode increases sharply, causing the efficient production of electrons in the sheath. In this stage, the displacement current makes a significant contribution to the total discharge current at the cathode (Fig. 9). A decrease in the pulse current is accompanied by the expansion of the decaying cathode sheath, in which the electron-avalanche multiplication factor is negative ($\Phi < 1$), so that the electron avalanches are gradually damped. This stage lasts until the expanding cathode sheath acquires a sufficiently high space charge from

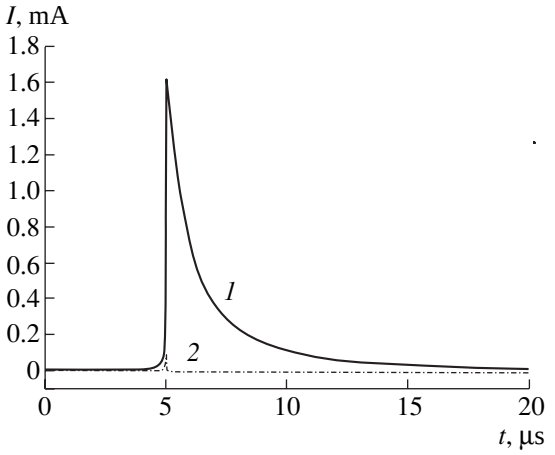

Fig. 9. Time evolutions of (*1*) the total current I_Σ in a pulse and (*2*) the displacement current I_{dis} at the cathode for the pressure P = 30 torr, the cathode spot area S = 0.34 mm^2, and the interelectrode distance d = 1 cm.

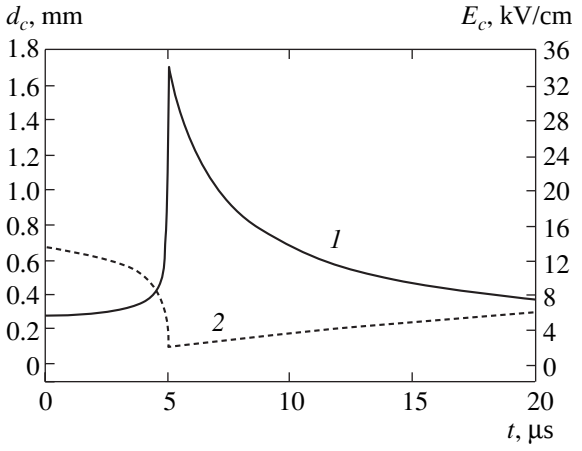

Fig. 10. Time evolutions of (*1*) the electric field E_c at the cathode and (*2*) the cathode sheath thickness d_c for the pressure P = 30 torr, the cathode spot area S = 0.34 mm^2, and the interelectrode distance d = 1 cm.

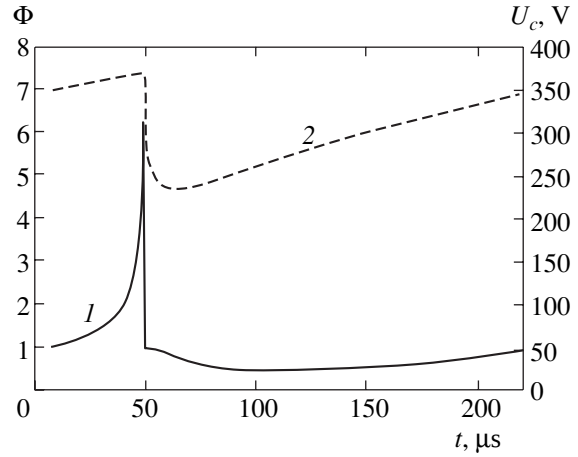

Fig. 11. Time evolutions of (*1*) the electron-avalanche multiplication factor Φ and (*2*) the voltage drop U_c across the cathode sheath for the pressure P = 30 torr, the cathode spot area S = 0.34 mm^2, and the interelectrode distance d = 1 cm.

the plasma, so that the electric field in the sheath again starts increasing and eventually gives rise to electron avalanches. Then, the sheath rapidly evolves into the compression stage, and the process repeats itself.

An analogous dynamic picture of the cathode sheath was obtained by Napartovich *et al.* [4], who calculated Trichel pulses in air. Hence, in contrast to the conclusion drawn by Yu.P. Raizer [15], we can state that the presence of negative ions near the corona-electrode surface does not play a governing role in the onset of the pulsed mode in a negative corona or in a glow discharge.

The periodic behavior of the main discharge parameters in the pulsed mode can be illustrated in the corresponding phase planes. The phase trajectories of the currents, the sheath thickness, and the electric field at the cathode are presented in Fig. 12, which shows that, at low mean currents, the pulsations of a glow cathode sheath are associated with the fact that the dynamic differential resistance of the sheath is negative.

3.5. Condition for the Pulsed Sheath to be Self-Sustaining

Here, we should point out an important circumstance associated with the pulsed mode of a cathode sheath. Our examination shows that, in an unsteady glow discharge, the condition for the pulsed cathode sheath to be self-sustaining can only be satisfied on average over certain time intervals; i.e., the modified condition (1') is satisfied. As a result, the seemingly plausible assertion that the mean electron-avalanche multiplication factor $\langle\Phi\rangle = \left\langle \frac{\gamma}{1+\gamma}\exp\int_0^{d_c}\alpha(x)dx \right\rangle$ equals unity turns out to be wrong for the pulsed mode. According to our simulations of the pulsed mode, we have $\langle\Phi\rangle \neq 1$.

3.5. Discussion of the Data from the Literature in Light of the Results Obtained

We have established that, in the pulsed mode, the time-averaged and dynamic *I–V* characteristics of the cathode sheath in a negative corona both have a negative slope. Lowering the degree to which the cathode sheath is subnormal (by sharply reducing the cathode

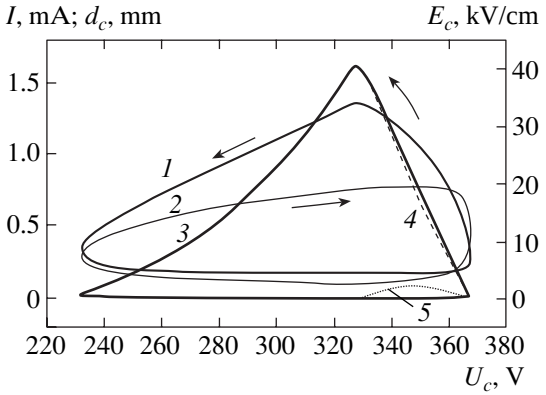

Fig. 12. Phase trajectories of the currents, the sheath thickness, and the electric field at the cathode for the pressure P = 30 torr, the cathode spot area S = 0.34 mm^2, and the interelectrode distance d = 1 cm: (*1*) the electric field E_c at the cathode, (*2*) the cathode sheath thickness d_c, (*3*) the total current I in the pulse, (*4*) the drift current at the cathode, and (*5*) the displacement current I_{dis} at the cathode. The arrows point in the direction of motion along the phase trajectories during the pulse.

spot area) or switching on additional ionization mechanisms (e.g., stepwise ionization) in the sheath will cause the negative slopes of the averaged and dynamic *I–V* characteristics to become far more gradual and even positive, thereby stabilizing the corona.

In this context, we should mention theoretical papers [16, 17], in which the termination of Trichel pulses at the current $I = I^*$ is attributed to gas heating near the cathode in a negative corona. In order to check this conclusion, we carried out a special series of experiments with a corona in air in a coaxial device. Since, in these experiments, the corona electrode (a thin wire) was strongly heated (up to 1100 K), the gas in the major portion of the interelectrode gap was maintained at room temperature by air puffing along the discharge axis.

We found that such strong gas heating near the cathode did not prevent the corona from evolving into the pulsed mode but acted merely to reduce the amplitude of the Trichel pulses at most by a factor of 2. Hence, the results obtained in this paper enable us to conclude that the gas heating is not the main factor that causes the pulsed mode in a negative corona to terminate, but merely accompanies the termination process.

In the first part of this study [3], we established that the onset of ionization instabilities in a glow cathode sheath (especially at high nitrogen pressures, $P > 0.5$ atm) can force the sheath to evolve into a prearc spot [14], which suppresses the pulsed mode of the corona. The stabilizing role of the prearc spot in suppressing the current pulsations of a negative corona has not yet been discussed in the literature.

Thus, Hernandez-Avila *et al.* [18] reported their observations of the pulsed mode of a discharge in chemically pure (99.999%) nitrogen at pressures of tens of atmospheres. In those experiments, the radius of the corona-electrode point was very small, $r = 1$–10 μm. The pulsations were observed to occur in the kilohertz frequency range at mean currents from 10 to 60 μA during repeated ignitions of the corona (immediately after the nitrogen gas puffing, the corona was ignited only at high currents, $I = 100$–600 μA, and experienced no pulsations).

The authors of [18] pointed out a certain similarity between the pulses recorded in their experiments and Trichel pulses in air and, by way of analogy, explained the onset of pulsations in terms of the increase in the partial pressure of electronegative impurities, which accumulated in the discharge chamber during the high-current stage of the corona, to a level of about $\sim 3 \times 10^{-3}$ torr, the nitrogen pressure being about 20 atm.

In our opinion, such low densities of electronegative impurities (about $\sim 10^{14}$ cm^{-3}) are insufficient to ensure conditions analogous to those under which the actual Trichel pulses are initiated, because, for impurity densities such as in the experiments of [18], the effective electron attachment length exceeds the interelectrode distance ($d = 10$ mm) by many orders of magnitude. Under these conditions, only a small amount of negative ions can be produced in the corona; therefore, the influence of impurities on the discharge parameters is insignificant.

Presumably, the onset of Trichel pulses in the experiments of [18] can be explained by an effect that is well known in gas-discharge practice—the conditioning (or cleaning) of the electrode by a discharge (in the case at hand, by a high-current corona). During repeated ignitions, the prearc spot appears at the preliminary cleaned electrode (and, accordingly, the corona evolves into the high-current pulsation-free regime) after the voltage drop across the interelectrode gap becomes sufficiently high (rather than just after ignition). In other words, the conditioning of the corona electrode allows one to obtain a glow cathode sheath at the electrode point in an unsteady subnormal state, in which the corona current pulsates.

4. CONCLUSION

In the experimental part of our study [3], we have revealed that the averaged *I–V* characteristic of a negative corona in nitrogen exhibits a hysteresis loop. The regular current pulsations are found to occur in the hysteresis region. The frequency spectrum and shape of the pulsations are radically different for metal and resistive anodes. In a negative corona with a resistive anode in nitrogen, the parameters of current pulses are close to those of Trichel pulses in air.

Here, we have presented the results of numerical calculations and have shown that both the time-averaged and dynamic *I–V* characteristics of a glow cathode sheath of a negative corona have a negative slope. This circumstance plays a key role in the onset of the pulsed mode of a low-current discharge.

Our simulations have also shown that lowering the degree to which the glow cathode sheath in a negative corona is subnormal (by sharply reducing the cathode spot area), or that switching on additional ionization mechanisms (e.g., stepwise ionization) in the sheath causes the negative slopes of the averaged and dynamic *I–V* characteristics of the sheath to become far more gradual and even positive, thereby stabilizing the discharge current.

ACKNOWLEDGMENTS

We are grateful to A.P. Napartovich for fruitful discussions of the results obtained and É.M. Bazelyan for valuable remarks on the text of this paper. This study was supported in part by the International Science and Technology Center, project no. 439.

REFERENCES

1. A. von Engel and M. Steenbeck, *Elektrische Gasentladungen, Ihre Physik und Technik* (Springer-Verlag, Berlin, 1932, 1934; ONTI, Moscow, 1935), Vols. 1, 2.

2. G. W. Trichel, Phys. Rev. **54**, 1078 (1938).
3. Yu. S. Akishev, M. E. Grushin, V. B. Karal'nik, and N. I. Trushkin, Fiz. Plazmy **27**, 550 (2001) [Plasma Phys. Rep. **27**, 520 (2001)].
4. A. P. Napartovich, Yu. S. Akishev, A. A. Deryugin, *et al.*, J. Phys. D **30**, 2726 (1997).
5. R. Morrow, Phys. Rev. A **32**, 1799 (1985).
6. D. K. Gupta, S. Mahajan, and P. I. John, J. Phys. D **33**, 681 (2000).
7. J. A. Cross, R. Morrow, and G. N. Haddad, J. Phys. D **19**, 1007 (1986).
8. J. A. Scott and G. N. Haddad, J. Phys. D **19**, 1507 (1986).
9. Yu. S. Akishev, M. E. Grushin, A. P. Napartovich, and N. I. Trushkin, in *Proceedings of the 12th International Conference on Gas Discharges and Their Applications, Greifswald, 1997*, Vol. 1, p. 153.
10. Yu. S. Akishev, M. E. Grushin, I. V. Kochetov, *et al.*, Fiz. Plazmy **25**, 998 (1999) [Plasma Phys. Rep. **25**, 922 (1999)].
11. M. Cernak and T. Kaneda, J. Appl. Phys. **83**, 5678 (1998).
12. M. Cernak, T. Hosokava, and I. Odrobina, in *Proceedings of the 10th International Conference on Gas Discharges and Their Applications, Swansea, 1992*, Vol. II, p. 238.
13. V. L. Granovskiĭ, *Electric Current in Gas: Steady-state Current* (Nauka, Moscow, 1971).
14. Yu. S. Akishev, A. P. Napartovich, V. V. Ponomarenko, and N. I. Trushkin, Zh. Tekh. Fiz. **55**, 655 (1985) [Sov. Phys. Tech. Phys. **30**, 388 (1985)].
15. Yu. P. Raizer, *Gas Discharge Physics* (Nauka, Moscow, 1987; Springer-Verlag, Berlin, 1991).
16. J. E. Jones, in *Proceedings of the 23rd International Conference on Phenomena in Ionized Gases, ICPIG, Toulouse, 1997*, Vol. IV, p. 18.
17. J. E. Jones, A. Goldman, and M. Goldman, in *Proceedings of the 12th International Conference on Gas Discharges and Their Applications, Greifswald, 1997*, p. 149.
18. J. L. Hernandez-Avila, M. Nur, N. Bonifaci, and A. Denat, in *Proceedings of the 22nd International Conference on Phenomena in Ionized Gases, Hoboken, 1995*, p. 129.

Translated by O. E. Khadin

Plasma Physics Reports, Vol. 27, No. 6, 2001, pp. 542–544. Translated from Fizika Plazmy, Vol. 27, No. 6, 2001, pp. 573–576.

LOW-TEMPERATURE PLASMA

Production of Excimer Molecules and the Excitation of Nitrogen in a Steady-State Low-Pressure Electric Discharge

A. K. Shuaibov, A. I. Dashchenko, and I. V. Shevera

Uzhgorod National University, Pidgirna ul. 46, Uzhgorod, 88000 Ukraine

Received November 8, 2000; in final form, December 18, 2000

Abstract—Conditions for the simultaneous production of argon and xenon chlorides and excited nitrogen molecules in a longitudinal dc glow discharge in Ar/Cl_2/air, Xe/Cl_2/air, and $Ar/Xe/Cl_2$/air mixtures are studied. The electrical parameters of the plasma and its optical characteristics in the 130- to 350-nm wavelength range are investigated. It is shown that a small admixture of air added to argon or xenon leads to the production of excited nitrogen molecules, whose decay is accompanied by the molecular band emission in the range $\Delta\lambda$ = 176–271 nm. The conditions for simultaneous emission of the ArCl(*B*–*X*), XeCl(*B*–*X*), and nitrogen molecular bands are determined. © *2001 MAIK "Nauka/Interperiodica".*

1. INTRODUCTION

A low-pressure glow discharge in the mixtures of noble gases with chlorine has been systematically studied over the last twenty years [1, 2]. Interest in this type of discharge is related to its applications in plasmochemistry [3], lighting engineering [4–6], quantum electronics [7], and other fields of science and technology. Low-pressure excimer lamps pumped by a dc glow discharge, which emit in the XeCl 308-nm (Xe/Cl_2 mixture) or KrCl 222-nm (Kr/Cl_2 mixture) bands, provide (without forced cooling) a radiation power of W = 10–20 W with an efficiency of 12–23% [4, 5]. To operate at shorter wavelengths and create multiwavelength excimer lamps, it appears promising to use argon-based working mixtures, such as the Ar/Cl_2 mixture (the system of ArCl 175-nm and $Cl_2(D'–A')$ 258-nm bands) and the more complicated $Ar/Xe/Cl_2$ mixture (λ = 308, 258, 236, and 175 nm [8]). At present, there are no data on the VUV and UV emission spectra of a dc glow discharge in Ar/Cl_2 and $Ar/Xe/Cl_2$ mixtures. In most cases, the working mixtures of excimer lamps contain residual air at a pressure of $P \le$ 10–30 Pa; under certain conditions, this air can significantly affect the optical characteristics and the service life of excimer lamps.

In this paper, we study the emission from a longitudinal dc glow discharge in the Ar/Cl_2/air, Xe/Cl_2/air, and $Ar/Xe/Cl_2$/air mixtures under experimental conditions close to those in low-pressure excimer lamps.

2. EXPERIMENTAL SETUP

A dc longitudinal discharge is ignited in a cylindrical quartz tube with an inner diameter of 5 mm. The distance between 10-mm-long and 5-mm-diameter hollow cylindrical electrodes made of a Ni foil is 100 mm. The electrodes are placed inside the discharge tube with open ends. To increase the service life of the excimer lamp, replace the gas mixture heated in the discharge, and prevent cataphoresis, the discharge tube is housed in a 10-l-volume buffer chamber. The chamber is hermetically connected to a half-meter-long vacuum monochromator equipped with a 1200-line/mm diffraction grating. The axis of the discharge tube coincides with the centers of both the entrance and exit monochromator slits. The recording system is the same as in [8–10]. The discharge is powered by a high-voltage dc power supply ($U_{ch} \le$ 30 kV, $I_{ch} \le$ 100 mA). To stabilize the discharge, a ballast resistor (r_b = 0.4–0.7 MΩ) is set into the anode circuit.

3. ELECTRICAL AND OPTICAL CHARACTERISTICS OF THE PLASMA

Figure 1 shows the current–voltage characteristics of a discharge in $Ar/Xe/Cl_2$/air mixtures. In the high-current phase, the glow discharge operates in the subnormal mode (I_{ch} = 2–6 mA), which is used most extensively in low-pressure excimer lamps [6]. At $I_{ch} \le$ 6 mA, the discharge switches into the normal mode, in which the discharge voltage U_{ch} is almost independent of the current. An increase in the argon content (and, consequently, the total pressure of the mixture) increases the ignition voltage and the value U_{ch} without changing the current-voltage characteristic.

The emission spectra of a glow discharge in the mixtures of Ar and Xe with small admixtures of chlorine and air are shown in Fig. 2. The spectrum of the Ar/air plasma (as well as that of Kr(Xe)/air plasmas under the same experimental conditions) consists of a set of narrow, 1.5-nm-wide, molecular bands with a wing on the

1063-780X/01/2706-0542$21.00

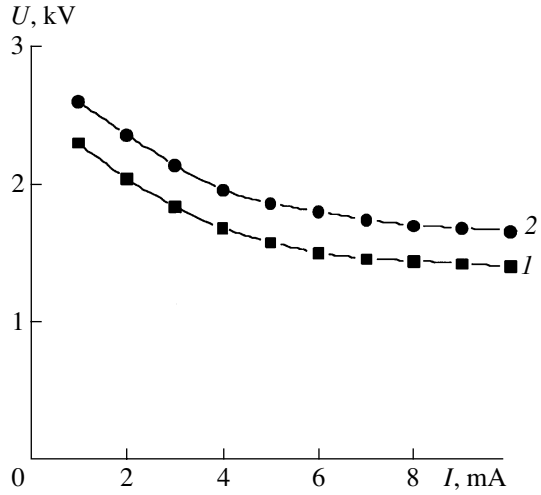

Fig. 1. Current-voltage characteristics of dc glow discharges in the Ar/Xe/Cl_2/air = (*1*) 1.33/0.08/0.08/0.013- and (*2*) 2.8/0.08/0.08/0.013-kPa mixtures.

short-wavelength side and a sharp edge on the long-wavelength side. The relative intensities of these bands, which are determined taking into account the relative spectral sensitivity of the vacuum monochromator–FEU-142 system, are presented in the table. With small admixtures of chlorine to Xe/air and Ar/air mixtures, the spectra contain both the ArCl(*B*–*X*) 175-nm, XeCl(*D*–*X*) 236-nm, XeCl(*B*–*X*) 308-nm, and Cl_2(*D*'–*A*') 258-nm bands and the above listed molecular bands in the range $\Delta\lambda$ = 176–271 nm (Fig. 2). Only the most intense bands of argon and xenon chlorides, as well as the Cl_2(*D*'–*A*') 258-nm band, survive as the chlorine partial pressure increases to 250–300 Pa at an Ar (or Xe) pressure of 2–3 kPa. Under these conditions, the total power of spontaneous emission from the entire lamp surface is 0.7–1.0 W, the efficiency being 3–5%. The highest power of spontaneous emission in the band system with λ = 175, 199, 222, 236, 258, and 308 nm (W = 2.2 W with an efficiency of 9%) is attained with an Ar/Kr/Xe/Cl_2 = 2.0/0.24/0.24/0.08 kPa mixture. Since the occurrence of molecular bands in the 176- to 271-nm range is independent of the noble gas species (Ar, Kr, or Xe), these bands can be related to the presence of a small air admixture in the working mixtures.

The emission spectra were identified using the data from [11]. In Fig. 2, the most intense bands in the 214- to 271-nm range belong to the third Kaplan system of N_2 ($A^3\Sigma_u^+$–E), whereas the band with an edge at λ = 235 nm belongs to the fourth positive system of molecular nitrogen ($B^3\Pi_g$–$D^3\Sigma_u^+$). All of the spectra contain a weak Cl_2 (*D*'–*A*') 258-nm band; presumably, this is due to chlorine emerging from the wall and the inner elements of the buffer chamber.

The simultaneous production of argon and xenon chlorides and excited nitrogen molecules is found to

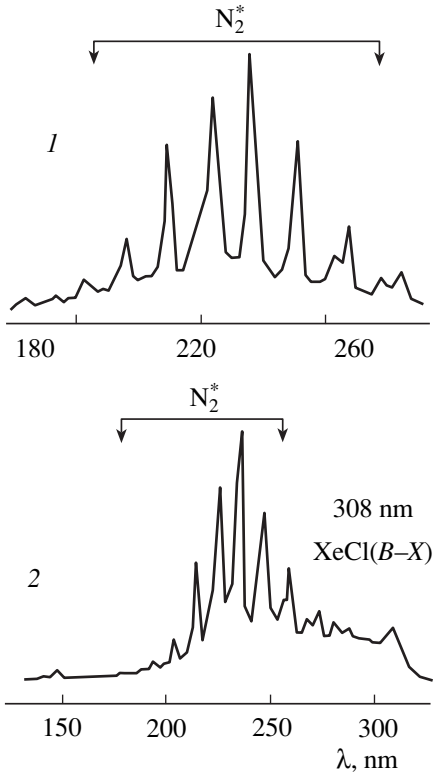

Fig. 2. Emission spectra from the plasma of a longitudinal glow discharge in argon and xenon with small admixtures of chlorine and air: (*1*) Ar/air = 4.0/0.013-kPa mixture and (*2*) Xe/Cl_2/air = 2.0/0.013/0.013-kPa mixture.

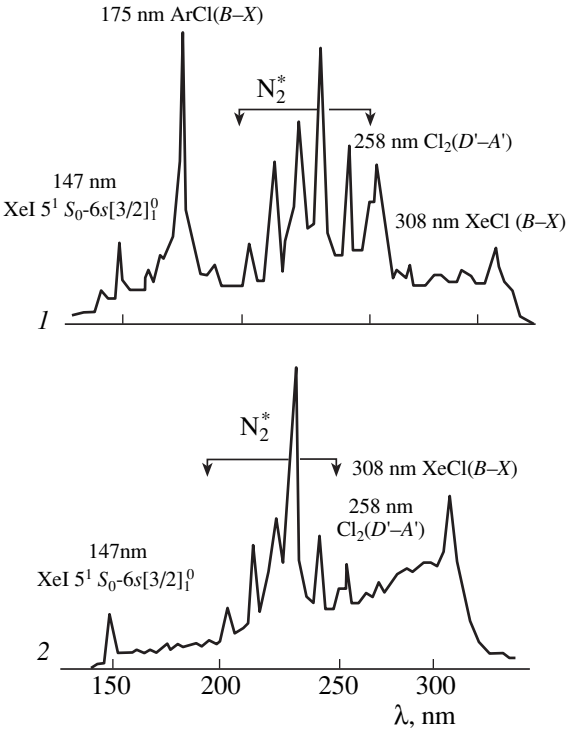

Fig. 3. Emission spectra from the plasma of a glow discharge in the Ar/Xe/Cl_2/air = (*1*) 6.0/0.04/0.08/0.013- and (*2*) 6.0/0.4/0.08/0.013-kPa mixtures for I_{ch} = 8 mA and U_{ch} = 1.2 kV.

Intensities of the emission bands of nitrogen molecules in a dc glow discharge in the Ar/air = 4.0/0.013-kPa mixture at I_{ch} = 5 mA

λ, nm	176	186	194	204	215	227	237	247	259	271
J/k_λ, rel. units	0.07	0.07	0.11	0.36	0.62	0.76	1.00	0.71	0.38	0.20

occur in a glow discharge plasma in Ar/Xe/Cl_2 mixtures with small admixtures of air. The emission spectra of such plasmas are shown in Fig. 3. At a low content of xenon ($P_{Xe} \le 0.10$ kPa), this type of plasma acts as a multiwavelength source of radiation in the ArCl and XeCl 175/236/308-nm molecular band system, the Cl_2 (D'–A') 258-nm band, and nitrogen molecular bands in the range 215–271 nm. The spectra also contain the XeI 147-nm resonant line. The dependence of the intensities of the ArCl(B–X) and XeCl(B–X) bands and the N_2 band with the 247-nm edge on the xenon pressure is shown in more detail in Fig. 4. At P_{Xe} = 0.08 kPa, the intensities of the excimer bands are approximately the same and the intensity of the 247-nm nitrogen band does not exceed 25–30% of the intensity of the XeCl(B–X) 308-nm band. As the xenon content increases ($P_{Xe} \ge 0.08$ kPa), the intensity of the 247-nm band varies slightly, whereas the intensity of the 175-nm band decreases significantly. Since the experiments are carried out at a fairly high argon pressure, the increase in the xenon pressure above 0.13 kPa leads to a contraction of the discharge and a decrease in the band intensities.

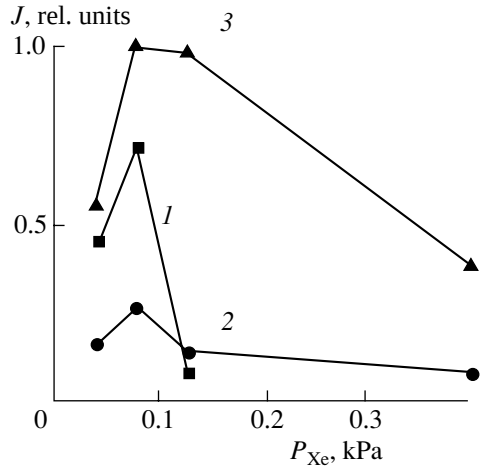

Fig. 4. Intensities of the emission bands of excimer molecules and nitrogen in a dc glow discharge in the Ar/Xe/Cl_2/air = 6.0/P_{Xe}/0.08/0.013-kPa mixture vs. the xenon pressure: (*1*) ArCl(B–X) 175-nm, (*2*) N_2^* 247-nm, and (*3*) XeCl(B–X) 308-nm bands.

4. CONCLUSION

In the emission spectrum of a longitudinal dc glow discharge in mixtures of noble gases with small admixtures of chlorine and air, a system of equidistant narrow ($\Delta\lambda$ = 1.5 nm) bands of excited molecular nitrogen in the 176- to 271-nm range has been found. The conditions for the simultaneous production of argon and xenon chlorides and excited nitrogen molecules at a total pressure of ≤6.0 kPa and I_{ch} = 2–20 mA have been determined (P_{Xe} = 0.08 kPa and the air pressure is 0.13 kPa). A discharge in the Ar/Xe/Cl_2 mixture (P_{Ar} = P_{Xe} = 2–3 kPa and P_{Cl_2} = 0.25–0.3 kPa) is a source of multiwavelength radiation with maxima at 175, 236, 258, and 308 nm, an output power of ≤1 W, and efficiency of ≤5%. It is of interest to use the system of nitrogen bands in short-wavelength lamps with various types of pumping (longitudinal glow discharge, transverse nanosecond discharge, and different types of RF discharges) in order to expand the operating spectral range of low-pressure lamps.

REFERENCES

1. V. V. Zaĭtsev, E. Yu. Zverevskaya, Ya. I. Zukher, and P. D. Netyagov, Teplofiz. Vys. Temp. **16**, 1152 (1978).
2. V. V. Zaĭtsev, P. D. Netyagov, and N. V. Bozhko, Teplofiz. Vys. Temp. **18**, 944 (1980).
3. B. S. Danilin and V. Yu. Kireev, *Application of a Low Temperature Plasma for Etching and Cleaning of Materials* (Énergoatomizdat, Moscow, 1987).
4. A. P. Golovitskiĭ, Pis'ma Zh. Tekh. Fiz. **18** (8), 73 (1992) [Sov. Tech. Phys. Lett. **18**, 269 (1992)].
5. A. P. Golovitskiĭ and S. V. Lebedev, Opt. Spektrosk. **82**, 251 (1997) [Opt. Spectrosc. **82**, 227 (1997)].
6. A. N. Panchenko and V. F. Tarasenko, Opt. Spektrosk. **84**, 389 (1998) [Opt. Spectrosc. **84**, 337 (1998)].
7. E. B. Gordon, V. G. Egorov, V. T. Mikhkel'soo, *et al.*, Kvantovaya Élektron. (Moscow) **15**, 285 (1988).
8. A. K. Shuaibov, Pis'ma Zh. Tekh. Fiz. **26** (9), 1 (2000) [Tech. Phys. Lett. **26**, 357 (2000)].
9. A. K. Shuaibov and A. I. Dashchenko, Kvantovaya Élektron. (Moscow) **30**, 279 (2000).
10. A. K. Shuaibov, L. L. Shimon, A. I. Dashchenko, and I. V. Shevera, Teplofiz. Vys. Temp. **38**, 386 (2000).
11. L. Wallace, Astrophys. J., Suppl. Ser. **4**, 445 (1962).

Translated by N. N. Ustinovskiĭ